Open-Source System and New Methods of Characterisation for Novel Piezoelectric Materials and Harvesters

Krany, Marcin Jan

Award date:
2020

Awarding institution:
University of Bath

Open-Source System and New Methods of Characterisation for Novel Piezoelectric Materials and Harvesters

submitted by

Marcin Jan Kraśny

for the degree of Doctor of Philosophy

of the

University of Bath

Department of Mechanical Engineering

August 2020

COPYRIGHT

Signature of Author.....

Rodzicom, Dzieciom, Żonie.

"The more he studied, the more vistas he caught of fields of knowledge yet unexplored, and the regret that days were only twenty-four hours long became a chronic complaint with him."

— Jack London, Martin Eden

ABSTRACT

Electronic devices capable of converting ambient vibration energy into useful electrical power are highly desirable for next generation of self-powered, wireless, and wearable devices. It enables them to work independently and with no need of replacement and management of batteries. Piezoelectric materials are of prime interest among researchers as successful candidate to act as the harvesting source for such devices. However, several challenges in the characterisation and energy extraction from ambient vibrations need to be addressed to enable successful commercial application. One of the key problems is a lack of dedicated measurement tools for complex characterisation of the electrical output when harvesting from structures that incorporate piezoelectric transducers. In addition, due to a complex mechanical-electrical form of operation of energy harvesters, their performance testing during operation is challenging as the functioning of the device depends on environmental parameters such as temperature, humidity, frequency, and excitation amplitude.

To open up research on piezoelectric energy harvesters to a broader audience, the main issues and challenges are discussed, and potential solutions with respect to new measurement techniques, experimental setups and method for characterisation of harvesting devices are proposed in this thesis. This is realised via the development of a novel, adjustable measurement system capable of complex characterisation of energy harvesting devices at room temperature and at elevated temperatures as encountered in real life applications. Additionally, a new method for evaluation of piezoelectric energy harvester during its operation allowing for estimation of device core parameters and simple, yet effective performance characterisation is also proposed.

In line with current world research in the field, significant improvements in the area of piezoelectric ceramics, piezoelectric composites and mechanical structures are also proposed. This is realised with a study on freeze-cast piezoelectric composites where complex porous structures were found to have enhanced energy harvesting figures of merit and increased piezoelectric coefficients, demonstrating improved effectiveness in energy harvesting system. Finally, a novel cantilever beam structure operating in bend-

twisting mode for broadening of the available frequency bandwidth and increased power density of piezoelectric energy harvester is proposed.

The work presented in this thesis further expands on the potential applications of freeze-cast porous piezoelectric materials, mechanical twist bending modes, and shows new opportunities for manufacturing of future electronic self-powered devices.

ACKNOWLEDGEMENTS

Most importantly, I wish to thank my supervisor Chris Bowen for entrusting me with the project and allowing me to work independently on things that interest me the most. Thanks for the patience, guidance, and rapid corrections to all my manuscripts.

I am grateful to my second supervisor Peter Wilson, thanks for always being there and for your support.

I am also in debt to John Taylor for solving all the math problems and forcing me to creative thinking and finding new ways for experimental solutions.

Special thanks to Nick for letting me stay at his place during the country transition and my final weeks in the lab. Also, for his persistence in unsuccessful attempts at teaching me rugby rules during our evening talks with wine.

Thank you to all the people related to NEMESIS project, namely Andrew, Emily, Eleanor, Hamideh, Holly, James, Manu, Mathew, Mengying, Vana and Yan, it has been a pleasure to work with you and to learn from you. I need to give a special mention to Peter 'Twitch' Harris, who helped get me started in the lab in my first few weeks, and Daniel Zabek for his pep talks (*"With piezo-electrics you can always make up some useless energy harvesting experiment and publish a paper"*) towards the end of my writing process.

Thanks to the best group of friends: Alek, Cys, Prach, Anagna and Oko for never ending support even though they still do not have any idea what piezoelectric effect is. Thanks for all the parties and late-night talks to you all! Let us keep this that way!

Finally, to the best wife Kasia, this PhD has been a long process with many tough periods and through all of this she has been there; Kocham Cię, dziękuję za cierpliwość.

It was quite a journey, thanks to you all!

NOTE ON FORMAT

This thesis has formed the basis of five research papers in refereed journals on the theme of electrical characterisation of vibration powered energy harvesting systems for self-powered sensors and electronic devices. Chapter 1 consists of broad introduction to the topic of piezoelectric energy harvesting. Chapter 2 describes an open-source automated measurement tool. Chapter 3 extends the work on characterisation and presents a novel indirect method to characterise piezoelectric devices. These two chapters presented in form of two research papers detail new measurement techniques and methodologies for complex characterisation of piezoelectric energy harvesters during operation. The remaining three papers presented in Chapters 4 and 5 explore improvements in piezoelectric material properties and mechanical structures for improved energy harvesting performance.

For ease of reading, each chapter is preceded with a *"Prologue"* followed by a *"Statement of Authorship"* which provides a detailed description of the author's contribution to the work presented. The main text of the published research paper is then presented in a style that is consistent with the thesis format. After the main body of the paper is presented, an additional *"Summary"* section is provided along with a list of key findings, their relation to the other research in the thesis, and a contribution to the overall thesis theme.

Each chapter and paper is organised with its own references list in an order that is compatible with the version published in a journal. In addition, a full list of references in alphabetical order is presented at the end of the thesis. Finally, the overall conclusions, impact of the thesis and proposed directions for future research are discussed in the Chapter 6.

CONTENTS

LIST OF FIGURES

LIST OF TABLES

LIST OF ACRONYMS

AC	Alternating Current
ADC	Analog to Digital Converter
BURPS	Burned out Polymer Spheres
C_L	Load Capacitance
CFRP	Carbon Fibre Reinforced Polymer
CSV	Comma Separated Values
DC	Direct Current
DMM	Digital Multimeter
DOF	Degree of Freedom
DUT	Device Under Test
E_C	Coercive Field
ENHAMER	Energy Harvesting Measurement Rig
ESI	Electronic Supplementary Information
ESR	Equivalent Series Resistance
FOM	Figure of Merit
FWB	Full Wave Bridge
GPIB	General Purpose Interface Bus
HIL	Hardware In the Loop
HT	High Temperature
I_{SC}	Short Circuit Current
IoT	Internet of Things
LCR	Impedance Capacitance Resistance
LEC	Low Electromechanical Coupling
MEMS	Micro Electro Mechanical Systems
MFC	Macro Fiber Composite
NEMESIS	Novel Energy Materials, Engineering Science and Integrated Systems
OOP	Object Oriented Programming
P_r	Remnant Polarisation

PCB	Printed Circuit Board
PDMS	Polydimethylsiloxane
P-E	Polarisation Electric
PVDF-TrFE	Poly(vinylidenefluorideco-trifluoroethylene)
PZT	Lead Zirconate Titanate
R_L	Load Resistance
RMS	Root Mean Square
RS232	Recommended Standard 232
RT	Room Temperature
SCPI	Standard Commands for Programmable Instruments
SEM	Scanning Electron Microscopy
SPICE	Simulation Program with Integrated Circuit Emphasis
SSHI	Synchronized Switch Harvesting on Inductor
TCP	Transmission Control Protocol
TFT	Thick Film Technology
UML	Unified Modelling Language
USB	Universal Serial Bus
V_{OC}	Open Circuit Voltage
VISA	Virtual Instrument Software Architecture

CHAPTER 1

INTRODUCTION

The global demand towards the miniaturization of electronic components in recent decades has led to a decrease in the energy consumption of electronic devices and an increase in computational power [1, 2]. Due to the wide spectrum of available sensors for sensing temperature, pressure, humidity, strain, fluid flow, and gases contamination, the role of sensor-based systems becomes increasingly important and the natural consequence of an increasing number of sensors is the development of sensor networks, where the individual sensory nodes exchange data with each other.

By scaling the network in terms of size, it is possible to build new, or connect already existing systems, to the Internet which can result in improved data accessibility and provide a capability for objects to be sensed and remotely controlled. Such networks are now called the "Internet of Things" (IoT) and have their origin in the '90s. However, the main development is only now possible due to new electronic hardware, reduced power requirements, and improved software technologies [2]. The adoption of the IoT in production automation can be an effective approach to deliver a competitive product to the market. For example, industrial machines and vehicles can be equipped with built-in sensors to monitor the working and environmental parameters such as oil temperature, tire pressure, bearing rotation, vibration level, air contamination, and others. These parameters can be transmitted remotely in real time allowing prediction of mechanical or electrical failures before they occur or recommending maintenance schedules. Spare parts can also be ordered in advance, to avoid express shipping costs or a disruption in production. The ability for continual monitoring or emergency reporting can lead to greatly improved safety and reliability in construction (i.e. bridges [3], buildings [4]), health monitoring or even military systems [5]. The implementation of these solutions, especially in heavy industries such as automotive, aerospace, mining or the oil and gas industry, can also improve the safety of people and high cost equipment. Interconnected sensor systems can also be successfully applied in a variety of other sectors which include biosensors for biomedical applications [6, 7], low power wireless sensors in automotive [8,

5], smart watches, and smart clothes or wearable electronics [9].

However, sensor-based systems alone are incapable of operating independently and are only one of the necessary components of an electronic device which must be supplied with electrical power to fulfil tasks such as data acquisition, signal processing, and communication. Today, it is possible to achieve efficient communication between microsensors with a limited power requirement as small as milliwatts [10]. Most commonly, such a device would be powered from mains power, however, in some applications it is not possible to deliver a mains power supply due to a lack of electrical connection in the sensor's vicinity or due to an inability to provide electrical cables, especially in remote or difficult to reach locations. Cable connections are also often exposed to mechanical damage, which can reduce system reliability. Moreover, additional wiring can limit the movement of machinery or introduce increased stiffness or friction. An alternative power supply method, widely used in mobile devices, is to employ a battery-operated system. Nevertheless, disadvantages such as a discontinuous power supply during battery replacement, limited access to device and maintenance costs may disqualify this solution, especially if there are large numbers of sensors in a network. Furthermore, batteries are often made of materials which are not easily biodegradable and can be toxic and detrimental to the environment [11].

The challenge of providing sufficient continuous power to IoT devices in inaccessible or remote environments can be tackled by implementing energy harvesting solutions that are able to scavenge ambient energy such as heat, light, water, vibrations or radio frequency and converting it into a useable electrical power. The main energy harvesting technologies are presented in the form of a diagram in Fig. 1-1 which shows each approach in terms of the application field and working principles. Additionally, the character of a generated electrical output is highlighted, i.e. AC or DC.

From these main energy harvesting methods, the conversion of light into electricity using solar panels is the most advanced and mature technology. However, in an environment with reduced access to daylight, the utilization of other ambient power sources is necessary; for example motion and vibrations. Among the available mechanical vibration based harvesting techniques, the most promising energy conversion mechanisms are the piezoelectric effect and triboelectric (electrostatic) effect [13]. In addition with regard to these two mechanisms, piezoelectric transducers offer higher power densities [12].

Piezoelectricity describes the attribute of certain materials constructed of asymmetric crystals to generate an electrical charge after kinetic excitation and the application of a mechanical force. The piezoelectric effect can be successfully employed to harvest energy from various sources such as industrial machinery and transport, air movement,

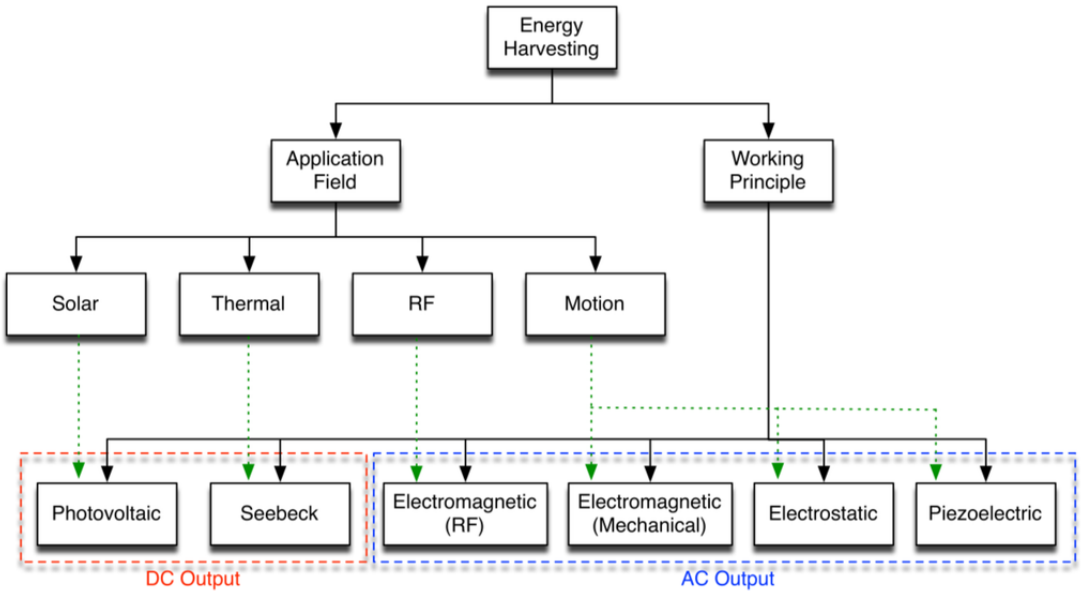

Figure 1-1: *Main energy harvesting technologies categorised by working principle and application field [12].*

human activity, or even an in-body motion such as chest and heart movement to power pacemakers and orthopaedic implants [12, 14]. Additionally, piezoelectric materials offer better compatibility with other technologies, such as Thick Film Technology (TFT) and micro-electro-mechanical-systems (MEMS) than e.g. electromagnetics, mainly due to the miniaturization limits of magnets [12].

Currently, the main activities of world research in the field of piezoelectric energy harvesting are focused on the development and improvements of piezoelectric materials, mechanical topologies of transducers (such as cantilevers), energy management [15, 16] and energy storage options (such as batteries and supercapacitors) [17, 18]. As stated by Zhou *et al.* in their broad review on mechanical energy harvesting, the major challenges in the field are in the development of high performance materials and devices [13].

To validate any improvements to the above, and at every stage of development of self-powered sensor devices, it is a requirement for adequate testing of all in-system components. However, currently there is no ready-to-use tool to deliver a complex characterisation of electrical output from energy harvesting devices. Thus, the main purpose of this thesis is to deliver a software and hardware solution that is easily applicable for a variety of measurements required by the broad range of applications. This is achieved by presenting an open software and open hardware tool: *Energy Harvesting Measurement Rig* (ENHAMER) described in detail in Chapter 2 in the form of a

published research paper.

Moreover, detailed system losses during vibration powered energy harvesting are challenging and difficult to measure. Thus, a novel and original method for characterisation of operating energy harvester with the indirect technique for device capacitance and generated current calculation is also proposed. Additionally, the method enables robust estimation of combined losses experienced by the harvester. This work is described in Chapter 3 in form of a published research paper.

In the following chapters a systematic improvement in materials via a unique method for manufacturing of piezoelectric composites with enhanced piezoelectric properties is described in the form of two published research papers. These publications are presented in Chapter 4. Finally, the performance of an energy harvesting device was improved by a proposed novel bend-twisting design of a cantilever beam that significantly enhanced the power available to be harvested in vibrating environment. This is presented in Chapter 5 as a published research paper.

All of the conducted research during the period of this PhD and work presented in this thesis is in line with the world research direction towards self-powered vibration powered energy harvesting sensor systems, wearable devices and IoT devices. With the final conclusions and future work described in Chapter 6, the author believes we are one step closer to make vibration powered devices an everyday reality.

References

[1] P. Glynne-Jones and N. White, "Self-powered systems: A review of energy sources," *Sensor Review*, vol. 21, no. 2, pp. 91–98, Jun. 2001.

[2] M. Walport, "The Internet of Things: Making the most of the Second Digital Revolution," Government Office for Science, Tech. Rep. GS/14/1230, Dec. 2014.

[3] E. Sazonov, H. Li, D. Curry, and P. Pillay, "Self-Powered Sensors for Monitoring of Highway Bridges," *IEEE Sensors Journal*, vol. 9, no. 11, pp. 1422–1429, Nov. 2009.

[4] K. Najafi, T. Galchev, E. E. Aktakka, R. L. Peterson, and J. McCullagh, "Microsystems for energy harvesting," in *Solid-State Sensors, Actuators and Microsystems Conference (TRANSDUCERS), 2011 16th International*. IEEE, 2011, pp. 1845–1850.

[5] S. W. Arms, C. P. Townsend, D. L. Churchill, J. H. Galbreath, and S. W. Mundell, "Power management for energy harvesting wireless sensors," vol. 5763, 2005, pp. 267–275.

[6] M. Koplow, A. Chen, D. Steingart, P. K. Wright, and J. W. Evans, "Thick film thermoelectric energy harvesting systems for biomedical applications," in *Medical Devices and Biosensors, 2008. ISSS-MDBS 2008. 5th International Summer School and Symposium On*. IEEE, 2008, pp. 322–325.

[7] B. Kirking, J. Krevolin, C. Townsend, C. W. Colwell Jr., and D. D. D'Lima, "A multiaxial force-sensing implantable tibial prosthesis," *Journal of Biomechanics*, vol. 39, no. 9, pp. 1744–1751, 2006.

[8] C. R. Bowen and M. H. Arafa, "Energy Harvesting Technologies for Tire Pressure Monitoring Systems," *Advanced Energy Materials*, vol. 5, no. 7, pp. n/a–n/a, Apr. 2015.

[9] H. Rao, D. Saxena, S. Kumar, G. V. Sagar, B. Amrutur, P. Mony, P. Thankachan, K. Shankar, S. Rao, and S. Bhat, "Low Power Remote Neonatal Temperature Monitoring Device." in *BIODEVICES*, 2014, pp. 28–38.

[10] Linear Technology, "Wireless Sensor Networks with very low power consumption at less than 50 microamper per node," Mar. 2016.

[11] ERP UK Ltd, "Why recycle batteries? | ERP Battery Recycling," http://www.erp-batteries.co.uk/why/, 2016.

[12] R. Caliò, U. B. Rongala, D. Camboni, M. Milazzo, C. Stefanini, G. de Petris, and C. M. Oddo, "Piezoelectric Energy Harvesting Solutions," *Sensors*, vol. 14, no. 3, pp. 4755–4790, Mar. 2014.

[13] M. Zhou, M. S. H. Al-Furjan, J. Zou, and W. Liu, "A review on heat and mechanical energy harvesting from human – Principles, prototypes and perspectives," *Renewable and Sustainable Energy Reviews*, vol. 82, pp. 3582–3609, Feb. 2018.

[14] C. R. Bowen, H. A. Kim, P. M. Weaver, and S. Dunn, "Piezoelectric and ferroelectric materials and structures for energy harvesting applications," *Energy & Environmental Science*, vol. 7, no. 1, pp. 25–44, Dec. 2013.

[15] S. R. Anton and H. A. Sodano, "A review of power harvesting using piezoelectric materials (2003–2006)," *Smart Materials and Structures*, vol. 16, no. 3, p. R1, 2007.

[16] M. Safaei, H. A. Sodano, and S. R. Anton, "A review of energy harvesting using piezoelectric materials: State-of-the-art a decade later (2008–2018)," *Smart Materials and Structures*, vol. 28, no. 11, p. 113001, Oct. 2019.

[17] Poonam, K. Sharma, A. Arora, and S. K. Tripathi, "Review of supercapacitors: Materials and devices," *Journal of Energy Storage*, vol. 21, pp. 801–825, Feb. 2019.

[18] Y. Liang, C.-Z. Zhao, H. Yuan, Y. Chen, W. Zhang, J.-Q. Huang, D. Yu, Y. Liu, M.-M. Titirici, Y.-L. Chueh, H. Yu, and Q. Zhang, "A review of rechargeable batteries for portable electronic devices," *InfoMat*, vol. 1, no. 1, pp. 6–32, Mar. 2019.

CHAPTER 2

OPEN-SOURCE, OPEN-HARDWARE ENERGY HARVESTING MEASUREMENT RIG (ENHAMER)

2.1 Prologue

Electrical characterisation of vibration powered energy harvesting devices requires reliable measurement systems. Currently there is no *off-the-shelf* available solution, thus researchers are forced to develop in-house complicated setups from variety of components such as electrodynamic shakers, signal generators, amplifiers, oscilloscopes, multimeters and others. Often due to their complexity, such systems are operated manually which reduces the repeatability of measurements and can lead to several complications with consistency and control over parameters during energy harvester characterisation.

In addition, the overall efficiency of the energy harvesting device depends on the energy losses introduced within all the system components, such as the piezoelectric transducer, mechanical structure, and associated electronics, e.g. rectifying circuit. Losses can be more severe in harsh industrial environments, which can negatively influence the reliability and lifetime of system components. Therefore, it is necessary to develop a protocol for testing the entire device and its subsystems in any configuration and under a range of environmental conditions.

Work presented in this chapter describes the technical difficulties in electrical characterisation of vibration powered energy harvesters, explains common challenges in measurements, offers guidance and solutions for testing at both room and elevated temperatures. Finally, an easy to incorporate measurement system with experiment routines in the form of an automated, software-controlled protocol is delivered as an open-source and open-hardware tool.

Paper 1: Statement of Authorship

<table>
<tr><td colspan="10">This declaration concerns the article entitled:</td></tr>
<tr><td colspan="10">A System for Characterisation of Piezoelectric Materials and Associated Electronics for Vibration Powered Energy Harvesting Devices</td></tr>
<tr><td colspan="10">Publication status (tick one)</td></tr>
<tr><td>Draft manuscript</td><td></td><td>Submitted</td><td></td><td>In review</td><td></td><td>Accepted</td><td></td><td>Published</td><td>✓</td></tr>
<tr><td colspan="10">Copyright status (tick the appropriate statement)</td></tr>
<tr><td colspan="3">I hold the copyright for this material</td><td></td><td colspan="5">Copyright is retained by the publisher, but I have been given permission to replicate the material here</td><td>✓</td></tr>
<tr><td>Publication details (reference)</td><td colspan="9">M. J. Kraśny and C. R. Bowen,
“A System for Characterisation of Piezoelectric Materials and Associated Electronics for Vibration Powered Energy Harvesting Devices”,
Measurement, p. 108285, Jul. 2020,
DOI: 10.1016/j.measurement.2020.108285.</td></tr>
<tr><td>Candidate’s contribution to the paper (detailed and also given as percentage)</td><td colspan="9">Formulation of ideas:
Solely the candidate (100%)

Design of methodology:
Solely the candidate (100%)

Experimental work:
Solely the candidate (100%)

Presentation of data in journal format:
Solely the candidate (100%)</td></tr>
<tr><td>Statement from Candidate</td><td colspan="9">This paper reports original research I conducted during the period of my Higher Degree by Research candidature.</td></tr>
<tr><td>Signed</td><td colspan="4">  </td><td>Date</td><td colspan="4">08.08.2020</td></tr>
</table>

A System for Characterisation of Piezoelectric Materials and Associated Electronics for Vibration Powered Energy Harvesting Devices

Marcin J. Kraśny[1,2], Chris R. Bowen[1]

[1] Department of Mechanical Engineering, University of Bath, Bath, BA2 7AY, UK
[2] Advanced Biological Imaging Laboratory, School of Physics, College of Science and Engineering, National University of Ireland, Galway (NUIG), Ireland

Abstract

Self-powered sensor systems that are able to harvest energy from surrounding vibrations are a promising solution for wearable devices, Internet of Things (IoT) and sensing in challenging industrial environments. An automated, adjustable system for testing piezoelectric energy harvester devices is necessary to ensure that developed solutions provide sufficient energy output, minimal losses and reliability of all components under a range of operating conditions. Herein we propose a novel and unique solution as a standalone software tool developed in Python with optional electronics to achieve automated characterisation of electrical properties of vibration powered energy harvesters. Due to its unique modular construction, the tool can be applied to a variety of experimental conditions, to enhance and facilitate piezoelectric materials characterisation and validate self-powered devices for wide spectrum of industrial applications, including long-term performance and fatigue testing. We demonstrate its performance and capabilities by testing piezoelectric materials and electronic circuits at a range of conditions such as (i) high temperature piezoelectric material characterization, (ii) high temperature rectifying circuit performance, and (iii) room temperature investigation of an energy harvesting device. We release the software and hardware described in this work as an open-source tool freely available to broader audience.

Keywords

test station, energy harvesting, piezoelectric, laboratory automation, instrumentation control, python, automatic test bench

2.1.1 Introduction

Energy harvesting that aims to convert energy from ambient environmental vibrations into useful electrical power is of growing interest by industrial and academic researchers across a range of disciplines. Currently, the core of world research in the field of piezoelectric energy harvesting has a focus on the development and improvement of piezoelectric materials, transducers, mechanical topologies (such as cantilevers), energy management [1, 2, 3] and energy storage options such as batteries and supercapacitors [4, 5]. In parallel, the development of low power consumable electronics such as wearable devices, medical devices and sensor systems which are driven by the Internet of Things (IoT) enables the use of energy harvesting techniques to be applied as a power source in such devices [2, 6, 7, 8].

It is not uncommon for researchers focused on development and improvement in piezoelectric energy harvesters to show the potential with an example energy harvesting demonstrator [8, 9, 10, 11, 12, 13, 14, 15, 16, 17, 18, 19, 20, 21, 22, 23, 24, 25, 26, 27, 28, 29, 30, 31, 32, 33, 34]. Moreover, the field of piezoelectric energy harvesters is explored by biomedical engineers developing electroactive materials, such as tissue engineering for piezoelectric scaffolds [35], which opens a new area for testing systems, similar to those for energy-harvesting [36, 37]. This multidisciplinary field of research creates possibilities for broad collaborations across researchers; however, this also requires knowledge and expertise on measurement techniques from a variety of disciplines, including material science, mechanical engineering and electronics engineering.

Typically, the characterisation of piezoelectric materials in terms of their fundamental properties requires readily available *off-the-shelf* and ready to use measurement setups. This includes standard impedance-capacitance-resistance (LCR) meters or impedance-phase analysers (for example Solartron 1296 [38], N4L PSM3750 [32], HP/Keysight4294A [39]) for capacitance and permittivity measurement. Testing protocols are described in available standards [40, 41, 42] and measurement practice is explained in details by Cain and Stewart *et al.* [43, 44, 45]. Moreover the commonly reported piezoelectric coefficients d_{33} and d_{31} can be measured with the widely used and recognized Berlincourt method; a detailed procedure with example instrumentation is presented by Stewart *et al.* [46].

For challenging conditions, such as testing at elevated temperatures for industrial

applications, the measurement of the most important parameters of the piezoelectric material, namely the Curie temperature [T_c] and operating temperature [T_d], is defined with standards [41, 47, 48]. Other approaches to measure properties such as the electromechanical coupling factor, relative permittivity, dielectric loss, ferroelectric hysteresis and material degradation are also described and well explained [38, 44, 49, 50, 51, 52, 53, 54, 55].

However, the primary current challenge with electrical characterisation of energy harvesters is the lack of *ready-to-use* measurement instrumentation and software solutions. In many cases, energy harvester test rigs are often based on a custom-built combination of variety of devices and instrumentation, such as signal generators, amplifiers, electrodynamic shakers, accelerometers, digital multimeters, ammeters, charge amplifiers, electrometers, oscilloscopes, resistance decades, and laser-vibration meters [8, 9, 10, 11, 12, 13, 14, 15, 16, 17, 18, 19, 20, 21, 22, 23, 24, 25, 26, 27, 28, 29, 30, 31, 32, 56, 57, 58]. An encapsulated example of such a station is presented in Fig. 2-1 as a block diagram. Additionally, these in-house developed setups are often controlled manually [33, 12, 59, 60, 14, 61, 21, 22, 23, 62] or with a custom LabView [6, 19, 56, 63, 64, 65, 66] or MATLAB [15] programs that are not available to the public. The closed-source policy, often with limited details on the measurement setup presented in research publications, limits the repeatability and comparability of results. It also creates a high entry threshold for people from other potential disciplines interested in testing energy harvesting devices.

The current standard that describes the measurement protocol for electrical characterisation of flexible energy harvesters was only recently published, and there is scope for further improvements [67]. The standard describes core measurements which are similar to most typical tests delivered by researchers in the field to date and are currently considered as a "gold standard". These tests include short circuit current (I_{SC}), open circuit voltage (V_{OC}), power delivered to a resistive load, and optimal electrical load. Furthermore, as suggested by standard and recent work by Salazar *et al.* [3], reliability and long-time performance at the operating temperature and humidity range should be measured and reported. Additionally, while it is not mentioned in the standard, it is common for researchers in the field of energy harvesting to deliver a capacitor charging curve with time as an ultimate proof of a harvester's performance and its ability to be applied as a potential power supply for electronic devices [6, 9, 10, 11, 15, 25, 27, 68].

2.1.2 Typical Vibration Energy Harvesting Testing Station

The successful characterization of electrical output of piezoelectric energy harvesters requires expertise in mechanical and electrical measurements, and often also requires advanced programming skills for synchronisation and control over a complex testing rig.

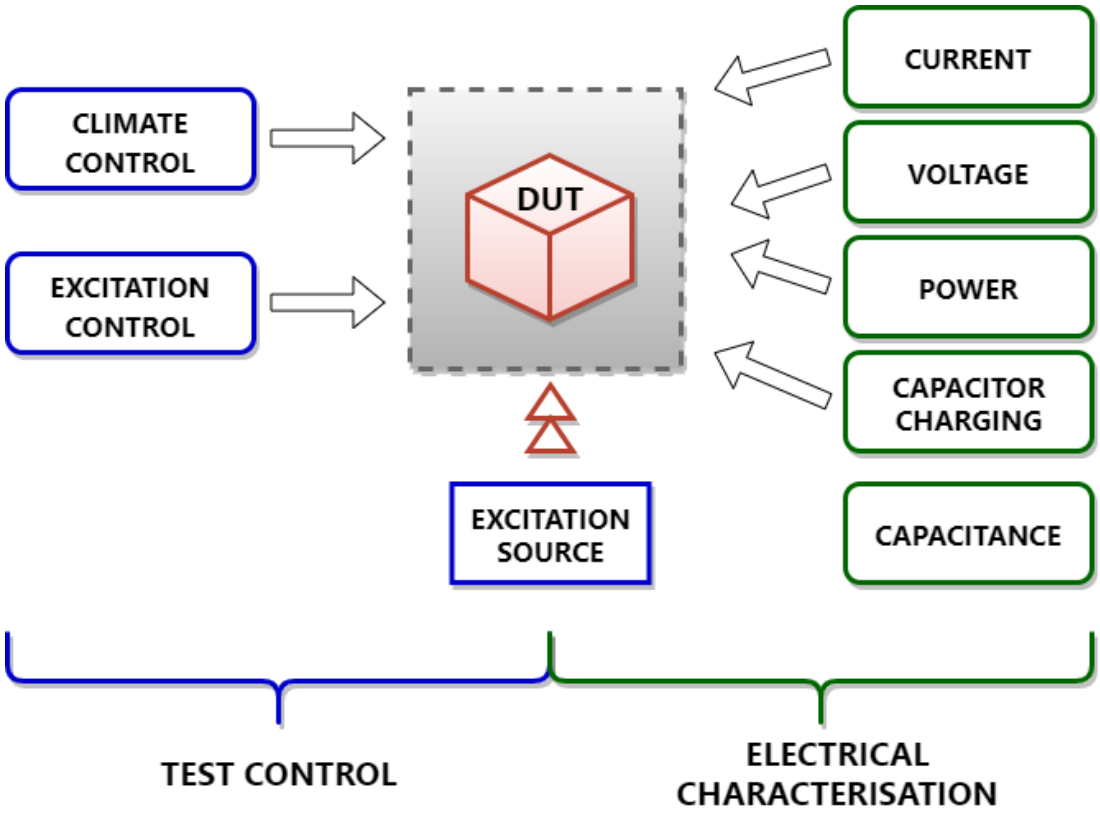

Figure 2-1: *General block diagram of a vibration powered energy harvesting experimental setup typically used for electrical characterisation and performance measurements of device under test (DUT). [Kraśny, M.J. (2020), DOI: 10.6084/m9.figshare.12585023, CC BY 4.0 license]*

The fundamental components of a typical measurement setup, with common challenges and potential technical difficulties, are now further explained.

Excitation Source

The core of a vibration energy harvesting test station is in vibration generation. An electrodynamic shaker controlled by an amplified signal from generator is the most frequently used system. In some experimental set-ups, the electrodynamic shaker can be replaced by a customised conventional loudspeaker [63, 65, 69]. Other excitation sources could be built from a piezoelectric motor or linear motors [70], rotating motor [9, 39, 58], or electro-magnet [61, 59, 33, 71]. Alternatively, manual stimulation via, for example, finger poking [29], objects dropping [72] or spring response of a mechanically prestressed energy harvesting structure [73] can be applied. Excitation of device under test (DUT) is measured in terms of acceleration, pressure or displacement. The ideal testing station

should allow testing in the controlled excitation force and frequency sweep.

Excitation Control

When an electrodynamic shaker is used to vibrate the piezoelectric device it is important to consider the nonlinear behaviour of the excitation signal (signal generator amplitude) on the resulting acceleration (m/s^2) as a function of frequency [74, 75]. When a frequency sweep test is performed, for example when undertaking a search of a piezoelectric cantilever's mechanical resonance it is required to excite the DUT with a constant acceleration over the whole frequency range of interest. This is a non-obvious drawback of using electrodynamic shakers, which can introduce significant errors if no excitation monitoring is provided. To overcome this problem an additional instrumentation for vibration control could be added to the system. Alternatively, a software regulator to actively control the acceleration over the measurement range could be implemented. As a replacement for the above, an interesting and simple solution was presented by Harris *et al.* [20, 24] and further used by Xie *et al.* [28]. Here the shaker is pre-calibrated with the use of laser vibrometer which results in a creation of a table where signal generator amplitudes and caused accelerations are recorded. Later, when the DUT is examined the software implementation allows for extrapolation of a necessary generator amplitudes for a desired acceleration from a calibration data.

Climate Control

There are limited reports of energy harvester systems operating at elevated temperatures that enable energy scavenging at temperatures of up to 300°C [53, 72, 76, 77]. The necessary electronics is also commonly tested at temperatures of up to 225°C [78]. Potential solutions that use an integrated heater were proposed by Hamideh *et al.* [53], and an adapted d_{33} Berlincourt setup was proposed by Huang *et al.* [54]. These configurations could be of use in low excitation range of vibrations limited by the mechanical resonance and acceleration power generated by a d_{33} meter. The more flexible solutions with a use of a high temperature furnace are presented by Barker *et al.* [76] and Le Boulbar *et al.* [52]. In this case, the sample is attached or stimulated by a rod excited by an external shaker which has access to the heated chamber through a dedicated hole in the furnace cover. This solution allows for testing of larger structures, such as cantilevers, in a wide range of frequencies and excitation amplitudes.

A use of climate control in testing systems is less well reported in the literature, but it is of importance when a device is dedicated for use in a range of industrial applications. Long-term analysis at a specific temperature and within controlled humidity range are

the obvious environmental conditions necessary to be considered when designing the final device. In addition, such testing is recommended by Salazar *et al.* [3] and is in accordance with the standard [67].

Short Circuit Current (I_{SC})

The generated current can be measured with electrometer, picoammeters or digital multimeters (DMM) as an average value (true RMS) or as a maximum peak value. Some reports also use a current amplifier to deliver charge measurement [14, 17, 79]. Problems to achieve true short circuit conditions may rise when a low current output is measured with high ohmic shunt resistances, such as when measuring current with a digital multimeter (DMM). Additionally, the peak value of current usually reported in studies might not necessarily provide sufficient detail of the performance of the energy harvester when compared to average value and total charge extracted over the whole excitation period [39, 79].

Open Circuit Voltage (V_{OC})

Commonly used equipment to measure open circuit voltage include digital multimeters (DMM), oscilloscopes or electrometers. The most important problem arising with the open circuit voltage output of the energy harvester is the input impedance of the measuring device [80, 81]. Additionally, the user must be aware that high input impedance of test equipment in combination with high equivalent impedance of the piezoelectric device (reactive capacitance) can increase the influence of the mains noise (or other capacitive or electrostriction coupled) on measurement. Similarly, like the short circuit current, an average value might be of higher importance to the overall device performance than a maximum (peak) value, especially when device is excited with a nonsymmetric or nonperiodic signal.

Dielectric Properties (Device Capacitance)

Typically, the instrumentation used to measure dielectric properties include an LCR or Impedance Analyzer meter. The capacitance of a piezoelectric device can alter as a function of temperature, excitation or strain induced in the piezoelectric transducer. It may also be of interest to consider measurement and calculation of an equivalent circuit model of an active capacitance of the device during operation, as proposed by Kraśny *et al.* [82].

Power Delivered to Resistive Load

It is tempting to use values of I_{SC} and V_{OC} to calculate the power delivered by the device, however, this calculation is not ideal since the short circuit current is measured under zero load resistance (with no voltage) and the open circuit voltage is measured over an effectively infinite load resistance (with no current). Therefore, such a situation is never met during operation of an energy harvester and the results obtained with such a calculation are not realistic and should be treated with caution.

To estimate the harvested power, a resistive load is applied to energy harvester, on which the voltage drop is measured, and power is calculated using Ohm's law. Discrete components or resistance decade (manual or software controlled) can be used. Since power should be dissipated through the attached resistance, the input impedance of measuring equipment must also be well-thought-out. To illustrate this, let us consider the case where value of load resistance (R_L) connected to energy harvester is 10 MΩ. When voltage across resistor is measured with a standard oscilloscope and a typical probe (1:10 attenuation ratio) then overall input impedance of test instrumentation is 10 MΩ. This creates a combination of input impedance of scope with the attached load resistance and results in an effective 5 MΩ resistance connected to the piezoelectric device under test (parallel connection of two resistances). For very low output energy harvesters and for tests at higher frequencies (i.e. where capacitive reactance of the instrumentation exceeds its resistance), the stray capacitances and inductances of the measurement circuit and probing should also be considered as this might further influence obtained results [79].

Capacitor Voltage-Time Charging Curve

A typical configuration to charge a storage capacitor uses a full wave bridge circuit that is formed from four silicon or Schottky diodes, followed by electrolytic capacitor. While it is not the most efficient power management circuit to be used with a piezoelectric energy harvester, its simplicity and broad use among researchers makes it an initial point of reference. Thus, this approach is recognised as gold standard in the field. It is essential to consider equivalent series resistance (ESR) of the attached smoothing capacitor, especially for low signal measurements since it can provide additional, and significant, system losses. In addition, an optimised ratio between internal capacitance of piezoelectric energy harvester and load capacitance may result in a higher voltage output [9].

Control Software Solutions

The above listed issues are just some of the basic concerns for the wide range of electrical measurements for energy harvester characterisation. The number of measurements and influencing factors that need to be accounted for can be overwhelming, especially for researchers from different fields with lack of advanced expertise in electronics. Moreover, the ability to achieve successful control over such a variety of instrumentation and devices is challenging, time consuming, and often requires advanced programming knowledge. Unfortunately, there is only a limited list of described software solutions for energy harvesting test rigs of which none is accessible to a new user.

The "Virtual Instrument", computer controlled test bench developed at the Technical University of Madrid is a solution designed for measurement of energy harvesters in a road traffic environment [83, 84]. The designed tool allows control over a road traffic simulator and can measure the power generated by piezoelectric-based harvesters and analyse the gathered data. The software and proposed hardware solution have been tailored to deal with this particular problem, which reduces its portability and adjustability to other measurements. Broader testing flexibility is allowed with tools presented by Kosmadakis *et al.* [65] and Batra *et al.* [66]. The solution presented by Batra allows to test output power in resistive load of samples mounted on the electrodynamic shaker, while Kosmadakis describes additional possibilities of characterisation of output voltage and current of a piezoelectric device mounted on an adapted speaker. Both systems use accelerometers to measure the excitation, but are missing the acceleration control module. An interesting measurement station was proposed by Ruan *et al.* [56], however the solution presented forces user to follow a very strict experimental routine. Although the presented tools are more generic and have potential for further development and improvements, similar to the "Virtual Instrument" described above, they are not open-source and are not available to other researchers. Moreover, the systems are developed in LabView, a software package from National Instruments that is used extensively in laboratories worldwide, but its high license price can make the software limited to a broader audience.

As described above, none of the in-house developed control software solutions are available to the public and are open-source. Thus, there is no easy-start or off-shelf solution ready to be applied for researchers interested in characterising energy harvesting materials and devices. Additionally, there is currently no tool capable of delivering a full set of automated measurements for characterising piezoelectric power harvested by the device, system energy efficiency, intermittent losses, and reliability of components at room and elevated temperatures. Therefore, we have developed and herein present an **Energy Harvesting Measurement Rig (*ENHAMER*)**. This is a modular testing

platform that enables the measurement of the full spectrum of piezoelectric energy harvester parameters that are considered as a gold standard in the field. ENHAMER offers an intuitive and easy to adjust control structure, allowing a quick start into automated testing according to user's protocol. It offers flexibility to work with different instrumentation delivered by commercial vendors or developed in-house. As a demonstration of its capability, we describe example configurations of the testing rig to measure the electrical response from piezoelectric energy harvesters and connected electronic circuits at room and at elevated temperatures.

We deliver the ENHAMER platform as an open-source and open-hardware, freely available tool capable of developing user-specific test scenarios. This is the first system developed to characterise and test reliability of self-powered systems employing energy harvesting devices and their components enabling high temperatures testing using dedicated open source hardware and software.

2.1.3 Proposed Measurement System

The introduced measurement system consists of two parts: software and hardware. However, the hardware modules are not obligatory and can be readily replaced or adjusted according to the users' demand. Here, the described system is built from variety of components which determine its overall limits and measurement ranges. It should be noted that the proposed solution is not limited to the instrumentation presented in this paper, moreover it is desirable to consider this as a base platform for further development, with upgrades of additional instrumentation libraries and user defined testing routines. In addition, the specific test performance such as sampling rate and measurement error are strictly dependent on the test architecture and configuration of instrumentation chosen by user.

ENHAMER Software

The ENHAMER program was developed and tested under Python 3 environment. The software is a bridge between the instrumentation and allows easy connection with other devices by standard communication protocols such as GPIB, RS232, TCP (Ethernet) or USB with use of Standard Commands for Programmable Instruments (SCPI) commands. In addition to standard python libraries, the program uses pyVISA a Virtual Instrument Software Architecture (VISA) python library for VISA back-end delivered by Keysight Technologies. Data acquired from instrumentation is managed and processed with the use of Pandas and Numpy Python's libraries. Installation of the program is easily achieved with the creation of a new environment in Anaconda Python distri-

bution through simple steps providing all necessary libraries with their dependencies. This procedure is described in detail in ENHAMER documentation available online [85]. This is of particular importance for new users, as importing a Python environment with all its dependencies enables easy start and run the example experiment routines with no trouble.

The ENHAMER program is divided into three layers of abstraction: (i) instrumentation, (ii) experiment routine and (iii) data acquisition and recording. These are now described.

Instrumentation

The instrumentation layer is organised with the full object-oriented programming (OOP) paradigm in which the main instrumentation library is a wrapper for VISA communication with a detailed definition of common communication methods and error handling. The individual device libraries, such as oscilloscope or signal generator, inherit the parent class, complementing the instrument's commands according to the specification of the device (i.e. SCPI commands necessary to configure signal generator). The fragment of the structure of the Instrumentation layer is presented as a Unified Modelling Language (UML) object diagram in Fig. 2-2 which shows the INSTRUMENT as an abstract class which is responsible for connection establishing with physical devices. Such an organisation of hierarchy provides unification in the communication protocol within the ENHAMER tool, which is further used in the following layers of 2.1.3 Experiment routine and 2.1.3 Data acquisition and recording. Finally, it provides template for simple and easy expansion of new devices.

Experiment Routine

The experiment routine takes advantage of Python's support for procedural programming techniques, where a series of computational steps (subroutines) are carried out with a given order. Execution flow is organised as a quasi-state-machine which is controlled by a simply defined experiment logic. The general block diagram of a control routine is presented in Fig. 2-3, which shows the sequential steps executed in an arbitrary order to deliver system configuration and is necessary to provide reliable measurements.

During the experiment routine the ENHAMER's logic acts to control the instrumentation, thereby organising the workflow with the priority given to allow settlement of environmental parameters such as temperature, frequency and acceleration (SET CONDITIONS). Then, the measurement mode, such as short circuit current or power, is configured (CONFIG MEAS. MODE). If the measurement mode requires a resistive

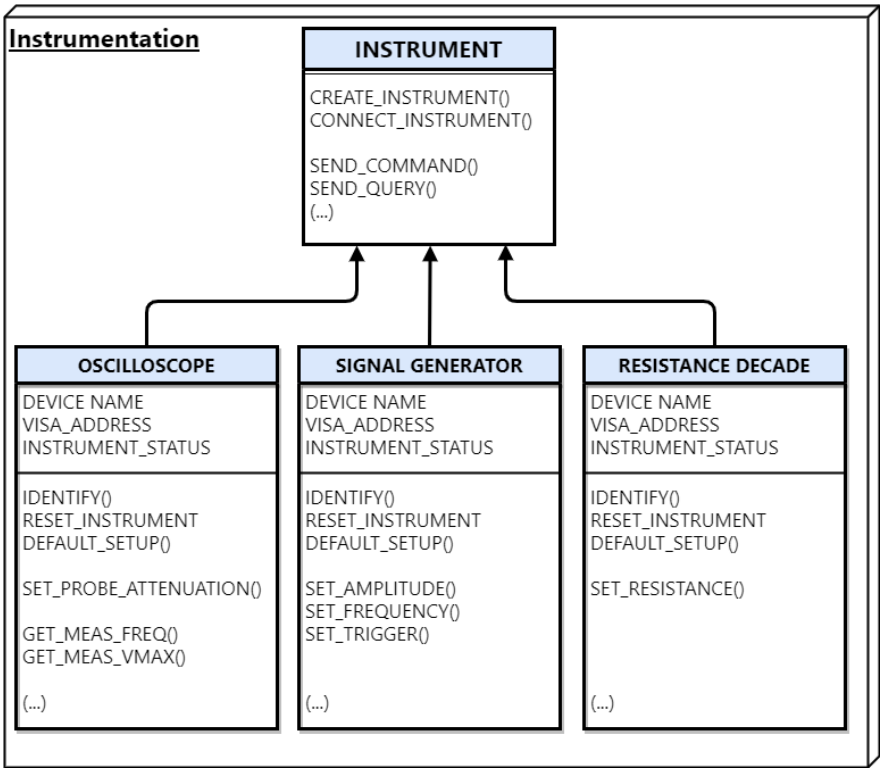

Figure 2-2: *Example of an instrumentation class diagram with three common instruments (oscilloscope, signal generator and resistance decade) typically used in vibration energy harvesting test stations. [Kraśny, M.J. (2020), DOI: 10.6084/m9.figshare.12585023, CC BY 4.0 license]*

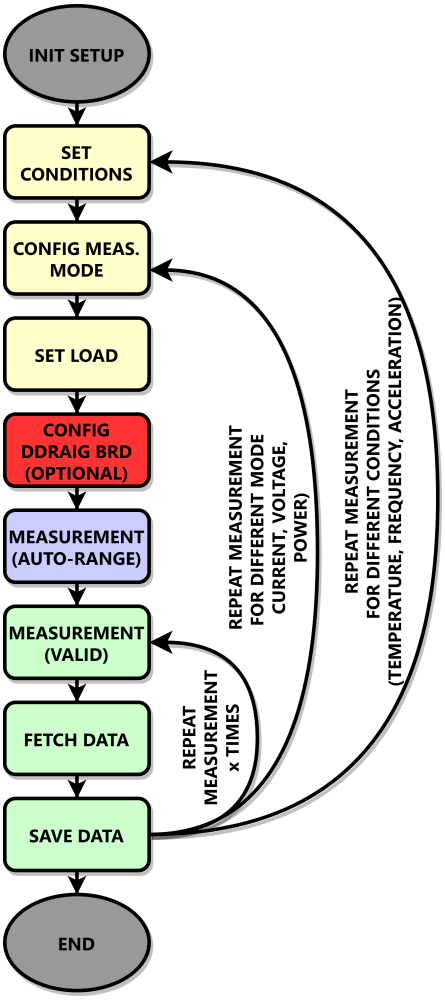

Figure 2-3: *General flow diagram of an experiment routine with the sequential steps followed by the software to perform an experiment. Initial and final setup are marked in grey elliptical blocks. Setting the experiment conditions in first three blocks is marked in yellow; configuration of optional control board marked in red; following measurement step in auto-range mode marked in purple; final data measurement and saving steps marked in green. Testing ranges, such as i.e. frequency sweep, is delivered with the looping responsible for appropriate configuration of the instrumentation at each frequency point. Similarly, measurement at each point of interest can be repeated x-times as defined by user. [Kraśny, M.J. (2020), DOI: 10.6084/m9.figshare.12585023, CC BY 4.0 license]*

load an adequate load resistance is then set (SET LOAD). If an optional hardware control board (described in further section: 2.1.3 Ddraig Control Board) is used it is now configured (CONFIG DDRAIG BRD). Optimal instrumentation measurement ranges are adjusted for maximum resolution by means of the auto-ranging (MEASUREMENT AUTO-RANGE). Finally, the measurement is performed (MEASUREMENT), and the gathered data is read out from the equipment (FETCH DATA) and stored in the appropriate files (SAVE DATA). The measurement can be repeated for statistical purposes or the procedure moves to other environmental conditions, such as temperature, frequency, acceleration or load resistance. The presented routine is simply a general example of a possible sequence and can be easily adjusted according to user testing protocol by removing unnecessary steps or by adding other actions that are substantial to the new routine.

To overcome a limited memory space available for data recording in oscilloscopes, electrometers, and multimeters and allow testing for extended periods, such as for long-term fatigue testing, we have deliberately divided measurements on the basis of excitation period. The user is able to decide on the recording period length, for example four full excitation cycles. This is followed by a user decision on the repetition count for statistical or long-term performance analysis. To provide an example, the user might want to test their device at 42 Hz (thus signal excitation period is $1/42 \approx 24$ ms), and record data over four full cycles. The measurement will be repeated 10 times to allow for statistical analysis. Therefore, the overall testing time will be ≈1 second, which is calculated as: *excitation period* $\times$ *4 cycles* $\times$ *10 repetitions [24 ms* $\times$ *4* $\times$ *10* $\approx$ *1 s]*. In addition, between each consecutive repetition, the user can decide to add a delay time to increase the measurement range, for example for the period of 10 minutes. The software will then record the output responses from the harvester over four excitation cycles at the beginning of each minute for the overall period of 10 minutes. For long-term testing, the experimental routine can be defined to operate on constant acceleration (or variable acceleration, if such test is required by the user specific testing conditions) for a time that is only limited by a failure of the instrumentation or hardware space available for collecting results in the connected PC.

Data Acquisition and Recording

The proposed measurement system is designed to control workflow and communication between standard laboratory instrumentation. This aim is achieved with the synchronisation of triggering signals amongst the equipment and by a programmatically implemented support for standard instrumentation protocols. Measured data can be gathered by oscilloscopes, electrometers and/or digital multimeters, as required by

the experimental procedure. Moreover, each experiment routine can be adjusted to perform measurements with dedicated instrumentation. Results are fetched from the instrumentation and organised in the output file with metadata containing a detailed description of the experiment parameters. In example each result file consists of a header with the project name and DUT description, experiment date and time followed by detailed information of the instrumentation, test frequency, acceleration level, etc. used.

As multiple devices can be used in the measurement setup, the data acquisition is defined as a separate layer of the ENHAMER system. This allows an easily achievable configuration of stored results. By default, it is proposed that data is saved in a csv (comma-separated values) format which can be then easily post-processed and analysed in user preferred software. Moreover, an additional logging function is introduced into the experiment routine. In a separate file, each log's entry consists of a time, device name and communication flow between instrumentation. If any fault occurs, it is logged with a separate error flag returned from the device. This is of significant benefit for further experiment analysis, routine error tracking or for scientific rigour and experiment documentation, thereby acting as a laboratory notebook.

ENHAMER Hardware

We now present an example measurement setup used in our laboratory and shown in Fig. 2-4. The measurement station illustrates the system organization, with the described instrumentation for both options of environmental testing at (i) room temperature (RT), performed with the DUT placed in a shielded cage and (ii) at elevated temperature (HT), with the DUT placed inside a furnace. A detailed explanation on the proposed sample montage is further given in the following section and presented in Fig. 2-5 and Fig. 2-6. Each of proposed testing configurations uses a separate shaker, however the control and measurement instrumentation are common and exchangeable.

For RT testing, the electrodynamic shaker that is responsible for generation of the excitation signal is screwed to a 10 kg steel block to form a stabile base to limit undesirable movements. For testing at elevated temperatures, the shaker is mounted on a scaffold constructed from a standard metal rack profiles screwed together with bottom part placed in a wooden mould (45 x 70 x 10 cm width, length and high) filled up with concrete. Such a construction constitutes a solid base with a total weight of 86 kg significantly reducing side vibrations caused by the shaker on the whole structure in comparison to a free-standing scaffolding structure.

The measurement range of the presented setup covers a wide frequency band of generated vibrational excitations (5 - 1000 Hz), temperature spectrum (room temper-

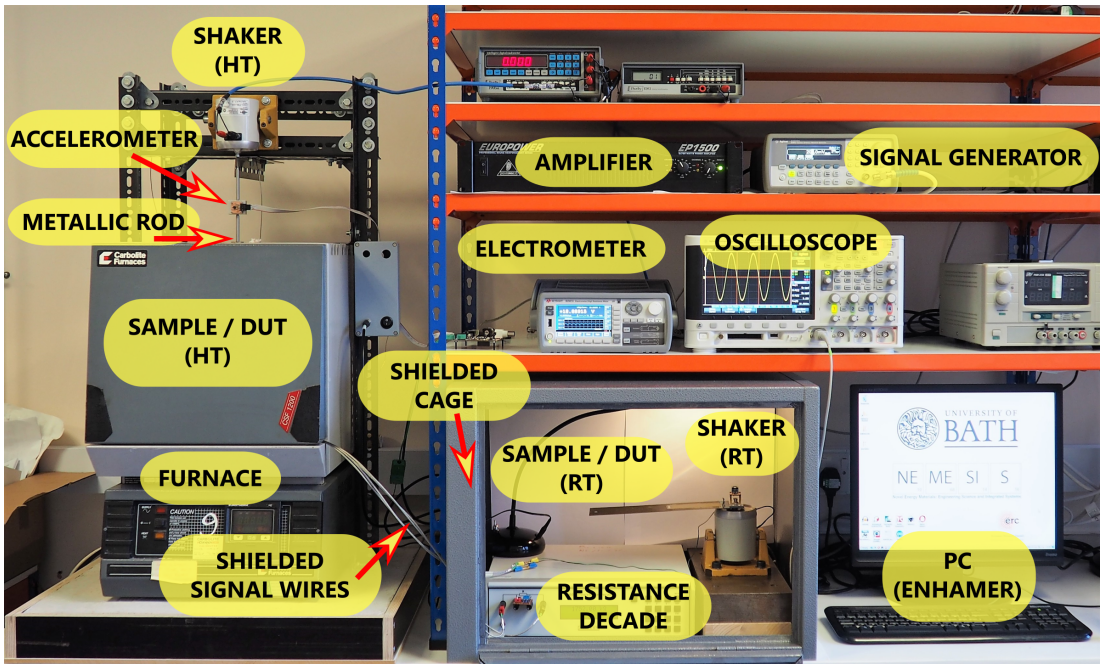

Figure 2-4: *Instrumentation organization - Energy Harvesting Measurement Rig (ENHAMER) with the described instrumentation options of environmental testing at room temperature performed with the DUT placed in a shielded cage and at elevated temperature with the DUT placed inside the furnace. [Kraśny, M.J. (2020), DOI: 10.6084/m9.figshare.12585023, CC BY 4.0 license]*

ature – 400°) and acceleration of up to 20 g (196 m/s^2). The range of frequencies is typical for energy sources utilized for energy harvesting [86] and the elevated temperatures spectrum enables testing systems working in harsh environments such as the oil and gas industry, geothermal wells, mining, power generation or transport and aviation [87, 88, 89, 90, 52].

The presented setup ranges depend strictly on the system components, namely accelerometer, electrodynamic shaker, amplifier, furnace, or heat resistance of the used wiring. By defining custom experiments' procedures and test configurations, the user has ability to use a variety of laboratory instrumentation such as oscilloscopes, electrometers or digital multimeters to gather the desirable data from materials or devices under test.

DUT - Sample Montage

For testing in room temperature mode, the sample can be attached to an electrodynamic shaker (LDS V201), as presented in Fig. 2-5. Both sample and shaker are placed in a metal box which is connected to earth ground. This creates a shielded

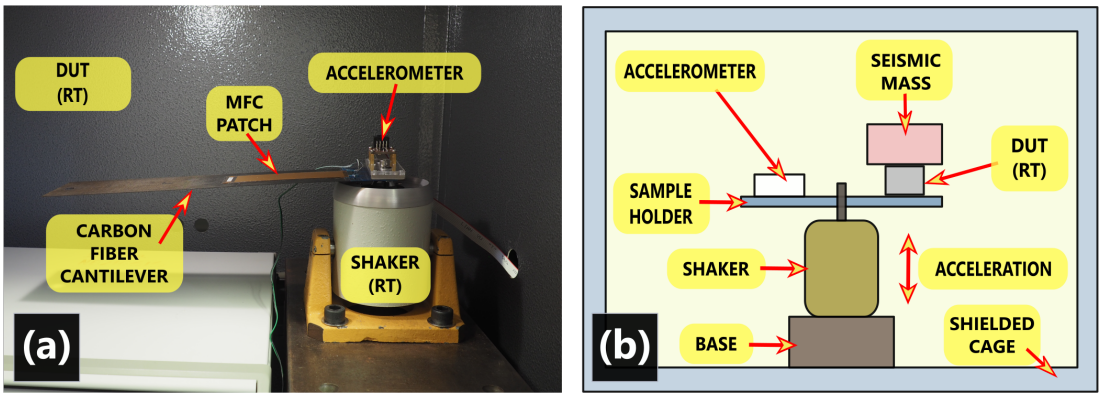

Figure 2-5: *Example of sample montage for room temperature testing of (a) piezoelectric cantilever; (b) schematic diagram of sample montage and placement in shielded cage for the testing procedure analogous to the presented in high temperature configuration shown in Fig. 2-6. [Kraśny, M.J. (2020), DOI: 10.6084/m9.figshare.12585023, CC BY 4.0 license]*

environment to minimise any induced noise from mains power, coupled to the measurement setup when undertaking high impedance DUT testing. The cage is also visible in the centre of Fig. 2-4.

For tests performed in the high temperature mode the DUT is placed in the chamber of a furnace (Fig. 2-4), as shown in more detail in Fig. 2-6. In this mode, the shaker (LDS V201), placed above the furnace, actuates a metallic rod (stainless-steel grade 416), to mechanically stimulate the sample holder with the DUT.

The sample mounting depends on the DUT and can be adjusted according to requirements; for example for tests of a cantilever form allowing measurement of d_{31} mode performance, see Fig. 2-5a. For example, of measurement of d_{33} mode with the seismic mass attached to the sample, see Fig. 2-5b and Fig. 2-6. A hybrid system is also possible, with an electronic circuit board placed in the furnace supplied by piezoelectric material placed on a cantilever outside the furnace (Fig. 2-5a). This will be further described in section 2.1.4 High temperature electronic circuit performance as a specific example.

Vibration Generation

A digital signal generator (Agilent 33220a) is responsible for excitation signal. Next, the signal is subject to an appropriate gain (Europower EP1500) to drive the electromagnetic shaker (LDS V201, Brüel & Kjær Instruments Inc). The applied excitation is monitored by a 3-axis accelerometer mounted next to a sample (Fig. 2-5 a&b) or to the rod above the furnace (Fig. 2-6c) for RT and HT tests accordingly.

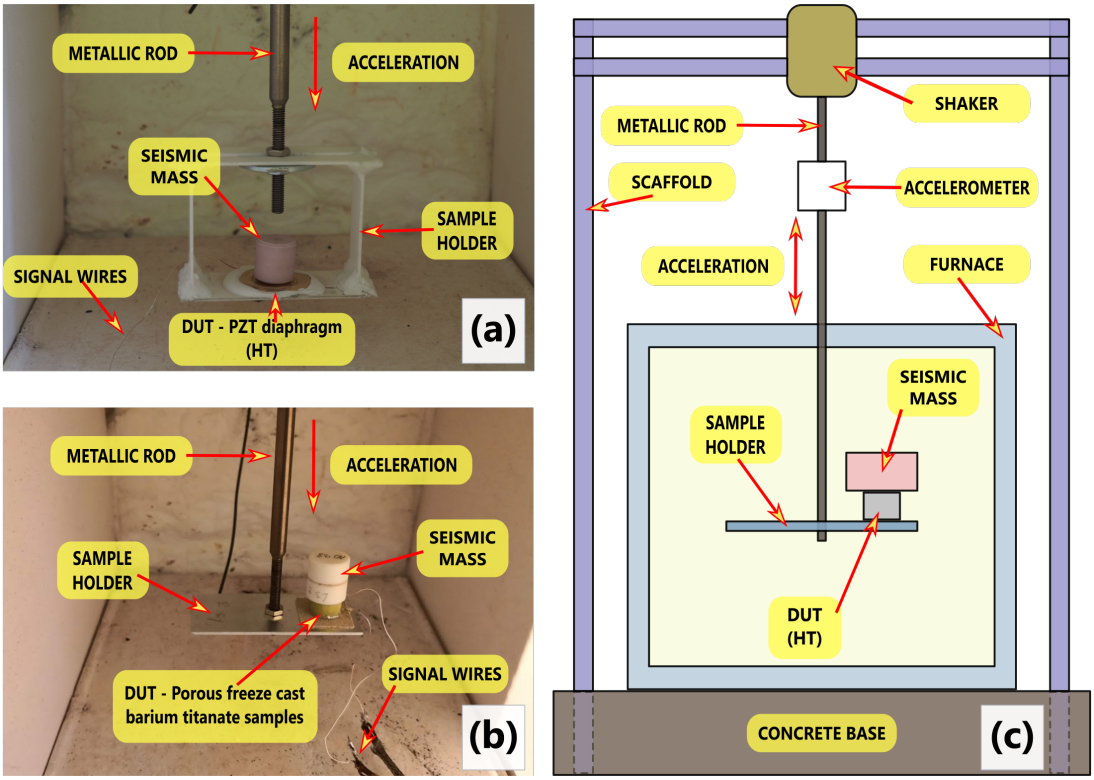

Figure 2-6: *Example of sample montage for high temperature testing of piezoelectric transducer; (a) image from testing of a PZT diaphragm; (b) image of testing of a porous barium titanate sample; (c) schematic diagram of sample montage and placement in the furnace chamber. [Kraśny, M.J. (2020), DOI: 10.6084/m9.figshare.12585023, CC BY 4.0 license]*

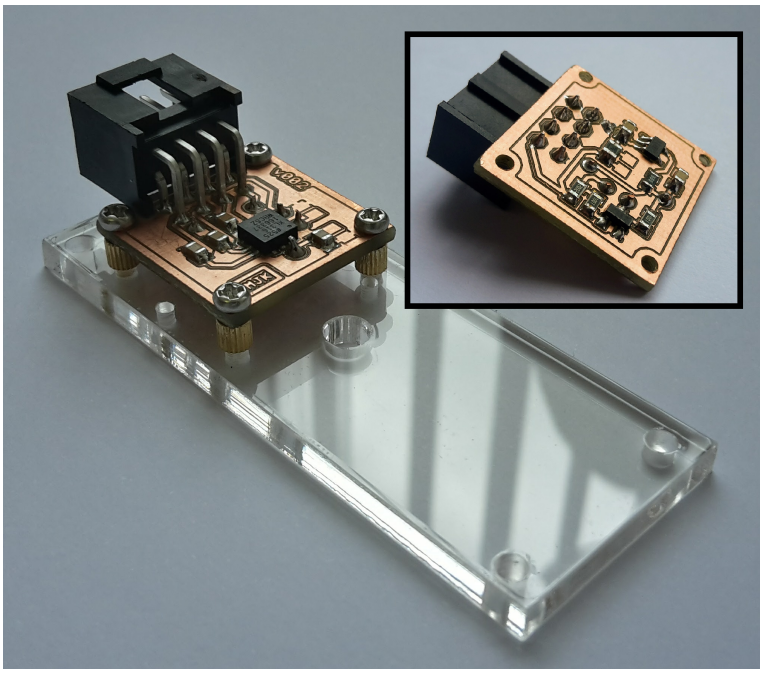

Figure 2-7: *ADXL316 module mounted on acrylic cut sample holder. Inset shows PCB bottom with power supply and filtering circuit. The test sample (DUT) can be placed on the clear spot, opposite to the accelerometer module. Acrylic holder has dimensions of 63 mm long and 25 mm wide and 3 mm thickness. ADXL316 module is double layer square PCB with a 20 mm side. [Kraśny, M.J. (2020), DOI: 10.6084/m9.figshare.12585023, CC BY 4.0 license]*

Acceleration Measurements and Control

Acceleration control is performed with an analogue accelerometer (Analog Devices, ADXL316) embedded with the conditioning circuit to a custom-built PCB, see Fig. 2-7. The module can be placed on the shaker's shaft, through a custom designed adapter (Fig. 2-6c), or directly close to the sample on a metal or acrylic base, as presented in Fig. 2-5 a&b and Fig. 2-7 and described in detail by Roscow *et al.* [27]. The accelerometer output is gathered by an oscilloscope.

As mentioned previously (see section: 2.1.2 Excitation Control), the acceleration level of the shaker varies as a function of frequency and can also depend on the attached load mass, for example sample and/or sample holder. To resolve this problem, an approach similar to Harris *et al.* [24] was applied. The user has an ability to perform a vibration calibration procedure with one of the ENHAMER's experiment routines. This results in creation of a look-up table where desirable acceleration levels correspond to dedicated signal generator parameters, namely frequency and amplitude. When the test is performed at the required acceleration, adequate generator parameters are set

after a linear interpolation from the previously calibrated data.

Such an approach allows performance of a sweep frequency measurement at constant acceleration levels within the calibrated range. Assuming the system was previously calibrated, it also allows the user to perform a reliable test with repeatable acceleration levels for the device without the use of an accelerometer attached to the testing platform, i.e. when the accelerometer cannot be mounted or multiple similar samples are compared. This approach to acceleration control was selected as it results in reduction of processing time and reduces the need of constant acceleration monitoring and regulation by an additional controller or software module.

As the proposed module is a three-axial accelerometer, during the calibration procedure all available channels can be recorded for recognition of construction self-resonance frequencies and unwanted side vibrations due to the mechanical construction. This can be further used to raise awareness of the errors in measurement frequency ranges (spots), or to determine the limitations of the measurement rig.

Load Resistance

The piezoelectric harvester can be loaded with a resistance in order to match the impedance at the operating frequency and to establish the maximum power output. ENHAMER, through its dedicated software libraries, can operate with manually chosen discrete resistors, manual resistance decade box (such as PeakTech 3265) or automated resistance decade, such as a Meatest M602a connected to a PC. With custom designed libraries, the load resistance could be attached with an in-house developed alternatives i.e. as motor controlled potentiometers, as proposed by Ruan *et al.* [56]. As the most commonly available resistance decades are limited to 10 MΩ, the optional Ddraig Control Board presented below offers possibility to increase the necessary resistance range through separately switched precise 10 MΩ and 20 MΩ resistors.

Ddraig Control Board

An optional circuit board was designed to ease measurement automatization. The main purpose behind this development is to deliver reliable and automated switching between consecutive measurements.

The software controlled *Ddraig Board* is responsible for switching between current, voltage, power and or rectifier and capacitor charging operating modes. A general schematic of the *Ddraig Board* circuit is presented in Fig. 2-8 and the assembled board is shown in Fig. 2-9, which indicates the main sub circuits such as DUT input (*B1* and *B2*) and measurement instrumentation connectors (*B3*-*B6*), power supply section, accelerometer connector, sockets for relays control connection, rectifier sub circuit, ex-

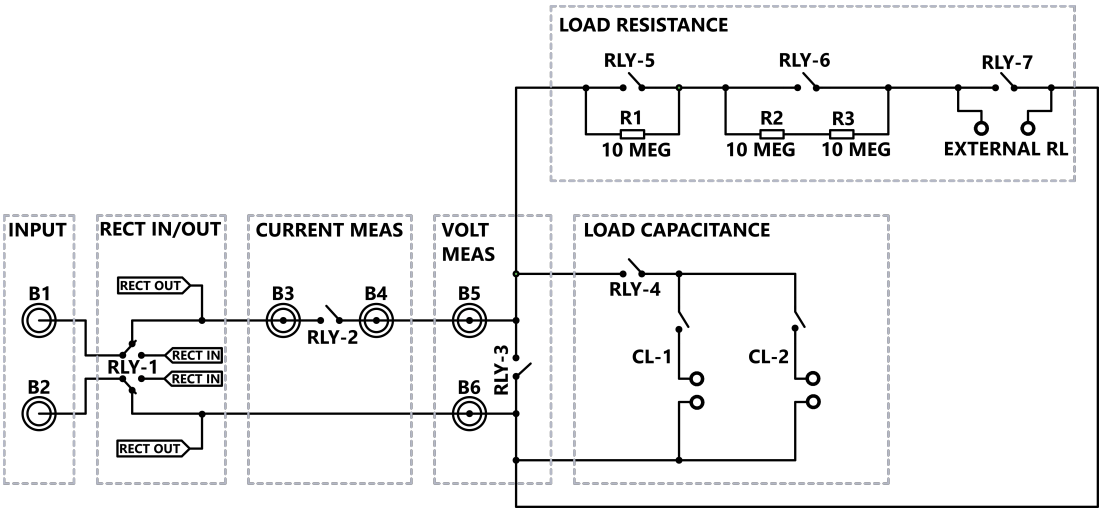

Figure 2-8: *General schematic of the proposed Ddraig Control Board with visible separate sections for output signal from excited piezoelectric sample connection (INPUT), next switch directing the signal to rectifier (RECT. IN/OUT) followed by connectors for ammeter (CURRENT MEAS.) and voltmeter (VOLT MEAS.). The final two sections allow connection of load capacitance for capacitor voltage-time charging curve test (with rectified signal) and load resistance for power delivered to resistive load measurement. [Kraśny, M.J. (2020), DOI: 10.6084/m9.figshare.12585023, CC BY 4.0 license]*

ternal load and capacitor connectors.

The Ddraig Control Board was designed as a double-sided PCB with wide spacing between signal traces and components to enable easy manufacturing process. The board can be ordered from any PCB-pool, manufactured with CNC machining (i.e. LPKF S63) or etched in thermo-transfer (toner-transfer) hand-made in-house lab if necessary. The electronic components used are common, low cost and easily accessible. Assembly of the circuit does not require advanced electronics skills and can be undertaken, even by unexperienced engineers.

The Ddraig Control Board can be supplied from a battery, laboratory power supply or any AC/DC power adaptor delivering DC voltage in the range of 8 - 15 V. Integrated on board power conditioning stage was designed with standard linear voltage regulators (LM317). The total power consumption of the board and heat generated by the voltage regulator needs to be considered if used with higher input voltages. The energy harvester and measurement instrumentation are connected through a standard 4-mm (commonly known as banana) plugs (*B1-B6* in Fig. 2-8 and Fig. 2-9). To minimise the effect of additional circuity on the measured piezoelectric output values, relays with low contact resistance (30 mΩ max G5CA -1A-E-DC5; Omron) were chosen (marked as *RLY-2* to *RLY-7* in Fig. 2-8 and Fig. 2-9). The board is designed to be controlled and operated

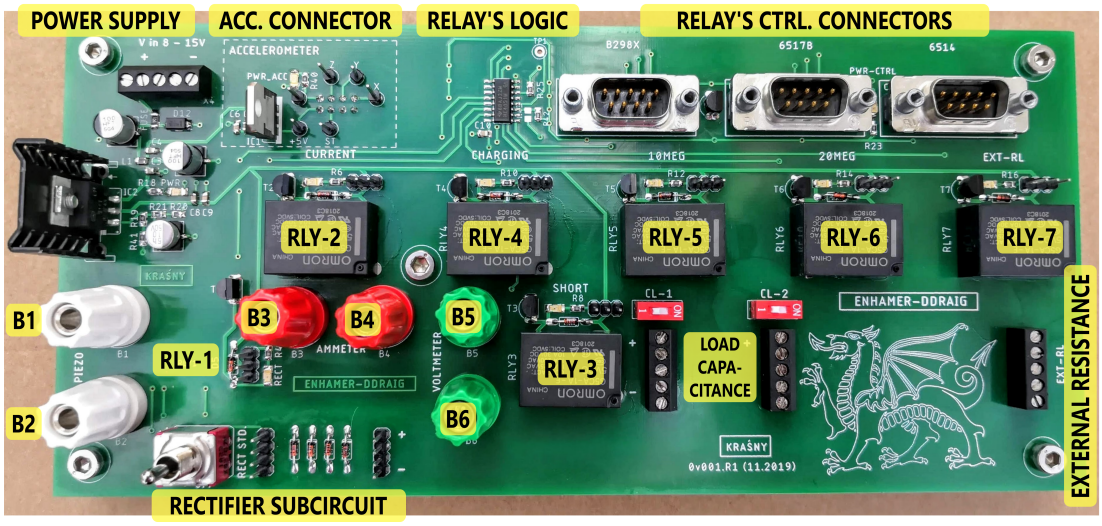

Figure 2-9: *Assembled Ddraig Control Board with visible sub circuits parts responsible for power conditioning and relays control, relays, control connectors, piezoelectric input connectors and load components connectors (resistance, capacitance). [Kraśny, M.J. (2020), DOI: 10.6084/m9.figshare.12585023, CC BY 4.0 license]*

through the digital I/O pins from the popular electrometers: Keysight 298X, Keithley 6517B or Keysight 6514 (through RS-232 connectors). Alternatively, the board can be operated through an Arduino board. Additionally, the board is supplied with conditioning circuit and connectors for described previously accelerometer (ADXL316) module. With the ability of automated switch between separate test modes, user is able to use i.e. custom designed and calibrated shunt or transimpedance amplifier-based circuits for precise current measurement (i.e. as proposed by [63, 65]).

The board is equipped with a standard full wave bridge assembled with user preferred diodes (by default 4x1N4148 silicon diodes are proposed). The rectifying bridge forms a separate sub circuit that is switchable programmatically through a relay (AXICOM-V23079-D) marked as *RLY-1* in Fig. 2-8 and Fig. 2-9. Additionally, through a dedicated socket and manually operated switch, an external second rectification circuit can be easily connected. This allows simple and rapid performance comparison between two sets of diodes or more sophisticated solutions referenced to a standard bridge. Moreover, the properly configured relays of the Ddraig Control Board allow testing of open circuit voltage output of an energy harvester with and without rectifier stage connected using the same instrumentation probing, without the need for re-wiring. If used with a mains powered oscilloscope, or electrometer, such a measurement is not easily achieved since it requires differential probes due to the ground reference of instrumentation.

The automatization of tests is particularly of importance for temperature sweep

measurements, as it allows a quick and user independent switch between short circuit current and open circuit voltage modes in the desired frequency range. This provide the benefits of a reduced human factor and error involved in manual re-wiring or instrumentation switch and by minimising the time difference between single measurements. It also allows more tests to be performed in same period of time. This increases the statistical reliability of the whole measurement and improves device characterisation.

2.1.4 Results and Discussion

The presented software tool was developed in Python. The programming language was selected due to its compatibility with a range of operating systems (Windows, Linux, MacOS) and simplicity of the language allowing ease communication via standard data transfer protocols with associated devices. It is also an open access language, which provides a significant advantage over costly commercial platforms such as MATLAB and LabView. Another advantage of Python over other programming languages is its interpreted execution (without the compiling process) which makes the software transparent and enables straightforward edit of the code. This is especially important when the tool is accessed by less advanced users, making the software simpler to understand and modify. It also improves readability of experimental procedure and delivers transparent and easy to investigate output flow.

ENHAMER was tested during software development at each step with known and expected input signals at different logging intervals to ensure its full functionality. As the software uses common instrumentation, its ability for data sampling rate, accuracy and error susceptibility is defined by the used devices' specification. The usability of the ENHAMER automated measuring system was proven by performing multiple measurements for materials characterisation or testing of electronic circuits. Three main groups of measurements will be shown as an example of its use and potential: (i) high temperature piezoelectric material characterization, (ii) high temperature electronic circuit performance, and (iii) room temperature characterization of an energy harvesting device.

High Temperature Piezoelectric Material Characterisation

High temperature piezoelectric material testing was performed on commercially available piezoelectric diaphragm (buzzer) at temperatures up to 230°C. The sample was placed in the furnace chamber and attached to the shaker's rod via a holder made of 96% alumina plates (Fig. 2-6a). A seismic mass weighing six grams was bonded to sample with a high temperature adhesive (Resbond 940LE). The sample was excited

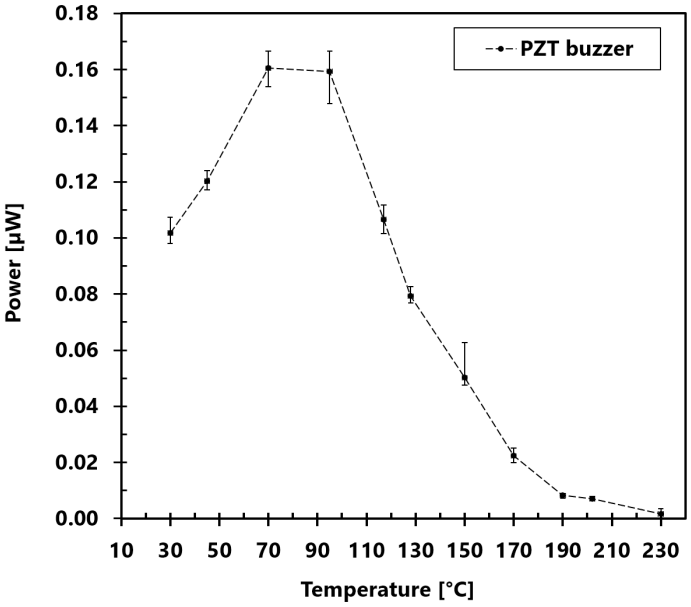

Figure 2-10: *Output power of lead zirconate titanate (PZT) buzzer as a function of temperature. Data points are average peak power; error bars represent maximum and minimum values at given temperature point. [Kraśny, M.J. (2020), DOI: 10.6084/m9.figshare.12585023, CC BY 4.0 license]*

off resonance at a sinusoidal signal at 125 Hz. Electrical contacts were formed from 0.25 mm diameter silver wires attached to the samples by silver conductive paint. The output signal was dissipated through the matched load resistance (R_L = 50 kΩ) controlled by the resistance decade (Meatest M-602). Finally, the output voltage (V) was measured by the oscilloscope (Agilent DSOX2024A with Agilent N2863B 1:10 probe) at temperature points of interest. The piezoelectric output was recorded for over 25 signal periods and data points are presented for average peak power with error bars representing maximum and minimum value at given temperature point. The power was calculated based on $P = V^2/R_L$ equation. Result of the measurements are presented in the Fig. 2-10 which shows the decrease of power at elevated temperatures (above 90°C) as the material is heated towards its Curie temperature and there is a loss in the remnant polarisation of the material. The output power vanishes at temperatures >200°C due to a complete depolarisation of the material. The initial increase of harvested power is possibly influenced by improved domain motion of the material and rise in piezoelectric activity has been previously observed for characterization of the piezoelectric d_{33} coefficients [54, 91, 92].

High Temperature Electronic Circuit Performance

While the system can characterise the piezoelectric element subject to vibration by the shaker, it is also possible to separate the transducer from the associated electronics, such as the rectifier circuit. Such an approach can be a part of a hardware-in-the-loop (HIL) test. Boards with rectification circuits were placed in the furnace chamber and were powered by the signal generated by a piezoelectric. A Macro Fiber Composite (MFC) patch (Product No. M-8528-P2) attached to a carbon fibre cantilever was mounted and excited at room temperature using a shaker since it was located outside of the furnace; see Fig. 2-5a and Fig. 2-4. The cantilever was manufactured using a process as described by Harris *et al.* [20]. The rectified output was then measured outside the furnace as described in previous example with the $R_L = 21$ kΩ. This approach can be used to eliminate the influence of the degradation of the piezoelectric transducer with temperature, as shown in the previous example and in Fig. 2-10, and characterize only the degradation of the rectification circuits of interest. Two rectifier circuits were assembled on an RO4360G2 (Rogers Corp.) laminate and placed inside the furnace. The electronic joints where soldered with high temperature soldering wire of melting point above 290°C and connected to instrumentation and MFC patch with shielded constantan wires. The tested circuits were full rectification bridges built from silicon (Si) and silicon carbide (SiC) based semiconductors (circuit 1: 4 x Si diodes 1N4148; circuit 2: 4 x SiC diodes IDH04G65C5). Measurements were performed at 37.1 Hz which was a resonance frequency of a cantilever, and the results are presented in Fig. 2-11. For the lower temperature range up to 160°C the silicon-based diodes are introducing less loses due to their lower conducting threshold voltage. However, as temperatures increases, the silicon-based device degrades due to increased junction current leakage and intrinsic carrier density, this results in a decrease of rectification efficiency and harvested power. As the energy of bandgap of semiconductor decreases as the temperature increases, the SiC diodes enable higher operating temperatures, see Fig. 2-11. Thus, the semiconductors with wider bandgap make a suitable alternative for a silicon-based device at elevated temperatures in excess of 150°C. The test also demonstrates the ability of the presented tool to perform a test of an electronic circuits at elevated temperatures separately from the energy harvesting transducer. A similar approach could be applied to the characterisation of improved rectifying circuits, such as those proposed in various work on synchronized switch harvesting on inductor (SSHI) [33, 34, 59, 60, 61, 62, 71]. This enables testing of IoT device system components individually in order to prove that all elements retain the desired specification in harsh environment, prior to testing of the complete system.

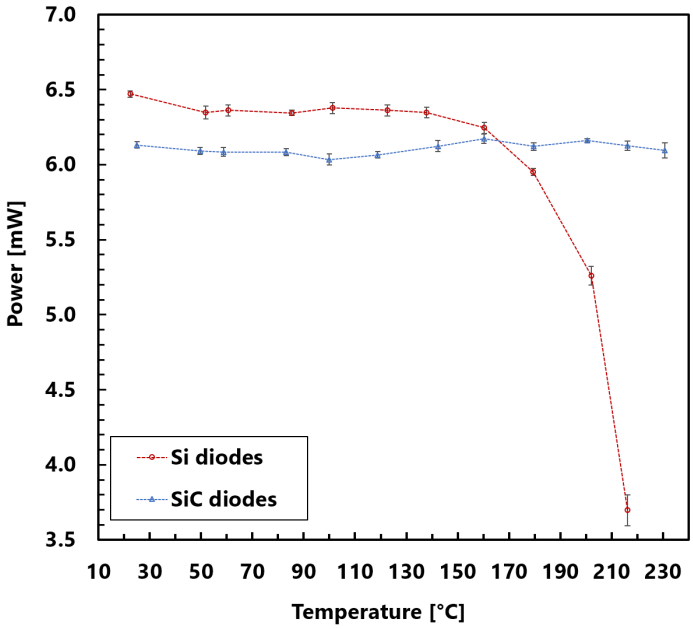

Figure 2-11: *Rectified power output from piezoelectric device in function of temperature. Error bars represent a standard deviation from the consecutive power values calculated over six full periods at each temperature point. [Kraśny, M.J. (2020), DOI: 10.6084/m9.figshare.12585023, CC BY 4.0 license]*

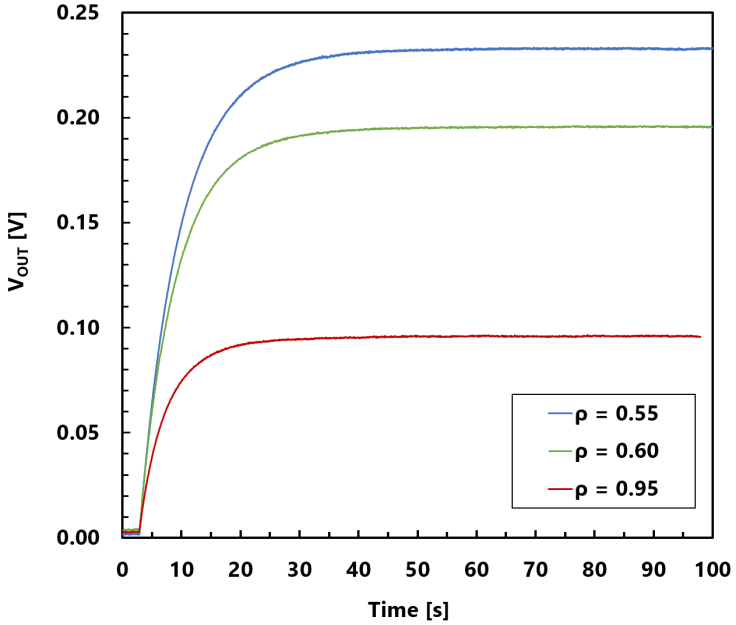

Figure 2-12: *Capacitor charging times - comparison between two porous freeze cast barium titanate samples (blue and green lines) and dense barium titanate (red). Legend indicates density level (ρ_{rel}) of the material. [Kraśny, M.J. (2020), DOI: 10.6084/m9.figshare.12585023, CC BY 4.0 license]*

Characterisation of an Energy Harvesting Device at Room Temperature

The presented tool was also used to demonstrate the improved harvesting capabilities of novel piezoelectric materials, such as a comparison of porous freeze cast barium titanate compared to the dense material [27]. Samples were placed in analogous manner as in previously described procedure for high temperature piezoelectric material characterization on an acrylic holder mounted on the top of the (RT) shaker. The experiment was performed at room temperature and parameters such as open circuit voltage and short circuit current were measured. Additionally, the energy harvester was connected to a 1 μF capacitor through a standard rectifying bridge and the times needed to charge as well as voltage level reached on the capacitor were measured (Fig. 2-12). The result show that the more porous material, with the lowest density (ρ_{rel}), produced the larger voltage on the storage capacitor due to the lower permittivity; for more details on the materials please refer to Roscow *et al.* [27].

2.1.5 Conclusions

ENHAMER, the new measurement tool described in this paper, provides a unique approach to deliver an adjustable and customizable automated characterisation of materials for vibration powered energy harvesting devices. The usability of the automated measuring system was demonstrated by performing several example tests for materials characterization or testing of electronic circuits including (i) high temperature piezoelectric material characterization, (ii) high temperature electronic circuit performance, and (iii) room temperature characterization of an energy harvesting device.

We have shown and described common challenges encountered in electrical characterisation of energy harvesters with a broad literature review to enhance the user knowledge. We propose successful solutions to overcome typical problems, such as acceleration control of electrodynamic shakers or minimisation of mains power noise in measurements. An optional circuit board (Ddraig board) was designed to simplify measurement automatization. This is a unique approach that has yet to be reported in the literature. The board allows improved control over the experiment by switchable sections dedicated to performing independent measurements without user intervention. Thus, increasing the measurement reliability by limiting the human error involved in multiple re-wiring or rearranging equipment during testing. During development of the system, a significant focus was placed on easy adaptation of the system to perform new experimental scenarios (routines) depending on the user demand.

The user is provided with example routines for basic testing of vibration powered energy harvesters and developed software allows easy implementation and extension of other instrumentation. In addition, software applies good practices for code and measurement protocol development by implementation of logging functionality with test description in form of metadata to satisfy the scientific rigour in experiments repeatability, reliability and reproducibility [93].

According to our best knowledge, this is the first system developed to characterise and test reliability of self-powered systems employing energy harvesting devices and their components in high temperatures with dedicated open source hardware and software. The ENHAMER tool is released with all of the described components, namely the Ddraig Control board, accelerometer circuit, samples and accelerometer holders under the open licenses and the whole research project with the full documentation can be find at: http://github.com/enhamer [85]. The presented solution enables an easy start and run for independent, reliable tests of future vibration powered energy harvesters.

Acknowledgments

Authors would like to acknowledge funding from the European Research Council under the European Union's Seventh Framework Program (FP/2007-2013)/ERC Grant Agreement no. 320963 on Novel Energy Materials, Engineering Science and Integrated Systems (NEMESIS).

References

[1] S. R. Anton and H. A. Sodano, "A review of power harvesting using piezoelectric materials (2003–2006)," *Smart Materials and Structures*, vol. 16, no. 3, p. R1, 2007.

[2] M. Safaei, H. A. Sodano, and S. R. Anton, "A review of energy harvesting using piezoelectric materials: State-of-the-art a decade later (2008–2018)," *Smart Materials and Structures*, vol. 28, no. 11, p. 113001, Oct. 2019.

[3] R. Salazar, M. Serrano, and A. Abdelkefi, "Fatigue in piezoelectric ceramic vibrational energy harvesting: A review," *Applied Energy*, vol. 270, p. 115161, Jul. 2020.

[4] Poonam, K. Sharma, A. Arora, and S. K. Tripathi, "Review of supercapacitors: Materials and devices," *Journal of Energy Storage*, vol. 21, pp. 801–825, Feb. 2019.

[5] Y. Liang, C.-Z. Zhao, H. Yuan, Y. Chen, W. Zhang, J.-Q. Huang, D. Yu, Y. Liu, M.-M. Titirici, Y.-L. Chueh, H. Yu, and Q. Zhang, "A review of rechargeable batteries for portable electronic devices," *InfoMat*, vol. 1, no. 1, pp. 6–32, Mar. 2019.

[6] D. Zhu, S. P. Beeby, M. J. Tudor, and N. R. Harris, "A credit card sized self powered smart sensor node," *Sensors and Actuators A: Physical*, vol. 169, no. 2, pp. 317–325, Oct. 2011.

[7] S. Barker, D. Brennan, N. G. Wright, and A. B. Horsfall, "Piezoelectric-powered wireless sensor system with regenerative transmit mode," *IET Wireless Sensor Systems*, vol. 1, no. 1, pp. 31–38, Mar. 2011.

[8] P. Gljušćić, S. Zelenika, D. Blažević, and E. Kamenar, "Kinetic Energy Harvesting for Wearable Medical Sensors," *Sensors*, vol. 19, no. 22, p. 4922, Jan. 2019.

[9] M. Ferrari, V. Ferrari, M. Guizzetti, D. Marioli, and A. Taroni, "Piezoelectric multifrequency energy converter for power harvesting in autonomous microsystems," *Sensors and Actuators A: Physical*, vol. 142, no. 1, pp. 329–335, Mar. 2008.

[10] Q. Zheng, H. Tu, A. Agee, and Y. Xu, "Vibration energy harvesting device based on asymmetric air-spaced cantilevers for tire pressure monitoring system," *Proceedings of power MEMS*, pp. 403–406, 2009.

[11] X.-r. Chen, T.-q. Yang, W. Wang, and X. Yao, "Vibration energy harvesting with a clamped piezoelectric circular diaphragm," *Ceramics International*, vol. 38, Supplement 1, pp. S271–S274, Jan. 2012.

[12] W. Wang, T. Yang, X. Chen, and X. Yao, "Vibration energy harvesting using a piezoelectric circular diaphragm array," *IEEE Transactions on Ultrasonics, Ferroelectrics, and Frequency Control*, vol. 59, no. 9, pp. 2022–2026, Sep. 2012.

[13] K. Ashraf, M. H. M. Khir, J. O. Dennis, and Z. Baharudin, "A wideband, frequency up-converting bounded vibration energy harvester for a low-frequency environment," *Smart Materials and Structures*, vol. 22, no. 2, p. 025018, Jan. 2013.

[14] W.-C. Chang, A.-B. Wang, C.-K. Lee, H.-L. Chen, W.-C. Ko, and C.-T. Lin, "Photoconductive Piezoelectric Polymer Made From a Composite of P(VDF-TrFE) and TiOPc," *Ferroelectrics*, vol. 446, no. 1, pp. 9–17, Jan. 2013.

[15] G. D. Szarka, S. G. Burrow, and B. H. Stark, "Ultralow Power, Fully Autonomous Boost Rectifier for Electromagnetic Energy Harvesters," *IEEE Transactions on Power Electronics*, vol. 28, no. 7, pp. 3353–3362, Jul. 2013.

[16] H.-y. Wang, L.-h. Tang, Y. Guo, X.-b. Shan, and T. Xie, "A 2DOF hybrid energy harvester based on combined piezoelectric and electromagnetic conversion mechanisms," *Journal of Zhejiang University SCIENCE A*, vol. 15, no. 9, pp. 711–722, Sep. 2014.

[17] S. Anton, K. Farinholt, and A. Erturk, "Piezoelectret foam–based vibration energy harvesting," *Journal of Intelligent Material Systems and Structures*, vol. 25, no. 14, pp. 1681–1692, Sep. 2014.

[18] M. Lallart, C. Richard, Y. Li, Y.-C. Wu, and D. Guyomar, "Load-Tolerant, High-Efficiency Self-Powered Energy Harvesting Scheme Using a Nonlinear Approach," *Energy Harvesting and Systems*, vol. 1, no. 3-4, pp. 197–208, Dec. 2014.

[19] Z. Xiao, T. qing Yang, Y. Dong, and X. cai Wang, "Energy harvester array using piezoelectric circular diaphragm for broadband vibration," *Applied Physics Letters*, vol. 104, no. 22, p. 223904, Jun. 2014.

[20] P. B. Harris, C. R. Bowen, D. N. Betts, and A. H. Kim, "Manufacture and characterisation of piezoelectric broadband energy harvesters based on asymmetric bistable laminates," 2014.

[21] P. Li, Y. Liu, Y. Wang, C. Luo, G. Li, J. Hu, W. Liu, and W. Zhang, "Low-frequency and wideband vibration energy harvester with flexible frame and interdigital structure," *AIP Advances*, vol. 5, no. 4, p. 047151, 2015.

[22] T. Shiraishi, N. Kaneko, M. Kurosawa, H. Uchida, Y. Suzuki, T. Kobayashi, and H. Funakubo, "Vibration-energy-harvesting properties of hydrothermally synthesized (K,Na)NbO3 films deposited on flexible metal foil substrates," *Japanese Journal of Applied Physics*, vol. 54, no. 10S, p. 10ND06, Sep. 2015.

[23] M. Wu, Y. Ou, H. Mao, Z. Li, R. Liu, A. Ming, and W. Ou, "Multi-resonant wideband energy harvester based on a folded asymmetric M-shaped cantilever," *AIP Advances*, vol. 5, no. 7, p. 077149, Jul. 2015.

[24] P. Harris, M. Arafa, G. Litak, C. R. Bowen, and J. Iwaniec, "Output response identification in a multistable system for piezoelectric energy harvesting," *The European Physical Journal B*, vol. 90, no. 1, p. 20, Jan. 2017.

[25] A. Alomari, A. Batra, M. Aggarwal, and C. R. Bowen, "A multisource energy harvesting utilizing highly efficient ferroelectric PMN-PT single crystal," *Journal of Materials Science: Materials in Electronics*, vol. 27, no. 10, pp. 10 020–10 030, Oct. 2016.

[26] L. Zhang, R. Takei, J. Lu, N. Makimoto, T. Itoh, and T. Kobayashi, "Development of energy harvesting MEMS vibration device sensor with wideband response function in low-frequency domain," *Microsystem Technologies*, Mar. 2019.

[27] J. I. Roscow, Y. Zhang, M. J. Kraśny, R. W. C. Lewis, J. Taylor, and C. R. Bowen, "Freeze cast porous barium titanate for enhanced piezoelectric energy harvesting," *Journal of Physics D: Applied Physics*, vol. 51, no. 22, p. 225301, 2018.

[28] M. Xie, Y. Zhang, M. J. Kraśny, A. Rhead, C. Bowen, and M. Arafa, "Energy harvesting from coupled bending-twisting oscillations in carbon-fibre reinforced polymer laminates," *Mechanical Systems and Signal Processing*, vol. 107, pp. 429–438, Jul. 2018.

[29] M. Xie, Y. Zhang, M. J. Kraśny, C. Bowen, H. Khanbareh, and N. Gathercole, "Flexible and active self-powered pressure, shear sensors based on freeze casting ceramic–polymer composites," *Energy & Environmental Science*, Jul. 2018.

[30] Z. Chen, J. He, J. Liu, and Y. Xiong, "Switching Delay in Self-Powered Nonlinear Piezoelectric Vibration Energy Harvesting Circuit: Mechanisms, Effects, and Solutions," *IEEE Transactions on Power Electronics*, vol. 34, no. 3, pp. 2427–2440, Mar. 2019.

[31] Y. Zhang, X. Liu, G. Wang, Y. Li, S. Zhang, D. Wang, and H. Sun, "Enhanced mechanical energy harvesting capability in sodium bismuth titanate based lead-free piezoelectric," *Journal of Alloys and Compounds*, vol. 825, p. 154020, Jun. 2020.

[32] C. Chen, B. Zhao, and J. Liang, "Revisit of synchronized electric charge extraction (SECE) in piezoelectric energy harvesting by using impedance modeling," *Smart Materials and Structures*, vol. 28, no. 10, p. 105053, Sep. 2019.

[33] M. Lallart and D. Guyomar, "An optimized self-powered switching circuit for non-linear energy harvesting with low voltage output," *Smart Materials and Structures*, vol. 17, no. 3, p. 035030, 2008.

[34] M. Lallart, "Nonlinear technique and self-powered circuit for efficient piezoelectric energy harvesting under unloaded cases," *Energy Conversion and Management*, vol. 133, pp. 444–457, Feb. 2017.

[35] Y. Li, C. Liao, and S. C. Tjong, "Electrospun Polyvinylidene Fluoride-Based Fibrous Scaffolds with Piezoelectric Characteristics for Bone and Neural Tissue Engineering," *Nanomaterials*, 2019.

[36] A. Wang, Z. Liu, M. Hu, C. Wang, X. Zhang, B. Shi, Y. Fan, Y. Cui, Z. Li, and K. Ren, "Piezoelectric nanofibrous scaffolds as in vivo energy harvesters for modifying fibroblast alignment and proliferation in wound healing," *Nano Energy*, vol. 43, pp. 63–71, Jan. 2018.

[37] A. Wang, M. Hu, L. Zhou, and X. Qiang, "Self-Powered Well-Aligned P(VDF-TrFE) Piezoelectric Nanofiber Nanogenerator for Modulating an Exact Electrical Stimulation and Enhancing the Proliferation of Preosteoblasts," *Nanomaterials*, vol. 9, no. 3, p. 349, Mar. 2019.

[38] M. G. Cain, M. Stewart, and M. G. Gee, "Degradation of piezoelectric materials," National Physical Laboratory Teddington, Tech. Rep. 148, 1999.

[39] J. Briscoe, N. Jalali, P. Woolliams, M. Stewart, P. M. Weaver, M. Cain, and S. Dunn, "Measurement techniques for piezoelectric nanogenerators," *Energy & Environmental Science*, vol. 6, no. 10, pp. 3035–3045, Sep. 2013.

[40] IEEE Std, "IEEE Standard on Piezoelectricity," *ANSI/IEEE Std 176-1987*, pp. 0_1–, 1988.

[41] BS EN 50324, *BS EN 50324-2:2002 - Piezoelectric Properties of Ceramic Materials and Components. Methods of Measurement. Low Power*, Oct. 2002.

[42] ——, *BS EN 50324-1:2002 - Piezoelectric Properties of Ceramic Materials and Components. Terms and Definitions*, Dec. 2001.

[43] M. Stewart, M. G. Cain, and D. A. Hall, "Ferroelectric hysteresis measurement and analysis." Teddington, NPL Report, May 1999.

[44] M. Stewart and M. G. Cain, "Measurement of high field dielectric properties of piezoelectric materials." Teddington, Measurement Good Practice Guide, May 1999.

[45] M. G. Cain and M. Stewart, "Piezoelectric resonance." NPL, Teddington, Measurement Good Practice Guide Guide No. 33, Jan. 2001.

[46] M. Stewart, M. Battrick, and M. G. Cain, "Measuring piezoelectric d33 coefficients using the direct method," NPL, Teddington, Measurement Good Practice Guide Guide No. 44, Jun. 2001.

[47] BS ISO 21819:1, *BS ISO 21819-1. Fine Ceramics (Advanced Ceramics, Advanced Technical Ceramics). Characteristic of Piezoelectric Properties under High-Load Conditions. Part 1. Resonant-Antiresonant Method under High Temperature Conditions*, iso 21819-1:2018 identical ed. BSI, Aug. 2018.

[48] BS ISO 21819-2, *BS ISO 21819-2 Fine Ceramics (Advanced Ceramics, Advanced Technical Ceramics) - Characteristic of Piezoelectric Properties under High-Load Conditions. Part 2: Electrical Transient Response Method under High Vibration Levels.*, iso 21819-2:2018 identical ed. BSI, Aug. 2018.

[49] K. W. Kwok, H. L. W. Chan, and C. L. Choy, "Evaluation of the material parameters of piezoelectric materials by various methods," *IEEE transactions on ultrasonics, ferroelectrics, and frequency control*, vol. 44, no. 4, pp. 733–742, 1997.

[50] P. M. Weaver, T. Stevenson, T. Quast, G. Bartl, T. Schmitz-Kempen, P. Woolliams, A. Blumfield, M. Stewart, and M. G. Cain, "High temperature measurement and characterisation of piezoelectric properties," *Journal of Materials Science: Materials in Electronics*, vol. 26, no. 12, pp. 9268–9278, Dec. 2015.

[51] L. Burianova, A. Kopal, and J. Nosek, "Characterization of advanced piezoelectric materials in the wide temperature range," *Materials Science and Engineering: B*, vol. 99, no. 1–3, pp. 187–191, May 2003.

[52] E. Le Boulbar and C. Bowen, "Study of Y-cut LiNbO3 (010) crystal under oscillated vibration at high temperature for energy harvesting in hostile environment,"

in *Applications of Ferroelectric, International Symposium on Integrated Functionalities and Piezoelectric Force Microscopy Workshop (ISAF/ISIF/PFM), 2015 Joint IEEE International Symposium on The*, May 2015, pp. 292–295.

[53] H. Khanbareh, M. Hegde, J. C. Bijleveld, S. van der Zwaag, and P. Groen, "Functionally graded ferroelectric polyetherimide composites for high temperature sensing," *Journal of Materials Chemistry C*, 2017.

[54] C. Huang, K. Cai, Y. Wang, Y. Bai, and D. Guo, "Revealing the real high temperature performance and depolarization characteristics of piezoelectric ceramics by combined in situ techniques," *Journal of Materials Chemistry C*, vol. 6, no. 6, pp. 1433–1444, 2018.

[55] M. G. Cain, M. Stewart, and M. G. Gee, "Experimental measurement methods for the evaluation of degradation in piezoelectric ceramics." Teddington, NPL Report, May 1998.

[56] J. J. Ruan, R. A. Lockhart, P. Janphuang, A. V. Quintero, D. Briand, and N. de Rooij, "An Automatic Test Bench for Complete Characterization of Vibration-Energy Harvesters," *IEEE Transactions on Instrumentation and Measurement*, vol. 62, no. 11, pp. 2966–2973, Nov. 2013.

[57] L. Zhao, "Synchronization extension using a bistable galloping oscillator for enhanced power generation from concurrent wind and base vibration," *Applied Physics Letters*, vol. 116, no. 5, p. 053904, Feb. 2020.

[58] X. Rui, Z. Zeng, Y. Zhang, Y. Li, H. Feng, X. Huang, and Z. Sha, "Design and Experimental Investigation of a Self-Tuning Piezoelectric Energy Harvesting System for Intelligent Vehicle Wheels," *IEEE Transactions on Vehicular Technology*, vol. 69, no. 2, pp. 1440–1451, Feb. 2020.

[59] J. Liang and W.-H. Liao, "Improved Design and Analysis of Self-Powered Synchronized Switch Interface Circuit for Piezoelectric Energy Harvesting Systems," *IEEE Transactions on Industrial Electronics*, vol. 59, no. 4, pp. 1950–1960, Apr. 2012.

[60] K. Makihara, S. Takeuchi, S. Shimose, and J. Onoda, "Innovative Digital Self-Powered Autonomous System for Multimodal Vibration Suppression," *AIAA Journal*, vol. 50, no. 9, pp. 2004–2011, Sep. 2012.

[61] Y. Wu, A. Badel, F. Formosa, W. Liu, and A. Agbossou, "Self-powered optimized synchronous electric charge extraction circuit for piezoelectric energy harvesting:," *Journal of Intelligent Material Systems and Structures*, Jan. 2014.

[62] K. Makihara and K. Asahina, "Analog self-powered harvester achieving switching pause control to increase harvested energy," *Smart Materials and Structures*, vol. 26, no. 5, p. 055007, May 2017.

[63] I. Kosmadakis, V. Konstantakos, T. Laopoulos, and S. Siskos, "An automated measurement bench for vibration-based energy harvesting systems," in *2013 IEEE 7th International Conference on Intelligent Data Acquisition and Advanced Computing Systems (IDAACS)*, vol. 01, Sep. 2013, pp. 15–20.

[64] C. L. Kuo, S. C. Lin, and W. J. Wu, "Fabrication and characteristic of piezoelectric bimorph MEMS generators based on stainless steel substrate for vibration generator," p. 9, 2014.

[65] I. Kosmadakis, V. Konstantakos, T. Laopoulos, and S. Siskos, "Vibration-based Energy Harvesting Systems Characterization Using Automated Electronic Equipment," *Sensors & Transducers*, vol. 187, no. 4, p. 75, 2015.

[66] A. K. Batra, J. R. Currie, A. A. Alomari, M. D. Aggarwal, and C. R. Bowen, "A versatile and fully instrumented test station for piezoelectric energy harvesters," *Measurement*, vol. 114, pp. 9–15, Jan. 2018.

[67] BS EN 62830-3:2017, *BS EN 62830-3:2017 - Semiconductor Devices. Semiconductor Devices for Energy Harvesting and Generation. Vibration Based Electromagnetic Energy Harvesting.* BSI, Apr. 2017.

[68] H. Kim, S. Priya, H. Stephanou, and K. Uchino, "Consideration of Impedance Matching Techniques for Efficient Piezoelectric Energy Harvesting," *IEEE Transactions on Ultrasonics, Ferroelectrics, and Frequency Control*, vol. 54, no. 9, pp. 1851–1859, Sep. 2007.

[69] P. Biswal, N. Verma, S. K. Kar, and B. Mukherjee, "Development and Performance Analysis of a Low Cost Experimental Set Up for Piezoelectric Based Energy Harvester Using Loudspeaker," in *2018 15th IEEE India Council International Conference (INDICON)*. Coimbatore, India: IEEE, Dec. 2018, pp. 1–5.

[70] J. J. L. Aranda, S. Bader, and B. Oelmann, "An Apparatus for the Performance Estimation of Pressure Fluctuation Energy Harvesters," *IEEE Transactions on Instrumentation and Measurement*, vol. 67, no. 11, pp. 2705–2713, Nov. 2018.

[71] M. Lallart, D. Guyomar, Y. Jayet, L. Petit, E. Lefeuvre, T. Monnier, P. Guy, and C. Richard, "Synchronized switch harvesting applied to self-powered smart systems: Piezoactive microgenerators for autonomous wireless receivers," *Sensors and Actuators A: Physical*, vol. 147, no. 1, pp. 263–272, Sep. 2008.

[72] Y. Sun, J. Chen, X. Li, Y. Lu, S. Zhang, and Z. Cheng, "Flexible piezoelectric energy harvester/sensor with high voltage output over wide temperature range," *Nano Energy*, vol. 61, pp. 337–345, Jul. 2019.

[73] A. A. Basari, S. Awaji, S. Wang, S. Hashimoto, S. Kumagai, K. Suto, H. Okada, H. Okuno, B. Homm, W. Jiang, and S. Wang, "Shape Effect of Piezoelectric Energy Harvester on Vibration Power Generation," *Journal of Power and Energy Engineering*, vol. 02, no. 09, pp. 117–124, 2014.

[74] Y. Uchiyama and M. Fujita, "Robust acceleration and displacement control of electrodynamic shaker," in *2006 IEEE Conference on Computer Aided Control System Design, 2006 IEEE International Conference on Control Applications, 2006 IEEE International Symposium on Intelligent Control*, Oct. 2006, pp. 746–751.

[75] H. M. Gomes, F. S. Ferreira, C. A. K. Thomes, and D. S. Gaspareto, "An automatic system for electrodynamic shaker control by acceleration power spectral density," *Mecanica Computacional*, vol. 26, pp. 2959–2970, 2007.

[76] S. Barker, K. V. Vassilevski, N. G. Wright, and A. B. Horsfall, "High temperature vibration energy harvester system," in *2010 IEEE Sensors*, Nov. 2010, pp. 300–303.

[77] G. Pangallo, S. Rao, R. Carotenuto, and F. G. D. Corte, "Piezoelectric energy harvesting system for hostile environments," in *2016 12th Conference on Ph.D. Research in Microelectronics and Electronics (PRIME)*, Jun. 2016, pp. 1–3.

[78] J. Watson and G. Castro, "A review of high-temperature electronics technology and applications," *Journal of Materials Science: Materials in Electronics*, vol. 26, no. 12, pp. 9226–9235, Jul. 2015.

[79] G. Zhang, Q. Liao, M. Ma, Z. Zhang, H. Si, S. Liu, X. Zheng, Y. Ding, and Y. Zhang, "A rationally designed output current measurement procedure and comprehensive understanding of the output characteristics for piezoelectric nanogenerators," *Nano Energy*, vol. 30, pp. 180–186, Dec. 2016.

[80] Y. Su, C. Dagdeviren, and R. Li, "Measured Output Voltages of Piezoelectric Devices Depend on the Resistance of Voltmeter," *Advanced Functional Materials*, vol. 25, no. 33, pp. 5320–5325, Sep. 2015.

[81] Y. Su, S. Li, Y. Huan, R. Li, Z. Zhang, P. Joe, and C. Dagdeviren, "The universal and easy-to-use standard of voltage measurement for quantifying the performance of piezoelectric devices," *Extreme Mechanics Letters*, vol. 15, pp. 10–16, 2017.

[82] M. J. Kraśny, C. R. Bowen, C. Michel, and J. T. Taylor, "Transient Analysis of a Current Driven Full Wave AC/DC Converter for Indirect Characterisation of Piezoelectric Devices During Energy Harvesting," *Energy Technology*, vol. 8, no. 3, Mar. 2020.

[83] M. Vázquez-Rodriguez, F. J. Jiménez, J. de Frutos, and D. Alonso, "Piezoelectric energy harvesting computer controlled test bench," *Review of Scientific Instruments*, vol. 87, no. 9, p. 095004, Sep. 2016.

[84] F. J. Jiménez, M. Vázquez-Rodriguez, D. Alonso, and J. de Frutos, "Virtual instrument to obtain an optimal linear model for piezoelectric elements involved in road traffic energy harvesting," *Computer Standards & Interfaces*, vol. 51, pp. 1–13, Mar. 2017.

[85] Marcin J. Kraśny, "Enhamer," https://github.com/enhamer/enhamer, Jun. 2020.

[86] S. P. Beeby, M. J. Tudor, and N. M. White, "Energy harvesting vibration sources for microsystems applications," *Measurement Science and Technology*, vol. 17, no. 12, p. R175, 2006.

[87] Y. Wang, Y. Jia, Q. Chen, and Y. Wang, "A Passive Wireless Temperature Sensor for Harsh Environment Applications," *Sensors*, vol. 8, no. 12, pp. 7982–7995, Dec. 2008.

[88] Y.-J. Lai, W.-C. Li, C.-M. Lin, V. V. Felmetsger, D. G. Senesky, and A. P. Pisano, "SiC/AlN piezoelectric energy harvesters for pulsed pressure sources in harsh environment applications," in *Dig. Tech. Solid-State Sens. Act. Microsyst. Workshop (Hilton Head'12)*, Hilton Head, SC, Jun. 2012, pp. 505–508.

[89] A. Dziedzic and D. Nowak, "Thick-film and LTCC passive components for high-temperature electronics," *Radioengineering*, vol. 22, no. 1, pp. 218–226, 2013.

[90] S. Shao, W. C. Lien, A. Maralani, and A. P. Pisano, "Integrated 4H-silicon carbide diode bridge rectifier for high temperature (773 K) environment," in *2014 44th European Solid State Device Research Conference (ESSDERC)*, Sep. 2014, pp. 138–141.

[91] M. W. Hooker, "Properties of PZT-based piezoelectric ceramics between-150 and 250 C," 1998.

[92] C. Miclea, C. Tanasoiu, L. Amarande, C. F. Miclea, C. Plavitu, M. Cioangher, L. Trupina, C. T. Miclea, and C. David, "Effect of temperature on the main piezoelectric parameters of a soft PZT ceramic," *Rom. J. Inf. Sci. Technol*, vol. 10, no. 3, pp. 243–250, 2007.

[93] F. C. Y. Benureau and N. P. Rougier, "Re-run, Repeat, Reproduce, Reuse, Replicate: Transforming Code into Scientific Contributions," *Frontiers in Neuroinformatics*, vol. 11, 2018.

2.2 Summary

A complex measurement tool with dedicated open source hardware and open software solution for electrical characterisation of piezoelectric energy harvesters is proposed and described in detail. The new software offers unique modular construction which allows easy modification, and exchange of instrumentation for rapid upgrades to provide additional measurement tools if necessary.

Common challenges and measurements difficulties are presented which can provide measurement solutions in a broad field of energy harvesting testing. This includes characterisation of energy harvesters at elevated temperatures and long-term testing, which is of importance for industrial applications before the deployment of piezoelectric energy harvesters as a reliable power supply source.

CHAPTER 3

IMPROVED CHARACTERISATION OF PIEZOELECTRIC ENERGY HARVESTERS AND SIMPLIFIED METHOD FOR SYSTEM LOSSES ESTIMATION AND MODELLING

3.1 Prologue

A novel, indirect method for the characterisation of piezoelectric parameters using a simplified procedure is presented. It allows estimation and modelling of system losses in an energy harvesting system. The paper describes a detailed analysis of full wave bridge rectifier (AC/DC converter) - the first stage after piezoelectric transducer in vibration powered energy harvesting device. A comprehensive explanation is given to the development of voltage-time load capacitor charging curve, and the maximum final voltage on a storage capacitor can be estimated from a simple equation.

The proposed method offers a new and simple approach for the measurement of piezoelectric parameters yet allows validation of complex energy harvester performance.

Paper 2: Statement of Authorship

<table>
<tr><td colspan="10">This declaration concerns the article entitled:</td></tr>
<tr><td colspan="10">Transient Analysis of a Current Driven Full Wave AC/DC Converter for Indirect Characterisation of Piezoelectric Devices During Energy Harvesting</td></tr>
<tr><td colspan="10">Publication status (tick one)</td></tr>
<tr><td>Draft manuscript</td><td></td><td>Submitted</td><td></td><td>In review</td><td></td><td>Accepted</td><td></td><td>Published</td><td>✓</td></tr>
<tr><td colspan="10">Copyright status (tick the appropriate statement)</td></tr>
<tr><td colspan="3">I hold the copyright for this material</td><td></td><td colspan="5">Copyright is retained by the publisher, but I have been given permission to replicate the material here</td><td>✓</td></tr>
<tr><td>Publication details (reference)</td><td colspan="9">M. J. Kraśny, C. R. Bowen, C. Michel, and J. T. Taylor,
“Transient Analysis of a Current Driven Full Wave AC/DC Converter for Indirect Characterisation of Piezoelectric Devices During Energy Harvesting”,
Energy Technology,
DOI: 10.1002/ente.201901317</td></tr>
<tr><td>Candidate’s contribution to the paper (detailed and also given as percentage)</td><td colspan="9">Formulation of ideas:
J. T. Taylor and C. R. Bowen and candidate contributed to the transient analysis of a full wave bridge rectifier. The proposed measurement method of system losses represented as an effective capacitance is solely by candidate.
Candidate (33%).

Design of methodology:
Equal contribution from all authors J. T. Taylor, C.R. Bowen and candidate; Candidate (33%).

Experimental work:
Rectifier experiments, simulations, data analysis and processing by candidate (100%).

Presentation of data in journal format:
Equal contribution from all authors; candidate (25%).</td></tr>
<tr><td>Statement from Candidate</td><td colspan="9">This paper reports original research I conducted during the period of my Higher Degree by Research candidature.</td></tr>
<tr><td>Signed</td><td colspan="5">  </td><td>Date</td><td colspan="3">08.08.2020</td></tr>
</table>

Transient Analysis of a Current Driven Full Wave AC/DC Converter for Indirect Characterisation of Piezoelectric Devices During Energy Harvesting

Marcin J. Kraśny[(1)], Chris R. Bowen[(1)], Coralie Michel[(1)], John T. Taylor[(2)]

[(1)] Department of Mechanical Engineering, [(2)] Department of Electrical Engineering
University of Bath, Bath, BA2 7AY, UK

Abstract

This article provides a new approach to extract piezoelectric energy harvester properties, namely, capacitance and current, from the increase of voltage with time on a storage capacitor after full wave rectification. The work provides a derivation of a more complete expression for the development of the output voltage with time, from which the equilibrium expression used in earlier publications appears as a limiting case. This new formulation enables an accurate estimate of the sinusoidal driving current and the shunt capacitance to be made without recourse to direct measurement. Using the analysis with both simulated and experimental data, a four-step procedure is proposed that requires only the measurement of the initial slope of the voltage–time profile and the final settling value. This approach allows the much studied method of converting the piezoelectric output into charge stored on a capacitor to provide a unique indirect measurement method of the driving current and device capacitance while the piezoelectric energy harvester operates at a variety of conditions, such as frequency, temperature, stress, and strain.

Keywords

current mode, rectifier, harvesting, piezoelectric, intrinsic capacitance

3.1.1 Introduction

Energy harvesting using piezoelectric materials provides a means to produce power, typically in the microwatt to milliwatt range, by conversion of mechanical vibrations or strain into electrical power using inertial or kinematic energy-harvesting approaches [1].

Applications for piezoelectric energy harvesting include the provision of autonomous, low-maintenance, and self-powered systems, such as wireless sensor networks, structural health monitoring and medical devices, and biomedical monitoring with a reduced reliance on batteries or electric cables [2, 3, 4, 5, 6, 7]. Since the charge created by a piezoelectric device during the application of alternating mechanical load is related to its change in polarization under tensile or compressive stresses, an alternating current is generated. As a result, methods such as full wave rectification are used to convert the AC output to DC and the resulting electrical energy is stored on a capacitor. Dell' Anna *et al.* have provided a detailed overview of the range of power management circuits currently available for piezoelectric energy harvesting [8]. Significant attention has been placed on the optimization of the load resistance [9, 10] along with improvements using synchronous switching [11] or peak detection [12]. There is also effort on the use of a double stage AC/DC architecture to optimize the DC voltage at the output of the diode bridge rectifier by means of a DC/DC converter equipped with maximum power point tracking and connected to a battery [13].

In this article, the output of a piezoelectric device when it is driven by a sinusoidal mechanical excitation and terminated in a rectifier-filter-type full wave bridge AC–DC converter is considered. As a result of its simplicity in terms of manufacture and use, it is a highly convenient and much studied method of harvesting the energy output of a piezoelectric device by storing the charge generated on a capacitor. The rectifier is typically a diode bridge and the filter the parallel combination of the load resistance and a capacitor providing a time constant sufficiently large that any residual ripple on the DC output voltage can be ignored. In addition, we consider here the case of low electromechanical coupling (LEC), as defined in Balato *et al.*, [13] although in principle the method can be extended to cases for both weakly and nonweakly electromechanical coupled systems [14]. Following Ottman *et al.* [15] the device is modelled as the parallel combination of a sinusoidal current source and a capacitor (the diodes are treated as ideal devices). The output voltage, and therefore the power dissipation in the load, increases with time and it is shown that the resulting profile falls into two phases: an initial phase where the voltage increases rapidly followed by a steady-state phase when the energy supplied per cycle is in equilibrium with the energy dissipated in the load in the same period.

Previous studies have focused on optimizing the power output of such systems in the steady-state phase of the response. Specifically, Ottman *et al.* [15] assumed that the vibration amplitude is not affected by the load resistance, while Guyomar *et al.* [16] hypothesized that the periodic external excitation and the speed of mass are in phase. More recently, these methods were developed by Shu and Lien [17] taking into account

the global behavior of the electromechanical system.

In this article, we present a more detailed analysis of the transient behavior of the state variables of the circuit at each stage of the rectification and filtering process than has been reported previously. This provides a more complete analytic expression for the output voltage as a function of time than in earlier works and the extra information thus obtained forms the basis of the characterization method described in Section 3.1.3. This method is presented as a four-step procedure that requires only the measurement of the initial slope of the voltage–time profile and the final settling value of the output voltage. We consider the influence of each of the embedded components on the rectification process and equations in a simple and understandable form are provided. The proposed method could be of significant benefit for researchers in the process of designing and improving the materials used for energy harvesting as well as for electronics engineers responsible for the circuit design of piezoelectricbased, self-powered devices.

The work presented in this article provides a quick and efficient tool for material characterization and allows easy performance comparison since it enables accurate estimates of the sinusoidal driving current and the shunt capacitance to be made without recourse to complicated direct measurement and expensive high input impedance electrometers or impedance analyzers by simply monitoring the voltage on the storage capacitor with time. What is more important and has not yet been reported in the literature to date is that it enables the piezoelectric device to be characterized under the conditions of frequency, temperature, stress, and strain experienced by the energy harvester during operation. This is of interest because piezoelectric and dielectric properties of the material, and the device, can change with time, frequency, electric field, temperature, and stress.

3.1.2 Rectification Model

Model Development

A vibrating piezoelectric element is modelled as a sinusoidal current source I_P in parallel with its internal electrode capacitance C_P. This model was proposed in by Ottman *et al.* [15] for the particular case of LEC and can be applied also to the analysis of devices such as pyroelectric generators [18]. The magnitude of the polarization current I_P varies with the mechanical excitation level of the piezoelectric element. Such a device generates an AC current and is therefore the first stage in an energy-harvesting circuit in an AC–DC converter, typically a full wave rectifier and a smoothing capacitor, C_L, as shown in Fig. 3-1. The driving current is of the form $I_P = I_0 sin\omega t$, where $\omega = 2\pi/T$ and T is the period of the vibration source and the DC load is represented by R_L.

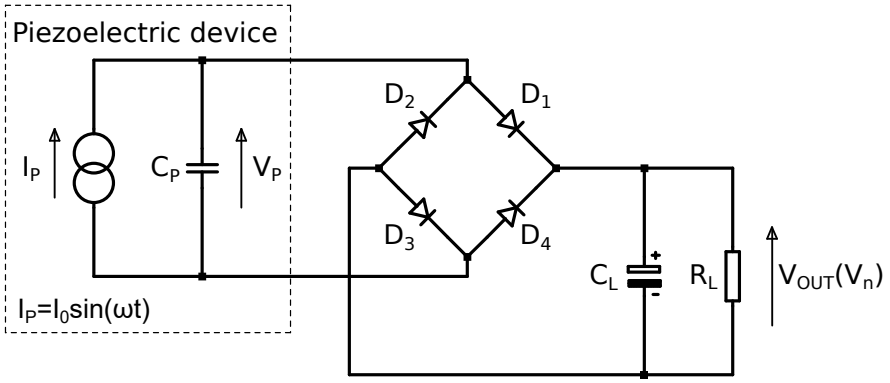

Figure 3-1: *Circuit schematic showing the equivalent circuit of a piezoelectric generator (on the left) connected to a diode bridge AC–DC converter* $I_P = I_0 sin\omega t$.

The operation of this circuit has been described in previous studies [15, 16, 17]. However, these references focused on the steadystate behavior of the voltage output, ignoring the initial transient performance of the state variables. The following analysis begins with the transient behavior, from which the steady-state response is derived as a limiting case. For completeness, a brief qualitative description of the operation of the circuit is given; a more detailed analysis of the full wave bridge rectifier voltage- and current-driven modes are provided in *Section 3.1.5, Supporting Information*.

Referring to Fig. 3-1, in the first half cycle of operation, assuming a boundary condition that all voltages in the circuit are zero at $t = 0$, I_P charges the parallel combination of C_P, C_L, and R_L, the diodes D_1 and D_3 being forward biased and ON. This phase continues until I_P passes through zero (at the end of the first half cycle, at which point D_1 and D_3 become reverse biased and switch OFF) and subsequently reverses. However, although the driving current now begins to increase negatively and the other pair of bridge diodes D_2 and D_4 are available to conduct in this direction, they cannot do so because the remaining positive voltage on C_P causes them to be reverse biased. D_2 and D_4 remain blocked in this way until the voltage on C_P is discharged by I_P. The effect of this voltage is to make the diodes conduct during part of the duty cycle only, which significantly modifies the circuit behavior compared to the case where $C_P = 0$ (i.e., capacitor not connected) and the circuit operation becomes non-linear. These two phases of operation are described by the two equivalent half circuits shown in Fig. 3-2, and Fig. 3-13, *Supporting Information*.

The duration of the blocking or *commutation* phase increases progressively as V_{OUT} increases, reducing the energy transfer from the piezoelectric device to the load (see Fig. 3-3a). V_{OUT} rises stepwise monotonically and eventually reaches a limiting (steady-state) value, $V_{n(n\to\infty)}$, at which point the energy input is in equilibrium with the energy

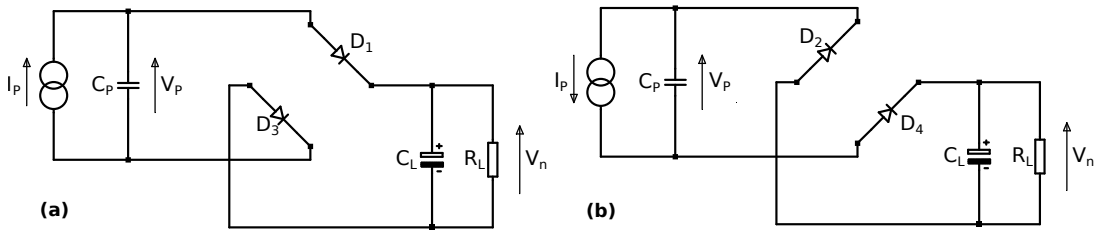

Figure 3-2: *Equivalent half circuits of the circuit of Fig. 3-1. a) The operation of the circuit in the half cycles where $I_P = I_0 sin\omega t$ is driving positively and b) for the negative half cycles; (b) also indicates the blocking effect of the charge on C_P in the negative half cycles.*

dissipated in the load, as shown in Fig. 3-3b. An example of the corresponding current waveform is shown in Fig. 3-4; these can be compared with more detailed views of the corresponding current waveforms in Fig. 3-14, *Supporting Information*.

In addition to the sinusoidal nature of the driving current, the following model assumptions are made:

1. The diodes are ideal and act as ideal switches with no series resistance or DC offset voltage;

2. $R_L \cdot (C_P + C_L) >> T$ so that the time constant $R_L \cdot (C_P + C_L)$ is much longer than the period of the exciting sinusoid, T.

This assumption enables the exponential expression for P (from Equation 3.2) to be simplified and, crucially, ensures that the sequence describing the development of the output voltage with time converges. Note that in general we can also state that $C_P << C_L$ since this will be the case in most practical situations. Note however that the value of C_L cannot be increased without limit as this also increases the time to convergence of the process and can render it impractical to use, as discussed in more detail subsequently.

Model Analysis

In the first half cycle of operation, termed phase zero, $0 \leq \tau \leq T/2$, as already described, C_P, C_L, and R_L are charged by the full positive phase of I_P. For this half cycle the circuit behaves in a linear manner and the first *Assumption* mentioned earlier allows us to calculate V_{OUT} at $t_1 = T/2$, which we call V_1

$$V_1(1) = PV_0 \tag{3.1}$$

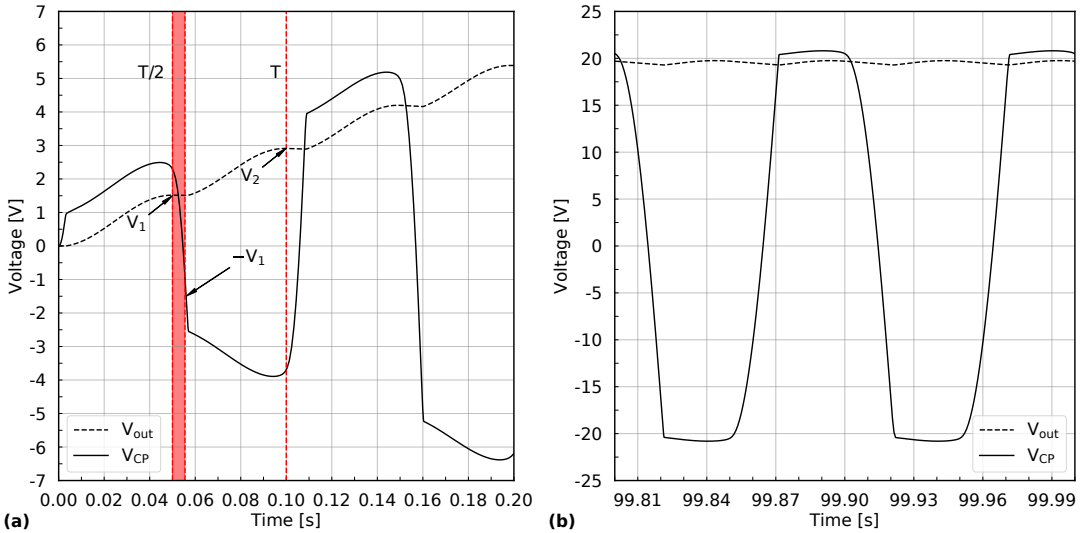

Figure 3-3: *Development of the output voltage (V_{OUT}) with time of the circuit of Fig. 3-1 and the voltage across C_P with time. a) The first few half cycles and the appearance of the blocked phase in the second half cycle, of duration τ_1 (marked with the red vertical block). b) The same pair of voltages at steady state (equilibrium) when V_{OUT} has reached a constant value except for a small residual ripple.*

where P is the transient response of an RC circuit [19].

$$P = 1 - e^{-(\frac{T}{2})/(C_P+C_L)R_L} \tag{3.2}$$

and

$$V_0 = \frac{2}{\pi} I_0 R_L \tag{3.3}$$

where V_0 is an average voltage derived from the average value of the current in a half cycle of a sinusoid. The term P is a constant depending on physical parameters of piezoelectric device and embedded circuit. Note that using *Assumption 2*, $R_L \cdot (C_P + C_L) >> T$, a simplified expression for P can be derived:

$$P \cong \frac{T}{2 \cdot (C_P + C_L) R_L} \tag{3.4}$$

For the next half cycle, i.e. $T/2 \leq t \leq T$, having passed the peak of the sinusoid, the voltage generated by the piezoelectric device declines and current flow through the diodes is blocked by the residual positive voltage, leaving V_1 constant, subject to some leakage through R_L, as shown in Fig. 3-3a. This phase lasts until C_P discharges and is subsequently recharged negatively to V_1, so that D_2 and D_4 are turned ON. The time taken for V_P to traverse the region between V_1 and $-V_1$ defines the part of the duty

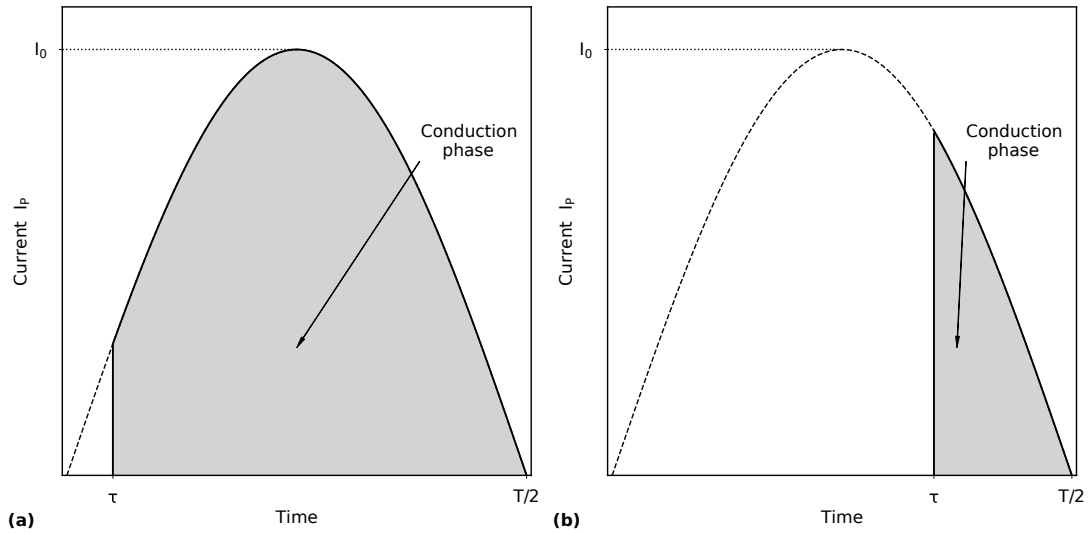

Figure 3-4: *One half cycle of the sinusoidal current I_P, showing the part of the cycle where conduction occurs, i.e., in the range $\tau \leq t \leq T/2$. a) The conduction phase during the first few half cycles. b) The same pair of currents at steady state (equilibrium) when V_{OUT} has reached a constant value and experiences short rechargeable pulses to counteract the residual ripple.*

cycle of duration τ_1 when the diode bridge is not conducting. This can be seen in the simplified current waveforms in Fig. 3-4, and in more detail in Fig. 3-14, *Supporting Information*.

The time taken for this to occur is calculated by analyzing the charging behavior of a capacitor C_P from a sinusoidal source I_P

$$I_P(n) = C_P \frac{dV_n}{dt} \tag{3.5}$$

which after integrating across a half sinusoid from τ_n to T/2 can be expressed, for the n^{th} half cycle, as

$$\cos \omega\tau_n = 1 - \frac{2\omega C_P}{I_0} V_n \tag{3.6}$$

The average value of the transferred current (I_{AV}) in a partially blocked half cycle (see Fig. 3-4), where the length of the commutation cycle is $< \tau_n, T/2 >$, is given by

$$I_{av} = I_0 \frac{2}{T} \int_{\tau_n}^{T/2} sin\omega_0 t dt = I_0 \frac{1}{\pi}(1 + cos\omega_0\tau_n) \tag{3.7}$$

where as $\tau_n \to 0, I_{AV} \to 2I_0/\pi$ as expected for the ideal, non-blocking case (see Equation 3.3). Substituting for cos $\omega\tau_n$ from Equation 3.6, the average value of the current

in a partially blocked half sinusoid is

$$I_{AV} = \frac{2I_0}{\pi}(1 - \frac{V_n}{V_0}A) \tag{3.8}$$

where the constant A is given by

$$A = 4fC_PR_L \tag{3.9}$$

and $f = \omega/2\pi$. This can be normalized to the ideal case where there is no blocking

$$F = (1 - \frac{V_n}{V_0}A) \tag{3.10}$$

The dimensionless, normalized factor F given in Equation 3.10 is a measure of the square root of the energy transmitted to the load normalized to the maximum possible value, i.e., when there is no blocking. In practice, as we have seen, no blocking occurs only in the first half cycle of operation. Using this information, we can now show how the sequence progresses. The output voltage after the next half cycle is therefore

$$V_2 = V_1 + P(V_0 - V_1)(1 - \frac{V_1}{V_0}A) \tag{3.11}$$

Substituting for V_0 from Equation 3.1

$$V_2 = V_1[1 + (1 - P)(1 - AP)] \tag{3.12}$$

Assumption 2 ensures that $P << 1$ and therefore the terms in P^2 and above can be neglected. The expression for V_2 can therefore be rewritten

$$V_2 = V_1[1 + r] \tag{3.13}$$

where

$$r = 1 - P(1 + A) \tag{3.14}$$

where r is the common ratio of the sequence.

Similarly, proceeding as in Equation 3.11, the expression for the next iteration follows immediately

$$V_3 = V_1(1 + r) + P[V_0 - V_1(1 + r)](1 - \frac{V_1(1 + r)}{V_0}A) \tag{3.15}$$

After rearrangement and neglecting terms in P^2 and above, this can be written

$$V_3 = V_1(1 + r + r^2) \tag{3.16}$$

Using this approach, it can be shown that the sum of the sequence after n iterations is given by the expression

$$V_n = V_1 \sum_{i=0}^{n-1} r^i = V_1 \cdot q_n \tag{3.17}$$

where the sequence q_n is a geometric progression and the sum to n terms of such a sequence is given by the expression

$$q_n = \sum_{i=0}^{n-1} r^i = 1 + r + r^2 + \ldots + r^{n-1} = \frac{1 - r^n}{1 - r} \tag{3.18}$$

and therefore Equation 3.17 becomes

$$V_n = V_1 \cdot q_n = V_1 \frac{1 - r^n}{1 - r} \tag{3.19}$$

where V_1 and r are given by Equation 3.1 and 3.14, respectively.

Crucially, an examination of the expression for r (Equation 3.14) shows that applying *Assumption 2*, $0 \leq r \leq 1$ and so the sequence q_n converges. As a result, in the limit as $n \to \infty$, Equation 3.17 becomes

$$V_{n(n\to\infty)} = \frac{V_1}{1 - r} \tag{3.20}$$

Substituting for r and V_1

$$V_{n(n\to\infty)} = \frac{V_0}{1 + A} \tag{3.21}$$

Equation 3.17 and 3.19 therefore describe the development of the transient output voltage with time, while Equation 3.21 is the steady-state value of the output voltage and has been reported elsewhere in the literature [15]. It is significant that the final setting value of the output voltage is independent of the load capacitance (C_L). Note also that the speed of convergence of the process can be deduced from Equation 3.19. As $r \to 1$, the time to convergence, namely, the point in the sequence when V_n approaches its final value as determined by Equation 3.20 and 3.21, tends to infinity. Since from Equation 3.14 the common ratio r depends on the parameter P and therefore the load time constant, the load capacitor C_L cannot be increased without limit, as indicated in Section 3.1.2.

3.1.3 Results and Discussion

Model Validation Using Circuit Simulation

To validate the model, a number of examples were simulated in LTspice (Analog Devices) [20] using a standard p-n silicon signal diode model (1N4148) and the results compared to Equation 3.17 and 3.21. As discussed, a parallel combination of a sinusoidal current source and a capacitor was used to model the piezoelectric energy harvester (see Fig. 3-1). The parameters of the simulations are related to fixed values of $C_P = 150$ nF , $C_L = 10$ μF, $R_L = 100$ kΩ, $f = 10$ Hz, and five values of peak driving current I_0: 100, 200, 300, 400, and 500 μA, as shown in Fig. 3-1.

The results of the comparison are shown in Fig. 3-5. In all cases, a high level of

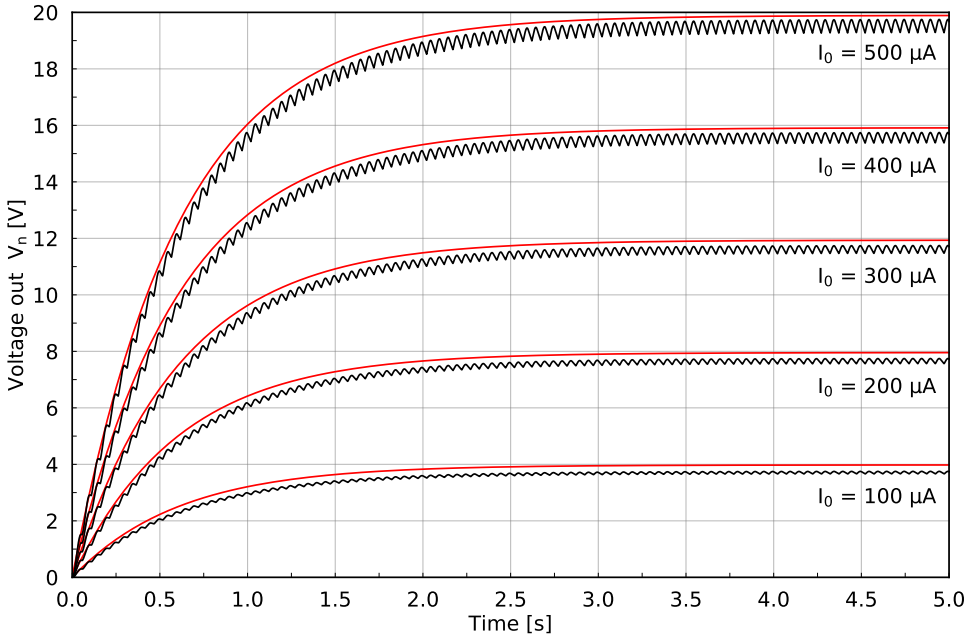

Figure 3-5: *Comparison of model (solid, red traces) with circuit simulation (black traces with ripple) based on parameters given in Section 3.1.3. Beginning at the top the traces show the results for I_0 = 500, 400, 300, 200, and 100 μA. C_P = 150 nF, C_L = 10 μF, R_L = 100 kΩ, and f = 10 Hz.*

agreement between the model equations and the LTspice output is evident in both the initial transient voltage with time and the steady-state regions of operation. Note that the model outputs are consistently greater than the LTspice values, since the model does not allow for the ON voltage of the diodes. This is not a problem where the final value of the output is a few volts or more, as in the examples shown in Fig. 3-5. In cases where this voltage is lower, the inclusion of a diode model will be necessary. Finally, it

should be noted that the LTspice output voltage contains a small residual ripple voltage due to the finite value of the time constant $R_L \cdot C_L$. As this does not contribute to the information intended to be gathered by the proposed method, no corresponding model of ripple was included.

Application of the Spice Model to Extract I_0 and C_P from the Voltage-Time Data

The proposed model is successful in calculating the development of the voltage on the storage capacitor C_L with time. We will now show that the model Equation 3.17 and 3.21 provide a method to estimate directly the two unknown parameters of the working piezoelectric energy harvester, I_0 and C_P, using simply the initial slope and final value of the voltage–time profile. This is possible since the development of V_{OUT} with time falls into two distinct phases, namely, the transient (Equation 3.17) and steady state (Equation 3.21), each with its own characteristic equation, shown in Fig. 3-6. Beginning with the sequence in Equation 3.17, it can be shown that

$$r \approx \frac{V_{n(n\to\infty)} - V_1}{V_{n(n\to\infty)}} \tag{3.22}$$

Furthermore, combining the expression for r (Equation 3.14) with the simplified form of P (Equation 3.4), the following expression for C_P can be derived

$$C_P = \frac{2R_L C_L(1-r) - T}{2R_L(r-1) + 4R_L} \tag{3.23}$$

Finally, inverting Equation 3.21

$$I_0 = \frac{\pi V_{n(n\to\infty)}(1 + 4fC_pR_L)}{2R_L} \tag{3.24}$$

where I_0 is the amplitude of the driving sinusoid, I_P.

Using these equations, a four-step parameter extraction procedure can be derived. This is shown schematically in Fig. 3-6. The procedure is as follows:

1. Record the steady-state value of the output voltage on C_L at ($V_{n(n\to\infty)}$);
2. Calculate r from the charging curve on the voltage–time profile using Equation 3.22;
3. Calculate C_P using Equation 3.23, r, and other known constant parameters (R_L and C_L);

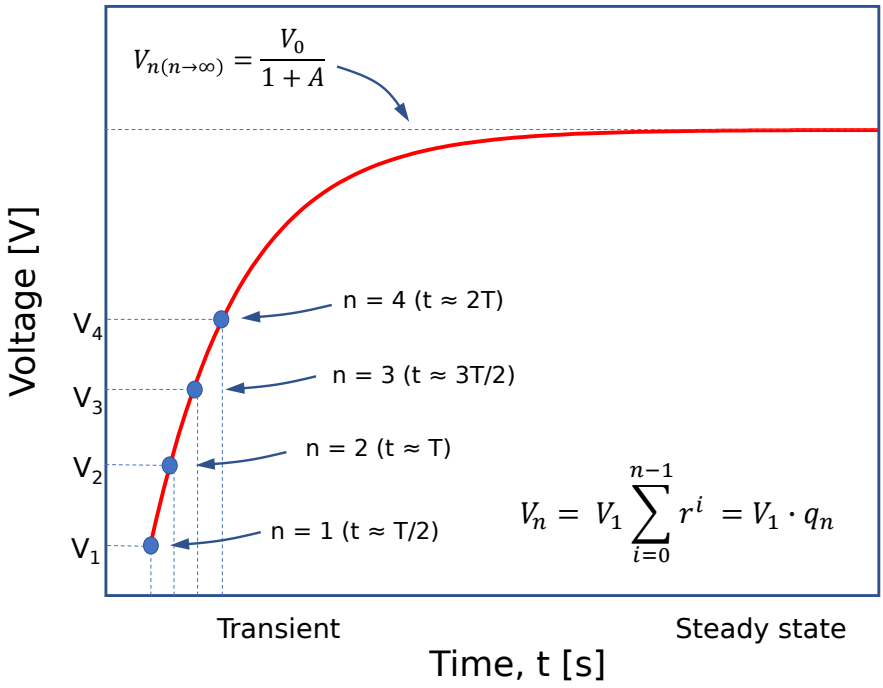

Figure 3-6: *Illustration of the development of the output voltage (voltage on capacitor C_L) with time, showing the transient and steady-state regions.*

4. Calculate I_0 using Equation 3.24, $V_{n(n\to\infty)}$, calculated value of C_P (Equation 3.23), and other known parameters (R_L and f).

To validate the proposed method, Table 3.1 and Fig. 3-7 compare the values for C_P and I_0 obtained using the four-step extraction procedure with the data shown in Fig. 3-5 that is based on the known values used in the simulations. The resulting values for I_0 and C_P indicate that the proposed procedure provides a good level of accuracy for both these key parameters.

For clarity the data in Table 3.1 are repeated in Fig. 3-7a. It should be noted that the data shown in Table 3.1 are calculated for the "RC to T" ratio equal to 10.15, which was chosen as a lowest condition for this parameter in the described case. For an "RC to T" ratio higher than 20 the resulting C_P calculation error is lower than 1.7% and the resulting I_0 error less than 2.0%. This is because *Assumption 2*, namely, $R_L(C_P + C_L) >> T$, becomes more valid, thereby improving the accuracy of the approximate expression for P, Equation 3.4. Fig. 3-7b is a plot of the extracted values of C_P and I_0 as a function of increasing the "RC to T" ratio from *Assumption 2*.

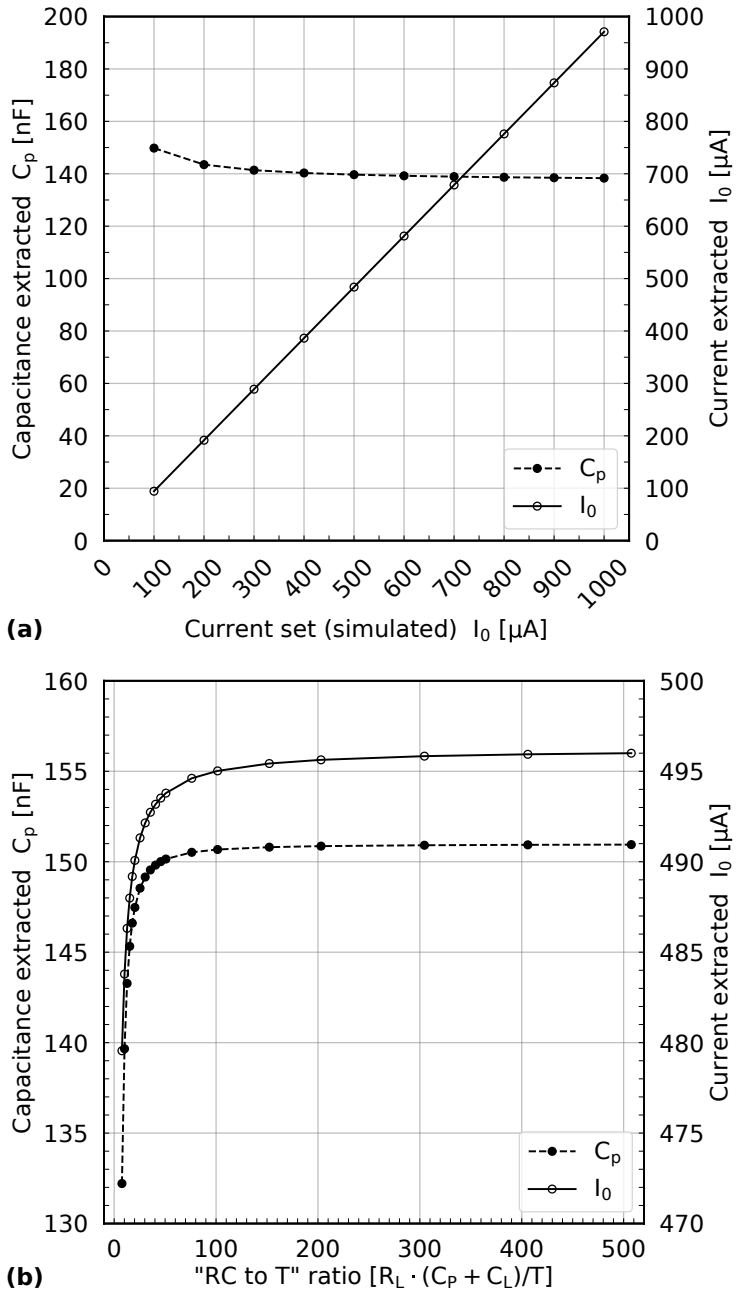

Figure 3-7: *a) I_0 (solid line) and C_P (dashed line) extracted from data in Fig. 3-5 at 10 Hz versus I_0 simulated in the extended range for up to 1 mA. b) The accuracy of the extracted values of I_0 (solid line) and C_P (dashed line) with increasing "RC to T" ratio from Assumption 2. The nominal values are I_0 = 500 μA, C_P = 150 nF, C_L = 10 μF, and R_L from 100 $k\Omega$ to 5 $M\Omega$.*

Table 3.1: *Extraction of C_P and I_0 based on data in Fig. 3-5 (f = 10 Hz). Percentage error values in parenthesis. Last row in table for I_0 = 1 mA is added to show a limiting case.*

I_0 set $[\mu A]$	V_1 (SPICE) $[V]$	$V_{n(n\to\infty)}$ (SPICE) $[V]$	r extracted (Eqn 3.22)	C_P extracted $[nF]$ (Eqn 3.23)	I_0 extracted $[\mu A]$ (Eqn 3.24)
100	0.296	3.754	0.921	149.80 (0.136%)	94.30 (5.70%)
200	0.601	7.751	0.922	143.49 (4.34%)	191.62 (4.19%)
300	0.907	11.752	0.923	141.38 (5.75%)	288.99 (3.67%)
400	1.212	15.756	0.923	140.31 (6.46%)	386.39 (3.40%)
500	1.518	19.760	0.923	139.66 (6.89%)	483.79 (3.24%)
1000	3.048	39.791	0.923	138.34 (7.78%)	970.90 (2.91%)

Application of Method to Real Experimental Data

We now apply the approach described in the previous sections to a real piezoelectric energy-harvesting configuration and extract I_0 and C_P from experimental data. A commercially available macrofibre composite (MFC) patch (MFC2414-P2) [21] with an active area of 24 mm by 14 mm was mounted on a carbon-reinforced fibre matrix (CRFM) cantilever beam of dimensions (300 mm length, 60 mm width, and 0.5 mm thickness) using epoxy resin (ARALDITE Standard). The manufacturing process of the beam is described in detail by Harris *et al.* [22]. The beam was clamped in a holder constructed from two metal plates (29 mm width, 88 mm length, and 2.6 mm thickness) and mounted on an electrodynamic shaker (LDS V455) in the same manner as described by Harris *et al.* [22]. The shaker was driven by the signal generated by a Keysight 33210A function generator amplified by the LDS PA1000 amplifier. Initially the voltage output from the beam was scanned in the frequency sweep mode from 5 to 50 Hz at a constant acceleration of 0.5 g (4.9 ms^2) to find the mechanical resonance frequency, at which the energy produced by the MFC patch is maximum. The first resonance mode was found at 6.5 Hz, followed by a second mode at 35 Hz. As the first resonance frequency results in the highest output signal, experiments were conducted using this mode. The combination of a relatively large area piezoelectric element and mechanical oscillation at the resonance frequency of the structure leads to a relatively large piezoelectric charge with short circuit currents in excess of 100 μA and open circuit voltages in excess of 40 V; this experimental configuration was selected to minimize any errors due to the resulting voltage drop introduced by the diodes in the rectifying circuit. The unclamped capacitance (constant stress capacitance) of the MFC2414-P2 patch was measured with an impedance-phase analyzer (Solartron 1260) with a dielectric interface (Solartron 1296) with 0.1 V_{RMS} signal at 6.5 Hz and was 32.0 nF. The capacitance measured with

a standard LCR meter (HP 4263B with 1.0 V_{RMS} signal at 100 Hz) was 31.3 nF. The claimed functionality of a piezoelectric generator modelled and simulated as a constant current source was proven with various load resistances and is described in detail in *Section 3.1.7, Supporting Information*.

The piezoelectric harvester was connected to a full wave bridge rectifier constructed from four 1N4148 (NXP Semiconductors) diodes with C_L = 10 μF (Rubycon radial aluminum electrolytic LLE series; 200 V capacitance measured with LCR meter at 100 Hz was 9.99 μF) and R_L = 500 kΩ (PeakTech 3265 resistance decade) as in the circuit schematic shown in Fig. 3-4. Since the piezoelectric charge Q generated is proportional to stress (and strain) and therefore the amplitude of the piezoelectric current (I_0) should be proportional to the excitation level the cantilever was driven with increasingly large accelerations of amplitude 0.2, 0.5, 0.8, and 1 g, which correspond to short circuit currents I_0 of 30, 66, 103, and 124 μA (Table 3.2); further details are shown in *Section 3.1.6, Supporting Information*. The voltage on the C_L capacitor was measured as a function of time with an electrometer's (Keithley 6517B) analogue output connected to an oscilloscope (Agilent DSO-X 2024A), responsible for recording of the charging curve. Initially the C_L capacitance and intrinsic piezoelectric capacitance C_P were discharged and then short circuited to ensure no residual charge was stored in those capacitances. Then the full charging cycle, for the given excitation, was repeated three to five times.

Table 3.2: *Extraction of C_P and I_0 based on experimental data in Fig. 3-9. Measurement error values in parenthesis are standard deviations.*

Excitation acceleration [g]	Measured I_0 [μA]	Calculated C_P [nF] (Eqn 3.23)	Calculated I_0 [μA] (Eqn 3.24)
0.2	30.32 ($\pm$0.53)	42.5 ($\pm$3.8)	29.47 ($\pm$0.58)
0.5	66.12 ($\pm$1.09)	43.6 ($\pm$2.9)	61.32 ($\pm$1.67)
0.8	102.70 ($\pm$1.63)	46.1 ($\pm$2.0)	92.68 ($\pm$ 1.30)
1.0	124.39 ($\pm$2.30)	43.1 ($\pm$2.0)	106.49 ($\pm$1.20)

From the recorded signal, the values of C_P and I_0 were calculated and results are shown in Table 3.2 and Fig. 3-8.

The capacitance (C_P) extracted from the experimental data using the four-step procedure described previously with the use of Equation 3.23 is a stable value, relatively independent of the level of excitation (average C_P = 44.2 nF) applied to the piezoelectric device.

The amplitude of the current I_0 was similarly calculated and compared to the short circuit current produced by the device. Calculated current values (using Equation 3.24)

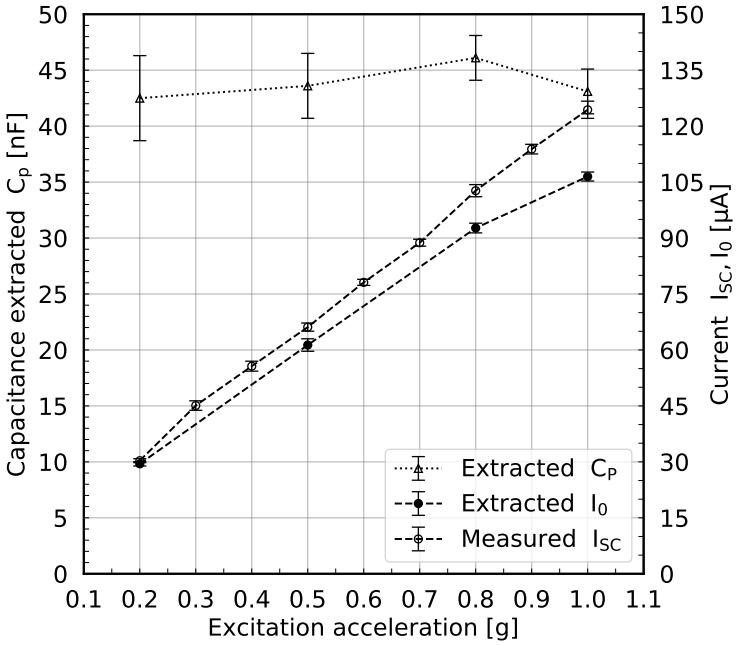

Figure 3-8: *Comparison with measured I_0 and calculated short circuit current and capacitance. Error bars represent standard deviations.*

increase with amplitude of excitation due to the increase in strain and therefore charge generation, as expected, and are within 10% of the values obtained by direct measurement. The accuracy of I_0 current extraction could be increased by calculating the P value with the previously extracted C_P (Equation 3.23) value using Equation 3.2 and substituting this value into the inverted Equation 3.3 to solve for I_0.

Fig. 3-9 is a plot of the measured output voltage as a function of time for the four values of acceleration used in the experiment, compared to the output of the proposed model calculated for the extracted values of I_0 and averaged value of C_P (44.2 nF).

The aforementioned case was also simulated with LTspice with the initial values of C_P = 32.0 nF and (measured short circuit currents) I_0 of 30.32, 66.12, 102.70, and 124.39 μA. The averaged value of retrieved C_P was 31.5 nF and retrieved values of I_0 are calculated with error smaller than 2%. Further detailed analysis is shown in *Section 3.1.8, Supporting Information*. Note that given the values of C_L, R_L, and the extracted value of C_P, the "RC to T" ratio from *Assumption 2* is 32.6.

However, the value of C_P extracted from experimental data is larger (44.2 nF) than the measured capacitance under zero excitation (32.0 nF). The greater values of capacitance calculated using Equation 3.24 in comparison with the low-signal measurement performed with an LCR meter are thought to be a result of electromechanical damping [23, 24, 25, 26]. The origin of losses of an energy-harvesting system is in

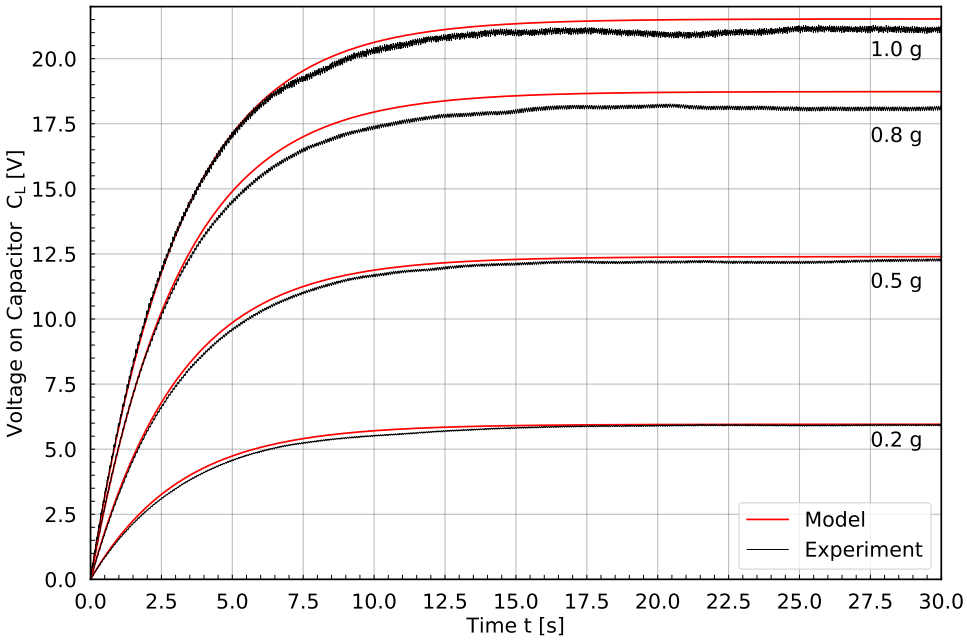

Figure 3-9: *Comparison of model (solid, red traces) with experimental data (black traces with ripple) based on parameters shown in Table 3.2. Beginning at the top the red traces show the results for I_0 = 106.49, 92.68, 61.32, and 29.47 μA. C_P = 44.2 nF, C_L = 10 μF, R_L = 500 kΩ, and f = 6.5 Hz.*

dielectric, piezoelectric, electrical, and mechanical change of the device's parameters under the influence of operating conditions. This can include dielectric dissipation, permittivity, friction, a stiffness change of the cantilever and piezoceramic, and electrical losses transformed into heat or wasted during energy conversion. Due to the complex and nonlinear behavior of these parameters an estimation of all of the aforementioned damping sources is a complex task. Damping effects of the system could be replaced by an equivalent C_X capacitance placed in parallel to the C_P intrinsic capacitance, where the value of the introduced capacitance is the difference between the experimentally measured value and the low-signal piezoelectric capacitance; in this case C_X = 12.2 nF. The introduced additional capacitance (C_X) would represent the damping ratios due to the electromechanical losses experienced by an active piezodevice during energy harvesting.

In summary, we present a simple yet effective method to estimate electromechanical losses of the operated energy harvester in a simple equivalent form of an additional capacitance, easily calculated from the simple experiment with a basic circuit based on a full wave bridge rectifier. Interestingly the majority of piezoelectric characterization undertaken using direct methods, such as an LCR meter or impedance analyzer, is only

possible with the piezoelectric element at steady (not stressed) conditions and at low electric field. However, the indirect approach presented here provides opportunities to characterize the properties of a piezoelectric energy-harvesting device at the operating of conditions at high excitation levels and high stress/strain levels without the need for complex characterization methods; this can be particularly attractive at excitation levels where there is potential for nonlinear behavior in mechanical and/or electrical properties of the harvester [26]. The approach is also valid for sinusoidal thermal fluctuations such as those applied during pyroelectric coefficient characterization or pyroelectric thermal harvesting where similar rectification methods are used [11, 18].

3.1.4 Conclusions

This work provides the derivation of a new, complete expression for the development of the output voltage with time of a vibrating piezoelectric energy harvester for the case of low electromechanical coupling, from which the equilibrium expression used in several earlier publications appears as a limiting case. This more complete formulation of the problem enables accurate estimates of the sinusoidal driving current (effectively the short circuit current of the harvesting) and the shunt capacitance (effectively the device capacitance) to be made without recourse to direct measurement.

This provides a novel approach to measure indirectly the driving current (which is related to the piezoelectric coefficient of the piezoelectric) and device capacitance (which is related to material permittivity) under the conditions of frequency, temperature, stress, and strain experienced by the piezoelectric energy harvester during operation. This enables a more detailed understanding of the behavior of a piezoelectric energy-harvesting device under its driving conditions without the need for complex characterization tools or methods. This is of interest since the piezoelectric and dielectric properties of the harvesting device can change while the harvester is operating at a range of conditions; which include time, frequency, electric field, temperature, and stress. There is potential to include a diode model and a resulting voltage drop to improve the accuracy of predicted C_P and I_P values and apply it to more sophisticated rectifying circuits, such as switching inductors.

Acknowledgements

The authors acknowledge the ERC Grant Agreement no. 320963 on Novel Energy Materials, Engineering Science and Integrated Systems (NEMESIS), C.R.B would like to acknowledge the ERC project (ERC-2017-PoC-ERC-Proof of Concept, Grant no. 789863).

Transient analysis of a current driven full wave AC/DC converter for indirect characterisation of piezoelectric devices during energy harvesting

Marcin J. Kraśny[(1)], Christopher R. Bowen[(1)], Coralie Michel[(1)], John T. Taylor[(2)]

[(1)] Department of Mechanical Engineering, [(2)] Department of Electrical Engineering
University of Bath, Bath, BA2 7AY, UK

SUPPORTING INFORMATION

3.1.5 Full Wave Bridge Rectifier - Principle of Operation

To perform a transient analysis of the current-driven full wave bridge rectifier (FWB) applicable for energy harvesting from piezoelectric device we start with building a final circuit (presented in Fig. 3-13) in three circuit stages with careful consideration of their behaviour and comparison to a baseline established by a well-known voltage-driven case. For ***STAGE 1*** consider the circuits of Fig. 3-10 with $C_L = 0$ (not connected) initially.

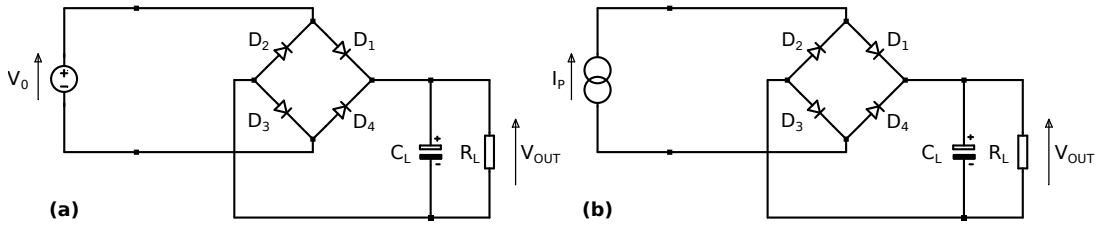

Figure 3-10: *Voltage-driven (a) and current driven (b) full-wave AC-DC converters using a bridge rectifier and driving an RC load.*

The voltage input (V_0) in Fig. 3-10(a) is 100 V_{pk} (peak) and the current input (I_P) in Fig. 3-10b (1 mA peak) was chosen so that $I_0 = V_0/R_L$ where $R_L = 100$ kΩ. The circuit was simulated using LTspice circuit simulator with real diode models and corresponding ideal voltage or current sources generating sinusoidal waveform of 10 Hz base frequency. The values of V_0 and I_0 were chosen to correspond with the real piezoelectric device signals expected to be generated under oscillating mechanical vibration.

The voltage outputs of these circuits are identical and are shown in Fig. 3-11a. At this stage both circuits are operating in linear fashion demonstrating, that to a first order of approximation, they therefore follow Ohm's law. This is explained since the diodes are conducting throughout the whole duty cycle and contribute small, constant

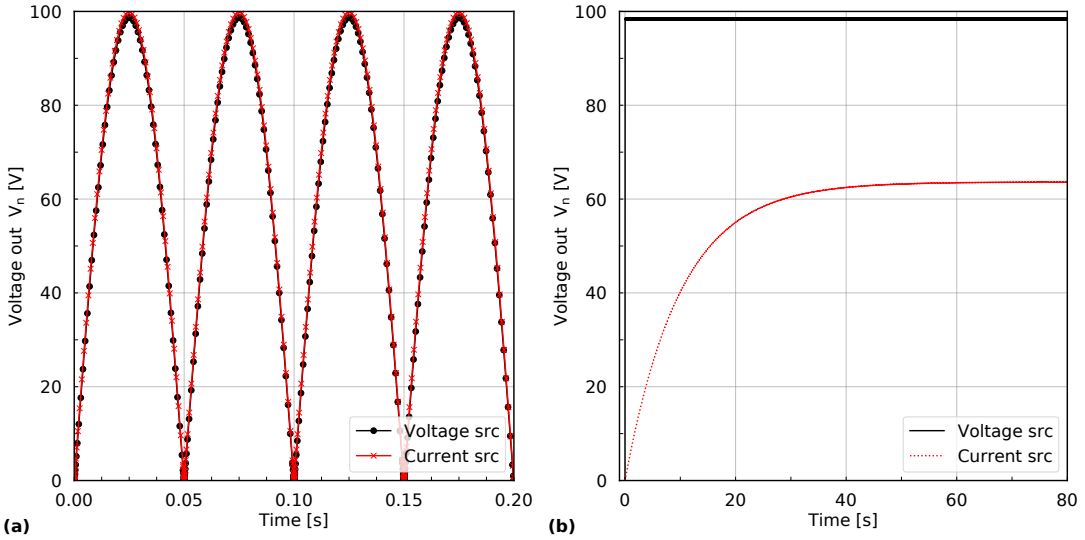

Figure 3-11: *(a) output voltages of the two converters in Fig. 3-10 when $C_L = 0$. For the voltage-driven case, $V_0 = 100$ V sinusoid of frequency 10 Hz. In both cases $R_L = 100$ kΩ and in the current-driven case $I_0 = 0.001$ A, which is scaled to realise the same nominal value of V_0 as in the voltage-driven circuit. (b) the output voltages of the two converters when $C_L = 100$ μF.*

DC offsets, except near the zero crossings where the diode non-idealities may become significant. The voltage output is the familiar FWB rectified waveform, i.e. a sine wave with alternate half cycles inverted. The periodic voltage or current wave form applied to the FWB may be expanded as a Fourier series [19]

$$v(t) = |V_0 sin(\omega t)| = \frac{2V_0}{\pi} - \frac{4V_0}{\pi}\sum_{n=1}^{\infty}\frac{cos(2n\omega_0 t)}{4n^2 - 1} \tag{3.25}$$

i.e. $v(t)$ consists of a mean value (Fourier coefficient $a_0 = 2V_0/\pi$) and a sequence of even-order harmonics ($\omega_0 = 2\pi f_0 = 2\pi/T$). The energy dissipated in the load resistor R_L is calculated therefore as

$$P_L = (\frac{2V_0}{\pi})^2/R_L \tag{3.26}$$

The common and the simplest approach to obtain a DC output voltage from the FWB rectifier is to connect a capacitor C_L in parallel to the load which leads to a circuit ***STAGE 2***. For $C_L = 100$ μF, realising a time constant (RC) of 10 seconds with $R_L = 100$ kΩ, the output simulated over several input cycles ($f_0 = 10$ Hz) is shown in Fig. 3-11b. If linear circuit principles apply the output voltage would be expected to settle to its mean value in Eq. 3.25, i.e. $V_{AVG} = 63.66$ V in this case. For the current driven circuit this is exactly what happens, as shown in the lower (dotted red) of the two

traces in the Fig. 3-11b. However, for the voltage-driven case, a completely different pattern of behaviour emerges, as indicated by the upper (solid black) trace. In this case, the output voltage rises rapidly to the peak input voltage V_0 and remains there subject a residual ripple voltage. The DC output power ratio calculated with Eq. 3.27 is therefore $\pi^2/4$ - times higher in the voltage-driven converter

$$\frac{P_{L_{V-s}}}{P_{L_{I-s}}} = \frac{(V_0)^2/R_L}{(\frac{2V_0}{\pi})^2/R_L} \tag{3.27}$$

where, $P_{L_{V-s}}$ and $P_{L_{I-s}}$ are output power values for voltage-source $(V-s)$ and current-source $(I-s)$ circuits accordingly.

A brief consideration of the two circuits reveals why they behave so differently. In the voltage-driven case, starting from $t = 0$, the output initially follows the input to its peak value, high currents passing through one pair of the bridge diodes. Once the peak of the sinusoid is passed, these diodes become reverse biased due to the charge stored on C_L and the charging current falls to zero. This phase continues until the input voltage nears its maximum negative peak when its modulus equals the output voltage, which by that time has fallen slightly due to charge losses in R_L. At this point the second pair of diodes starts to conduct resulting in a current pulse that recharges C_L to its peak value. Therefore, in the voltage-driven version, charge transfer to the load takes the form of short pulses of current making up for losses in the load (and observed as ripple on the output voltage). Thus, the action of the voltage-driven circuit is not linear. On the other hand, in the current-driven case, the diodes conduct throughout the duty cycle and so, as already noted, contribute only small, constant, DC offsets except near the zero crossings. Linear circuit principles therefore apply to a good level of approximation which explains why the development of the output voltage with time is different from the (not linear) voltage-driven case.

It is also tempting to enquire why the voltage-driven circuit delivers significantly more power to the load than the current-driven version. In fact, both sources (voltage and current) can deliver arbitrary amounts of power depending on the circuit embedding. The nonlinear behaviour of the voltage driven FWB rectifier circuit changes the embedding (i.e. the diodes are not simply linear low voltage sources in this case) and so the behaviour of the two circuits at this stage is no longer comparable.

The current-driven converter circuit described is entirely linear because the diodes conduct throughout the whole duty cycle. However, in practice the circuit of Fig. 3-10b is not realistic when used for piezoelectric devices analysis. An equivalent model as in Fig. 3-13 and Fig. 3-1, is proposed and described in main paper.

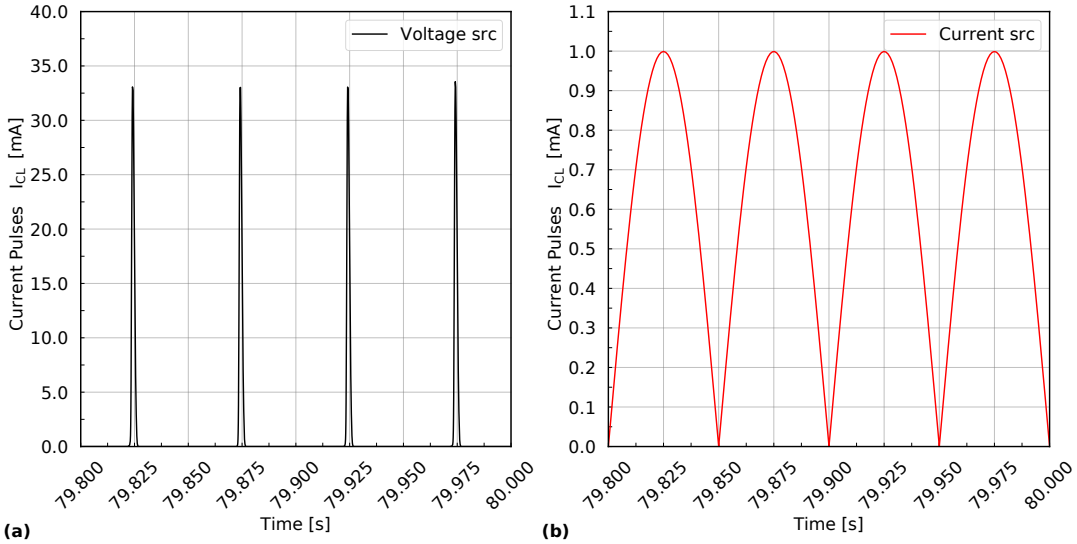

Figure 3-12: *(a) current flow (I_{CL}) to the load in voltage-driven case. (b) current flow (I_{CL}) to the load in current-driven case. Both for* ***STAGE 2*** *circuit.*

3.1.6 Short Circuit Current

Short circuit current of a piezoelectric device was measured in function of driving excitation. The beam was placed on the shaker as described in Section 3.1.3 of the main paper. Experiment was proceeded at constant frequency (6.5 Hz) and variable excitation acceleration with the peak amplitude from 0.05 to 1.1 g. The current (I_{SC}) was measured with electrometer's (Keithley 6517B) analogue output connected to oscilloscope (Agilent DSO-X 2024A). Measurement range of the electrometer was adjusted accordingly to the maximum measured value for a given excitation range. Current was measured over full 3 periods, and experiment was repeated 6 times for each acceleration. The resulted plot (Fig. 3-15) shows average peak values of the short circuit current with error bars representing standard deviation.

3.1.7 Ideal Current-Source

Validation of a proposed piezoelectric device model as an ideal current source was performed experimentally with results confronted to simulated data. The model of a piezoelectric device applied in this study presents piezoelectric device with an intrinsic capacitance connected in parallel. In results when connected with only an external load resistance the circuits represent a basic RC filter circuit.

The beam was placed on the shaker as described in Section 3.1.3 of the main paper. Experiment was proceeded at constant excitation of the beam (frequency = 6.5 Hz and

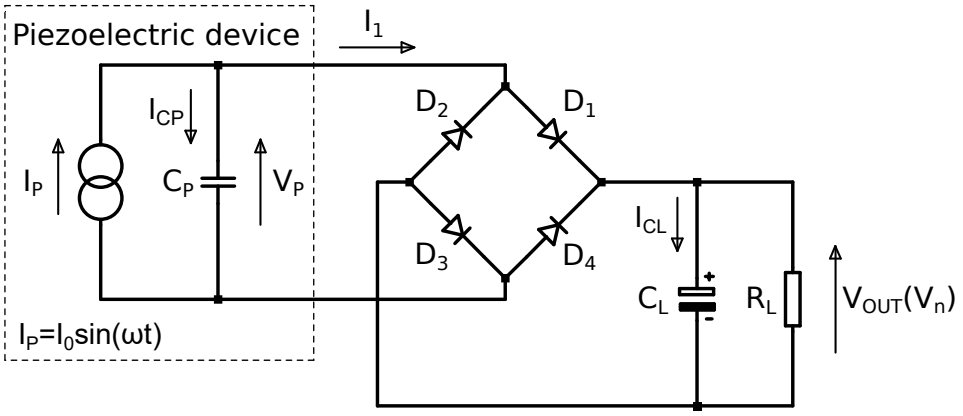

Figure 3-13: *Circuit schematic showing the equivalent circuit of a piezoelectric generator (on the left) connected to a diode bridge AC-DC converter.*

acceleration amplitude of 0.8 g which results in measured short circuit current of 100 μA) with the variable load (Peak Tech 3265 resistance decade) in the range of 100 Ω – 11 MΩ. The equivalent circuit is presented in insert in Fig. 3-16. Current I_1 was measured with electrometer's (Keithley 6517B) analogue output connected to oscilloscope (Agilent DSO-X 2024A), responsible for recording of the resulted current. Experimental circuit was then simulated with the model of an ideal current source and two values of intrinsic capacitance C_P (i) 32 nF and (ii) 44.2 nF which correspond to measured and calculated values of piezoelectric device as described in main paper. Results of experiment and simulations are presented in Fig. 3-16. Experimentally realised curve validates the model of piezoelectric device as current source with good level of approximation. Additionally, better matching of the resulted characteristic with the ideal (simulated) data for C_P = 44.2 nF indicates the change of capacitance as discussed in main paper.

3.1.8 Results

Table 3.3 with detailed experimental results compared to simulated data for identical initial parameters. The case described in the experiment was simulated with LTspice with the initial values of C_P= 32.0 nF and I_0= 30.32 μA, 66.12 μA, 102.70 μA and 124.39 μA. The retrieved values of C_P are 32.05, 31.47, 31.28 and 31.22 nF and I_0 are 29.68 μA, 65.18 μA, 101.49 μA and 123.02 μA accordingly. Resulted average value of C_P for simulation of the described case was: 31.51 nF and for experiment 44.2 nF. Increased capacitance value is discussed in the main paper.

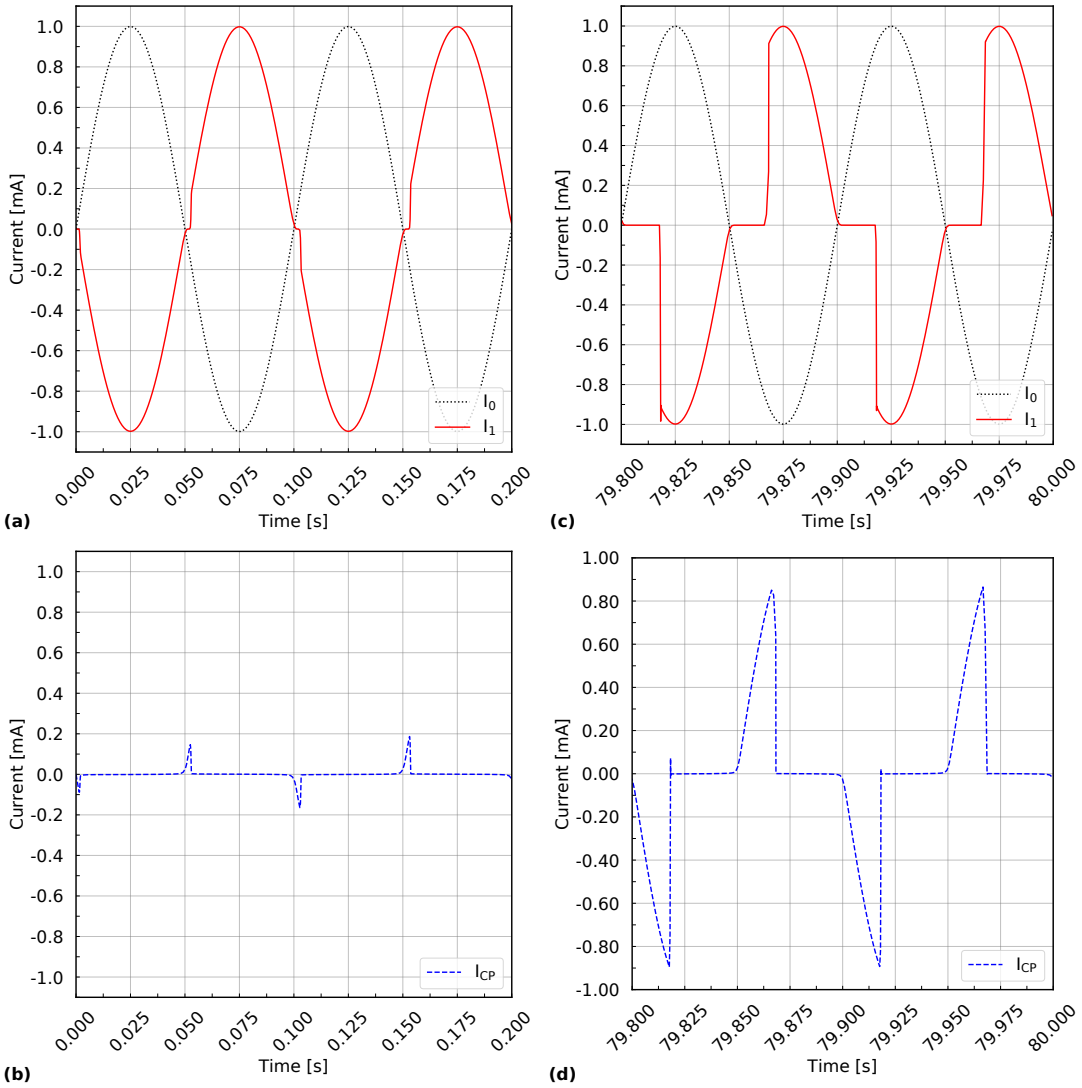

Figure 3-14: *Example current waveforms corresponding to the currents described in Fig. 3-13. (a, b) at the beginning of a load capacitor charging (transient), (c, d) at the end of a load capacitor charging (steady state)*

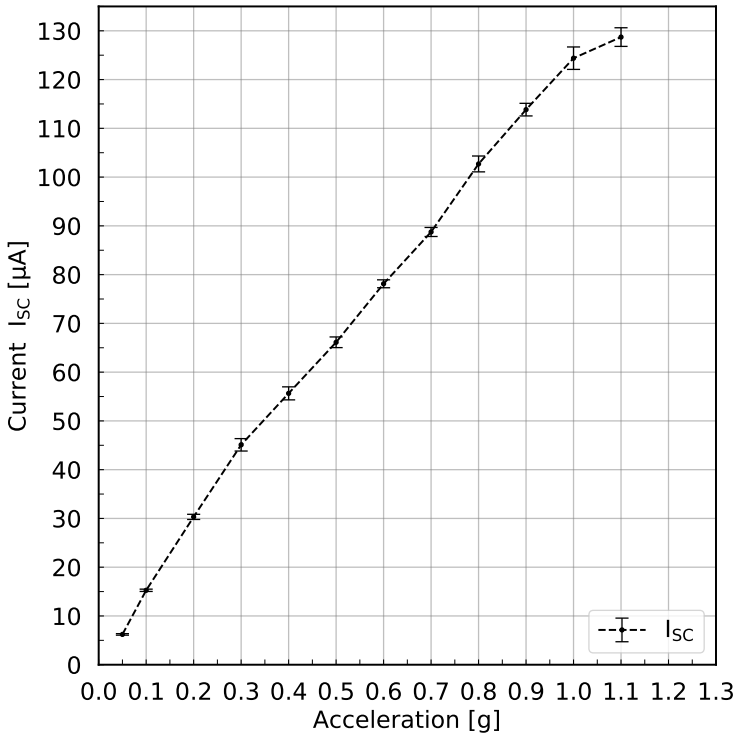

Figure 3-15: *Short circuit current as a function of acceleration. Error bars represent standard deviations.*

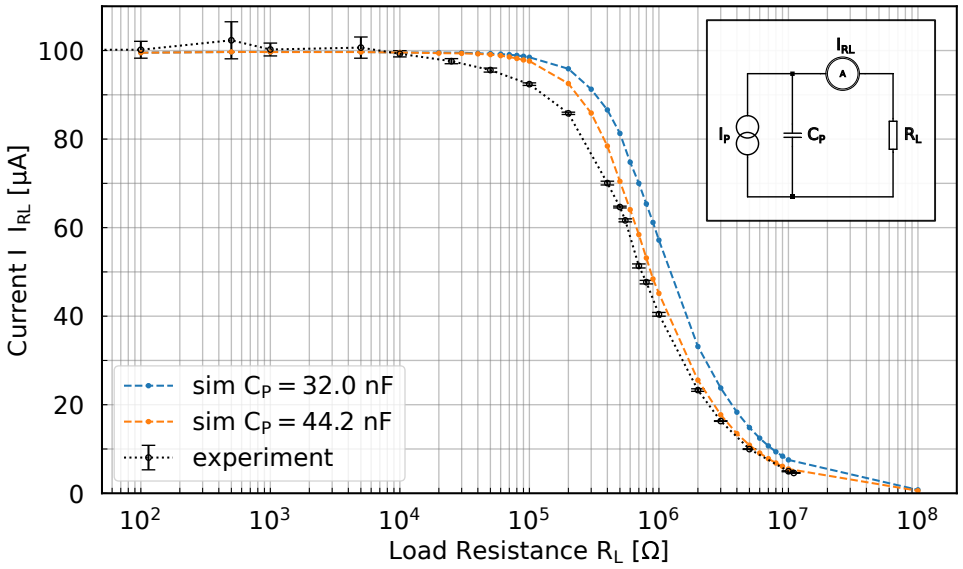

Figure 3-16: *Comparison of simulated load current with experiment; insert with current-driven R_C filter used as test circuit.*

Table 3.3: *Extraction of C_P and I_0 based on simulated experimental data in Fig. 3-9. Percentage error values in parenthesis.*

SPICE SIMULATION					EXPERIMENT					
I_0 set [μA]	V_1 [V]	$V_{n(n\to\infty)}$ [V]	C_P [nF] (Eqn (23))	I_0 [μA] (Eqn (24))	Excitation acceleration [g]	Measured I_{SC} [μA]	V_1 [V]	$V_{n(n\to\infty)}$ [V]	C_P [nF] (Eqn 3.23)	I_0 [μA] (Eqn 3.24)
30.32	0.15	6.67	32.05 (0.16%)	29.68 (2.11%)	0.2	30.32	0.14	6.04	42.5 (32.81%)	29.47 (-2.80%)
66.12	0.33	14.73	31.47 (-1.66%)	65.18 (1.42%)	0.5	66.12	0.30	12.45	43.6 (36.25%)	61.32 (-7.26%)
102.70	0.50	22.97	31.28 (-2.25%)	101.49 (1.18%)	0.8	102.70	0.45	18.44	46.1 (44.06%)	92.68 (-9.76%)
124.39	0.60	27.85	31.22 (-2.44%)	123.02 (1.10%)	1.0	124.39	0.52	21.72	43.1 (34.69%)	106.49 (-14.39%)

References

[1] C. R. Bowen, H. A. Kim, P. M. Weaver, and S. Dunn, "Piezoelectric and ferroelectric materials and structures for energy harvesting applications," *Energy Environ. Sci.*, vol. 7, no. 1, pp. 25–44, Dec. 2013.

[2] Z. L. Wang and J. Song, "Piezoelectric Nanogenerators Based on Zinc Oxide Nanowire Arrays," *Science*, vol. 312, no. 5771, pp. 242–246, Apr. 2006.

[3] X. Wang, J. Song, J. Liu, and Z. L. Wang, "Direct-current nanogenerator driven by ultrasonic waves," *Science*, vol. 316, no. 5821, pp. 102–105, 2007.

[4] R. Yu, C. Pan, J. Chen, G. Zhu, and Z. L. Wang, "Enhanced Performance of a ZnO Nanowire-Based Self-Powered Glucose Sensor by Piezotronic Effect," *Advanced Functional Materials*, vol. 23, no. 47, pp. 5868–5874, 2013.

[5] Q. Yang, Y. Liu, C. Pan, J. Chen, X. Wen, and Z. L. Wang, "Largely enhanced efficiency in ZnO nanowire/p-polymer hybridized inorganic/organic ultraviolet light-emitting diode by piezo-phototronic effect," *Nano letters*, vol. 13, no. 2, pp. 607–613, 2013.

[6] C. Yan, W. Deng, L. Jin, T. Yang, Z. Wang, X. Chu, H. Su, J. Chen, and W. Yang, "Epidermis-Inspired Ultrathin 3D Cellular Sensor Array for Self-Powered Biomedical Monitoring," *ACS Appl. Mater. Interfaces*, vol. 10, no. 48, pp. 41 070–41 075, Dec. 2018.

[7] H. Liu, J. Zhong, C. Lee, S.-W. Lee, and L. Lin, "A comprehensive review on piezoelectric energy harvesting technology: Materials, mechanisms, and applications," *Applied Physics Reviews*, vol. 5, no. 4, p. 041306, Dec. 2018.

[8] F. Dell'Anna, T. Dong, P. Li, Y. Wen, Z. Yang, M. R. Casu, M. Azadmehr, and Y. Berg, "State-of-the-Art Power Management Circuits for Piezoelectric Energy Harvesters," *IEEE Circuits and Systems Magazine*, vol. 18, no. 3, pp. 27–48, thirdquarter 2018.

[9] J. Scruggs, "On the Causal Power Generation Limit for a Vibratory Energy Harvester in Broadband Stochastic Response," *Journal of Intelligent Material Systems and Structures*, vol. 21, no. 13, pp. 1249–1262, Sep. 2010.

[10] F. Lu, H. P. Lee, and S. P. Lim, "Modeling and analysis of micro piezoelectric power generators for micro-electromechanical-systems applications," *Smart materials and structures*, vol. 13, no. 1, p. 57, 2003.

[11] K. Makihara, Y. Yamamoto, K. Yoshimizu, C. Horiguchi, H. Sakaguchi, and K. Fujimoto, "A novel controller to increase harvested energy from negating vibration-suppression effect," *Smart Materials and Structures*, vol. 24, no. 3, p. 037005, Mar. 2015.

[12] L. Karthikeyan and B. Amrutur, "Signal-Powered Low-Drop-Diode Equivalent Circuit for Full-Wave Bridge Rectifier," *IEEE Transactions on Power Electronics*, vol. 27, no. 10, pp. 4192–4201, Oct. 2012.

[13] M. Balato, L. Costanzo, A. Lo Schiavo, and M. Vitelli, "Optimization of both Perturb & Observe and Open Circuit Voltage MPPT Techniques for Resonant Piezoelectric Vibration Harvesters feeding bridge rectifiers," *Sensors and Actuators A: Physical*, vol. 278, pp. 85–97, Aug. 2018.

[14] L. Costanzo, A. Lo Schiavo, and M. Vitelli, "Power Extracted From Piezoelectric Harvesters Driven by Non-Sinusoidal Vibrations," *IEEE Transactions on Circuits and Systems I: Regular Papers*, vol. 66, no. 3, pp. 1291–1303, Mar. 2019.

[15] G. K. Ottman, H. F. Hofmann, A. C. Bhatt, and G. A. Lesieutre, "Adaptive piezoelectric energy harvesting circuit for wireless remote power supply," *IEEE Transactions on Power Electronics*, vol. 17, no. 5, pp. 669–676, Sep. 2002.

[16] D. Guyomar, A. Badel, E. Lefeuvre, and C. Richard, "Toward energy harvesting using active materials and conversion improvement by nonlinear processing," *IEEE transactions on ultrasonics, ferroelectrics, and frequency control*, vol. 52, no. 4, pp. 584–595, 2005.

[17] Y. C. Shu and I. C. Lien, "Analysis of power output for piezoelectric energy harvesting systems," *Smart Mater. Struct.*, vol. 15, no. 6, p. 1499, 2006.

[18] C. R. Bowen, J. Taylor, E. LeBoulbar, D. Zabek, A. Chauhan, and R. Vaish, "Pyroelectric materials and devices for energy harvesting applications," *Energy Environ. Sci.*, vol. 7, no. 12, pp. 3836–3856, Nov. 2014.

[19] John D. Ryder, *Electronic Fundamentals and Applications*, 3rd ed. London: Pitman, 1964.

[20] E. Mike, "LTspice," Analog Devices, Apr. 2019.

[21] "MFC," https://www.smart-material.com/MFC-product-main.html.

[22] P. B. Harris, C. R. Bowen, D. N. Betts, and A. H. Kim, "Manufacture and characterisation of piezoelectric broadband energy harvesters based on asymmetric bistable laminates," 2014.

[23] A. M. González, Á. García, C. Benavente-Peces, and L. Pardo, "Revisiting the Characterization of the Losses in Piezoelectric Materials from Impedance Spectroscopy at Resonance," *Materials*, vol. 9, no. 2, p. 72, Jan. 2016.

[24] M. Goldfarb and L. D. Jones, "On the efficiency of electric power generation with piezoelectric ceramic," *Journal of Dynamic Systems, Measurement, and Control*, vol. 121, no. 3, pp. 566–571, 1999.

[25] D. A. Hall and P. J. Stevenson, "High field dielectric behaviour of ferroelectric ceramics," *Ferroelectrics*, vol. 228, no. 1, pp. 139–158, 1999.

[26] D. A. Hall, "Review Nonlinearity in piezoelectric ceramics," *Journal of Materials Science*, vol. 36, no. 19, pp. 4575–4601, Oct. 2001.

3.2 Summary

The work presents a detailed analysis of a full wave bridge rectifier circuit which can be applied as a simple, yet reliable tool for qualitative testing of energy harvesters. It offers piezoelectric device characterisation by measurements performed close to a real-life application and conditions which significantly simplifies the overall comparison of different piezoelectric materials and devices. By application of the proposed method, a complex analysis of the performance of an energy harvester can be achieved in environmental conditions, allowing for estimation of in-system losses and long-term reliability.

An additional note on precise measurement can be added to the above paper. Appropriate recording of capacitor charging curves with a piezoelectric device excited by an electrodynamic shaker might be a challenging task due to difficulties in initiating the charging from 'zero state' conditions. This is realised by discharging a load capacitance (C_L), which is relatively simple to achieve, even in manually controlled measurement setups. The problems might be encountered with discharging intrinsic capacitance (C_P) which is re-charged with each excitation cycle of a working shaker.

The electrodynamic-shaker and the mechanical structure with a piezoelectric harvester requires time to adjust to the vibrating frequency and reach a stable mode of operation. Thus, the measurement of capacitor-charging curve cannot truly begin at the point of ignition of the shaker, since this would result in these initial non-linearities being reflected in the performance of the device under test. To overcome this problem, a measurement should start after some dwell time in which mechanical excitation generated by the shaker and the cantilever/harvester response reaches their equilibrium. A valid registration of a charging curve then initiates from a short circuit condition which should be released in sync with the shaker excitation signal.

However, if recording of the piezoelectric signal is started asynchronously to the excitation, there is a risk of recording of an initial spike in the load capacitor charging curve as a result of piezoelectric generator operating only through the part of a cycle. The presence of such spike can reduce the accuracy of the proposed method. As a solution to this problem the best results are achieved when excitation level is synchronised, with the release of a short circuit condition of the vibrating piezoelectric structure. With the use of ENHAMER Ddraig board described in Chapter 2 an appropriate triggering condition can be set in the experiment routine allowing easy application of this method for characterisation.

CHAPTER 4

IMPROVED PIEZOELECTRIC DEVICE PERFORMANCE

4.1 Prologue

Two papers presented in this chapter describe significant enhancements in the field of piezoelectric porous ceramics and composite materials.

The first research *"Freeze cast porous barium titanate for enhanced piezoelectric energy harvesting"* introduces an investigation of exploiting aligned porosity to increase of piezoelectric figures of merit and, as a result, an improved energy harvesting performance. The study investigates barium titanate ($BaTiO_3$), a biocompatible alternative to lead zirconate titanate (PZT), which is presented in a second study described in this chapter: *"Flexible and active self-powered pressure, shear sensors based on freeze casting ceramic–polymer composites"*.

In this work a unique method of manufacturing piezoelectric composite material is proposed. Here the material properties are initially enhanced with the use of aligned porosity, as described in the previous paper, and are followed by an additional step resulting in increase of the material piezoelectric coefficients exceeding the values reported for a dense material. This enhancement is achieved by filling the empty cavities, created with a freeze-casting method, with a biocompatible polymer polydimethylsiloxane (PDMS). Increased performance of a material is a result of a combination of flexural effect induced with the polymer layer in the lamellar structure of PZT. In addition, a simple method for shear stress harvesters (d_{15}) sensor mode development is shown and this can find an application in acceleration sensors as this mode has lower material temperature dependency.

Paper 3: Statement of Authorship

<table>
<tr><td colspan="10">This declaration concerns the article entitled:</td></tr>
<tr><td colspan="10">Freeze cast porous barium titanate for enhanced piezoelectric energy harvesting</td></tr>
<tr><td colspan="10">Publication status (tick one)</td></tr>
<tr><td>Draft manuscript</td><td></td><td>Submitted</td><td></td><td>In review</td><td></td><td>Accepted</td><td></td><td>Published</td><td>✓</td></tr>
<tr><td colspan="10">Copyright status (tick the appropriate statement)</td></tr>
<tr><td colspan="4">I hold the copyright for this material</td><td></td><td colspan="4">Copyright is retained by the publisher, but I have been given permission to replicate the material here</td><td>✓</td></tr>
<tr><td>Publication details (reference)</td><td colspan="9">J. I. Roscow, Y. Zhang, M. J. Kraśny, R. W. C. Lewis, J. Taylor, and C. R. Bowen, “Freeze cast porous barium titanate for enhanced piezoelectric energy harvesting”, J. Phys. D: Appl. Phys., vol. 51, no. 22, p. 225301, 2018,
DOI: 10.1088/1361-6463/aabc81.</td></tr>
<tr><td>Candidate’s contribution to the paper (detailed and also given as percentage)</td><td colspan="9">Formulation of ideas:
J. I. Roscow

Design of methodology:
Energy harvesting demonstration by candidate (100%),
Sample preparation and material characterisation by J.I.Roscow.

Experimental work:
Testing rig and measurements of energy harvesting by candidate (100%),
Sample preparation and material characterisation by J.I.Roscow.

Presentation of data in journal format:
J. I. Roscow except the experimental part on energy harvesting demonstrator which was done by candidate.</td></tr>
<tr><td>Statement from Candidate</td><td colspan="9">This paper reports original research I conducted during the period of my Higher Degree by Research candidature.</td></tr>
<tr><td>Signed</td><td colspan="5">  </td><td>Date</td><td colspan="3">08.08.2020</td></tr>
</table>

Freeze Cast Porous Barium Titanate for Enhanced Piezoelectric Energy Harvesting

James I. Roscow[(1)], Yan Zhang[(1)], Marcin J. Kraśny[(1)], R.W.C. Lewis[(2)], John T. Taylor[(3)], Chris R. Bowen[(1)]

[(1)] Department of Mechanical Engineering, University of Bath, Bath, BA2 7AY, UK
[(2)] Renishaw Plc., Wooton-under-Edge, Gloucestershire, UK
[(3)] Department of Electrical and Electronic Engineering, University of Bath, Bath, BA2 7AY, UK

Abstract

Energy harvesting is an important developing technology for a new generation of self-powered sensor networks. This paper demonstrates the significant improvement in the piezoelectric energy harvesting performance of barium titanate by forming highly aligned porosity using freeze casting. Firstly, a finite element model demonstrating the effect of pore morphology and angle with respect to poling field on the poling behaviour of porous ferroelectrics was developed. A second model was then developed to understand the influence of microstructure-property relationships on the poling behaviour of porous freeze cast ferroelectric materials and their resultant piezoelectric and energy harvesting properties. To compare with model predictions, porous barium titanate was fabricated using freeze casting to form highly aligned microstructures with excellent longitudinal piezoelectric strain coefficients, d_{33}. The freeze cast barium titanate with 45 vol.% porosity had a d_{33} = 134.5 pC/N compared to d_{33} = 144.5 pC/N for dense barium titanate. The d_{33} coefficients of the freeze cast materials were also higher than materials with uniformly distributed spherical porosity due to improved poling of the aligned microstructures, as predicted by the models. Both model and experimental data indicated that introducing porosity provides a large reduction in the permittivity ($\varepsilon_{33}^{\sigma}$) of barium titanate, which leads to a substantial increase in energy harvesting figure of merit, $d_{33}^2/\varepsilon_{33}^{\sigma}$, with a maximum of 3.79 pm^2/N for barium titanate with 45 vol.% porosity, compared to only 1.40 pm^2/N for dense barium titanate. Dense and

porous barium titanate materials were then used to harvest energy from a mechanical excitation by rectification and storage of the piezoelectric charge on a capacitor. The porous barium titanate charged the capacitor to a voltage of 234 mV compared to 96 mV for the dense material, indicating a 2.4-fold increase that was similar to that predicted by the energy harvesting figures of merit.

Keywords

piezoelectric, porosity, energy harvesting, freeze casting, finite element analysis

4.1.1 Introduction

Energy harvesting, the process of recapturing energy from ambient sources, such as mechanical vibrations and waste heat, and converting it to useful electrical energy, has received increasing attention in recent years with the development of low powered electronics and wireless sensor technologies [1]. Ferroelectric ceramics are of particular interest in this field due to their ability to directly convert vibrational energy to electrical energy via the piezoelectric effect and thermal fluctuations into electrical energy via the pyroelectric effect [2, 3]. Figures of merit (FOM) for both piezoelectric and pyroelectric energy harvesting have been derived based on the change of polarisation of a poled ferroelectric material due to an applied stress (piezoelectric) or change in temperature (pyroelectric). The piezoelectric harvesting figure of merit for off-resonance, low frequency (<<100 kHz) vibration is given by [4]:

$$FoM_{ij} = \frac{d_{ij}^2}{\varepsilon_{33}^{\sigma}} \tag{4.1}$$

where d_{ij} is the piezoelectric strain coefficient (the subscripts denote the direction of applied stress (j) with respect to the poling direction (i)) and $\varepsilon_{33}^{\sigma}$ is the permittivity at constant stress. The pyroelectric energy harvesting figure of merit is given by [5]:

$$F_E' = \frac{p^2}{c_E^2 \cdot \varepsilon_{33}^{\sigma}} \tag{4.2}$$

where p is the pyroelectric coefficient and c_E is the volume specific heat capacity. A simple analysis of the figures of merit above demonstrate that when selecting a ferroelectric to harvest mechanical or thermal vibrations it should have a high piezoelectric strain or pyroelectric coefficient and a low permittivity. However, ferroelectric materials with the highest piezoelectric and pyroelectric coefficients often have high permittivity. One approach to improve the figures of merit is to introduce porosity, which has been

shown to provide a cost-effective way of tuning the properties of these materials by reducing the permittivity whilst maintaining a relatively high d_{33} [6] or p [7].

Directly after sintering, a polycrystalline ferroelectric ceramic initially exhibits no piezoelectric or pyroelectric properties as domains within the material are randomly orientated [8]. To make the ferroelectric material electro-active they are poled by applying an electric field to orientate the ferroelectric domains which exist below the Curie temperature, yielding a net polarisation that provides a piezoelectric and pyroelectric response. It has been shown previously that the decrease in piezoelectric response in porous ferroelectrics is largely due to difficulties in poling these materials as the poling field preferentially concentrates in the low permittivity pores, thereby leading to regions of ferroelectric material remaining unpoled after the poling field is removed [9, 10]. Understanding the effect of the porous structure on the poling behaviour of ferroelectrics may therefore aid the design of composites materials with low permittivity and high d_{33} coefficients. The processing method used to form a porous ceramic structure determines the connectivity, distribution and alignment of the final porous structure [11], and this paper aims to demonstrate the types of microstructure that are necessary to improve piezoelectric energy harvesting capabilities of porous ferroelectric ceramics.

The introduction of porosity into ferroelectric ceramics such as lead zirconate titanate (PZT) and barium titanate ($BaTiO_3$) reduces the permittivity of the ceramic-air composite [12] and has been shown to be beneficial in terms of increasing figures of merit for a number of applications including piezoelectric hydrostatic acoustic sensors [13, 14, 15, 16, 17], pyroelectric thermal detection devices [18, 19] and, more recently, for both piezoelectric [6, 10, 20] and pyroelectric energy harvesting [7, 21]. The presence of high levels of uniformly distributed porosity (i.e. isolated 3–0 or interconnected 3–3 pore connectivity, see Fig. 4-1a and b, respectively) lead to a relatively small decrease in d_{33} up to a porosity fraction of 50 vol.%, with a large decrease in d_{33} at higher porosity levels[1] [15, 16, 17, 20]. Freeze cast PZT-based materials with excellent alignment of both pore and ceramic channels (3–1 and 2–2 connectivity, see Fig. 4-1c and d, respectively) have been shown to have higher d_{33} coefficients [7, 21, 22, 23, 24] than porous PZT with uniformly distributed porosity at similar levels of porosity [15, 16]. For example, a freeze cast PZT with over 65 vol.% porosity was reported to have d_{33} values of up to 91% that of the dense material, whilst the permittivity was found to be just 33% that of dense PZT [22], yielding an exceptionally high piezoelectric energy harvesting figure of merit using Eqn. 4.1 [6]. Ionotropic gelation has also recently been used to produce highly aligned 3–1 porous PZT with excellent potential for energy

[1] It should be highlighted that while the d_{33} can remain relatively unchanged, the large reductions in d_{31} of porous ferroelectric materials make them unsuitable for energy harvesters that operate in this mode, i.e. bending mode cantilever devices.

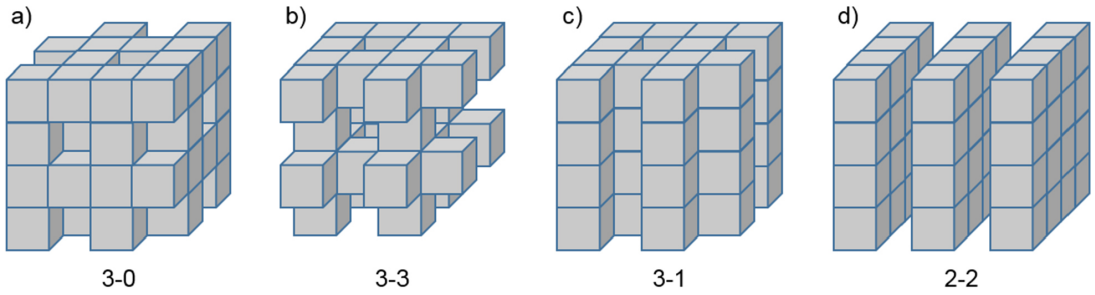

Figure 4-1: *Schematic showing selected types of connectivity for two-phase composites. The first number refers to the connectivity of the ferroelectric phase and the second number refers to the connectivity of the porosity.*

harvesting due to their high d_{33} coefficients [25, 26].

Effect of Porous Structure on Poling and d_{33}

The inhomogeneous field distribution during the poling of porous ferroelectrics is thought to lead to incomplete poling of the system and a decrease in d_{33} compared to the dense material [9, 10]. This occurs as the electric field applied during poling preferentially concentrates in the low permittivity phase, a condition of Gauss' law [27]. There have been several recent investigations into the effect of pore shape, orientation and connectivity on the electric field distribution and polarization-switching dynamics in dielectric materials [28, 29, 30, 31]. Porous structures with ideal 3–1 connectivity, i.e. isolated 1D pore channels in a continuous piezoelectric-matrix as in Fig. 4-1c, have been simulated via finite element analysis and shown to have homogenous electric field distributions throughout the material when an external field is applied parallel to the dielectric phase [28]. In composites with 3–0 (isolated pores, Fig. 4-1a) and 3–3 (interconnected pores, Fig. 4-1b) connectivity, an increase in porosity is found to reduce the local electric field in the high permittivity ceramic phase as the electric field preferentially concentrates in the low permittivity pores [29], which partially explains the changes in polarisation-electric field (P-E) loops observed in PZT [7] and (Pb,Nb)(Ti,Zr)O_3 (PZTN) [29] with increasing porosity. A detailed study on the effect of pore aspect ratio and orientation with respect to applied electric field demonstrated that elongated pores aligned perpendicular to the applied field exhibited broadening of the P-E loops compared with equiaxed pores, however, the least disruption to electric field was observed when elongated pores were aligned parallel to the electric field [30]. Experimental studies have demonstrated that elongated pores aligned perpendicular to the poling direction led to lower d_{33} values compared to spherical pores [30, 32, 33], which is in agreement with theoretical studies [28, 29, 30, 31].

With regards to developing porous ferroelectrics for energy harvesting, microstructures that promote homogenous field distributions throughout the material with local electric fields close to the applied field in both the ceramic phase and the pores are likely to be easier to pole than structures with broad field distributions during the poling process. This would explain the high d_{33} coefficients reported for freeze cast porous piezoelectric materials with an orientated structure [7, 21, 22, 23, 24] compared with uniformly distributed porosity [15, 16], which is of benefit for energy harvesting in terms of the relevant figure of merit, see Eqn. 4.1.

Effect of Porosity on Mechanical Properties

The impact of porosity on mechanical properties is also of importance for applications related to vibrational mechanical harvesting. Porosity increases the mechanical compliance [16, 34] and also decreases the strength of ceramics [35]. However, aligning the high stiffness ceramic phase along the primary loading axis, as is the case of freeze cast porous ceramics, improves the mechanical properties compared to those with uniformly distributed porosity [36]. In order to harvest energy from mechanical loads, porous ferroelectric ceramics must be sufficiently stiff and strong to survive their operating conditions, which is likely to be a further advantage of using highly aligned freeze cast materials rather than those with uniformly distributed porosity.

In this paper both a single pore model and a porous microstructural model are presented to evaluate the effect of the porous structure on the resultant piezoelectric properties and energy harvesting performance. Firstly, the single pore model is used to understand the effect of the angle and orientation of a pore in a barium titanate matrix on the poling behaviour of the material, which provides an explanation of the excellent d_{33} coefficients reported in literature for aligned microstructures. Secondly, the porous microstructural model is used to understand the effect of microstructural features commonly observed in porous freeze cast materials on the piezoelectric and dielectric properties. To provide experimental data, barium titanate with highly aligned porosity has been produced via the freeze casting method to improve the degree of poling and provide an experimental comparison to the observations from the modelling studies, as well as allowing comparison to previous results for barium titanate with equiaxed porosity, which was fabricated from the same starting powder and under the same sintering conditions (detailed in Section 4.1. 4.1.4) [20]. The use of barium titanate also mitigated against lead-loss that would occur during sintering of a porous lead zirconate titanate. Finally, a practical demonstration of the benefits of aligned porosity on piezoelectric energy harvesting capabilities of ferroelectric ceramics is presented by subjecting poled porous and dense barium titanate materials to mechanical vibrations

and charging a capacitor using the harvested electrical energy.

4.1.2 Single Pore Model

Finite element analysis has been used to demonstrate the effect of pore shape and orientation on the electric field distribution during the poling of a ferroelectric ceramic. A single elliptical pore with constant area fraction ($A_f = 0.0785$) and relative permittivity, $\varepsilon_r = 1$, was placed within a high permittivity barium titanate matrix, $\varepsilon_r = 1500$ (measured experimentally). The angle of the pore was varied from 0° (i.e. parallel to the field) to 90° (perpendicular to the field) and the aspect ratio varied from 1 to 10 (with an aspect ratio of one corresponding to a circular pore). An electric field greater than the coercive field of the barium titanate was applied to top and bottom boundary lines of the model to simulate the poling electric field across the material. The electric field in each element was analysed to determine whether the local field exceeded the coercive field ($E_c = 0.5$ kV/mm [37]), i.e. the necessary field to switch the orientation of a domain in a ferroelectric material. The applied field used in this model was selected as it provided good contrast between poled and unpoled regions; increasing the applied field (analogous to increasing the poling voltage) results in higher poled fractions of material, however, in real materials this is limited by electrical breakdown in the pores that discharges the poling field [38].

An example electric field contour plot for a pore orientated at 45° to the field with aspect ratio = 4, is shown in Fig. 4-2a, and the resulting distribution of poled material for a range of pore angles is shown in Fig. 4-2b. It can be seen from Fig. 4-2a that the electric field concentrates in the low permittivity pore and low electric field regions are present in the $BaTiO_3$ phase in immediate vicinity of the pore, at pore-ceramic interfaces perpendicular to the applied field. This results in varying fractions of the $BaTiO_3$ becoming poled as shown in Fig. 4-2b, in which the blue areas are those in which the local electric field is below the coercive field and is therefore likely to remain unpoled. The resulting fraction of poled material as a function of pore angle with respect to field is shown in Fig. 4-2c. High aspect ratio pores aligned parallel to the applied field yield the highest fraction of poled material (angle = 0° in Fig. 4-2b and c), whereas high aspect ratio pores aligned perpendicular to the poling field (angle = 90° in Fig. 4-2b and c) resulted in the lowest poled fraction. If we were to extend the aspect ratio further we would reach the extreme case of parallel and series structures, i.e. a 3–1 or 2–2 composite in three dimensions (see Fig. 4-1). These results indicate the potential for achieving high degrees of poling in porous ferroelectric structures by having pores with a high aspect ratio and aligning them parallel to the poling axis, such as those achieved by the freeze casting process; this is discussed in more detail in

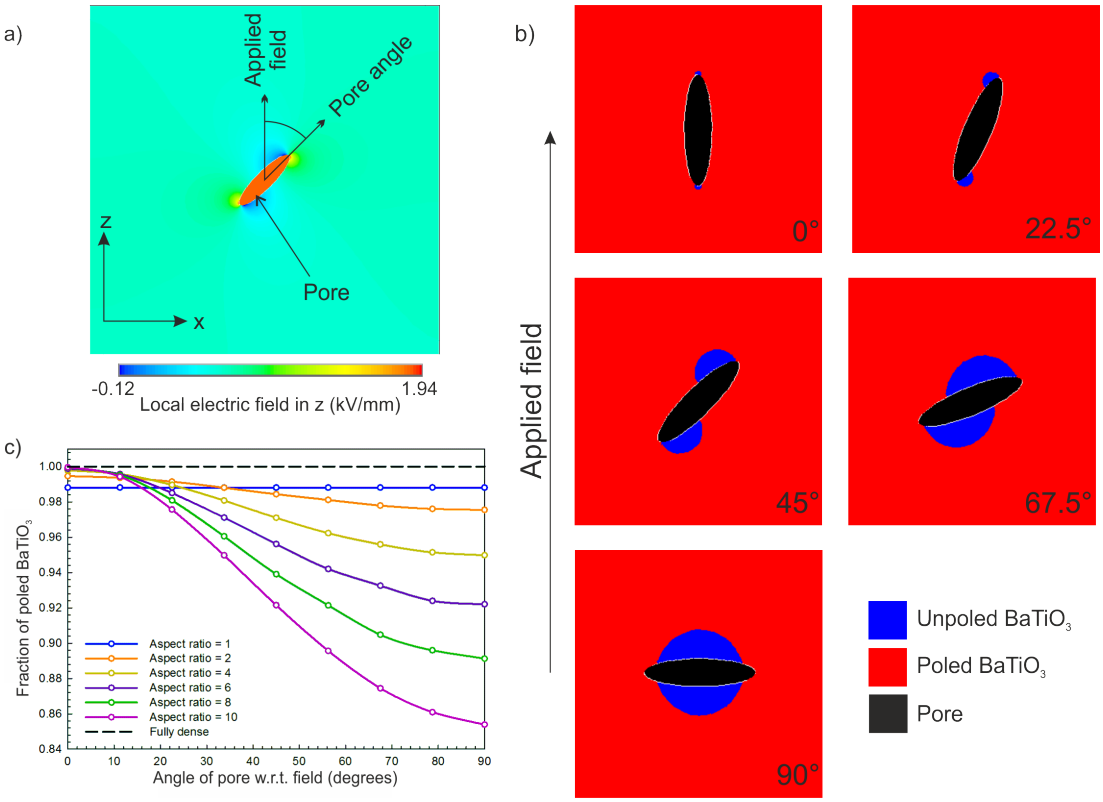

Figure 4-2: *(a) Contour plot of electric field distribution in and around a single pore (aspect ratio, AR = 4, angle = 45°) contained within a barium titanate matrix; (b) regions of poled (red) and unpoled (blue) barium titanate with single pore (black) angle varied from 0° to 90° with respect to applied field; and (c) effect of aspect ratio and angle of pore with respect to direction of applied field on the fraction of barium titanate poled in z-direction, i.e. the area in which the local field exceeds the coercive field of barium titanate (E_c = 0.5 kV/mm [37]).*

Section 4.1.3.

4.1.3 Porous Network Model

We now expand upon the single pore model presented in Section 4.1.2 to investigate three dimensional aligned structures that better represent the type of microstructure formed via unidirectional freeze casting of water-based solutions. A porous network finite element approach has been implemented that has been used previously to describe the properties of lead zirconate titanate (PZT) with uniformly distributed porosity [9] and barium titanate with porous sandwich layer structures [10]. Firstly, however, it is necessary to understand the freeze casting process and the type of porous structures formed in more detail.

Freeze Casting Process

Freeze casting is a process whereby a liquid suspension of a solvent and ceramic particles is frozen before the solvent phase is sublimated under reduced pressure and low temperature, i.e. converted from the solid directly to the vapour phase. As the solvent freezes the ceramic is ejected from the ice front forming regions of compacted ceramic powder. When the frozen solvent is sublimated pores are left that have the morphology of the solvent crystals, hence the process often being referred to as 'ice-templating' [39, 40]. The remaining ceramic powder compact is then sintered at high temperature to densify the ceramic walls. A variety of porous structures can be achieved through control of the freezing conditions and the properties of the liquid suspension, however, the majority of work to date in terms of freeze cast porous ceramics has focussed on forming highly aligned structures that are beneficial in terms of their mechanical properties [36]. Similarly, the literature on freeze cast porous ferroelectric ceramics focusses on the fabrication and properties of porous structures aligned to the poling direction that, as previously discussed, are found to have high piezoelectric strain coefficients [7, 22, 23, 24]. The excellent alignment is achieved by unidirectional freezing of a suspension, which encourages the crystallising solvent to grow preferentially along the direction of the temperature gradient.

The solvent used in the liquid suspension is a key factor in determining the final porous structure of the freeze cast material. Water is a commonly used solvent and is the focus of the porous structures examined in this work, although tetra-butyl alcohol and camphene have also been extensively researched and the work here also has relevance to the properties of aligned structures formed using these solvents [40]. The crystal structure and the crystal growth kinetics of the solvent determine the pore morphology of the freeze cast material. For example, ice has a hexagonal crystal structure and highly anisotropic growth kinetics so that crystals grow preferentially along their basal plane with limited dendritic growth perpendicular to this plane [41]. During unidirectional freezing the basal plane of the ice crystals are aligned to the freezing direction, in effect growing in a 2D sheet. As the ice grows during water-based freeze casting the ceramic particles are ejected from the solidification front into channels between the sheets of ice, thus forming the characteristic lamellar 2–2 structure [7, 21, 39, 40] (see Fig. 4-1d for schematic representation of 2–2 structure).

The temperature gradient provides the driving force for the directional growth of the crystallising solvent, meaning that high temperature gradients are favourable for producing highly aligned structures [40]. When the temperature gradient, the driving force for directional growth, is too low the solvent crystals are more likely to tilt away from the primary freezing axis, resulting in reduced alignment [39]. Doublesided freez-

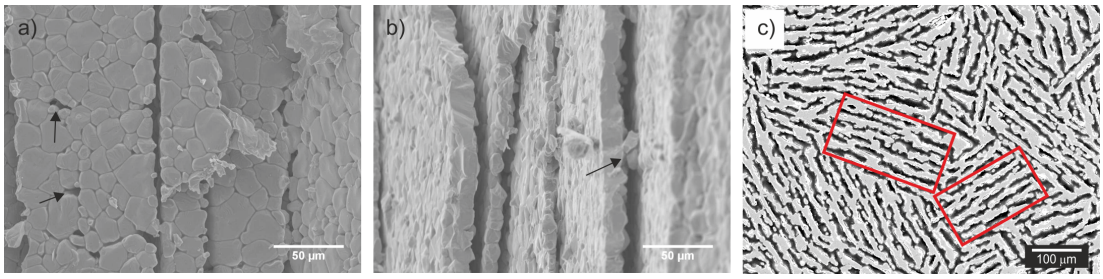

Figure 4-3: *SEM images of porous barium titanate fabricated via unidirectional freeze casting with 30 vol.% solid loading in suspension (see Section 4.1.4 for more details) with examples of (a) porosity in the ceramic channels and (b) a bridge between adjacent ceramic lamellae, indicated in both images by arrows; the freezing direction is vertical in both images; and (c) SEM of porous barium titanate taken transverse to freezing direction (pores with dark contrast) with boxes indicating regions of freeze material whereby pore and ceramic lamellae are parallel, such as those modelled in Section 4.1.3.*

ing set ups, whereby suspensions are frozen from both the top and bottom surfaces simultaneously can further improve alignment [21, 42].

The width of the lamellar ice channels can also be controlled by adjusting the freezing rate, with finer pore structures achieved using faster rates [39]. Reducing the pore width of the freeze cast materials has been shown to improve their mechanical strength compared to coarse structures at the same porosity [36]. However, freezing too fast leads to entrapment of particles within the ice, resulting in little or no pore alignment or long range order. Using a freezing rate that is too slow can lead to unstable freezing conditions, causing lateral growth of ice crystals between adjacent lamellae [43]. Some entrapment of particles within the ice is likely to occur during freezing, which may form characteristic bridges between the ceramic lamellae that are commonly observed in freeze cast structures [7].

The main factor controlling the final porosity of the material is the solid loading of the liquid suspension. Freeze casting has been used to create both highly dense ceramics (<1 vol.% porosity), using very low freezing rates and high solid loading (∼50 vol.% solid loading), and high porosity materials, such as aerogels (>90 vol.% porosity) [40]. As the solid loading is increased the viscosity of the suspension increases and redistribution of the ceramic particles away from the solidification front becomes more difficult [44]. This may affect the long range order of the porous structure post-sintering, as well as increasing the likelihood of air bubbles becoming trapped during the freezing process, which cause spherical pores in the sintered ceramic.

Modelling Procedure

Freeze casting is a complex process and this paper is not intended as a comprehensive review of the research conducted in this field. However, it is important to understand some of the processing challenges that arise during freeze casting of porous ceramics in order to model their properties in the context of the poling behaviour of a ferroelectric material. As discussed in Section 4.1.3, control of the freezing process is essential to generate a highly aligned microstructure, and even with relatively good control of cooling rate and particle size some 'defects' (defined in this sense as microstructural features which detract from an ideal 2–2 structure) are likely to be present, such as porosity in the ceramic channels and ceramic bridges that form in the pore channels. These two defect types are commonly observed in water-derived freeze cast structures as shown in Fig. 4-3a and b.

For the purposes of this modelling study, an idealised structure for a porous water-based freeze cast material can be defined as a lamellar 2–2 structure with no porosity in the ceramic channels and no ceramic bridges in the pore channels. The model enables an examination of the poling behaviour in regions of the material whereby the pore and ceramic channels are aligned parallel to one another; a transverse image of freeze cast barium titanate (i.e. freezing direction is out of plane) is shown in Fig. 4-3c with the boxed regions indicating where lamellar ceramic/pore channels are parallel to one another.

Two kinds of defects were introduced into the model in varying fractions to understand the effects of these features on the poling behaviour of the freeze cast materials: (i) pores in the ceramic lamellae that form in freeze cast materials due to incomplete compaction or sintering of the ceramic powder on rejection from the solidification front of the solvent (Fig. 4-3a); and (ii) ceramic elements that are present in the pore channels, i.e. the ceramic bridges that form during freezing casting due to engulfment of particles by the ice front and unstable growth conditions (Fig. 4-3b). As with the single pore model the finite element analysis was conducted in Ansys APDL.

Defining the Model Geometry

A 30 x 30 x 30 mesh of cubic elements was used as the starting point for all structures (Fig. 4-4a) before designating pore channels (Fig. 4-4b). Bridges between and porosity within the ceramic channels was then introduced in randomly selected positions within the network (Fig. 4-4c). The fraction of porosity introduced into the ceramic channels was controlled by the parameter α_{cc} and the fraction of ceramic elements in the pore channels (i.e. the bridges) was controlled by the parameter α_{pc}. The parameters are

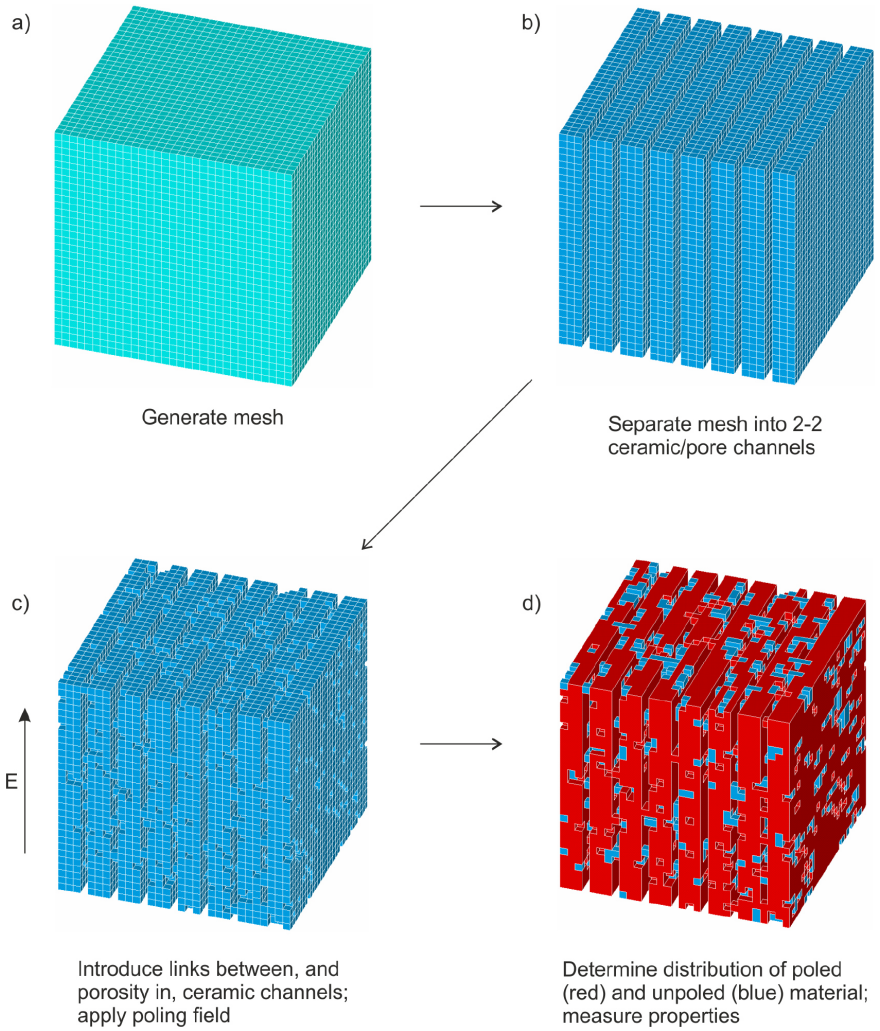

Figure 4-4: *Schematic of process to form porous network geometry in Ansys. (a) A cubic mesh with 30^3 elements was initially generated before (b) defining pore channels (i.e. an ideal 2-2 structure), (c) introducing porosity in the ceramic channels and bridges in pore channels and (d) applying a poling field to establish the distribution of poled and unpoled $BaTiO_3$ and porosity, and measuring the effective material properties.*

defined such that an ideal 2–2 structure with no porosity in the ceramic channels or ceramic in the pore channel had both α_{cc} and α_{pc} equal to zero, i.e. the structure in Fig. 4-4b. The variables α_{cc} and α_{pc} were varied from zero to 0.3 and 0.4, respectively. This range was selected as it exceeds the desirable levels of ceramic channel porosity and pore channel bridges in a freeze cast material and was observed to give a good indication of the effect of the two types of 'defect' on the poling behaviour and piezoelectric properties of freeze cast ferroelectric ceramics. Fig. 4-5 demonstrates the effect of varying α_{cc} (top row) and α_{pc} (bottom row) on porous structure, whereby the images are 2D slices taken parallel to the poling direction.

The pore channel width was maintained constant at one element wide as the model indicated that increasing it did not significantly affect the poling behaviour and would have meant the presence of a ceramic element in the pore channel did not necessarily constitute a bridge between neighbouring lamellae. The spacing between the pore channels (i.e. the ceramic channel width) was varied to provide additional control over the porosity, as in Fig. 4-5, where the top row of images have a ceramic channel width of three elements and the bottom row of images have a width of two. Once the porous network had been generated the ceramic elements were assigned the properties of unpoled barium titanate (elastic modulus = 120 GPa, Poisson's ratio = 0.3, ε_r = 1187.5 [45]) and pore elements were assigned the properties of air (elastic modulus = 0, $\varepsilon_r = 1$). The mesh size was deemed to yield a good balance between computing speed and reliability. As networks were generated randomly, five different structures were evaluated for each combination of α_{cc} and α_{pc} parameters.

The poling procedure was simulated to achieve a distribution of poled and unpoled barium titanate. Electrodes were 'applied' by coupling the voltages of the nodes at the top and bottom surfaces and applying a poling field between them, see Fig. 4-4c. Elements in which the local electric field exceeded the coercive field, i.e. $E_f > E_c$, were assigned the properties of poled barium titanate [37], as shown in Fig. 4-4d in which red elements are those which have been poled and blue elements are those that remain unpoled. Once the distribution of poled material had been established the effective piezoelectric properties of the network were measured.

Porous Network Model Results

The results for the longitudinal piezoelectric strain coefficient are shown in Fig. 4-6 for varying the ceramic fraction in the pore channel, α_{pc}, with a constant ceramic channel porosity, α_{cc}, and Fig. 4-7 for varying α_{cc}, constant α_{pc}. The data has been fitted using second order polynomial functions to highlight general trends. Firstly, considering Fig. 4-6, increasing the fraction of barium titanate in the pore channels (increasing α_{pc})

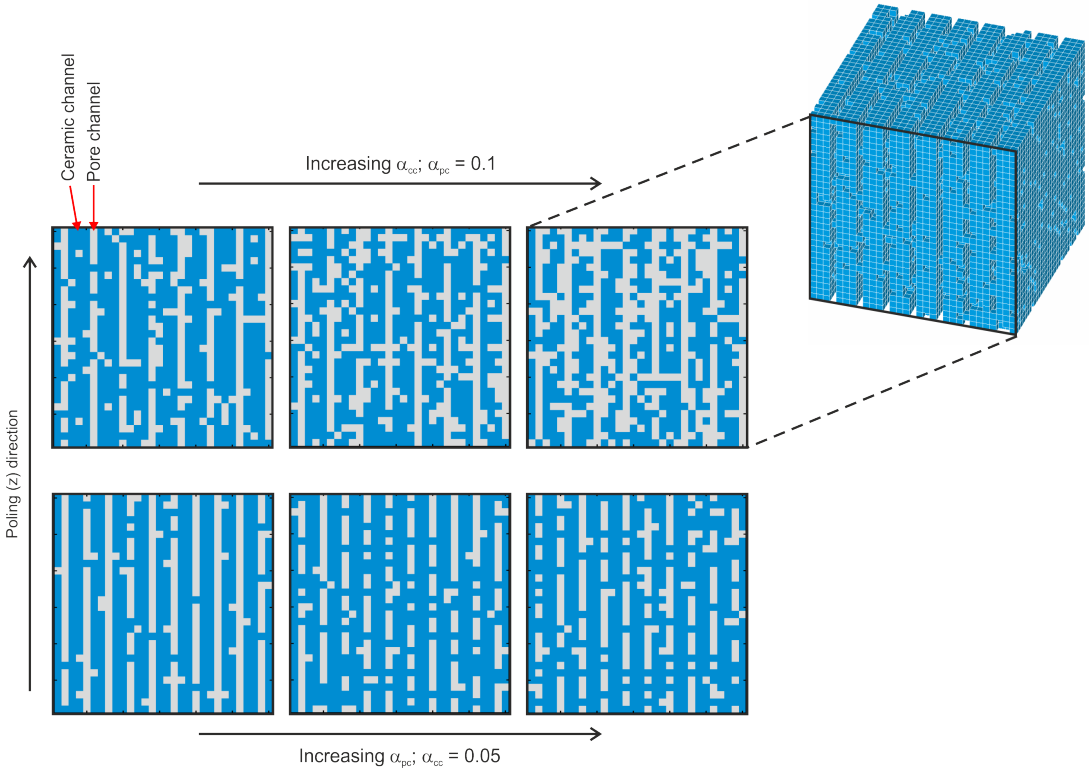

Figure 4-5: *Cross-section images (see top right for reference) of modelled porous structures showing the effect of the variables, α_{cc}, i.e. the fraction of porosity in the ceramic channels, and α_{pc}, the fraction of ceramic in the pore channels on the porous structure; pores are light grey in colour and the ceramic phase is blue. The top three images have increasing α_{cc} with α_{pc} = 0.1 and the bottom three images have increasing α_{pc} with α_{cc} = 0.05. The ceramic channel width is wider in the top three images compared to the bottom three images, which allowed additional control over the overall porosity fraction.*

resulted in a decrease in the measured d_{33} at a given porosity; the highest d_{33} values were achieved in structures with well-defined pore channels parallel to the poling (z) direction. This was due to regions of low electric field occuring in the immediate vicinity of a ceramic-pore interface perpendicular to the applied field (as can be seen in the single pore model, Fig 4-2), so that $BaTiO_3$ ceramic elements in the pore channels tended to be in low field regions and therefore remained unpoled, thus adding to the relative density of the material but not contributing to the measured d_{33}. The results shown in Fig. 4-7 are more intuitive in that increasing porosity within the ferroelectric channels (increasing α_{cc}) led to lower poled fractions that resulted in reduced d_{33} coefficients. A linear relationship between d_{33} and fraction of barium titanate poled was observed for all α_{cc} and α_{pc} values, see Fig. 4-7e, demonstrating a clear link between fraction poled and the resulting piezoelectric response as reported previously [9, 10].

A comparison between model predictions of an ideal 2-2 structure ($\alpha_{cc}, \alpha_{pc} = 0$), freeze cast structures (with varying ceramic channel porosity, α_{cc}, and ceramic in pore channel, α_{pc}) and uniform porous $BaTiO_3$ is shown in Fig. 4-7. For an ideal 2-2 porous structure, d_{33} remained at 140 pC/N regardless of the porosity fraction, since the highly aligned structure promoted a homogenenous poling field so that all the $BaTiO_3$ elements were poled. At low α_{cc} and α_{pc}, i.e. close to an ideal 2-2 structure, the predicted d_{33} was higher than that of barium titanate with uniformly distributed porosity of the same density, as has been shown experimentally by comparing highly aligned freeze cast porous PZT and PZT with uniform porosity manufactured by the burned out polymer spheres (BURPS) process [7, 15, 16, 22, 23, 24]. However, when α_{pc} was increased, and the pore channels became less well-defined due to higher fractions of $BaTiO_3$, higher d_{33} coefficients were observed in the uniformly distributed porous structures compared to the freeze cast microstructures, even when there was a low pore fraction within the ceramic $BaTiO_3$ channels (low α_{cc}). This indicates that in order to achieve high d_{33} coefficients clear pore channels are more important than highly dense ferroelectric channels. This is possibly caused by a restriction of strain in the poled material due to the presence of unpoled ceramic bridges in the porous channels. For example, when an external field was applied to the model a piezoelectric strain was observed in the highly poled dense channels, but no strain was induced in the stiff unpoled $BaTiO_3$ bridges within pore channels due the applied field. When there was a low fraction of unpoled ceramic in the pore channels (i.e. a low α_{pc}) the poled ceramic channels were relatively unrestricted in their piezoelectric expansion due to the applied field so that a high net piezoelectric response was observed throughout the material, leading to a high d_{33}. However, when the fraction of ceramic in the pore channel was increased to $\alpha_{pc} > 0.2$ there was sufficient unpoled ceramic bridges in the pore channels to restrict the

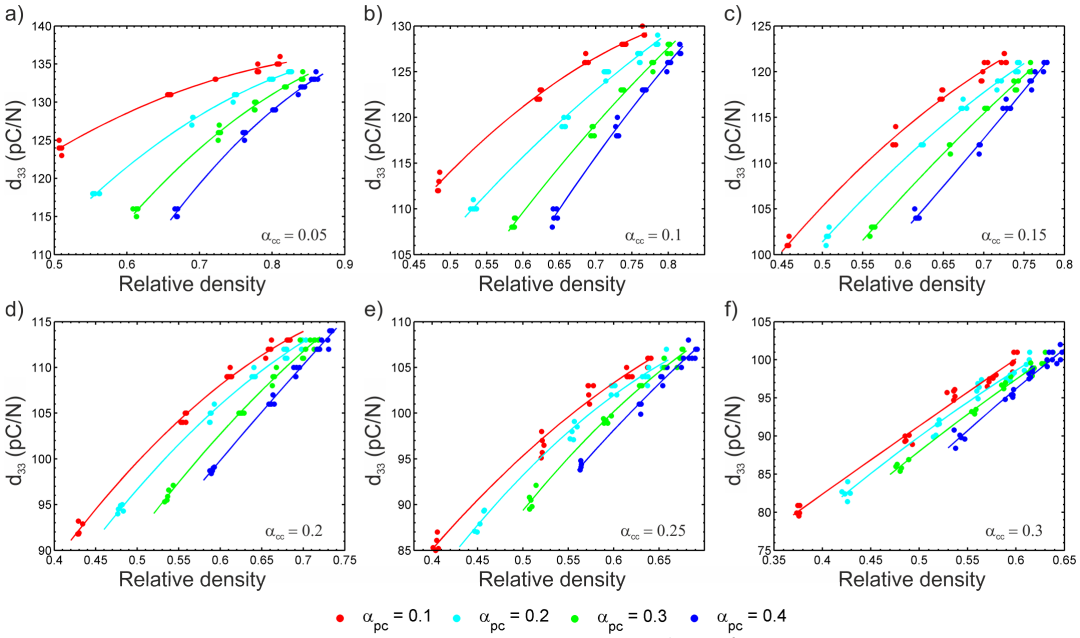

Figure 4-6: *Effect of fraction of barium titanate in pore channel, α_{pc}, on the longitudinal piezoelectric strain coefficient, d_{33}, for increasing fractions of porosity in ceramic channel, α_{cc}, in (a) - (e). For a given α_{cc} and α_{pc}, the relative density of the modelled material was controlled by adjusting the width of the ceramic channels.*

induced piezoelectric strain in the ceramic channels so that that the net piezoelectric strain of the structure fell below that of the material with uniformly distributed porosity, particularly when α_{cc}, i.e. the amount of porosity in the ceramic channels, was also high and there was a lower fraction of poled material in these channels. Having well-defined pore channels and long range order was therefore found to be beneficial in terms of promoting high d_{33} coefficients in the modelled freeze cast porous ferroelectric materials.

Example permittivity data obtained from the porous network model are shown in Fig. 4-8a for constant pore channel ceramic fraction, α_{pc}, with varying pore fraction in ceramic channels, α_{cc} and Fig. 4-8b for constant α_{cc}, varying α_{pc}, alongside the permittivity for an ideal 2–2 connected (α_{cc}, $\alpha_{pc} = 0$) and barium titanate with uniformly distributed porosity. The ideal 2–2 structure followed a linear trend of a parallel rule of mixtures model [46] and as α_{cc} and α_{pc} approached zero, i.e. towards an ideal 2–2 structure, the permittivity increased to what is effectively an upper bound. When $\alpha_{pc} > 0.1$ the permittivity of the freeze cast structure became close to that of the uniform porous barium titanate. Fig. 4-8c is included to show that at the limits of the parameters studied here, i.e. $\alpha_{cc} = 0.3$, $\alpha_{pc} = 0.4$, the permittivity of the aligned structure was lower than the uniform porous material. In terms of the energy harvesting figure of merit

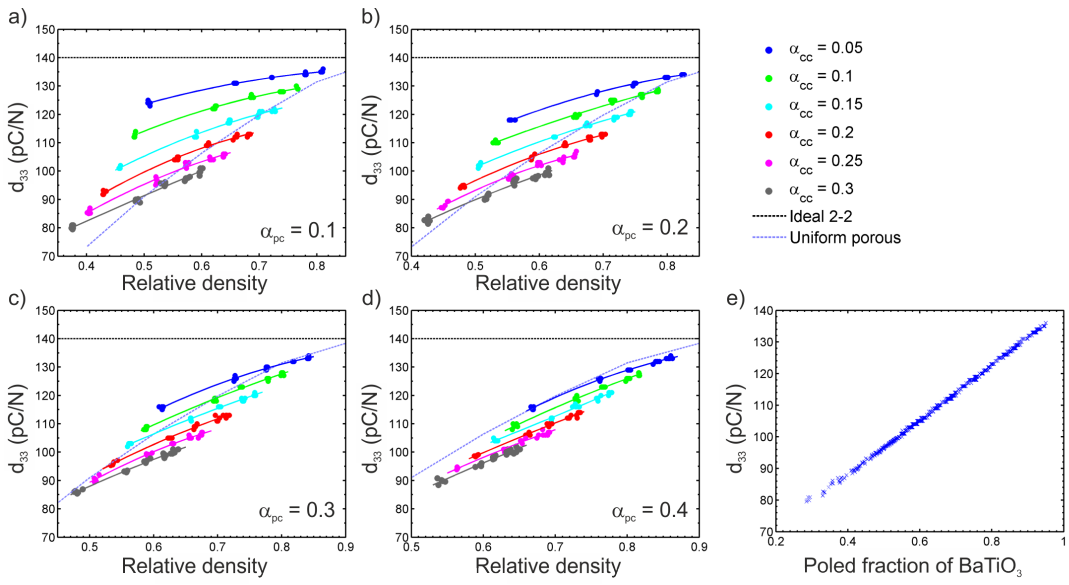

Figure 4-7: *Effect of pore fraction in ceramic channel, α_{cc}, on longitudinal piezoelectric strain coefficient, d_{33}, for increasing fractions of ceramic in pore channels, α_{pc}, in (a) - (d) with comparison to an ideal 2-2 structure ($\alpha_{cc}, \alpha_{pc} = 0$) and barium titanate with uniformly distributed porosity, see black and violet dashed lines, respectively; and (e) shows the relationship between the fraction of barium titanate poled and the resulting piezoelectric strain coefficient, d_{33}.*

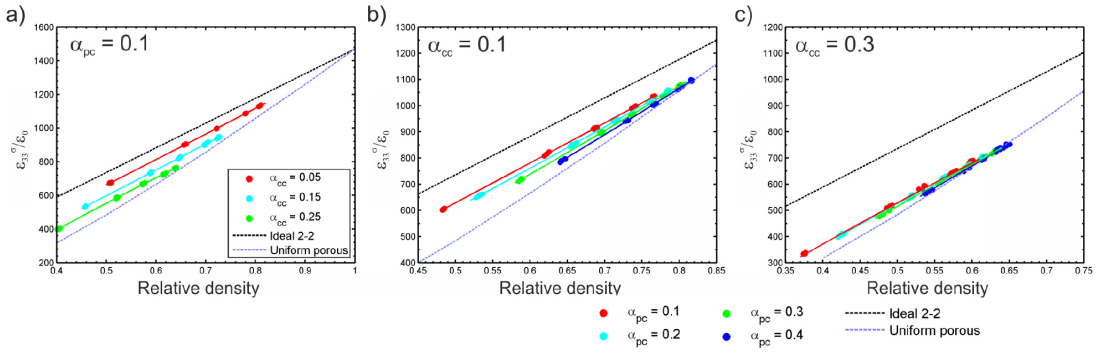

Figure 4-8: *Variation of relative permittivity $\varepsilon^{\sigma}_{33}/\varepsilon_0$ with relative density for (a) varying ceramic channel porosity α_{cc}, α_{pc} = 0.1, (b) varying ceramic fraction in pore channel α_{pc}, α_{cc} = 0.1, and (c) varying ceramic fraction in pore channel α_{pc}, α_{cc} = 0.3. The relative permittivity for an ideal 2-2 structure (α_{cc}, α_{pc} = 0) and uniformly distributed porous barium titanate as a function of relative density are shown for comparison (black and violet dashed lines, respectively) in all figures.*

(Eqn. 4.1) a low permittivity is beneficial, however, these structures also had relatively low d_{33} coefficients.

Calculated harvesting figures of merit, $d^2_{33}/\varepsilon^{\sigma}_{33}$, for the modelled data are shown in Fig. 4-9. Introducing porosity was generally found to increase the figure of merit compared to the dense value of ~1.40 pm^2/N, with the ideal 2–2 structure providing an upper limit for the increases that could be achieved by forming highly aligned freeze cast barium titanate. For example, the uniformly distributed porous material was predicted to have an energy harvesting figure of merit of ~2 pm^2/N at 50 vol.% porosity, whereas for the ideal 2–2 structure the predicted figure of merit was ~3 pm^2/N at the same porosity, double that of the dense material. Having a low fraction of porosity in the ceramic channels (α_{cc}) and a low fraction of ceramic in the pore channels (α_{pc}) yielded high figures of merit compared to both dense and porous material due to the high piezoelectric strain coefficient, d_{33}, that resulted from high fractions of the ferroelectric phase becoming poled, see Fig. 4-6 and Fig. 4-7.

4.1.4 Experimental

To provide experimental validation of the finite element model observations and a comparison to previous work on barium titanate with uniformly distributed, equi-axed porosity [20], freeze cast barium titanate samples were fabricated with a range of porosities (37–56 vol.% porosity). This section details the experimental procedure, results and discussion, and finally a demonstration of the energy harvesting capabilities of the porous ferroelectric materials compared to the dense material, in which samples

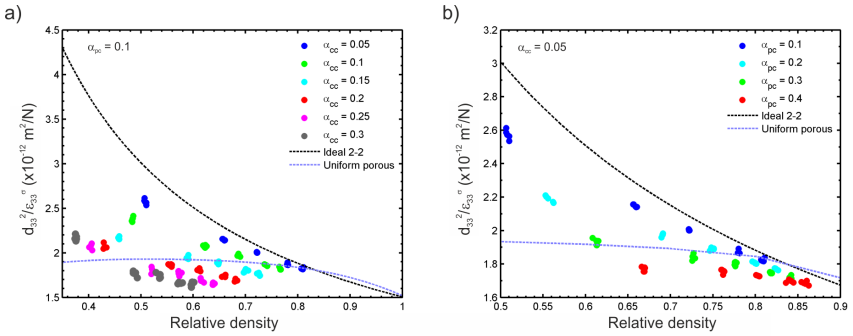

Figure 4-9: *Modelled data showing effect of (a) variation of ceramic channel porosity, α_{cc}, at constant pore channel ceramic fraction (α_{pc} = 0.1) and (b) variation of pore channel ceramic fraction, α_{pc}, at constant ceramic channel porosity (α_{cc} = 0.05) on the longitudinal energy harvesting figure of merit of porous barium titanate, $d_{33}^2/\varepsilon_{33}^\sigma$. The figure of merit for an ideal 2-2 structure (α_{cc}, α_{pc} = 0) and uniformly distributed porous barium titanate as a function of relative density are shown for comparison (black and violet dashed lines, respectively) in both figures.*

were mechanically excited and the derived electrical energy used to charge a reference capacitor.

Experimental Method

Barium titanate suspensions with varying solid loading contents (20, 25, 30, 32.5 vol.%) were prepared with commercial $BaTiO_3$ powder (particle size, d_{50} = 2.1 μm, Ferro, UK), 1 wt.% organic binder (polyethylene glycol, Sigma, UK) and dispersant (polyacrylic acid, Sigma, UK), and deionized water. A single-side freeze casting set up was used whereby the suspension was poured into a polydimethylsiloxane (PDMS) mould and placed onto a heat sink cooled by liquid nitrogen to -90°C. The mould used was open ended and aluminium adhesive tape was used to contain the suspension. Care was taken not to introduce air bubbles when filling the moulds. The ice was sublimated from the frozen bodies by freeze drying (Mini Lyotrap, LTE Scientific, UK) for 24 h. These were then sintered at 1300°C for 2 h with a 2 h dwell at 400°C to remove the organic binder; heating and cooling rates during the sintering process were ±60°C/h. Individual samples were cut to ∼2 mm thick from the sintered bodies at least 6 mm from the freezing surface. Samples were ground flat, cleaned and silver electrodes applied (RS Components, Product No. 186-3600, UK). The ceramic powder and sintering profile were the same as those used in previous investigations [10, 20] to enable comparison between the properties of barium titanate with different porous structures.

The relative density and porosity of the sectioned pellets was measured via the

Archimedean method [47]. The samples were corona poled in air at 115°C with 14 kV applied from a 35 mm point source, with the field maintained whilst the rig cooled to 40°C. Piezoelectric strain coefficients, d_{33} and d_{31} were measured 24 h after poling via the Berlincourt method (Take Control Piezometer PM25, UK). Impedance spectroscopy (Solartron 1260 and 1296 Dielectric Interface, UK) was used to measure the permittivity. Microstructural analysis was undertaken using scanning electron microscopy (SEM, JEOL JSM-6480LV).

Microstructural Analysis

SEM images of barium titanate freeze cast from suspensions with 20 vol.% initial solid loading (relative density, $\rho_{rel} = 0.45$) are shown in Fig. 4-10a and b and 30 vol.% solid loading samples ($\rho_{rel} = 0.55$) are shown in Fig. 4-10c and d. Comparing Fig. 4-10a and c it can be seen that the barium titanate freeze cast from the 30 vol.% loading suspension had more defined pore and ceramic channels than the samples cast from the 20 vol.% suspension. One possible reason for this is reducing the solid loading content resulted in more shrinkage during sintering (30% radial shrinkage for 20 vol.% suspension, 24% radial shrinkage for 30 vol.% suspension) that may have resulted in coalescence of adjacent ceramic lamellae. In addition, adjusting the solid loading of the suspension can alter the freezing temperature and viscosity [40] and therefore it may be that a more aligned freeze cast structure could have been achieved if the freezing conditions were altered depending on the suspension properties. The grain size, which can be seen in Fig. 4-10c and d, did not change significantly with varying solid loading content or porosity level, with grain sizes generally between 10 and 30 μm, which was similar to previous studies into the effect of porous structure on the energy harvesting properties of barium titanate [10, 20].

Transverse images, i.e. perpendicular to freezing direction, in Fig. 4-11 and polished images of sample cross-sections (i.e. the direction shown in Fig. 4-10) were used to calculate the average ceramic and pore channel width of the freeze cast barium titanate. Transverse pore structures of three solid loadings (20, 30 and 32.5 vol.%) with corresponding relative densities of $\rho_{rel} = 0.45$, 0.55 and 0.62 are shown in Fig. 4-11a-c, respectively. Increasing the solid loading content led to an increase in ceramic channel average width, which was found to be $\sim$9 μm for barium titanate cast from 20 vol.% suspension compared to $\sim$15 μm for 30 and 32.5 vol.% initial solid loading. On comparing the average ceramic wall thickness measured from transverse images in Fig. 4-11 to the SEM images in Fig. 4-10, it appears the ceramic channels were generally 1–2 grains thick with a degree of anisotropy of the grains as the ceramic channel width was smaller than the typical grain size observed when imaging side-on to the ceramic walls,

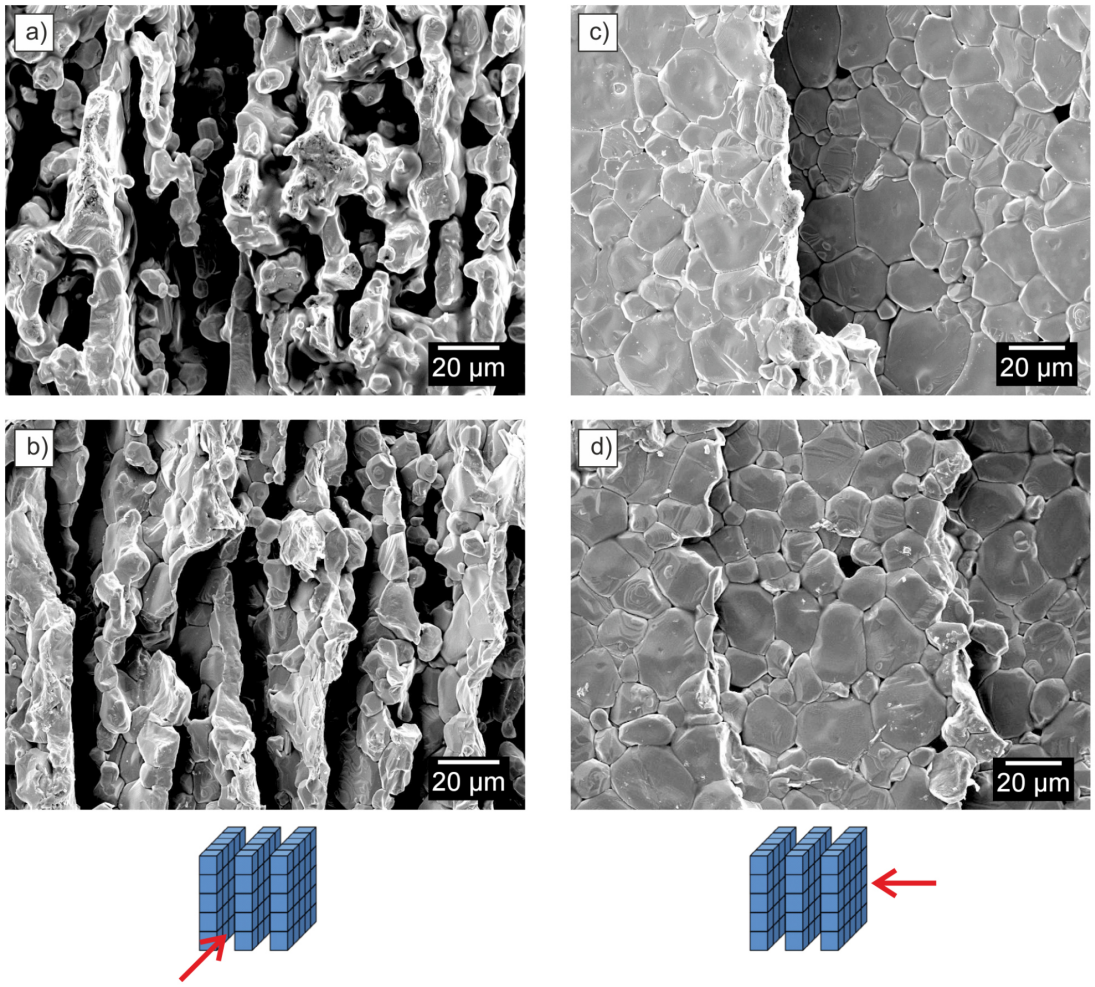

Figure 4-10: *SEM images of freeze cast barium titanate with (a) 55 vol.% and (b) 45 vol.% porosity (ρ_{rel} = 0.45 and 0.55, respectively); images (c) and (d) were taken from samples with 55 and 40 vol.% porosity, respectively, showing grain size did not change with porosity or solid loading content of frozen suspension. The freezing direction was vertical in all images; schematic representations of the direction of images with respect to the freeze cast structure are shown below the SEM images.*

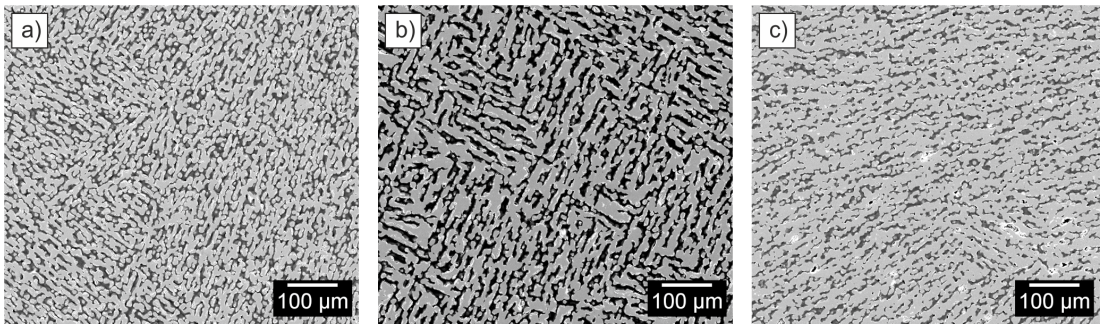

Figure 4-11: *Transverse SEM images (perpendicular to freezing direction) of barium titanate freeze cast with varying solid loadings and different resulting porosities, (a) 20 vol.%, ρ_{rel} = 0.45, (b) 30 vol.%, ρ_{rel} = 0.55 and (c) 32.5 vol.%, ρ_{rel} = 0.62.*

as in Fig. 4-10b and d; this indicates that freeze casting may also lead to some degree of texturing within the ceramic phase that may be of interest to study further. Pore channel width peaked for the 30 vol.% barium titanate at ∼14 μm, with both the 20 and 32.5 vol.% material having a pore channel width of <10 μm although it is thought this is due to differing mechanisms. Firstly, as previously discussed, a low solid loading sample experiences higher shrinkage during sintering, which may have led to a reduction in the pore channel width as neighbouring ceramic lamellae shrink closer together during sintering. The samples cast from suspensions with a high solid loading content had less solvent and more ceramic, which is likely to lead to relatively thicker ceramic channels compared to the pore channels.

Results and Discussion

The measured d_{33} data for freeze cast barium titanate are plotted in Fig. 4-12a as a function of relative density alongside data for uniformly distributed porous (3–3) barium titanate manufactured via the BURPS process [20]. The d_{33} coefficients of the freeze cast materials were consistently higher than materials with uniformly distributed porosity, with a maximum of 134.5 pC/N measured in barium titanate with a porosity of 45 vol.% (relative density, ρ_{rel} = 0.55), which was 93% that of the dense $BaTiO_3$, where the maximum measured d_{33} was 144.5 pC/N, and can be seen to be higher than the d_{33} of the uniformly distributed porous samples across the whole range of relative densities. This was a similar trend to that observed in the finite element models, see Fig. 4-6 and 4-7, in which the highly aligned structures had superior piezoelectric strain coefficients to the uniformly distributed porous samples. The variability in the data indicates there was some variation occurring during the processing that results in some samples having better pore channel and ceramic phase alignment than others, as

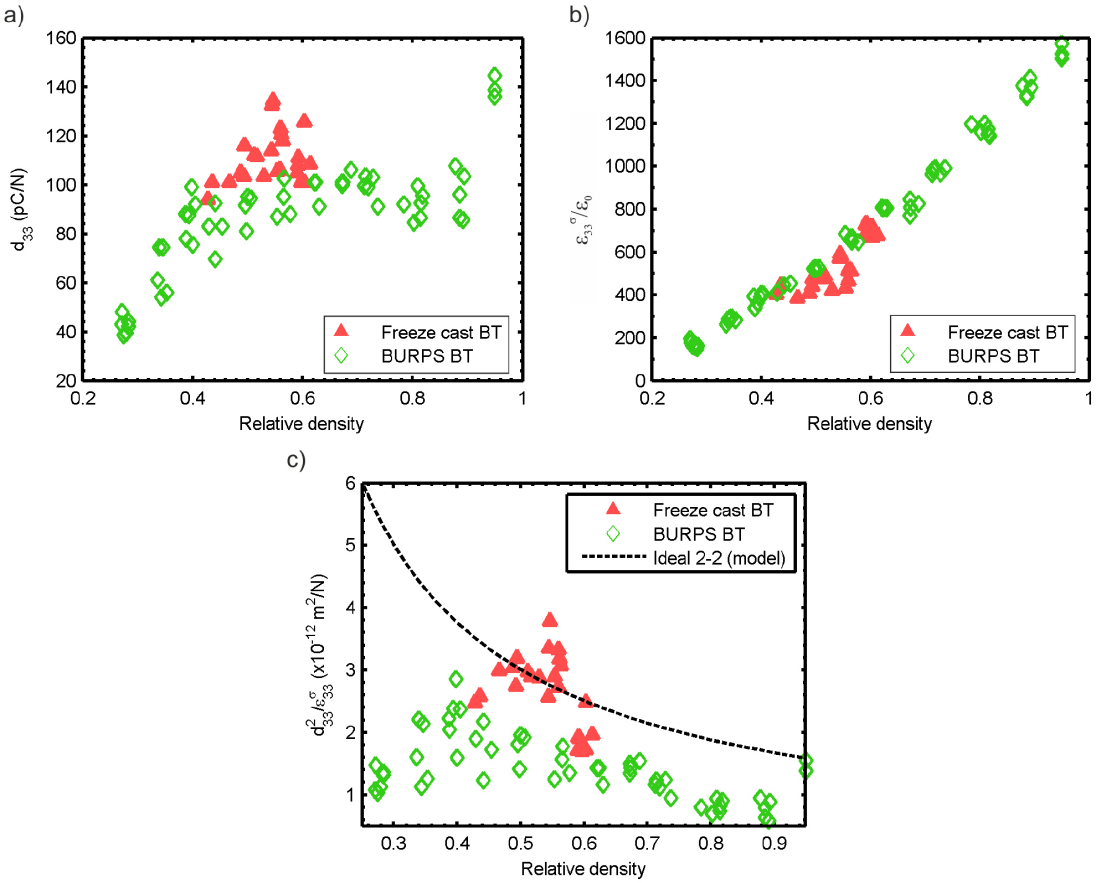

Figure 4-12: *Comparison of freeze cast (red) and uniform porous (green, manufactured using burned out polymer spheres (BURPS) process, from [20]) for (a) longitudinal piezoelectric strain coefficient, d_{33}, (b) relative permittivity, $\varepsilon^{\sigma}_{33}/\varepsilon_0$, and (c) energy harvesting figure of merit ($d^2_{33}/\varepsilon^{\sigma}_{33}$) as a function of relative density.*

observed in the results of the modelling study in Section 4.1.3, which can significantly affect the piezoelectric properties. The slight decline in d_{33} observed as relative density increased beyond ~0.55 may be a result of increasing fractions of ceramic in the pore channels, which was shown to be detrimental to the longitudinal piezoelectric properties in the porous network model, see Fig. 4-6 and 4-7.

Relative permittivity at 1 kHz is shown in Fig. 4-12b as a function of relative density. It can be seen that the aligned freeze cast barium titanate had a slightly lower permittivity than the uniform porous barium titanate, which was not predicted by either finite element model presented in this paper or indeed other models discussed elsewhere [46, 48]. However, these models assume there is no physical change in the material properties with the introduction of porosity or processing conditions as the model input properties are those measured from the fully dense ceramic. As discussed

in Section 4.1.4, the grains in the freeze cast material appeared to be elongated in the freezing direction, whereas the barium titanate formed via the BURPS process that the freeze cast permittivity data are compared to in Fig. 4-12b had equi-axied grains [20] and it is known that the microstructure can alter significantly the properties of barium titanate. For example, the dielectric properties of barium titanate are influenced by grain size, with permittivity decreasing as grain size increases, which is thought to be a result of changing domain wall mobility with grain size [49, 50, 51]. Also, single crystal barium titanate has highly anisotropic dielectric properties [52] with lower permittivity in the poling direction compared [37] and texturing the material can affect the measured permittivity [53].

While any grain size or texturing effects are also likely to alter the piezoelectric properties of barium titanate [51, 53, 54], such as d_{33}, the model and experimental data suggests that the piezoelectric coefficient is more dependent on the poling behaviour due to the porous structure, which may explain why the experimental d_{33} data in Fig. 4-12a is closer to the behaviour as predicted by the model. Further work is required to fully understand the experimental permittivity data, however, it is of interest to note that reduced permittivity (compared to the finite element model presented here and rule of mixtures model for a parallel-connected structure [46]) is beneficial in terms of the energy harvesting figure of merit, see Eqn. 4.1.

The high d_{33} coefficients measured in the freeze barium titanate samples led to significantly increased energy harvesting figures of merit compared to uniformly distributed porous barium titanate, see Fig. 4-12c, and when combined with the reduction in permittivity yielded a two-fold increase in harvesting figure of merit compared to the dense material. A maximum of 3.79 pm^2/N was found in the freeze cast barium titanate at a relative density of 0.55 and many samples were found to have a figure of merit of $>$3.0 pm^2/N, more than twice that of dense barium titanate. This was higher than was predicted by the finite element model due to low permittivity in the experimental results; the model data for an ideal 2–2 structure are shown in Fig. 4-12c (black dashed line) for comparison with the experimental data.

Piezoelectric Energy Harversting Demonstrator

A piezoelectric energy harvesting system, shown in Fig. 4-13, was used to demonstrate the improved harvesting of the porous freeze cast barium titanate compared to the dense material with three samples selected for comparison: a dense barium titanate pellet with a figure of merit of 1.39 pm^2/N, and two freeze cast samples, with a relative density of 0.55 and 0.60 and harvesting figure of merit of 3.24 pm^2/N and 2.19 pm^2/N, respectively; see Table 4.1 for more details. The samples all had a thickness of $\sim$1.8 mm and a

Table 4.1: *Details of samples used in piezoelectric energy harvesting experiments.*

ρ_{rel}	d_{33} (pC/N)	ε_r	$d_{33}^2/\varepsilon_{33}^\sigma$ (pm^2/N)	V_{OC} (V) (peak-to-peak)	I_{SC} (nA) (peak-to-peak)	V_{cap} (mV)	C (pF)
0.95	136	1504	1.39	0.63	360	96	742
0.60	118	717	2.19	0.97	231	196	256
0.55	129	580	3.24	1.15	213	234	187

diameter of ∼10 mm to keep the volume similar. The piezoelectric samples were fixed to a Perspex beam attached to a shaker (LDS V201, Brüel & Kjær, DK) with conductive silver epoxy (CircuitWorks Conductive Epoxy, Chemtronics, USA). The perpendicular distance from the central axis of the shaker to the location of the sample was minimised so as not to induce any bending effects. An end mass weighing six grams was attached to the sample with silver epoxy, see Fig. 4-13a. The samples were excited offresonance at 97 Hz on the shaker driven at 205 mV by a signal generator passed through an amplifier with the gain set to 20 dB (x10 amplification); calibration using an accelerometer found these conditions to give a maximum acceleration force of approximately 11 g. The open circuit voltage and short circuit current were measured using a B2987A Electrometer (Keysight, UK). The experimental set up is shown in Fig. 4-13b. The voltage generated by a sample was then measured again after being passed through a full rectifying bridge circuit with four 1N4148 diodes (NXP Semiconductors, NL), which enabled calculation of the voltage drop across the rectifier. Finally, a 1 μF capacitor (63 V, Philips 030K0, USA) (C_L in Fig. 4-13c) was charged across a load resistance of 10 MΩ measured with a differential probe of 20 MΩ input impedance, resulting in an equivalent load resistance of 6.67 MΩ (R_L in Fig. 4-13c). To reduce noise, the tests were conducted in a Faraday cage with shielding and grounding connected to the electrometer guard and chassis ground, respectively. Open circuit voltage and short circuit current experiments were repeated six times for each sample and the data averaged; capacitor charging experiments were repeated three times per sample. The voltage drop across the rectifying bridge was 0.2 V. Capacitances of the samples were measured with the HP 4263B LCR Metter with test signal level of 1 V at 100 Hz.

The open circuit voltage, V_{OC}, and short circuit current, I_{SC}, are shown in Fig. 4-14a and b, respectively; data sets have been smoothed and averaged. The open circuit voltage increased with increasing porosity, with a maximum peak-topeak open circuit voltage, V_{OC} = 1.15 V for the barium titanate with ρ_{rel} = 0.55 compared to V_{OC} = 0.62 V for the dense barium titanate. A higher open circuit voltage is beneficial for energy harvesting to reduce the effect of the voltage drop associated with diodes in the rectifying circuit. The theoretical open circuit voltage generated by a piezoelectric due

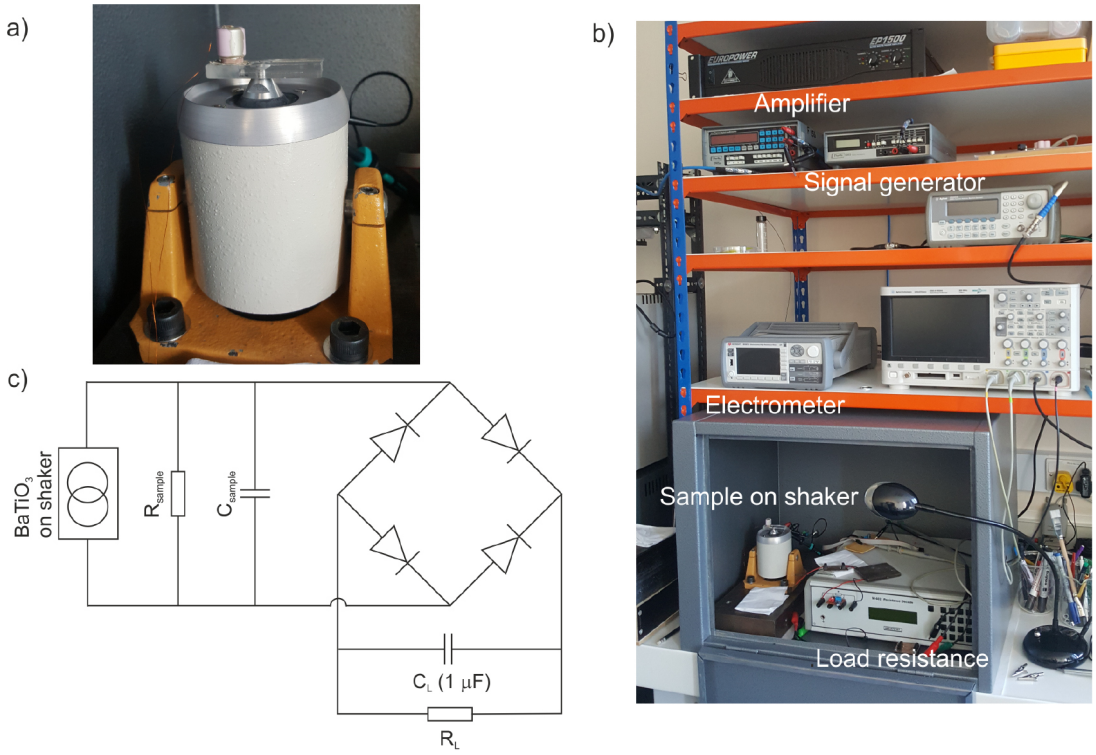

Figure 4-13: *Experimental setup for piezoelectric energy harvesting experiments; (a) sample was attached to a perspex beam fixed to a shaker with silver epoxy and a 6 g end mass attached to the other side, (b) shows the full set up with relevant measuring apparatus labelled and (c) is the circuit diagram for the rectifying circuit and measurement of voltage across capacitor that was charged using electrical energy converted from input mechanical energy by the barium titanate samples.*

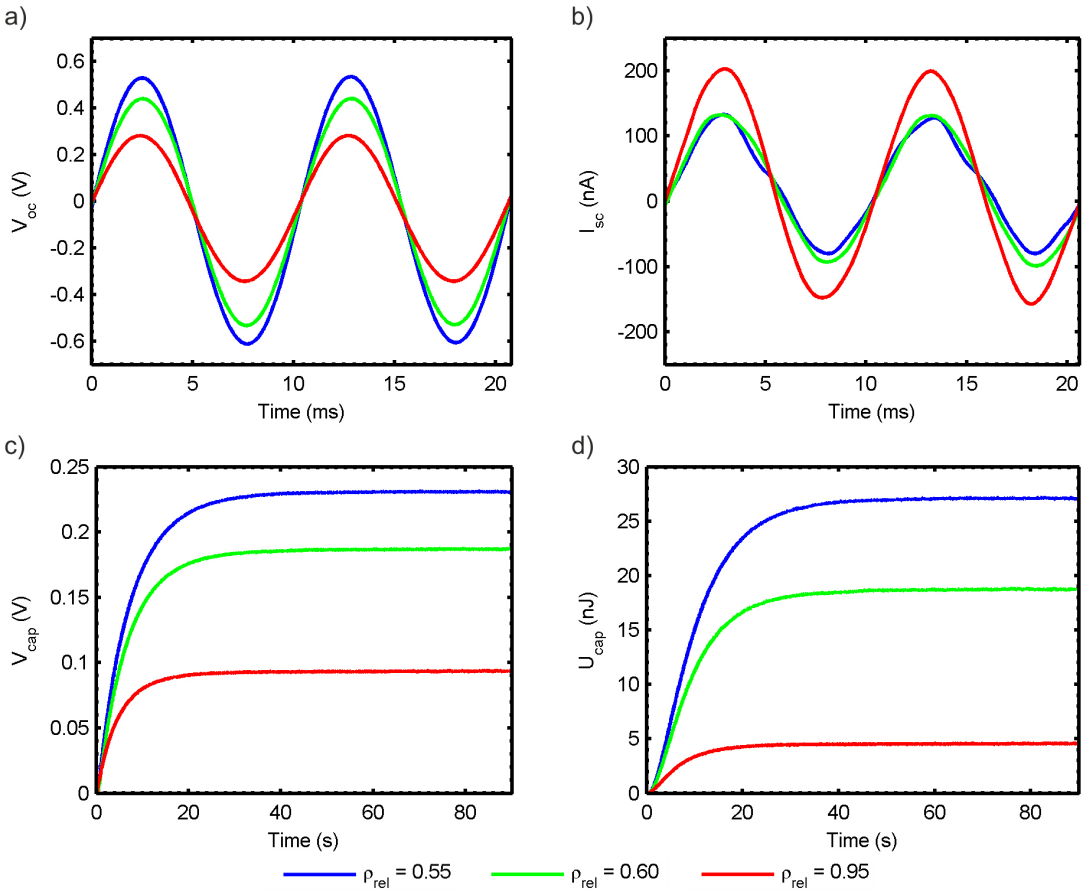

Figure 4-14: *Results from shaker experiment showing comparison between two porous freeze cast barium titanate samples (blue and green lines) and dense barium titanate (red) for (a) open circuit voltage, (b) short circuit current and capacitor charging curves after rectification in terms of (c) voltage (V_{cap}) and (d) enegy, where $U_{cap} = \frac{1}{2} \cdot C_L \cdot V_{cap}^2$ ($C_L = 1\mu F$, see Fig. 4-13). Sample details are shown in Table 4.1.*

to an applied stress, σ, can be calculated from the following equation [55]:

$$V_{OC} = \frac{d_{33}}{\varepsilon_{33}^{\sigma}} \cdot t \cdot \sigma \tag{4.3}$$

where t is the sample thickness. The piezoelectric strain coefficient, d_{33}, and sample thickness was similar in the three tested samples and so under the same loading conditions V_{OC} was expected to be approximately inversely proportional to the permittivity of the sample, as was observed experimentally. The short circuit current, I_{SC}, decreased with increasing porosity and decreasing permittivity, see Fig. 4-14a and Table 4.1.

The dense sample had the highest peak-to-peak short circuit current, I_{SC} = 360 nA, compared to the samples with ρ_{rel} of 0.60 and 0.55, which had peak-to-peak short

circuit currents of 231 and 213 nA, respectively. The reason for the fall in current with increasing porosity is thought to be an effect of the varying capacitances of the samples. The current produced by the sample due to mechanical excitation, I, is equal to the change in charge, dQ, with time, dt:

$$I = \frac{dQ}{dt} \tag{4.4}$$

and the change in charge due to a change in voltage, dV, can be written as:

$$dQ = C_{sample} \cdot dV \tag{4.5}$$

assuming constant capacitance, C_{sample}, of the piezoelectric during the experiment. If we differentiate with respect to time and rearrange we get the relationship:

$$I = \frac{dQ}{dt} = C_{sample} \cdot \frac{dV}{dt}. \tag{4.6}$$

From Eqn. 4.6 it can be seen that for a given change in voltage with time, dV/dt, the dense sample was expected to produce the most current as it had the highest capacitance, four times greater than the capacitance of the highest porosity sample, see Table 4.1. However, as the porous samples had a lower permittivity they produced higher voltages per unit stress (for example see Eqn. 4.3 and Fig. 4-14a) therefore the peak current of the dense barium titanate due to an applied stress was not four times greater than the barium titanate with $\rho_{rel} = 0.55$, as predicted by their respective capacitances, but was only ∼1.7 times greater due to a combination of higher capacitance yielding increased current outputs whilst simultaneously causing a reduction in the voltage generated due to an applied stress.

Fig. 4-14c shows that the porous barium titanate more effectively charged the capacitor than the dense material with a maximum voltage of $V_{cap} = 234$ mV achieved for the sample with $\rho_{rel} = 0.55$, compared to $V_{cap} = 96$ mV for the dense sample (average V_{cap} from three measurements). The time to achieve the peak voltage in the barium titanate with $\rho_{rel} = 0.55$ was 40 seconds. The energy stored on the capacitor during charging is shown in Fig. 4-14d, which was calculated from the relationship $U_{cap} = \frac{1}{2} \cdot C_L \cdot V_{cap}^2$ where $C_L = 1$ μF. As the energy stored on the capacitor is proportional to V_{cap}^2 the energy stored was almost six times higher for the barium titanate with $\rho_{rel} = 0.55$ (27.2 nJ) compared to the dense sample (4.64 nJ). The results from these experiments indicate the rate and magnitude of harvested energy increased with increasing porosity, as was predicted by the piezoelectric energy harvesting figures of merit of the three samples tested, demonstrating proof-of-concept for the use of porous ferroelectric materials in

piezoelectric energy harvesters.

This study has demonstrated the potential benefits of porosity on the energy harvesting performance of ferroelectric ceramics. As barium titanate has lower piezoelectric activity compared to PZT-based materials it is worth comparing the properties of the two material systems. The calculated longitudinal energy harvesting figures of merit for the dense ceramics are 11.68 pm^2/N for PZT-5H (calculated from data reported in [37]) compared to 1.40 pm^2/N for barium titanate (this work). A piezoelectric harvesting device fabricated with PZT as the active material would therefore be expected to yield a higher power output than the barium titanate reported here, with freeze cast porous PZT likely to have increased harvesting capabilities compared to dense PZT, as has been reported previously for pyroelectric energy harvesting [7].

4.1.5 Conclusions

This paper has demonstrated the potential for the controlled introduction of porosity into ferroelectric ceramics as a method to improve their longitudinal energy harvesting capabilities. Two new finite element models were presented that investigated the effect of pore structure on the poling behaviour and piezoelectric properties of porous ferroelectric materials in varying levels of detail, followed by an experimental study whereby highly aligned porous barium titanate was fabricated via the freeze casting method and found to have improved energy harvesting properties compared to dense barium titanate.

Firstly, a single pore model showed that high aspect ratio pores aligned to the poling direction aided the poling of the porous ferroelectric material through promotion of homogeneous poling fields that yield high fractions of poled ferroelectric phase, compared to pores with lower aspect ratios not aligned to the poling axis. This model provides an explanation for high piezoelectric strain coefficients that have been reported in freeze cast ferroelectric ceramics, highlighting the importance of the link between pore morphology and structure and the resulting piezoelectric properties of porous ferroelectric materials.

A second finite element model was then used to more accurately model 2–2 connected porous structures commonly achieved through water-based freeze casting. A porous microstructural network approach was used to investigate the effect of porosity in the ceramic channels and ceramic bridges in the pore channels. Increasing the fraction of porosity in the ceramic channels reduced the fraction of material poled and therefore the effective longitudinal piezoelectric strain coefficient, d_{33} of the material. However, of greater interest was the detrimental effect of the presence of ceramic bridges in the pore channels, which tended to remain unpoled due to their location within the

porous structure, whilst acting to restrict the induced strain in the highly poled ceramic channels, leading to lower d_{33} coefficients than similar porosity structures with clear pore channels.

Freeze cast porous barium titanate samples were fabricated and characterised in terms of their piezoelectric and dielectric properties and compared to dense barium titanate and porous barium titanate with spherical, uniformly distributed pores. The freeze cast material had similar d_{33} coefficients as the dense material up to ∼50 vol.% porosity, significantly higher than the barium titanate with uniformly distributed porosity. The permittivity of the material was found to decrease with increasing porosity in all cases, leading to excellent piezoelectric energy harvesting figures of merit, with a maximum of 3.79 pm^2/N achieved at 45 vol.% porosity (relative density, $\rho_{rel} = 0.55$), compared to ∼1.40 pm^2/N for dense barium titanate.

Finally, the benefits of introducing porosity into ferroelectric materials in terms of the piezoelectric energy harvesting performance were demonstrated. Dense and freeze cast porous barium titanate samples were mechanically excited on a shaker and the electrical response used to charge a 1 μF capacitor. The porous samples were found to charge the capacitor at a faster rate than the dense material, as predicted by the energy harvesting figures of merit. The maximum measured voltage across the charged capacitor was found to be 234 mV for freeze cast barium titanate with 45 vol.% porosity compared with 96 mV for dense barium titanate, corresponding to a 2.4- fold improvement. The energy stored by the capacitor after charging was approximately six times higher for the porous freeze cast barium titanate compared to the dense material. This work highlights the significant benefits for piezoelectric energy harvesting by forming ferroelectric microstructures containing highly aligned pores using freeze casting.

Acknowledgments

J. I. Roscow would like to thank EPSRC for providing financial support during his PhD. Y. Zhang would like to acknowledge the European Commission's Marie Skłodowska-Curie Actions (MSCA), through the Marie Skłodowska-Curie Individual Fellowships (IF-EF) (H2020-MSCA-IF-2015-EF-703950- HEAPPs) under Horizon 2020. C. R. Bowen would like to acknowledge funding from the European Research Council under the European Union's Seventh Framework Programme (FP/2007-2013)/ERC Grant Agreement No. 320963 on Novel Energy Materials, Engineering Science and Integrated Systems (NEMESIS).

References

[1] F. K. Shaikh and S. Zeadally, "Energy harvesting in wireless sensor networks: A comprehensive review," *Renewable and Sustainable Energy Reviews*, vol. 55, pp. 1041–1054, Mar. 2016.

[2] C. R. Bowen, H. A. Kim, P. M. Weaver, and S. Dunn, "Piezoelectric and ferroelectric materials and structures for energy harvesting applications," *Energy & Environmental Science*, vol. 7, no. 1, pp. 25–44, Dec. 2013.

[3] C. R. Bowen, J. Taylor, E. LeBoulbar, D. Zabek, A. Chauhan, and R. Vaish, "Pyroelectric materials and devices for energy harvesting applications," *Energy & Environmental Science*, vol. 7, no. 12, pp. 3836–3856, Nov. 2014.

[4] R. A. Islam and S. Priya, "Realization of high-energy density polycrystalline piezoelectric ceramics," *Applied Physics Letters*, vol. 88, no. 3, p. 032903, Jan. 2006.

[5] C. R. Bowen, J. Taylor, E. Le Boulbar, D. Zabek, and V. Y. Topolov, "A modified figure of merit for pyroelectric energy harvesting," *Materials Letters*, vol. 138, pp. 243–246, Jan. 2015.

[6] J. Roscow, Y. Zhang, J. Taylor, and C. R. Bowen, "Porous ferroelectrics for energy harvesting applications," *The European Physical Journal Special Topics*, vol. 224, no. 14-15, pp. 2949–2966, Nov. 2015.

[7] Y. Zhang, M. Xie, J. Roscow, Y. Bao, K. Zhou, D. Zhang, and C. R. Bowen, "Enhanced pyroelectric and piezoelectric properties of PZT with aligned porosity for energy harvesting applications," *Journal of Materials Chemistry A*, vol. 5, no. 14, pp. 6569–6580, Apr. 2017.

[8] G. H. Haertling, "Ferroelectric Ceramics: History and Technology," *Journal of the American Ceramic Society*, vol. 82, no. 4, pp. 797–818, 1999.

[9] R. W. C. Lewis, A. C. E. Dent, R. Stevens, and C. R. Bowen, "Microstructural modelling of the polarization and properties of porous ferroelectrics," *Smart Materials and Structures*, vol. 20, no. 8, p. 085002, Jun. 2011.

[10] J. I. Roscow, R. W. C. Lewis, J. Taylor, and C. R. Bowen, "Modelling and fabrication of porous sandwich layer barium titanate with improved piezoelectric energy harvesting figures of merit," *Acta Materialia*, 2017.

[11] E. Mercadelli, A. Sanson, and C. Galassi, "Porous Piezoelectric Ceramics," in *Piezoelectric Ceramics*, E. Suaste-Gomez, Ed. Sciyo, Oct. 2010, vol. Chapter 6.

[12] R. E. Newnham, D. P. Skinner, and L. E. Cross, "Connectivity and piezoelectric-pyroelectric composites," *Materials Research Bulletin*, vol. 13, no. 5, pp. 525–536, May 1978.

[13] S. Marselli, V. Pavia, C. Galassi, E. Roncari, F. Craciun, and G. Guidarelli, "Porous piezoelectric ceramic hydrophone," *The Journal of the Acoustical Society of America*, vol. 106, no. 2, pp. 733–738, Aug. 1999.

[14] H. Kara, R. Ramesh, R. Stevens, and C. Bowen, "Porous PZT ceramics for receiving transducers," *IEEE Transactions on Ultrasonics, Ferroelectrics, and Frequency Control*, vol. 50, no. 3, pp. 289–296, Mar. 2003.

[15] C. R. Bowen, A. Perry, A. C. F. Lewis, and H. Kara, "Processing and properties of porous piezoelectric materials with high hydrostatic figures of merit," *Journal of the European Ceramic Society*, vol. 24, no. 2, pp. 541–545, Jan. 2004.

[16] T. Zeng, X. Dong, S. Chen, and H. Yang, "Processing and piezoelectric properties of porous PZT ceramics," *Ceramics International*, vol. 33, no. 3, pp. 395–399, Apr. 2007.

[17] A. Yang, C.-A. Wang, R. Guo, Y. Huang, and C.-W. Nan, "Porous PZT Ceramics with High Hydrostatic Figure of Merit and Low Acoustic Impedance by TBA-Based Gel-Casting Process," *Journal of the American Ceramic Society*, vol. 93, no. 5, pp. 1427–1431, 2010.

[18] A. Navarro, R. W. Whatmore, and J. R. Alcock, "Preparation of Functionally Graded PZT Ceramics Using Tape Casting," *Journal of Electroceramics*, vol. 13, no. 1, pp. 413–415, Jul. 2004.

[19] C. P. Shaw, R. W. Whatmore, and J. R. Alcock, "Porous, Functionally Gradient Pyroelectric Materials," *Journal of the American Ceramic Society*, vol. 90, no. 1, pp. 137–142, 2007.

[20] J. I. Roscow, J. Taylor, and C. R. Bowen, "Manufacture and characterization of porous ferroelectrics for piezoelectric energy harvesting applications," *Ferroelectrics*, vol. 498, no. 1, pp. 40–46, Aug. 2016.

[21] Y. Zhang, Y. Bao, D. Zhang, and C. R. Bowen, "Porous PZT Ceramics with Aligned Pore Channels for Energy Harvesting Applications," *Journal of the American Ceramic Society*, vol. 98, no. 10, pp. 2980–2983, Oct. 2015.

[22] R. Guo, C.-A. Wang, and A. Yang, "Effects of pore size and orientation on dielectric and piezoelectric properties of 1–3 type porous PZT ceramics," *Journal of the European Ceramic Society*, vol. 31, no. 4, pp. 605–609, Apr. 2011.

[23] S.-H. Lee, S.-H. Jun, H.-E. Kim, and Y.-H. Koh, "Piezoelectric Properties of PZT-Based Ceramic with Highly Aligned Pores," *Journal of the American Ceramic Society*, vol. 91, no. 6, pp. 1912–1915, 2008.

[24] ——, "Fabrication of Porous PZT–PZN Piezoelectric Ceramics With High Hydrostatic Figure of Merits Using Camphene-Based Freeze Casting," *Journal of the American Ceramic Society*, vol. 90, no. 9, pp. 2807–2813, 2007.

[25] W. Liu, N. Li, Y. Wang, H. Xu, J. Wang, and J. Yang, "Preparation and properties of 3–1 type PZT ceramics by a self-organization method," *Journal of the European Ceramic Society*, vol. 35, no. 13, pp. 3467–3474, Nov. 2015.

[26] W. Liu, L. Lv, Y. Li, Y. Wang, J. Wang, C. Xue, Y. Dong, and J. Yang, "Effects of slurry composition on the properties of 3-1 type porous PZT ceramics prepared by ionotropic gelation," *Ceramics International*, vol. 43, no. 8, pp. 6542–6547, Jun. 2017.

[27] I. S. Grant and W. R. Phillips, *Electromagnetism*. John Wiley & Sons, Oct. 1990.

[28] L. Padurariu, L. P. Curecheriu, and L. Mitoseriu, "Nonlinear dielectric properties of paraelectric-dielectric composites described by a 3D Finite Element Method based on Landau-Devonshire theory," *Acta Materialia*, vol. 103, pp. 724–734, Jan. 2016.

[29] F. Gheorghiu, L. Padurariu, M. Airimioaei, L. Curecheriu, C. Ciomaga, C. Padurariu, C. Galassi, and L. Mitoseriu, "Porosity-dependent properties of Nb-doped Pb(Zr,Ti)O3 ceramics," *Journal of the American Ceramic Society*, vol. 100, no. 2, pp. 647–658, 2017.

[30] R. Khachaturyan, S. Zhukov, J. Schultheiß, C. Galassi, C. Reimuth, J. Koruza, H. von Seggern, and Y. A. Genenko, "Polarization-switching dynamics in bulk ferroelectrics with isometric and oriented anisometric pores," *Journal of Physics D: Applied Physics*, vol. 50, no. 4, p. 045303, Dec. 2016.

[31] C. Padurariu, L. Padurariu, L. Curecheriu, C. Ciomaga, N. Horchidan, C. Galassi, and L. Mitoseriu, "Role of the pore interconnectivity on the dielectric, switching and tunability properties of PZTN ceramics," *Ceramics International*, vol. 43, no. 7, pp. 5767–5773, May 2017.

[32] T. Zeng, X. Dong, C. Mao, Z. Zhou, and H. Yang, "Effects of pore shape and porosity on the properties of porous PZT 95/5 ceramics," *Journal of the European Ceramic Society*, vol. 27, no. 4, pp. 2025–2029, Jan. 2007.

[33] H. L. Zhang, J.-F. Li, and B.-P. Zhang, "Microstructure and electrical properties of porous PZT ceramics derived from different pore-forming agents," *Acta Materialia*, vol. 55, no. 1, pp. 171–181, Jan. 2007.

[34] A. P. Roberts and E. J. Garboczi, "Elastic Properties of Model Porous Ceramics," *Journal of the American Ceramic Society*, vol. 83, no. 12, pp. 3041–3048, 2000.

[35] S. Deville, E. Saiz, R. K. Nalla, and A. P. Tomsia, "Freezing as a Path to Build Complex Composites," *Science*, vol. 311, no. 5760, pp. 515–518, Jan. 2006.

[36] J. Seuba, S. Deville, C. Guizard, and A. J. Stevenson, "Mechanical properties and failure behavior of unidirectional porous ceramics," *Scientific Reports*, vol. 6, no. 1, p. 24326, Apr. 2016.

[37] D. Berlincourt and C. Near, "Properties of Morgan Electro Ceramic Ceramics," *Morgan Electroceramics*, vol. Technical Publication TP- 226, p. 12, 1999.

[38] T. Hang, J. Glaum, Y. A. Genenko, T. Phung, and M. Hoffman, "Investigation of partial discharge in piezoelectric ceramics," *Acta Materialia*, vol. 102, pp. 284–291, Jan. 2016.

[39] S. Deville, E. Saiz, and A. P. Tomsia, "Ice-templated porous alumina structures," *Acta Materialia*, vol. 55, no. 6, pp. 1965–1974, Apr. 2007.

[40] S. Deville, *Freezing Colloids: Observations, Principles, Control, and Use: Applications in Materials Science, Life Science, Earth Science, Food Science, and Engineering*, ser. Engineering Materials and Processes. Springer International Publishing, 2017.

[41] ——, "Freeze-Casting of Porous Ceramics: A Review of Current Achievements and Issues," *Advanced Engineering Materials*, vol. 10, no. 3, pp. 155–169, 2008.

[42] T. Waschkies, R. Oberacker, and M. J. Hoffmann, "Control of Lamellae Spacing During Freeze Casting of Ceramics Using Double-Side Cooling as a Novel Processing Route," *Journal of the American Ceramic Society*, vol. 92, no. s1, pp. S79–S84, 2009.

[43] S. Deville, E. Maire, G. Bernard-Granger, A. Lasalle, A. Bogner, C. Gauthier, J. Leloup, and C. Guizard, "Metastable and unstable cellular solidification of colloidal suspensions," *Nature Materials*, vol. 8, no. 12, pp. 966–972, Dec. 2009.

[44] N. O. Shanti, K. Araki, and J. W. Halloran, "Particle Redistribution During Dendritic Solidification of Particle Suspensions," *Journal of the American Ceramic Society*, vol. 89, no. 8, pp. 2444–2447, 2006.

[45] C. R. Bowen, A. C. Dent, R. Stevens, M. G. Cain, and A. Avent, "A new method to determine the un-poled elastic properties of ferroelectric materials," *Science and Technology of Advanced Materials*, vol. 18, no. 1, pp. 264–272, Dec. 2017.

[46] Gallantree H R, "Piezoelectric ceramic/polymer composites," *Br. Ceram. Proc.*, vol. 41, p. 161, 1989.

[47] BS EN 623-2, *BS EN 623-2:1993 - Advanced Technical Ceramics. Monolithic Ceramics. General and Textural Properties. Determination of Density and Porosity*, 1993.

[48] A. V. Goncharenko, V. Z. Lozovski, and E. F. Venger, "Lichtenecker's equation: Applicability and limitations," *Optics Communications*, vol. 174, no. 1, pp. 19–32, Jan. 2000.

[49] G. Arlt, D. Hennings, and G. de With, "Dielectric properties of fine-grained barium titanate ceramics," *Journal of Applied Physics*, vol. 58, no. 4, pp. 1619–1625, Aug. 1985.

[50] A. Bell, "Grain size effects in barium titanate-revisited," in *Proceedings of 1994 IEEE International Symposium on Applications of Ferroelectrics*, Aug. 1994, pp. 14–17.

[51] Y. Tan, J. Zhang, Y. Wu, C. Wang, V. Koval, B. Shi, H. Ye, R. McKinnon, G. Viola, and H. Yan, "Unfolding grain size effects in barium titanate ferroelectric ceramics," *Scientific Reports*, vol. 5, no. 1, p. 9953, May 2015.

[52] Berlincourt D and Jaffe H, "Elastic and piezoelectric coefficients of single crystal barium titanate," *Phys. Rev.*, vol. 111, p. 143, 1958.

[53] S. Wada, K. Takeda, T. Muraishi, H. Kakemoto, T. Tsurumi, and T. Kimura, "Preparation of [110] Grain Oriented Barium Titanate Ceramics by Templated Grain Growth Method and Their Piezoelectric Properties," *Japanese Journal of Applied Physics*, vol. 46, no. 10S, p. 7039, Oct. 2007.

[54] Y. Huan, X. Wang, J. Fang, and L. Li, "Grain Size Effects on Piezoelectric Properties and Domain Structure of BaTiO3 Ceramics Prepared by Two-Step Sintering," *Journal of the American Ceramic Society*, vol. 96, no. 11, pp. 3369–3371, 2013.

[55] S. Priya, "Criterion for material selection in design of bulk piezoelectric energy harvesters," *IEEE Transactions on Ultrasonics, Ferroelectrics, and Frequency Control*, vol. 57, no. 12, pp. 2610–2612, Dec. 2010.

Paper 4: Statement of Authorship

<table>
<tr><td colspan="10">This declaration concerns the article entitled:</td></tr>
<tr><td colspan="10">Flexible and active self-powered pressure, shear sensors based on freeze casting ceramic–polymer composites</td></tr>
<tr><td colspan="10">Publication status (tick one)</td></tr>
<tr><td>Draft manuscript</td><td></td><td>Submitted</td><td></td><td>In review</td><td></td><td>Accepted</td><td></td><td>Published</td><td>✓</td></tr>
<tr><td colspan="10">Copyright status (tick the appropriate statement)</td></tr>
<tr><td colspan="4">I hold the copyright for this material</td><td></td><td colspan="4">Copyright is retained by the publisher, but I have been given permission to replicate the material here</td><td>✓</td></tr>
<tr><td>Publication details (reference)</td><td colspan="9">M. Xie, Y. Zhang, M. J. Kraśny, C. Bowen, H. Khanbareh, and N. Gathercole, “Flexible and active self-powered pressure, shear sensors based on freeze casting ceramic–polymer composites”,
Energy Environ. Sci., Jul. 2018,
DOI: 10.1039/C8EE01551A.</td></tr>
<tr><td>Candidate’s contribution to the paper (detailed and also given as percentage)</td><td colspan="9">Formulation of ideas:
Material structure originated by Dr. Xie and Dr. Zhang.

Design of methodology:
Cooperative work between Dr. Xie, Prof. Bowen and candidate (33%).

Experimental work:
Shaker experiment and data processing by candidate (100%)
Dr. Xie designed sensor configurations, performed flexibility test, finger tapping experiment and data processing. Dr. Zhang fabricated the PZT–PDMS composite and sensors, performed poling and the d_{33} measurement of PZT–PDMS composites.
Dr. Khanbareh designed tire experimental setup. Mr Gathercole performed the d_{31} experiment.

Presentation of data in journal format:
Equal contribution from Dr Xie, Prof. Bowen and candidate (33%).</td></tr>
<tr><td>Statement from Candidate</td><td colspan="9">This paper reports original research I conducted during the period of my Higher Degree by Research candidature.</td></tr>
<tr><td>Signed</td><td colspan="5">  </td><td>Date</td><td colspan="3">08.08.2020</td></tr>
</table>

Flexible and Active Self-Powered Pressure, Shear Sensors Based on Freeze Casting Ceramic–Polymer Composites

Mengying Xie[(1)], Yan Zhang[(1,2)], Marcin J. Kraśny[(1)], Chris R. Bowen[(1)], Hamideh Khanbareh[(1)], Nicholas Gathercole[(1)]

[(1)] Department of Mechanical Engineering, University of Bath, Bath A2 7AY, UK
[(2)] State Key Laboratory of Powder Metallurgy, Central South University, 410083, China

Abstract

Self-powered flexible electronics are of particular interest and important for next generation electronics due to their light weight, flexible and self-sustainable properties. Many self-powered sensors made from piezoelectric composite materials are either inflexible or possess low piezoelectricity. In this work, we demonstrate self-powered flexible and highly active pressure and shear sensors based on freeze casting ceramic–polymer structures. A lamellar lead zirconate titanate (PZT) structure is initially developed via freeze-casting and the piezoelectric composites are formed by impregnating a polydimethylsiloxane (PDMS) matrix into the aligned pore channels. The structured PZT–PDMS composites exhibited a high effective longitudinal piezoelectric coefficient ($d_{33}*$) of 750 pC/N, which is higher than that of the monolithic ceramic due to the combination of bending and flexural effects. The use of freeze casting enables the manufacture of complex and arbitrary shaped 3D piezoelectric architectures, along with the unique advantages of low-cost and ease of fabrication. A 14×14 mm^2 PZT–PDMS pressure sensor was able to bend to a small radius of 8 mm and maintain a high d_{33}. Furthermore, the manufactured self-powered sensors are demonstrated in a range of applications, such as acceleration, strain and touch sensors that use the d_{33}, d_{31} and d_{15} coefficients to detect longitudinal, transverse and shear loads. This work expands on the potential applications of freeze casting and provides new opportunities for the manufacture of future electronic sensors.

Keywords

energy harvesting, flexible, self-powered, freeze cast, piezoelectric composites

4.1.6 Introduction

Future portable electronics requires devices that are flexible, lightweight and self-powered. There is increasing interest in a range of sensors based on strain, touch and acceleration; with particular emphasis on self-powered sensors or those that can work in combination with energy harvesters [1, 2, 3] to provide an alternative to conventional batteries with potential to deliver sustainable energy to supply low power electronic devices using ambient forms of energy.

Piezoelectric materials, such as lead zirconate titanate (PZT) [4, 5] and lead magnesium niobate-lead titanate (PMN-PT) [6], have been directly used as self-powered sensors [7, 8, 9, 10, 11, 12, 13, 14, 15, 16] to sense strain, force and acceleration. The piezoelectric charge coefficient d_{ij}, represents the ability to convert mechanical loads into an electric charge and plays a key role in their sensing and energy harvesting performance. Although bulk piezoelectric ceramics have high piezoelectric performance, they are too brittle to be integrated into the flexible electronics. Piezo-composite materials that contain piezoelectric nano- or micro-scale components that are randomly distributed into a polymer matrix [10, 17, 18] are candidates for flexible energy harvesters and self-powered sensing applications. Composite materials take advantage of the flexibility from the polymer matrix and piezoelectricity from the fillers. However, the use of randomly dispersed ceramic fillers often leads to a lack of connectivity, which gives rise to poor levels of polarisation and piezoelectric activity [19]. In addition, the permittivity mismatch between the two phases result in an unfavorable electric field distribution that restricts poling of the composite and further reduces piezoelectric properties. A higher connectivity of the ferroelectric ceramic can be achieved with either conventional mechanical dice and fill [13], the use of sacrificial templates [20], and a dielectrophoresis technique that uses an AC electric field to align the ceramic filler [21]. However, processes such as dice and fill can damage the ceramic due to the brittle nature of the materials and it is difficult to create complex shapes and device structures. As a result, new types of composite nanogenerators with nano- and micro-scale fibers or patterned structures for selfpowered devices have been explored. These nanogenerators include silver nanowires [14], barium titanate ($BaTiO_3$) nanoparticles [22], $BaTiO_3$ nanofibers [15, 23] in poly(vinylidenefluorideco-trifluoroethylene) (PVDF-TrFE), and PMN-PT nanowires in polydimethylsiloxane (PDMS) [24]. Such nanogenerators exhibit good mechanical flexibility, but their piezoelectric properties are often not reported in the literature and

are often relatively low. For example, the d_{33} of aligned $BaTiO_3$ nanowire is $d_{33} = 43$ pm/V [25], which is less than that of the bulk ceramic, where $d_{33} \sim 86$ pm/V [26]. In such nanogenerators, the strain can be applied to induce buckling to provide increased effective piezoelectric coefficients [15] but a buckling mode is not easily exploited in real applications.

It is well-known that the magnitude of the piezoelectric coefficient of ferroelectric ceramics is usually $d_{15} \geq d_{33} \geq d_{13}$ [27]. In addition, the d_{15} mode is less susceptible to pyroelectric effects due to temperature changes since the charge generated during vibration is collected by electrodes placed perpendicular to the polarization direction. As a result, any pyroelectric charge induced by a temperature change does not contribute to the signal [28]. The d_{15} mode is therefore of interest for sensing as the d_{15} shear mode has the potential to be effective when used in sensing and energy harvesting applications [20, 29]. Self-powered piezoelectric sensors are widely used to sense longitudinal [21] (d_{33}-mode) and transverse strains [15] (d_{31}-mode); for example a flexible three dimensional piezoelectric polymer composite made with a polyurethane foam template was recently reported for a pressure and bending sensor [20]. However, there is less work on shear (d_{15}-mode) based force sensors. One challenge is to design and manufacture shear force sensors, as it can require a complex configuration or device structure since the electrodes are applied normal to the direction of polarization.

In this paper we demonstrate the manufacture of flexible and highly active strain, acceleration and shear sensor arrays using aligned PZT–PDMS composite materials. The porous PZT was fabricated using a freeze casting technique and the ceramics were shaped into specific architectures for each sensor application. Freeze casting [30] is a cost-effective shaping technique that uses ice as template to create a directional porous structure. Due to the unidirectional freezing of the ice crystal, a porous microstructure with unidirectional channels is created, where the pores are formed as a replica of the ice crystals. For the manufacture of piezoelectric composites, freeze casting has the potential to be an easier and more practical shaping technique to create a continuous organized ceramic structure that is necessary for high piezoelectric activity. The PDMS was impregnated into the aligned pores of the freeze-cast PZT to create the PZT–PDMS composite materials. Due to the unidirectional channels formed by PZT and flexible polymer matrix, the composite structure achieved enhanced piezoelectric properties and was able to maintain performance after bending to small radius. Due to the advantages of high activity, flexible nature and ability to form into device geometries, we developed three self-powered sensors that are potential to sense longitudinal (d_{33}), transverse (d_{31}) and shear (d_{15}) motion.

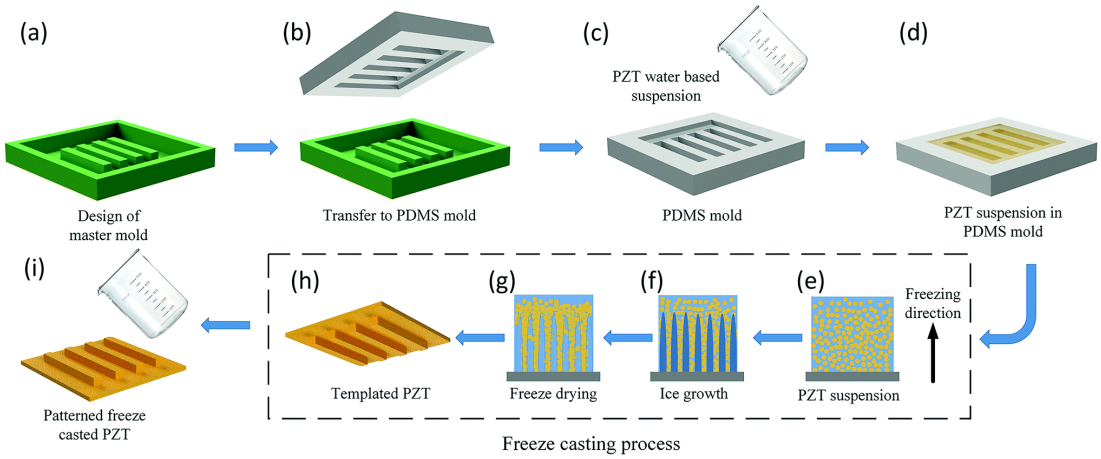

Figure 4-15: *Schematic of the fabrication process to form a freeze cast sensor array. (a) Design and fabrication of a master mold by additive manufacture. (b) Transfer of 3D pattern to a PDMS mold. (c and d) Fill the PDMS mold with prepared PZT water-based suspension. (e–h) Application of the freeze-casting process. (i) Encapsulate the patterned porous PZT sample in a PDMS matrix.*

4.1.7 Results and Discussion

Fabrication of the Sensor Structure

The fabrication processes of the flexible force sensors array are shown in Fig. 4-15. The PDMS-encapsulated hierarchical PZT structure was fabricated using the freeze casting method. For the first step, Fig. 4-15a, a master mold was 3D printed and the pattern was then transferred to a flexible PDMS mold by simple casting, see Fig. 4-15b. The prepared PZT water-based suspension was poured into the patterned PDMS mold, Fig. 4-15c and d, which was then transported to a conducting cold plate that was placed in a liquid nitrogen container for freezing. Fig. 4-15e–g shows the freeze-casting process inside of the PDMS mold, which is frozen from the base of the mold. Under super-cooled conditions (Fig. 4-15f), lamellar ice crystals begin to grow upwards and at equilibrium ice crystals push the PZT particles aside. The PZT particles then accumulate between growing ice crystals and consequently form a lamellar structure. When solidification is complete, as in Fig. 4-15g, the templated PZT-ice sample is demolded and freeze-dried to sublimate the ice, Fig. 4-15h. In order to densify the structured material and gain appropriate mechanical strength, the hierarchical porous PZT structures are then sintered. After firing process the samples were corona poled and electrodes were formed with silver conductive paint (RS Pro 186-3593). Finally the unidirectional channels in PZT ceramics are filled with a thin layer of PDMS and solidified.

As described in the introduction, one advantage of the freeze casting method is

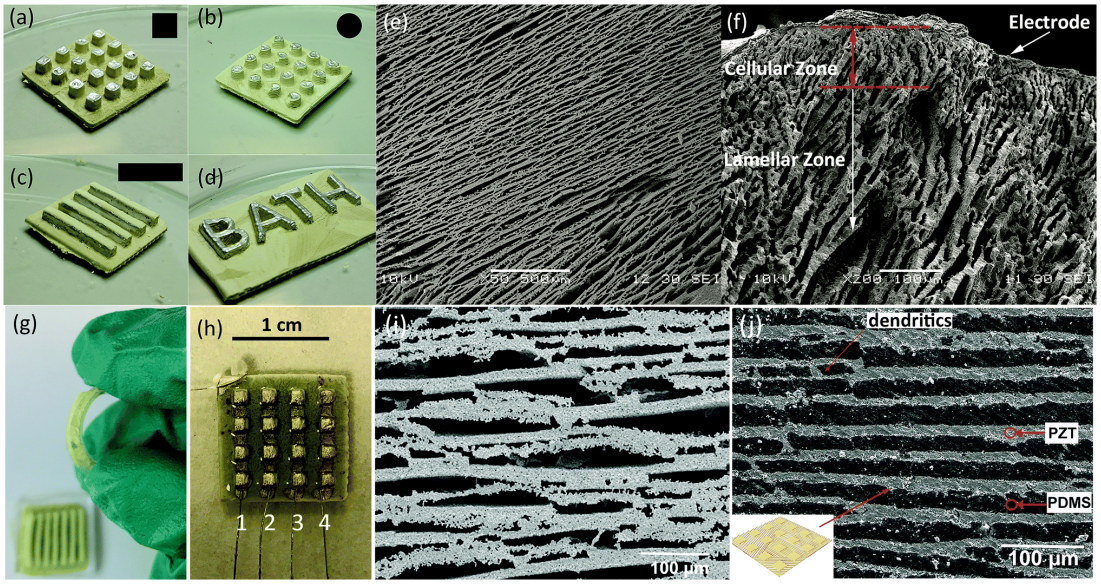

Figure 4-16: *Characteristics of the porous PZT and PZT–PDMS composites manufactured by freeze casting. (a–d) Images of freeze cast porous PZT ceramics with different geometric patterns before sintering, e.g. square, round, rectangular, arbitrary showing the capability of producing arbitrary structures. (e) SEM image of a porous PZT ceramic with porosity of 50 vol%, which shows highly aligned unidirectional lamellar microstructure. (f) SEM cross section of the porous PZT structure that shows both dense, cellular zones and lamellar regions. (g) Flexible PZT sensor encapsulated in PDMS. (h) Flexible pressure sensor with painted silver electrodes encapsulated in PDMS. (i and j) SEM image of lamellar PZT structure without and with PDMS, respectively.*

that it enables the production of the desired arbitrary 3D architecture with simple and low-cost processes, since the geometry of the master mold can be readily altered. The size of the patterns and devices can also be modified by simply changing the design of the PDMS mold. Fig. 4-16 demonstrates four geometric configurations of porous PZT ceramics formed using PDMS molds; these include cubes, cylinders, rectangular elements, and an arbitrary architecture as shown in Fig. 4-16a–d respectively.

Morphology

In this work, freeze-cast porous PZT ceramics with a porosity level of 50 vol% was studied due to their high figure of merit for sensing [31] and harvesting [32], along with appropriate mechanical strength. Fig. 4-16e shows a scanning electron microscopy (SEM) image of the lamellar microstructure of the sintered porous PZT. The SEM reveals highly aligned unidirectional channels with long range order on the bottom surface of the sintered PZT. Fig. 4-16f shows the cross section of one pillar in the

PZT-air composites of Fig. 4-16c. The upper $\sim$ 100 μ m is dense and consists of a cellular zone that was formed at the beginning of the freeze casting cycle in PDMS mold [33] since this is in contact with the cold face; and on the dense surface a thin layer of silver electrode has been applied. Ceramic materials are inherently brittle, whether in dense or porous form. Therefore, in this work we have impregnated PDMS into the aligned pores in order to introduce flexibility to the ceramic. Due to the low surface energy of 25 mN/m [34], the uncured PDMS is able to readily infiltrate and fill the micron-size channels to form the PZT–PDMS composites. This PZT–PDMS composite exhibits moderate flexibility, which is not possible with dense or porous PZT of the same thickness, see Fig. 4-16g. A final electroded and poled PZT–PDMS pressure sensor made of this PZT–PDMS composite is shown in Fig. 4-16h showing the individual electrodes on the upper faces of the pillars, with a common electrode at the base of the sensor. Fig. 4-16i and j shows the freeze cast PZT before and after filling with PDMS, where in Fig. 4-16j it can be seen that PDMS fills the pore space in the lamellar PZT structure.

Piezoelectric Properties of the Composites

The longitudinal d_{33} piezoelectric coefficient is a parameter that determines device performance for sensing and harvesting. The monolithic and dense PZT materials has a control reference of d_{33} $\sim$670 pC/N. In this work, the d_{33} of freeze casting PZT–air composites with 50 vol% air is 440 pC/N. In our previous study, it has been explained that the introduction of the porosity reduces the fraction of active material compared to dense PZT, which results in a lower polarization [32]. However, after filling the unidirectional channels with PDMS polymer, the d_{33} increases from 440 pC/N to 750 pC/N. This 70% enhancement is assumed to be a result of flexure due to the elastomer and device architecture, which provides a high effective piezoelectric coefficient (termed a $d_{33}*$).

In order to understand the mechanism of the enhancement, the polarization-electric field response of the freeze cast PZT–air and PZT–PDMS composites were investigated. Fig. 4-17 shows the polarisation–electric field (P–E) hysteresis loops of the freeze cast PZT–air and PZT–PDMS composites with maximum electric field of 13 kV/cm; higher electric fields could not be applied due to the dielectric breakdown. The minimum thickness between top and bottom electrodes is 1 mm. The remnant polarization (P_r) decreased from 3.4 μ C/cm^2 to 2.3 μ C/cm^2 after filling and coercive field decreased from 6.6 kV/cm to 6 kV/cm. This decrease of P_r is due to the active lamellar PZT ceramics being clamped by the PDMS polymer matrix [35]. The clamping of the lamellar PZT induces charges on the composite surface, via the d_{33} effect, that act to reduce

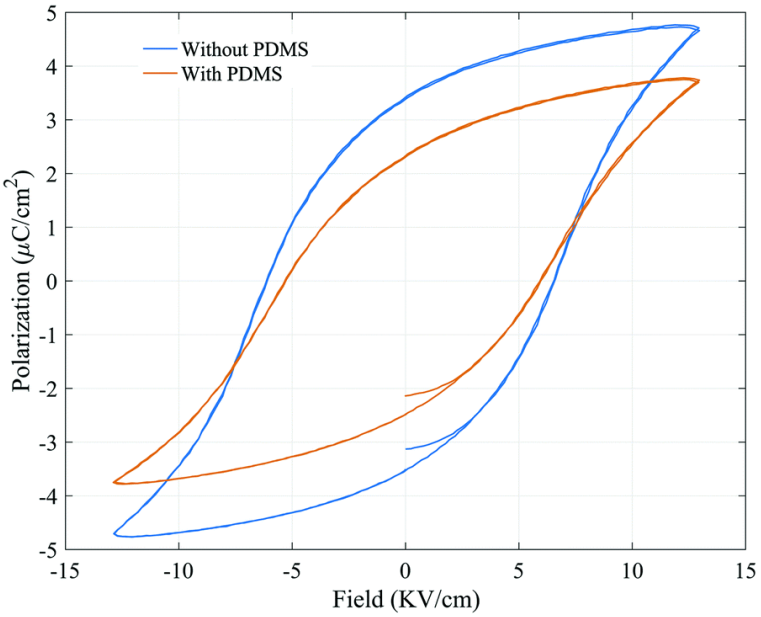

Figure 4-17: *Polarisation–electric field (P–E) hysteresis loops of freeze cast lead zirconate titanate (PZT) with and without polydimethylsiloxane (PDMS) polymer matrix.*

the measured polarization. From the decrease in polarization after pore infiltration with PDMS, we can confirm that the enhancement of the effective $d_{33}*$ in PZT–PDMS composites is not due to any increased polarization due to the polymer infiltration; this is expected since PDMS is not a ferroelectric and is simply a dielectric material [36].

Therefore, we assume the structure of the PZT–PDMS composites helps to improve the piezoelectric response. The improvement of effective d_{33} ($d_{33}*$) is due to two reasons; (i) the increased connectivity of the piezoelectric phase, and (ii) the combined effect of compression and flexure that enhances the effective d_{33} in the composite when it has been compressed. In the range of 0 to 45% strain, PDMS can be regarded as an linear elastic and incompressible material, whose Poisson's ratio is close to 0.5 [37, 38]. When the composite sensor is pressed vertically in the polarization direction, due to the incompressible property of the PDMS, it tends to expand horizontally. In addition to the compression, this expansion introduces an additional flexural response to the lamellar PZT structures. Therefore, the d_{33} increases in comparison to the PZT–air composites and dense PZT ceramics, which does not exhibit any flexural component.

Flexibility of the Composite

Flexibility is important property for applications related to portable electronics. The flexibility of sensors has often been carried out with a bend test by placing the sensor

on an object of increasing curvature [39, 40, 41]. In order to demonstrate the flexibility and stability of our sensors, the piezoelectric coefficient d_{33} of a sensor was measured at relaxed state after attaching the sensor to cylinders with a fixed radius of curvature, e.g. 8, 9.5, 12.5, 16, 20, and 25 mm. Fig. 4-18a shows a flexible PZT–PDMS sensor tightly wrapped around a cylinder with a radius of 16 mm. Fig. 4-18b shows the percentage change of d_{33} after each bending of the device to the different radius of curvatures. It can be seen that d_{33} does not change until the sensor was attached to a cylinder with radius of 16 mm. The d_{33} slightly decreased to ∼89% of the original value when attached to 16 mm cylinder and is thought to be due to the presence of cracks in freeze cast PZT structure and silver electrodes as four upper electrodes share one common bottom electrode. As shown in Fig. 4-16j, the PZT network is totally embedded in PDMS and when the PZT–PDMS composite is subjected to flexure with a small strain, small cracks which close on removal of the mechanical load, which is similar to the metals embedded in PDMS [42]. However, when the bending radius was increased to 16 mm, irreversible damage occurs to the PZT networks and silver electrodes, thereby leading to a permanent decrease in the d_{33}. A crack is indicated in Fig. 4-18a and after this initial drop at a radius of curvature of 16 mm the d_{33} value stabilizes with subsequent increases in curvature. The result demonstrates that our sensor is highly active with high flexibility and stability compared to traditional piezoelectric composites. The bending-induced crack could be avoided by fabricating thinner substrates or individual bottom electrodes for each sensing element.

Sensor Configurations

We now demonstrate self-powered sensors using the high activity PZT–PDMS composites. These sensors are employed for sensing by exploiting different modes, which include longitudinal d_{33}, transverse d_{31}, and shear d_{15} with purposely tailored geometries formed by freeze casting, as shown in Fig. 4-19a–c where the poling direction in through thickness in all cases and the electrode position is shown for each case. In the following text, we will demonstrate several applications with these three sensing mode sensors.

Strain Sensor ($\mathbf{d_{31}}$ mode)

We have used the composite as a d_{31} sensor to measure the strain of the vehicle wheel and here we replicated tire deformation during operation. In order to achieve accurate surface strains for a given distortion of a section of car tire thread, a dynamic test was carried out as shown in Fig. 4-20a. A section of standard passenger vehicle tire was

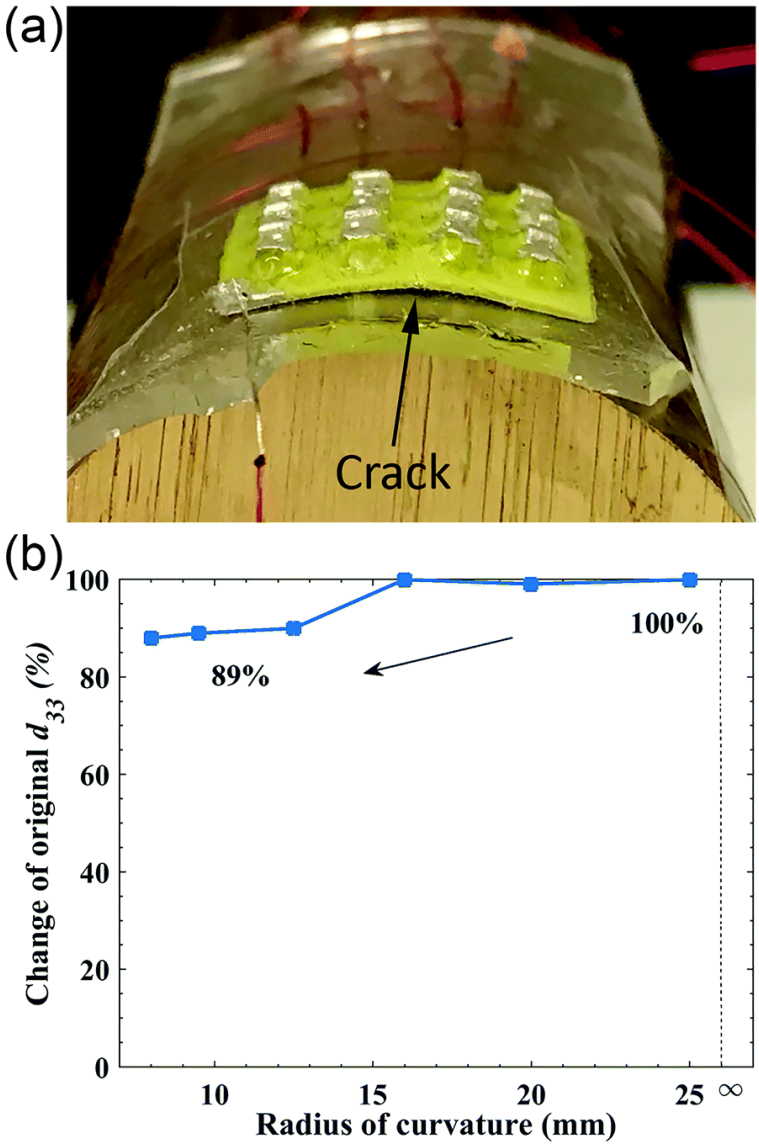

Figure 4-18: *Flexibility of PZT–PDMS composite sensors. (a) Flexible sensor attached to a brass cylinder (radius of the cylinder in picture is 16 mm). (b) Percentage of original d_{33} after attaching to brass cylinder of increasing curvature.*

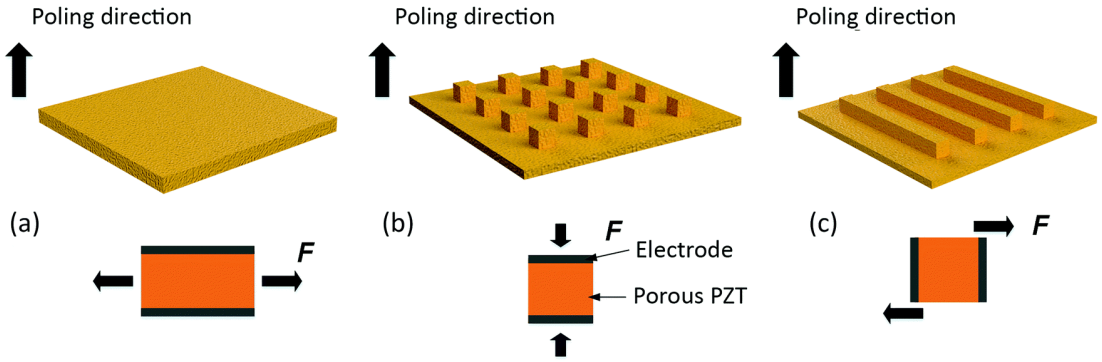

Figure 4-19: *Schematic of the three piezoelectric sensor configurations with three sensing modes, e.g. (a) longitudinal [d_{33}], (b) transverse [d_{31}], and (c) shear [d_{15}]. The freezing direction is parallel to the poling direction so that PZT material is aligned in this direction.*

fitted to an Instron 1342 with a 100 kN load cell servo-hydraulic test machine and the strain gauge was positioned along the central axis of the tire; as shown in the inset of Fig. 4-20a. The vehicle tire was tested under a cyclic compression by applying a load at a test frequency of up to 10 Hz. The d_{31} sensor, as in the inset of Fig. 4-20b, was attached to the central axis of the tire surface. The details of the measurement can be found in *Video 1 (Supplement)*. Fig. 4-20b shows the strain measured by micro strain gauge (micro measurement) positioned at the central axis of the tire under cyclic compression of 0–3.5 kN and the open circuit voltage response of the d_{31} sensor placed at the same position. The measured sensor response corresponds to the strain gauge signal and reaches its maximum at ∼1.2 V which correlates with 250 $\mu\varepsilon$.

Pressure (d_{33} mode) and Shear (d_{15} mode) Touch Sensors

Pressure (d_{33} mode) and shear (d_{15} mode) sensor were developed to detect light finger tapping and finger shearing. Fig. 4-21a is a schematic of the setup to assess the pressure and shear sensor's response to light finger tapping and shearing. In order to simplify the measurement, each pillar shares a single bottom electrode and the pressure sensor contains of four individual upper electrodes labeled as line 1, 2, 3, and 4, see Fig. 4-16h. Firstly we demonstrated a light finger tapping test on single sensing line of the d_{33} sensor. The open circuit voltage was measured using Keithley 6517B electrometer with high input impedance (>200 TΩ) for voltage measurement and <1 fA noise. The electrometer was connected through its analog output to the Agilent DSO-X 2024A oscilloscope. Fig. 4-21b shows the testing procedure with one of the four lines of the d_{33} pressure sensor and it was able to generate a voltage over 1 V.

The ability to form a sensor array is important as it can acquire the force distribution

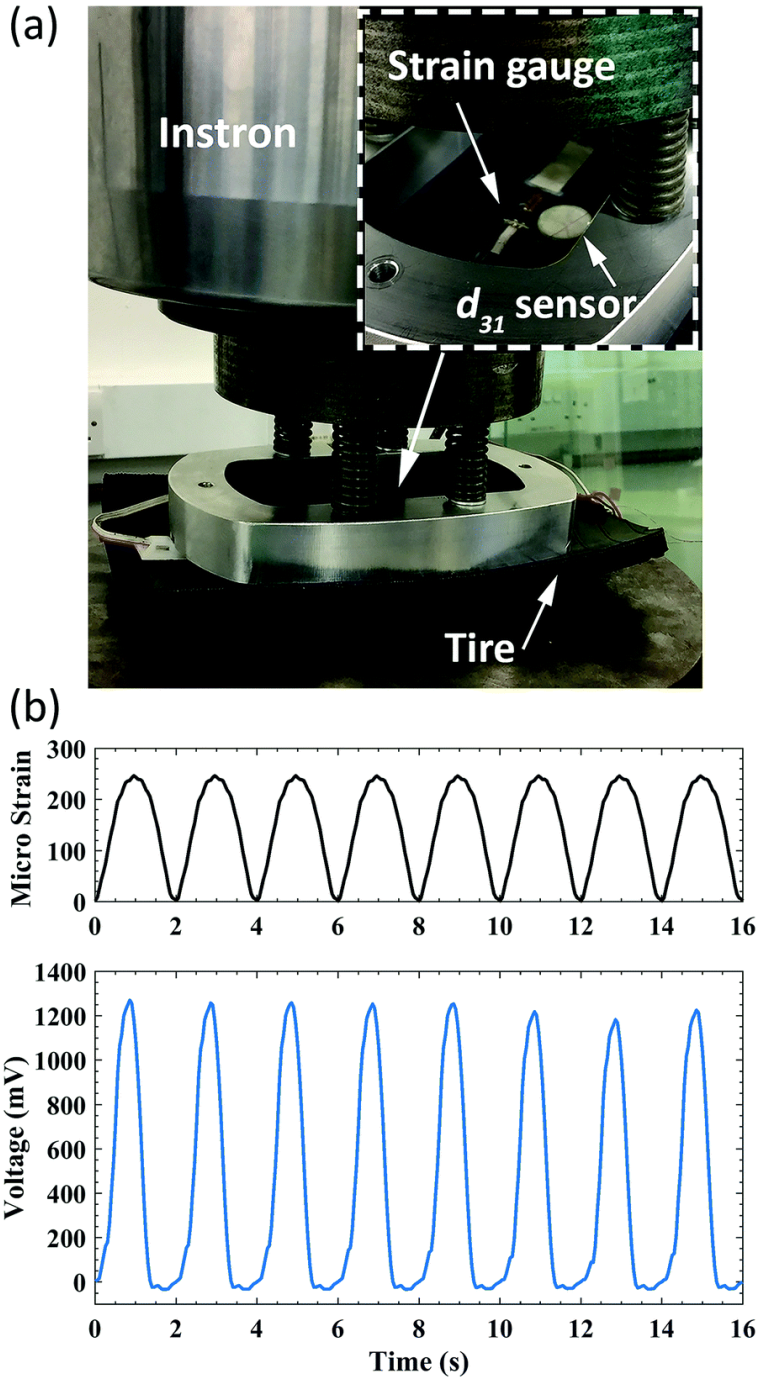

Figure 4-20: *d_{33} sensor measurement with part of a standard passenger vehicle tire. (a) The testing rig in the Instron dynamic test machine. (b) The strain of the tire side wall due to tire deformation and voltage response of the d_{31} sensor.*

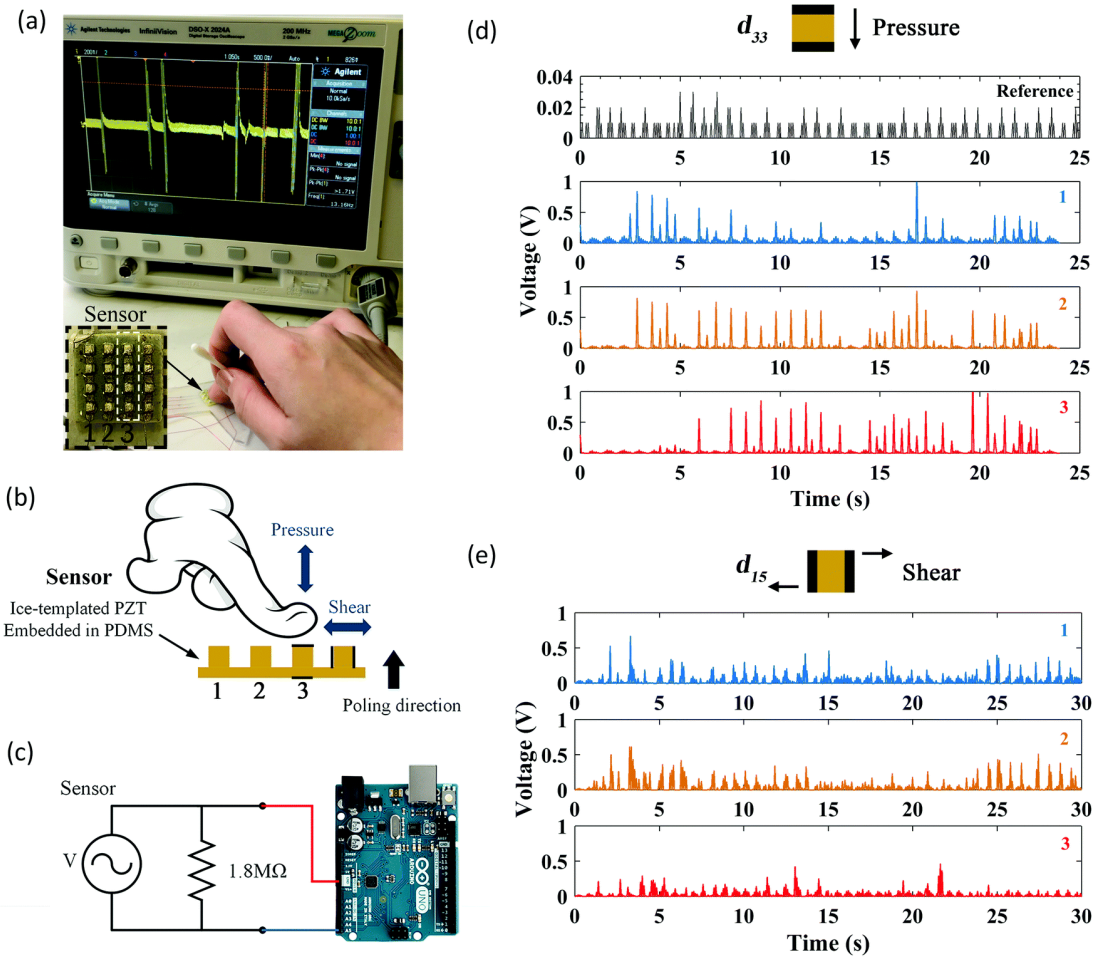

Figure 4-21: *d_{33} and d_{15} sensor array's response to light finger tapping and shearing and the study of sensor sensitivity. (a) Schematic of the finger tapping measurement, (b) d_{33} mode pressure sensor response with active single sensing line. (c) Schematic of the measurement circuit. (d) Voltage response of the d_{33} pressure sensor to light finger tapping (a reference voltage signal without touching, voltage response of sensor array 1, 2, 3 with light finger tapping and shearing). (e) Voltage response of d_{15} shear sensor to light finger shearing.*

and map the applied force. In order to characterize the response of the d_{33} and d_{15}-mode sensor array to light finger tapping and shearing, the tapping and shearing test was then performed with d_{33} and d_{15} sensor connected to the Arduino Uno development board. In the following experiment, we measured the responses of several sensing lines at the same time. The sensor was placed on desk and four sensing lines were connected to an Arduino UNO microcontroller board. Fig. 4-21c shows the circuit, where each sensing line was connected to the analog to digital converter (ADC) input and loaded with a 1.8 MΩ resistor. As one electrode was connected to ADC's input and second to common ground, the Arduino is not able to deliver the values of negative readings, thus the voltage responses in Fig. 4-21d and e are all positive. The sensor response of the d_{33}-mode pressure and d_{15}-mode shear sensor are shown in Fig. 4-21d and e respectively. For sensors in operation, it is important to have a 'zero' reference, hence the response without any finger tapping and shearing is shown in Fig. 4-21d. It can be noticed that there is small noise (voltage $<$ 20 mV) in the response signal during the tapping, which correspond to our previously shown reference signal. With further software development of sensing application this noise could be removed by extracting its reference signal from the sensors reading.

In addition, we studied the sensitivity of the d_{33} mode pressure and d_{15} mode shear sensors by investigating sensor voltage response to different accelerations and force. Sensors were attached to the "L" shape holders made of 0.9 mm thick steel plate with the use of PDMS solution, see Fig. 4-22a. For the d_{33} sensor a seismic mass was placed on the top using two zirconia masses with a total weight of 13 gram was placed, similarly at the end of the d_{15} sensor structure one zirconia bead of a 6 gram mass was placed as a tip mass. On the side of the holder, a reference accelerometer was placed and the sensor electrodes were connected with differential probes to the measuring oscilloscope.

Both type of sensors were tested with the acceleration levels from -3 to 3 g ($\pm$ 29.42 m/s^2, g = 9.8 m/s^2). Measurement results are presented in Fig. 4-22b and c for longitudinal mode test and shear mode respectively. For the shear mode sensor, the presented readout comes from only one (of four) pillar's, see Fig. 4-16c, while the response for longitudinal sensor is an output from all four electroded pillars (1, 2, 3 and 4) connected in parallel. Both sensing modes show excellent linearity in the presented measurement range and strong repeatability. In the acceleration region of 0.5–3 g the sensor sensitivity varies from ∼26.7 mV/g (445 mV/N) for a singular shear structure to up to ∼90.2 mV/g (694 mV/N) for the longitudinal sensing mode.

Finally, we demonstrate a real-time sensitive response of the pressure sensor in d_{33}-mode in *Video 2 (Supplement)*. This involved dropping a small mass of 0.1 g, half of a

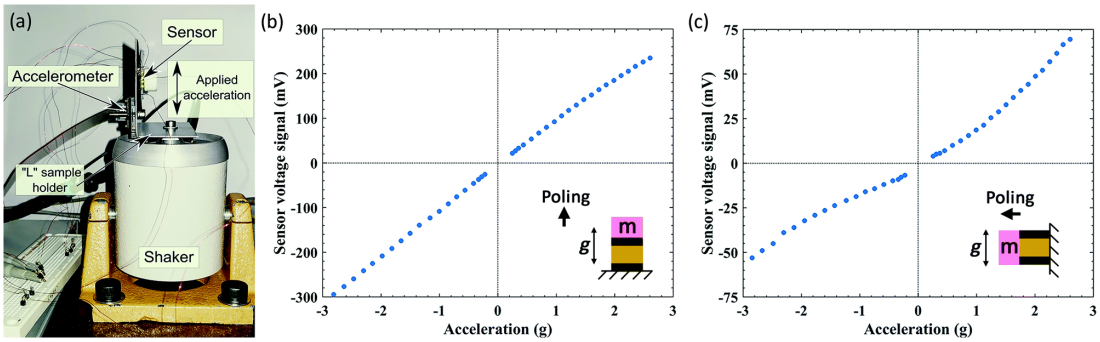

Figure 4-22: *Sensor sensitivity vs. acceleration/force. (a) Experimental setup of the sensor sensitivity measurement (vertical mount of "L" holder for shear sensor measurements). (b and c) Voltage response of the d_{33} sensor and d_{15} sensor to shaker acceleration (m is the seismic mass attached to the sensor).*

cotton bud, 2 cm above from the pressure sensor which is followed by a light sequence of finger tapings onto the pressure sensor. In the *Video 2 (Supplement)*, the drop of cotton bud with input potential energy of 1.96×10^{-5} J could generate a voltage of ∼200 mV. In combination with the sensitivity test, the touch test shows the ability of the sensor to detect light levels of excitation and the sensor's capability to distinguish the activated region. This could find a potential application in robotic arms for collision or handling detection. Moreover, as the manufacturing process allows creation of a variety of custom forms and shapes of the sensor it could be easily adjusted to the desired application, for example as a robotic skin with pressure and shear functionality.

4.1.8 Conclusions

We have demonstrated novel flexible and highly active selfpowered force sensor arrays based on highly active composites of lead zirconate titanate (PZT) and polydimethylsiloxane (PDMS). PZT ceramics with highly aligned pore channels have been prepared by freeze casting water-based PZT suspensions, with porosity levels of 50 vol%. The PZT–PDMS composites possess a high effective piezoelectric coefficient, $d_{33}*$ ∼750 pC/N, which is 110% times higher than dense PZT ceramics. This enhancement is due to the connectivity of active piezoelectric materials, and the combined effect of compression and flexure due to the elastomer. The sensor could be flexed to a radius of 8 mm and while continuing to exhibit high piezoelectric activity. The manufacturing approach is simple, but capable of producing complex device architectures. With these superior properties, sensors operating at different modes, e.g. longitudinal, transverse and shear, were fabricated and tested with tire, shaker and even light finger tapping. These sensors perform actively with high flexibility and stability compared to the tradi-

tional piezoelectric composites. These prototype PZT–PDMS sensors could be further reduced in scale by fabricating a master mold using methods such as a high-resolution 3D printer and readily configured to combine d_{33}, d_{31}, and d_{15} sensing modes into a single multi-axis sensor. This work therefore expands on the potential applications of freeze casting and provides new opportunities for the manufacture of future electronic sensors.

4.1.9 Experimental Section

Fabrication

Lead zirconate titanate powder (PZT-NCE55) was commercially available and purchased from Noliac and was used to prepare the water-based suspension. The suspension fabrication processes were introduced in our previous work [32] and the suspension was ball-milled for 24 hours in zirconia media to create a homogeneous and fine suspension. The PZT powder was dispersed in deionized water to form a suspension with solid loading level of 40 vol%, with polyvinyl alcohol and polyacrylic acid which served as the binder and dispersant respectively. The freezing rate was approximately 0.01 $^{\circ}C/\mu m$. The filament used for 3D printing was a common printing material acrylonitrile butadiene styrene. PDMS precursor (Sylgard 184A) and curing agent (Sylgard 184B) were purchased from Dow Corning Corp. The mixing ratio of the precursor and curing agent was 10:1. The templated PZT-ice sample was demolded and freeze-dried for 24 hours in a vacuum chamber of a freeze-dryer to sublimate the ice. The porous PZT structures were sintered at 1250°C for 2 hours and cool down naturally in a furnace. Then PZT was corona poled at 130°C for 15 min with a DC voltage of 14 kV. The poled PZT ceramics were then painted with silver electrodes and finally encapsulated in PDMS and cured in oven at 80°C for overnight.

Characterization

The microstructures of the sintered porous PZT ceramics were characterized with scanning electron microscopy (SEM, JSM6480LV, Tokyo, Japan). The porosity level of composite was derived from density data obtained by the Archimedes' method. The longitudinal piezoelectric charge coefficient d_{33} was measured using a Berlincourt Piezometer (PM25, Take Control, UK). Impedance and relative permittivity were measured with Solartron 1260 and 1296 Dielectric Interface. The polarization response of the composite materials was measured with Radiant RT66B-HVi Ferroelectric Test system.

Measurement

A shaker measurement rig was assembled with signal generator Agilent 33220A, Amplifier (Europower EP 1500) and Electrodynamic shaker BRÜEL & KJÆR LDS 201. The sample holder with tested sample was placed on the top of the shaker and excited in the z-axis with a peak amplitude of up to 3 g at constant frequency of 25 Hz. The longitudinal [d_{33}] sensor was placed horizontally on the shaker thus its excitation was parallel to the poling direction. The shear mode sensor [d_{15}], was mounted vertically on the shaker thus its excitation was orthogonal to the poling direction. The shaker with sample under test was placed in the shielded chamber to reduce the noise level upcoming from the mains power line. An analog accelerometer (Analog Devices ADXL316) embedded with the conditioning circuit to a custom-built PCB (Printed Circuit Board) board was mounted on the sample holder and used for reference. The measurement setup was controlled with the custom designed scripts in Python programming language responsible for control, gathering and storing of the test data to the PC files. Each measurement for a given acceleration level was repeated 10 times, and results presented are the average values from these measurements.

Supplementary Data

Electronic supplementary information (ESI) available: Videos of the responses of sensors. See DOI: 10.1039/c8ee01551a

Author Contributions

Dr Xie, Mr Kraśny and Prof. Bowen conceived and designed the experiment. Dr Xie designed sensor configurations, fabricated the sensor molds and PZT–PDMS sensors, performed flexibility test, finger tapping experiment and data processing. Dr Zhang fabricated the PZT–PDMS composite and sensors, performed poling and the d_{33} measurement of PZT–PDMS composite material. Dr Xie and Dr Yan performed microscopy. Mr Kraśny performed shaker experiment and data processing. Dr Khanbareh designed tire experimental setup. Mr Gathercole performed the d_31 experiment. Dr Xie and Prof. Bowen contributed to the general idea. Prof. Bowen supervised the work. Dr Xie, Mr Kraśny and Prof. Bowen contributed to the writing of the article. All authors contributed to the discussion of the article.

Acknowledgement

Dr M. Xie, Mr M. J. Kraśny, Mr N. Gathercole and Prof. C.R. Bowen, would like to acknowledge the funding from the European Research Council under the

European Union's Seventh Framework Programme (FP/2007–2013)/ERC Grant Agreement no. 320963 on Novel Energy Materials, Engineering Science and Integrated Systems (NEMESIS). Dr Y. Zhang would like to acknowledge the European Commission's Marie Skłodowska-Curie Actions (MSCA), through the Marie Skłodowska-Curie Individual Fellowships (IF-EF) (H2020-MSCA-IF-2015-EF-703950-HEAPPs) under Horizon 2020.

References

[1] C. R. Bowen, H. A. Kim, P. M. Weaver, and S. Dunn, "Piezoelectric and ferroelectric materials and structures for energy harvesting applications," *Energy & Environmental Science*, vol. 7, no. 1, pp. 25–44, Dec. 2013.

[2] C. R. Bowen, J. Taylor, E. LeBoulbar, D. Zabek, A. Chauhan, and R. Vaish, "Pyroelectric materials and devices for energy harvesting applications," *Energy & Environmental Science*, vol. 7, no. 12, pp. 3836–3856, Nov. 2014.

[3] Z. L. Wang, J. Chen, and L. Lin, "Progress in triboelectric nanogenerators as a new energy technology and self-powered sensors," *Energy & Environmental Science*, vol. 8, no. 8, pp. 2250–2282, Jul. 2015.

[4] Y. Yang, Y. Zhou, J. M. Wu, and Z. L. Wang, "Single Micro/Nanowire Pyroelectric Nanogenerators as Self-Powered Temperature Sensors," *ACS Nano*, vol. 6, no. 9, pp. 8456–8461, Sep. 2012.

[5] K. Zhang, S. Wang, and Y. Yang, "A One-Structure-Based Piezo-Tribo-Pyro-Photoelectric Effects Coupled Nanogenerator for Simultaneously Scavenging Mechanical, Thermal, and Solar Energies," *Advanced Energy Materials*, vol. 7, no. 6, p. 1601852, 2017.

[6] R. Zhang, B. Jiang, and W. Cao, "Elastic, piezoelectric, and dielectric properties of multidomain 0.67Pb(Mg1/3Nb2/3)O3–0.33PbTiO3 single crystals," *Journal of Applied Physics*, vol. 90, no. 7, pp. 3471–3475, Oct. 2001.

[7] G.-T. Hwang, Y. Kim, J.-H. Lee, S. Oh, C. K. Jeong, D. Y. Park, J. Ryu, H. Kwon, S.-G. Lee, B. Joung, D. Kim, and K. J. Lee, "Self-powered deep brain stimulation via a flexible PIMNT energy harvester," *Energy & Environmental Science*, vol. 8, no. 9, pp. 2677–2684, Aug. 2015.

[8] G.-T. Hwang, H. Park, J.-H. Lee, S. Oh, K.-I. Park, M. Byun, H. Park, G. Ahn, C. K. Jeong, K. No, H. Kwon, S.-G. Lee, B. Joung, and K. J. Lee, "Self-Powered Cardiac Pacemaker Enabled by Flexible Single Crystalline PMN-PT Piezoelectric Energy Harvester," *Advanced Materials*, vol. 26, no. 28, pp. 4880–4887, 2014.

[9] T. I. Lee, W. S. Jang, E. Lee, Y. S. Kim, Z. L. Wang, H. K. Baik, and J. M. Myoung, "Ultrathin self-powered artificial skin," *Energy & Environmental Science*, vol. 7, no. 12, pp. 3994–3999, Nov. 2014.

[10] N. R. Alluri, S. Selvarajan, A. Chandrasekhar, B. Saravanakumar, J. H. Jeong, and S.-J. Kim, "Piezoelectric BaTiO3/alginate spherical composite beads for energy harvesting and self-powered wearable flexion sensor," *Composites Science and Technology*, vol. 142, pp. 65–78, Apr. 2017.

[11] Y. Mao, P. Zhao, G. McConohy, H. Yang, Y. Tong, and X. Wang, "Sponge-Like Piezoelectric Polymer Films for Scalable and Integratable Nanogenerators and Self-Powered Electronic Systems," *Advanced Energy Materials*, vol. 4, no. 7, p. 1301624, 2014.

[12] T. Sharma, S.-S. Je, B. Gill, and J. X. J. Zhang, "Patterning piezoelectric thin film PVDF–TrFE based pressure sensor for catheter application," *Sensors and Actuators A: Physical*, vol. 177, pp. 87–92, Apr. 2012.

[13] A. Safari, M. Allahverdi, and E. K. Akdogan, "Solid freeform fabrication of piezoelectric sensors and actuators," *Journal of Materials Science*, vol. 41, no. 1, pp. 177–198, Jan. 2006.

[14] H.-J. Chen, S. Han, C. Liu, Z. Luo, H.-P. D. Shieh, R.-S. Hsiao, and B.-R. Yang, "Investigation of PVDF-TrFE composite with nanofillers for sensitivity improvement," *Sensors and Actuators A: Physical*, vol. 245, pp. 135–139, Jul. 2016.

[15] X. Chen, X. Li, J. Shao, N. An, H. Tian, C. Wang, T. Han, L. Wang, and B. Lu, "High-Performance Piezoelectric Nanogenerators with Imprinted P(VDF-TrFE)/BaTiO3 Nanocomposite Micropillars for Self-Powered Flexible Sensors," *Small*, vol. 13, no. 23, p. 1604245, 2017.

[16] M. Lee, J. Bae, J. Lee, C.-S. Lee, S. Hong, and Z. L. Wang, "Self-powered environmental sensor system driven by nanogenerators," *Energy & Environmental Science*, vol. 4, no. 9, pp. 3359–3363, Aug. 2011.

[17] M. Lee, C.-Y. Chen, S. Wang, S. N. Cha, Y. J. Park, J. M. Kim, L.-J. Chou, and Z. L. Wang, "A Hybrid Piezoelectric Structure for Wearable Nanogenerators," *Advanced Materials*, vol. 24, no. 13, pp. 1759–1764, 2012.

[18] K.-I. Park, M. Lee, Y. Liu, S. Moon, G.-T. Hwang, G. Zhu, J. E. Kim, S. O. Kim, D. K. Kim, Z. L. Wang, and K. J. Lee, "Flexible Nanocomposite Generator Made of BaTiO3 Nanoparticles and Graphitic Carbons," *Advanced Materials*, vol. 24, no. 22, pp. 2999–3004, 2012.

[19] R. E. Newnham, D. P. Skinner, and L. E. Cross, "Connectivity and piezoelectric-pyroelectric composites," *Materials Research Bulletin*, vol. 13, no. 5, pp. 525–536, May 1978.

[20] G. Zhang, P. Zhao, X. Zhang, K. Han, T. Zhao, Y. Zhang, C. K. Jeong, S. Jiang, S. Zhang, and Q. Wang, "Flexible three-dimensional interconnected piezoelectric ceramic foam based composites for highly efficient concurrent mechanical and thermal energy harvesting," *Energy & Environmental Science*, vol. 11, no. 8, pp. 2046–2056, Aug. 2018.

[21] D. B. Deutz, N. T. Mascarenhas, J. B. J. Schelen, D. M. de Leeuw, S. van der Zwaag, and P. Groen, "Flexible Piezoelectric Touch Sensor by Alignment of Lead-Free Alkaline Niobate Microcubes in PDMS," *Advanced Functional Materials*, vol. 27, no. 24, p. 1700728, 2017.

[22] Y. Zhao, Q. Liao, G. Zhang, Z. Zhang, Q. Liang, X. Liao, and Y. Zhang, "High output piezoelectric nanocomposite generators composed of oriented BaTiO3 NPs@PVDF," *Nano Energy*, vol. 11, pp. 719–727, Jan. 2015.

[23] Y. Song, Y. Shen, H. Liu, Y. Lin, M. Li, and C.-W. Nan, "Enhanced dielectric and ferroelectric properties induced by dopamine-modified BaTiO3 nanofibers in flexible poly(vinylidene fluoride-trifluoroethylene) nanocomposites," *Journal of Materials Chemistry*, vol. 22, no. 16, pp. 8063–8068, Mar. 2012.

[24] S. Xu, Y.-w. Yeh, G. Poirier, M. C. McAlpine, R. A. Register, and N. Yao, "Flexible Piezoelectric PMN–PT Nanowire-Based Nanocomposite and Device," *Nano Letters*, vol. 13, no. 6, pp. 2393–2398, Jun. 2013.

[25] Z. Zhou, H. Tang, and H. A. Sodano, "Vertically Aligned Arrays of BaTiO3 Nanowires," *ACS Applied Materials & Interfaces*, vol. 5, no. 22, pp. 11 894–11 899, Nov. 2013.

[26] F. Felten, G. A. Schneider, J. M. Saldaña, and S. V. Kalinin, "Modeling and measurement of surface displacements in BaTiO3 bulk material in piezoresponse force microscopy," *Journal of Applied Physics*, vol. 96, no. 1, pp. 563–568, Jul. 2004.

[27] I. Kanno, K. Akama, K. Wasa, and H. Kotera, "Evaluation of Intrinsic Shear Piezoelectric Coefficient d15 of c-Axis Oriented Pb(Zr,Ti)O3 Films," *Applied Physics Express*, vol. 2, no. 9, p. 091402, Sep. 2009.

[28] T. R. Licht, H. Andersen, and H. B. Jensen, "Recent Developments in Accelerometer Design," *Bruel Kjaer Technical Review*, vol. 2, no. 1, pp. 1–22, 1987.

[29] R. E. Newnham, A. Safari, J. Giniewicz, and B. H. Fox, "Composite piezoelectric sensors," *Ferroelectrics*, vol. 60, no. 1, pp. 15–21, Oct. 1984.

[30] S. Deville, E. Saiz, R. K. Nalla, and A. P. Tomsia, "Freezing as a Path to Build Complex Composites," *Science*, vol. 311, no. 5760, pp. 515–518, Jan. 2006.

[31] J. F. Tressler, S. Alkoy, and R. E. Newnham, "Piezoelectric Sensors and Sensor Materials," *Journal of Electroceramics*, vol. 2, no. 4, pp. 257–272, Dec. 1998.

[32] Y. Zhang, M. Xie, J. Roscow, Y. Bao, K. Zhou, D. Zhang, and C. R. Bowen, "Enhanced pyroelectric and piezoelectric properties of PZT with aligned porosity for energy harvesting applications," *Journal of Materials Chemistry A*, vol. 5, no. 14, pp. 6569–6580, Apr. 2017.

[33] Y. Zhang, Y. Bao, D. Zhang, and C. R. Bowen, "Porous PZT Ceramics with Aligned Pore Channels for Energy Harvesting Applications," *Journal of the American Ceramic Society*, vol. 98, no. 10, pp. 2980–2983, Oct. 2015.

[34] D. Fuard, T. Tzvetkova-Chevolleau, S. Decossas, P. Tracqui, and P. Schiavone, "Optimization of poly-di-methyl-siloxane (PDMS) substrates for studying cellular adhesion and motility," *Microelectronic Engineering*, vol. 85, no. 5, pp. 1289–1293, May 2008.

[35] L. J. Nelson, C. R. Bowen, R. Stevens, M. Cain, and M. Stewart, "High field behaviour of piezoelectric fibre composites," *Proceedings of SPIE - The International Society for Optical Engineering*, vol. 5053, pp. 544–555, 2003.

[36] C. Racles, A. Bele, M. Dascalu, V. E. Musteata, C. D. Varganici, D. Ionita, S. Vlad, M. Cazacu, S. J. Dünki, and D. M. Opris, "Polar–nonpolar interconnected elastic networks with increased permittivity and high breakdown fields for dielectric elastomer transducers," *RSC Advances*, vol. 5, no. 72, pp. 58 428–58 438, Jul. 2015.

[37] D. Armani, C. Liu, and N. Aluru, "Re-configurable fluid circuits by PDMS elastomer micromachining," in *Technical Digest. IEEE International MEMS 99 Conference. Twelfth IEEE International Conference on Micro Electro Mechanical Systems (Cat. No.99CH36291)*, Jan. 1999, pp. 222–227.

[38] D. W. Inglis, "A method for reducing pressure-induced deformation in silicone microfluidics," *Biomicrofluidics*, vol. 4, no. 2, p. 026504, Jun. 2010.

[39] X. Wu, Y. Ma, G. Zhang, Y. Chu, J. Du, Y. Zhang, Z. Li, Y. Duan, Z. Fan, and J. Huang, "Thermally Stable, Biocompatible, and Flexible Organic Field-Effect Transistors and Their Application in Temperature Sensing Arrays for Artificial Skin," *Advanced Functional Materials*, vol. 25, no. 14, pp. 2138–2146, 2015.

[40] A. M. Gaikwad, G. L. Whiting, D. A. Steingart, and A. C. Arias, "Highly Flexible, Printed Alkaline Batteries Based on Mesh-Embedded Electrodes," *Advanced Materials*, vol. 23, no. 29, pp. 3251–3255, 2011.

[41] M. Ramuz, B. C.-K. Tee, J. B.-H. Tok, and Z. Bao, "Transparent, Optical, Pressure-Sensitive Artificial Skin for Large-Area Stretchable Electronics," *Advanced Materials*, vol. 24, no. 24, pp. 3223–3227, 2012.

[42] T. Adrega and S. P. Lacour, "Stretchable gold conductors embedded in PDMS and patterned by photolithography: Fabrication and electromechanical characterization," *Journal of Micromechanics and Microengineering*, vol. 20, no. 5, p. 055025, Apr. 2010.

4.2 Summary

Both papers provide case studies on the effect of introducing porosity into ferroelectric ceramics as a method to improve their energy harvesting capabilities. Freeze-casting is a successful method for controlled alignment of pores which was confirmed experimentally with the manufacture of a highly aligned porous barium titanate that exhibited improved energy harvesting properties compared to a dense barium titanate ceramic.

The work was then further expanded by presentation of an active composites of lead zirconate titanate (PZT) and PDMS in novel flexible and self-powered force sensor arrays. Measurement of the piezoelectric coefficient d_{33} showed a 10% increase (670 pC/N to 750 pC/N) in comparison to dense ceramic, and a 70% increase (440 pC/N to 750 pC/N) in comparison to porous material after freeze-casting.

This work therefore proposes a fundamental and counter-intuitive change in piezoelectric materials manufacturing, where reduced amount of active material improves the overall active performance of a final device (*"less is more"*). This expands on the potential applications of fragile piezoelectric ceramics, opening new opportunities for the manufacture of future electronic sensors and energy harvesting devices.

CHAPTER 5

IMPROVED MECHANICAL HARVESTER

5.1 Prologue

The most used mechanical structure exploited in energy harvesting applications is a resonant cantilever beam, where harvesting performance is heavily reduced if a device is not vibrated at the resonant frequencies of the structure. This mechanical characteristic results in the need for the cantilever beam to be tuned for a specific vibration frequency. As highlighted in Chapter 1, broadening of the applicable frequency range of mechanical structures for energy harvesting applications is a common research field explored in recent studies since many ambient forms of vibrations include a wide range of frequencies.

The final research paper presented in this thesis investigates mechanical structure improvements on the performance of a cantilever based piezoelectric energy harvesting device. Adjustments in the mechanical structure are achieved to increase the electrical power harvested using a novel mechanical structure which offers bend-twist coupling.

Paper 5: Statement of Authorship

<table>
<tr><td colspan="10">This declaration concerns the article entitled:</td></tr>
<tr><td colspan="10">Energy harvesting from coupled bending-twisting oscillations in carbon-fibre reinforced polymer laminates</td></tr>
<tr><td colspan="10">Publication status (tick one)</td></tr>
<tr><td>Draft manuscript</td><td></td><td>Submitted</td><td></td><td>In review</td><td></td><td>Accepted</td><td></td><td>Published</td><td>✓</td></tr>
<tr><td colspan="10">Copyright status (tick the appropriate statement)</td></tr>
<tr><td colspan="3">I hold the copyright for this material</td><td></td><td colspan="5">Copyright is retained by the publisher, but I have been given permission to replicate the material here</td><td>✓</td></tr>
<tr><td>Publication details (reference)</td><td colspan="9">M. Xie, Y. Zhang, M. J. Kraśny, A. Rhead, C. Bowen, and M. Arafa,
“Energy harvesting from coupled bending-twisting oscillations in carbon-fibre reinforced polymer laminates”,
Mechanical Systems and Signal Processing, vol. 107, pp. 429–438, Jul. 2018,
DOI: 10.1016/j.ymssp.2018.01.026.</td></tr>
<tr><td>Candidate’s contribution to the paper (detailed and also given as percentage)</td><td colspan="9">Formulation of ideas:
M. Xie, Y. Zhang, C. Bowen and candidate (25%).

Design of methodology:
Cooperative work between Dr. Xie, Prof. Bowen and candidate (33%).

Experimental work:
Cantilever structure and design by Dr A.Rhead.
Model provided by Prof. M. Arafa,
Shaker experiment and data processing by candidate (100%).

Presentation of data in journal format:
Equal contribution from Dr Xie, Prof. M. Arafa, Prof. Bowen and candidate (25%).</td></tr>
<tr><td>Statement from Candidate</td><td colspan="9">This paper reports original research I conducted during the period of my Higher Degree by Research candidature.</td></tr>
<tr><td>Signed</td><td colspan="5">  </td><td>Date</td><td colspan="3">08.08.2020</td></tr>
</table>

Energy Harvesting from Coupled Bending-Twisting Oscillations in Carbon-Fibre Reinforced Polymer Laminates

Mengying Xie[(1)], Yan Zhang[(1)], Marcin J. Kraśny[(1)], Andrew Rhead[(1)], Chris R. Bowen[(1)], Mustafa Arafa[(2)],

[(1)] Department of Mechanical Engineering, University of Bath, Bath A2 7AY, UK
[(2)] Department of Electrical Engineering, American University in Cairo, Egypt

Abstract

The energy harvesting capability of resonant harvesting structures, such as piezoelectric cantilever beams, can be improved by utilizing coupled oscillations that generate favourable strain mode distributions. In this work, we present the first demonstration of the use of a laminated carbon fibre reinforced polymer to create cantilever beams that undergo coupled bending-twisting oscillations for energy harvesting applications. Piezoelectric layers that operate in bending and shear mode are attached to the bend-twist coupled beam surface at locations of maximum bending and torsional strains in the first mode of vibration to fully exploit the strain distribution along the beam. Modelling of this new bendtwist harvesting system is presented, which compares favourably with experimental results. It is demonstrated that the variety of bend and torsional modes of the harvesters can be utilized to create a harvester that operates over a wider range of frequencies and such multi-modal device architectures provides a unique approach to tune the frequency response of resonant harvesting systems.

Keywords

piezoelectric, energy harvesting, bend-twist coupling, lumped-parameter model, composite

5.1.1 Introduction

The conversion of mechanical vibrations into useful electrical energy has been a subject of intensive research due to its application in self-powered sensors and wireless systems.

A common architecture for vibration-based energy harvesting devices is a base-excited elastic structure, such as a mass-spring system or a cantilever beam, which is typically used in conjunction with electromagnetic and piezoelectric devices. One of the challenges in designing continuous systems, such as beams and plates, for piezoelectric energy harvesting applications lies in the placement of the energy generating materials, which are usually piezoelectric sheets or layers that are bonded or embedded within a host structure. These structures often have unique strain distributions in their vibration modes, and the highly strained parts of the structure that are most effective for energy harvesting occur only in localized regions. The placement of the energy generation materials at such discrete locations while leaving other parts of the structure uncovered causes the structure to be partially utilized for energy harvesting, which lowers the power density. This is the case, for example, for a cantilever beam undergoing flexural vibration at its first bending mode, where maximum strain occurs near the root. To overcome this difficulty, systems that operate across multiple vibration modes have been proposed [1, 2] in order to utilize two or more vibration mode shapes for energy harvesting. The exploitation of more than one vibration mode also enables the device to harvest vibrations over a wider frequency range since in many cases the ambient vibrations to be harvested often span a range of frequencies and amplitudes.

Vibration modes involving mixed deformations, in particular bending and twisting motions, are particularly appealing in this respect since these motions can be controlled by design of the harvesting structure. The study of coupled bend-twist oscillations has been of interest to the aeronautical engineering community for decades owing to its application in the vibration analysis of aircraft wings and rotating turbine blades. Recent interest in morphing structures has spurred research in the use of piezoelectric actuators to achieve a controlled bend-twist deformation [3, 4, 5]. The use of bend-twist oscillations in energy harvesting applications is relatively recent. In this context, reference is made to the work of Abdelkefi *et al.* [6] who designed a unimorph cantilever beam undergoing bending–torsion vibrations consisting of a single piezoelectric layer and two asymmetric tip masses, thereby generating a twisting moment from a base excitation. This structure was tuned to provide a broader band energy harvester by adjusting the first two global natural frequencies to be relatively close to each other. Reference is also made to the work of Gao *et al.* [7] in which torsional vibration at the second mode of a cantilever beam with an eccentric proof mass was employed for energy harvesting using a lead zirconate titanate (PZT) material. The main advantages of this design approach were the small displacement amplitudes and low natural frequency. Shan *et al.* [8] employed vortex-induced vibrations to design a piezoelectric energy harvester with bending-torsion vibration.

An effective way of designing structures with inherent bend-twist coupling behaviour is the use of composite laminates. By tailoring the laminate lay-up these anisotropic structures can be deliberately designed to exhibit interactions between extension, shear, bending and twisting [9], which are not present in conventional isotropic materials. In this work, we shall employ for the purpose of energy harvesting, a laminated carbon fibre reinforced polymer (CFRP) composite cantilever beam that has a laminate lay-up that is selected to achieve coupled bending and twisting deformations. Specifically, this includes the use of a laminate with an unbalanced stacking sequence in which not all plies with a positive rotation in the stacking sequence have a counterpart ply with an equal and negative rotation. Such an unbalanced structure introduces extension-shear coupling and when the laminate (or a single ply with fibres misaligned with the load direction) is subject to a unaxial tensile or compressive load it will attempt to shear. The sign of the shear is dependent on whether the load is tensile or compressive. Under a bending deformation, loading changes from being compressive on one side of the neutral axis to tensile on the other and this leads to plies on opposite surfaces attempting to shear in opposite directions, thereby resulting in twisting of the laminate. This approach is particularly attractive since it removes the need for more complex design configurations; such as the use of an eccentric proof mass or asymmetric tip masses. The ability to tailor the bend-twist coupled laminate architecture also provides scope for a wide design space to tailor the cantilever response to the vibration spectrum being harvested. To utilize larger portions of the beam for power generation, we employ two different types of PZT materials that are attached to the beam's surface. One PZT patch (MFC M8557-P1) responds to uniaxial straining (extension-mode) since the active piezoelectric material is aligned along its length and is placed close to the beam's root for effective harvesting of the bending mode. The other material (MFC M8557-F1) operates in the shear-mode, and in this case the piezoelectric is aligned at 45° to its length, and is placed along the beam's mid span where torsional shear strains are higher. This effort is expected to eventually yield energy harvesting devices with greater power densities, and greater bandwidths which are increasingly in high demand for small sensors and other applications where miniaturization is of the essence.

The remainder of this paper is organized into four sections. Section 5.1.2 details the fabrication of the laminated composite beams. Section 5.1.3 presents a mechanical model of the device and provides an analysis of its frequency response. Experimental work is carried out in Section 5.1.4. Finally, Section 5.1.5 is dedicated to conclusions and recommendations.

5.1.2 Fabrication of Composite Bend-Twist Laminate

The cantilever beam used in this work was made of unidirectional CFRP plies (Cytec MTM 49-3/T800HB-140-36%). Plies were laid down by hand in the order of the stacking sequence with debulking under vacuum applied after every 4^{th} ply to remove air pockets. Once all plies were laid the laminate was cured in an autoclave at 125° with a pressure of 7 bar for 2 h using a vacuum bag moulding process. A rigid aluminium plate was placed on top of the laminate and a flexible 3 mm thick silicone rubber sheet were used at bottom and top to form smooth outer surfaces. Fig. 5-1 shows a schematic of the cantilever beam, together with its dimensions and the position of the piezoelectric patches. The cantilever consists of 10 symmetric plies with the layup of $[0, 30, 0, 45, -45]_s$, where 0° ply is along the span of the beam. This laminate system was chosen

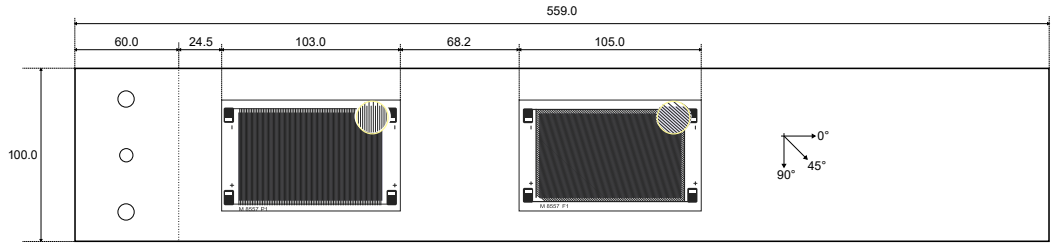

Figure 5-1: *Schematic of the cantilever beam and position of piezo-patches. The cantilever was clamped at left hand side. Near the root the piezoelectric element was a MFC M8557-P1 (uniaxial mode), and an MFC M8557-F1 (shear mode) at the mid-span.*

since (i) the symmetric nature of the laminate ensures that it will remain flat and warp free after high temperature curing, and (ii) to achieve bend-twist coupling the laminate should have an unbalanced lay-up, as described above. The width of the cantilever beam was 100 mm and the thickness was 1.45 mm after curing. The beam had a free length of 499 mm with an additional 60 mm for clamping between two aluminium plates.

The PZT materials used in this work are Macro Fibre Composites (MFC) which consist of PZT fibres embedded in an epoxy matrix with interdigitated electrodes. One PZT patch (Smart Material, MFC M8557-P1) responds to uniaxial straining, with piezoelectric fibres aligned along its length, was placed close to the beam's root (at a distance of 24.5 mm from the beam's fixation, as shown in Fig. 5-1). The second patch (Smart Material, MFC M8557-F1) operates in the shear-mode where the piezoelectric fibres in the MFC are at 45° to its length axis. This MFC was placed along the beam's mid span (at a distance of 68.2 mm from the root patch, as shown in Fig. 5-1) where torsional shear strains are higher.

The stiffness of the cantilever beam was experimentally determined by statically

loading a clamped-free beam at centre of its tip on an Instron 3365 tensile testing machine equipped with a 100 N load cell, while measuring the tip deflection, which is labelled as x in Fig. 5-4. Fig. 5-2 shows the resulting force-deflection behaviour, which clearly indicates a linear relationship up to 50 mm of deflection, which corresponds to almost 3 N of applied force.

Due to the bend-twist coupling, the tip of the beam developed an angle of twist θ that increased with the tip displacement, as shown in Fig. 5-3a. Fig. 5-3b demonstrates

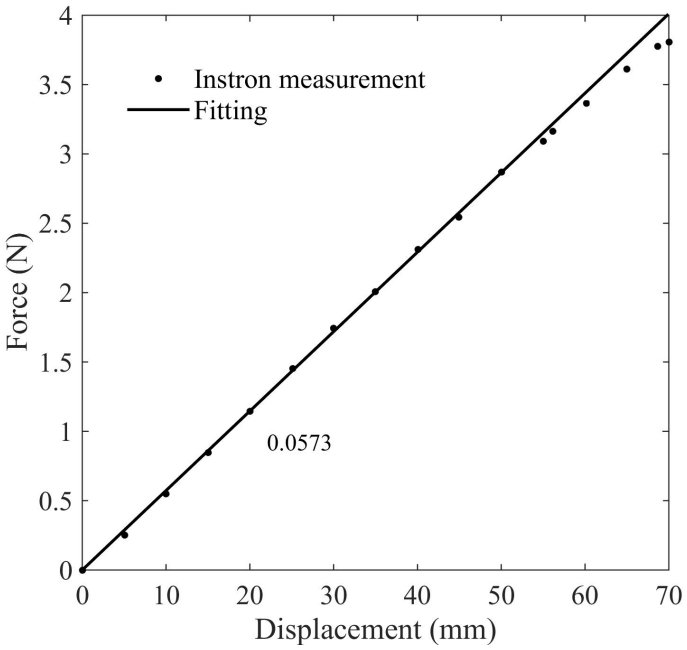

Figure 5-2: *Force-deflection curve of cantilever indicating a linear response for a deflection up to 50 mm (∼3 N).*

that for deflections less than 50 mm, the twisting angle increased linearly with displacement, which correlates with the force-displacement observations. It can be noticed when the displacement was zero, the tip of the beam had small twist, which is a result of the residual stresses in the laminate due to unbalanced layup. However, both force and angle had a nonlinear behaviour at displacements above 50 mm, and beyond 50 mm twisting became more obvious than bending.

5.1.3 Mechanical Model

Fig. 5-4 shows a schematic of the cantilever beam with the two PZT patches undergoing bending and twisting deflections. While structures undergoing coupled bend-twist deformations are essentially two dimensional, the aim of this work is to develop a sim-

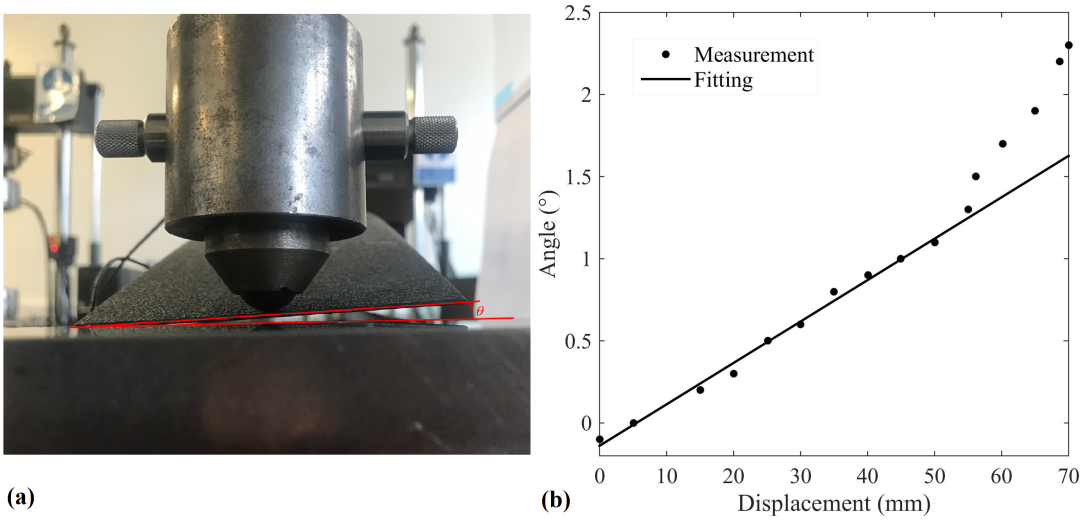

Figure 5-3: *Bend-twist coupling of the cantilever beam. (a) Image of cantilever undergoing bend-twist coupling, θ is the twisting displacement (b) Relationship between twisting angle and deflection (linear below 50 mm, slope = 0.0252 °/mm).*

plified lumped-parameter model to enable the analysis of the system as a two degree of freedom (2-DOF) model. In this way, the transverse displacement x of the centroid of the cross-section at the tip, and the angular displacement θ of the tip section are taken as representative degrees of freedom that designate bending and twisting deformations of the cantilever beam, respectively.

The laminated composite beam is modelled as an equivalent rigid body of mass m and mass moment of inertia I, as shown in Fig. 5-5. The body is attached to a base by a rigid massless arm of length l. A linear spring of stiffness k connects the mass to the base, whereas a torsional spring of stiffness k_T connects the mass to the link. This simplified model provides some physical insight into the problem and allows a study of the effect of the individual design parameters on the system response. The beam is modeled as a 2-DOF mass that undergoes coupled bend-twist oscillations. The bending displacement is denoted by x and resembles the transverse displacement of the beam tip. The twist displacement is denoted by θ and represents the angle of twist of the beam tip cross-section under no external torsional loads. Both degrees of freedom are piezoelectrically coupled and the electrical outputs are connected to resistive loads.

The total kinetic energy of the system is given by:

$$T = \frac{1}{m} m\dot{x}^2 + \frac{1}{2} I(\dot{\theta} + \dot{\phi})^2 \tag{5.1}$$

where m and I are the effective mass and mass moment of inertia, respectively, and the

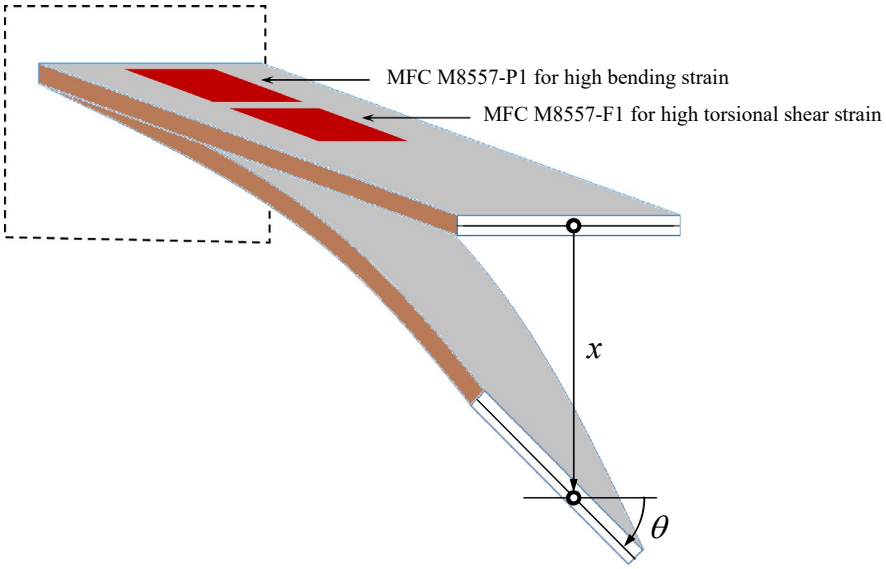

Figure 5-4: *Schematic of a deformed of cantilever beam of a rectangular cross-section undergoing a coupled bend-twist deformation pattern featured by a transverse displacement x and an angle of twist θ of the tip cross section.*

angle ϕ represents the cross-section rotation due to torsional loads. These will typically arise as a result of backward coupling twisting moments generated by the torsional MFC M8557-F1 patches. From geometry, it can be observed that:

$$(x - y) = l\theta \tag{5.2}$$

where l denotes the arm length that designates the inherent bend-twist coupling. Eq. 5.1 can hence be expressed as:

$$T = \frac{1}{2}m\dot{x}^2 + \frac{1}{2}I(\frac{\dot{x}}{l} - \frac{\dot{y}}{l} + \dot{\theta})^2 \tag{5.3}$$

The total strain energy of the system is given by:

$$V = \frac{1}{2}k(x - y)^2 + \frac{1}{2}k_T\phi^2 \tag{5.4}$$

where k_T is the torsional stiffness of the beam. Using Lagrange's equations, the equations of motion of the system are obtained as:

$$\begin{bmatrix} m + I/l^2 & I/l \\ I/l & I \end{bmatrix} \begin{Bmatrix} \ddot{x} \\ \ddot{\phi} \end{Bmatrix} + \begin{bmatrix} k & 0 \\ 0 & k_T \end{bmatrix} \begin{Bmatrix} x \\ \phi \end{Bmatrix} = \begin{Bmatrix} ky + I\ddot{y}/l^2 \\ I\ddot{y}/l \end{Bmatrix} \tag{5.5}$$

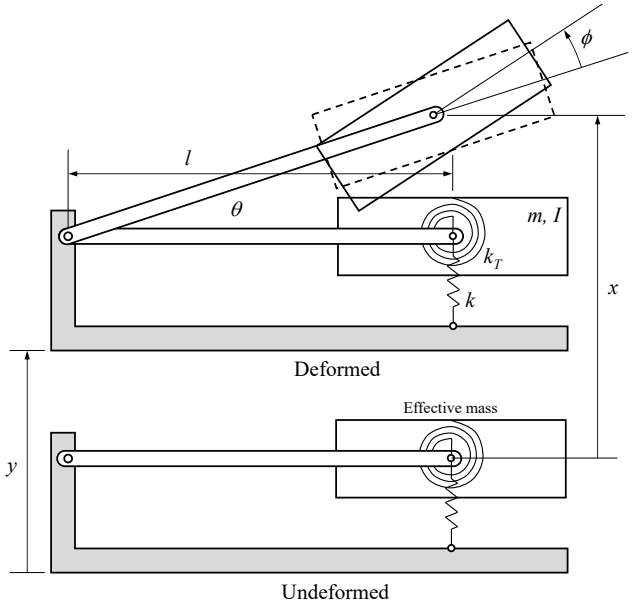

Figure 5-5: *Lumped-parameter model of the bend-twist coupled system.*

Eq. 5.5 can be written in a general form as:

$$[M]\left\{\ddot{\delta}\right\} + [K]\{\delta\} = \{F\} \tag{5.6}$$

Damping is arbitrarily introduced through a proportional damping matrix in the form:

$$[C] = \alpha[M] + \beta[K] \tag{5.7}$$

where α and β are damping coefficients for the mass and stiffness matrices, respectively. Eq. 5.7 describes the mechanical behaviour of the beam and can be used to obtain the steady-state response under a sinusoidal base excitation of the form $y(t) = Y sin\omega t$. The system parameters are obtained from experimental observations and, whenever possible, from equivalent lumped-parameter models. Table 5.1 lists the parameters used in this study. Values of the damping coefficients α and β have been chosen to provide quality factors match those observed experimentally.

5.1.4 Experimental Work

The MFC device is a flexible lead zirconate titanate (PZT) based sheet of aligned rectangular piezoelectric fibres sandwiched between epoxy layers and interdigitated electrodes with a manufacturer's specified capacitance of 12.84 nF and 13.26 nF for M8557-P1 and M8557-F1, respectively [10]. The M8557-P1 patch is designed to be affected by

Table 5.1: *System parameters.*

Parameter	Value	
m	35.28	g
I	$5 \cdot 10^{-5}$	kgm^2
l	2.3	m
k	57	N/m
k_T	4	Nm/rad
α	3	
β	0	

expanding motion (extension-mode), while M8557-F1 with fibres rotated at 45° to the root was used to respond to the beam's twisting motion (shear-mode).

The cantilever beam was mounted vertically on to an electrodynamic shaker (LDS V455) by two aluminium plates. Fig. 5-6a shows a schematic of the experimental setup and Fig. 5-6b shows an image of the system, along with the cantilever beam. An electrodynamic shaker was controlled by an amplified (LDS PA 1000) signal generated by NI USB-6211 (National Instruments) with a dedicated LabView script. The shaker system was calibrated using a Lab View routine to provide constant acceleration at the desired range of frequencies. An LDS 455 shaker was calibrated by exciting the shaker with a sine wave of controlled amplitude and frequency running through the LDS PA 1000 amplifier. A matrix of voltage amplitudes and frequencies was sent to the shaker, and the response was measured using a Polytech laser differential Vibrometer which then measured the velocity using the PSV-400-M4 scanning head, OFV-5000 controller and VD-09 velocity decoder. The peak acceleration was calculated from the velocity data and saved in the calibration file using a LabView routine running on a computer. When a specific acceleration is required at a desired frequency, another routine interpolates between the nearest voltages to deliver the needed acceleration magnitude [11].

The electrical output from the MFCs was connected to electrical load, set by resistance decade (JJ JUNIOR Resistance Decade from Educational Measurements Ltd). Finally, the signal was gathered by oscilloscope (Agilent Infiniium 54835A with 10 MΩ/10 pF TEK P6137 oscilloscope probe).

The power output from the MFC patches was determined from the equation,

$$P_{OUT} = U_{RMS}^2 / R_L \tag{5.8}$$

where U_{RMS} is the root mean square of the voltage output across the load resistor and R_L is electrical resistance of the load resistor; in this case R_L=10 kΩ.

The power output generated by the MFC piezoelectric materials is sensitive to the

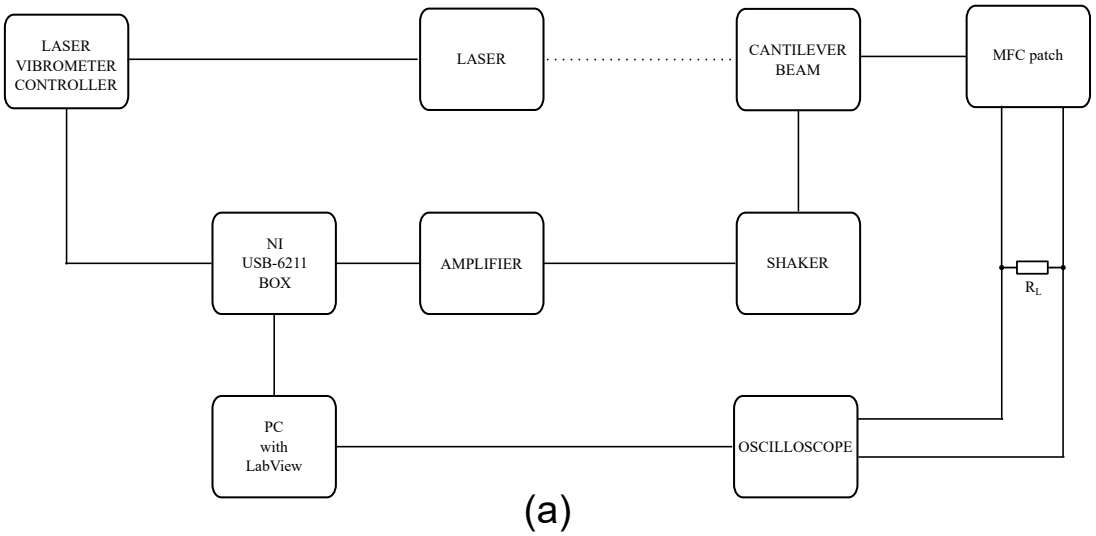

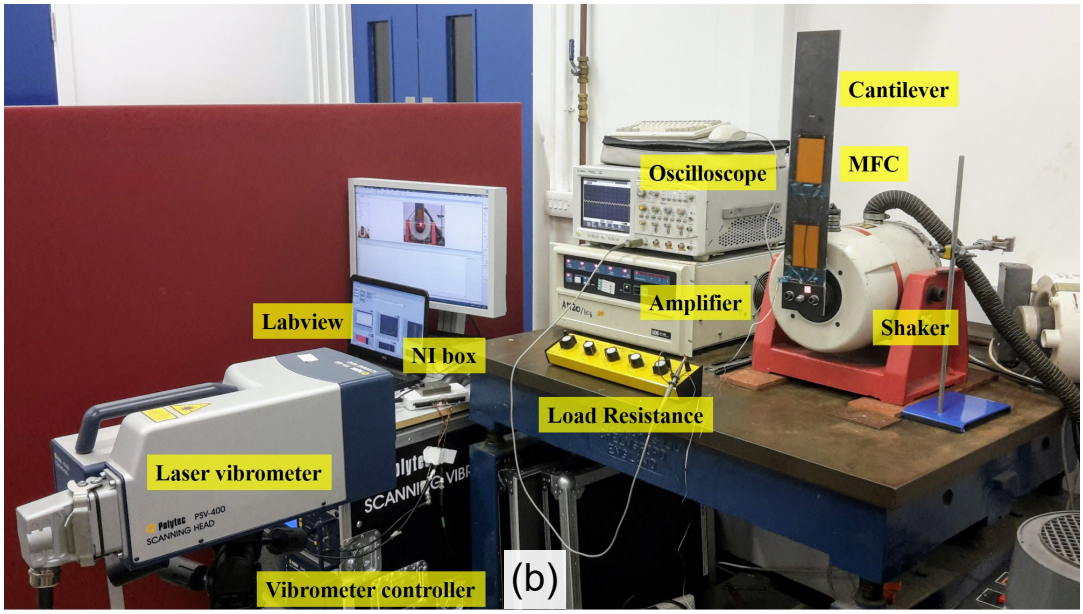

Figure 5-6: *Experimental setup. (a) Schematic of experiment setup. R_L is the load resistance. (b) Experiment setup showing bend-twist cantilever beam that is mounted vertically on to the shaker.*

matching impedance, which is dependent on the excitation frequency. The optimum load impedance fulfils the condition delivered from equation for a capacitive reactance,

$$\omega R_L C_P = 1 \tag{5.9}$$

which can be transformed to form:

$$R_L = \frac{1}{2\pi C_P f_t} \tag{5.10}$$

where C_P is a capacitance of the piezoelectric device, $\omega = 2\pi f_t$ is the angular frequency, and f_t is the desired testing frequency from the frequency range of interest. For the sweep function in the frequency range of interest between 6 and 45 Hz, the optimum load impedance varied from 2 MΩ to 267 kΩ. In order to minimize the influence of the matching impedance, the value of 10 kΩ was used throughout the harvesting experiments.

5.1.5 Results and Discussion

For energy harvesting characterization, the electrodynamic shaker was excited at a constant 1 g (9.8 m/s^2) and the vibration frequency was swept from 5 to 52 Hz to cover a range of vibration modes. Fig. 5-7 shows the measured power output from both the extension-mode (M8557-P1) and shear-mode (M8557-F1) MFC patches. The extension-mode MFC attached on the root of the cantilever generated power at a lower frequency of 6.5 Hz only, which reached a peak of 1.15 mW. However, the shear-mode MFC at the mid span had a small power peak at 6.5 Hz and two higher peak powers at 37 and 45 Hz (0.7 mW and 0.4 mW, respectively). Since the MFC on the root harvested the bending and the MFC in the mid-span harvested the twisting of the cantilever beam, the bending mode and twisting mode can be characterized experimentally and Fig. 5-7 indicates that the bending mode is 6.5 Hz and the twisting mode is 37 and/or 45 Hz. The small peak in power at 6.5 Hz from the shearmode MFC is thought to be due to the bending of the beam.

Fig. 5-8 shows the prediction of the 2-DOF model as the steady-state response of the tip displacement relative to the base motion ($x - y$) and angle of twist (ϕ) for the range of frequencies studied experimentally. It can be observed that the 2-DOF model predicts resonance frequencies at 6.4 Hz and 45 Hz, which compares very favourably with the experimental values in Fig. 5-7. The first mode is dominated by transverse deformation, which explains the high electrical output of the extension-mode PZT patch, and the other mode is dominated by twist, which is expected to yield an output from the shear-

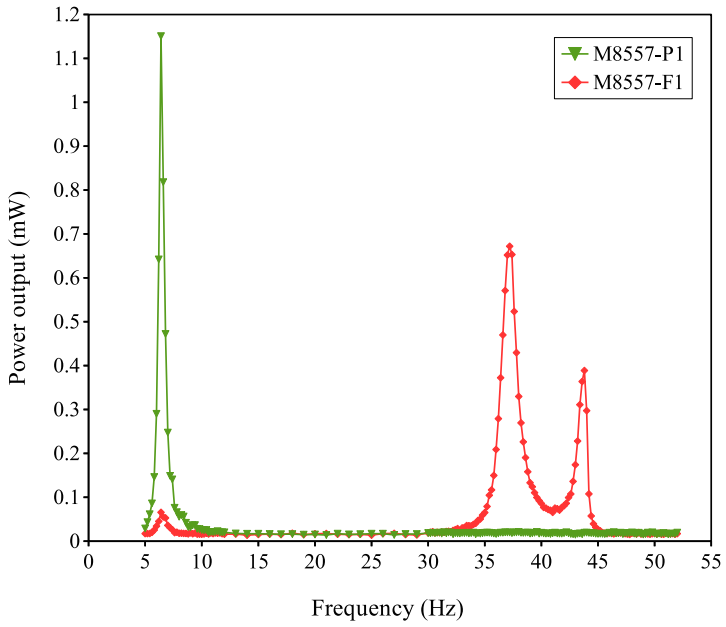

Figure 5-7: *Power output from MFC patches at excitation level of 1 g in frequency range of 5–52 Hz. Green (▽) output from M8557-P1 (extension-mode), red (◇) output from M8557-F1 (shear-mode).*

mode PZT patch. The third resonance obtained experimentally at 37 Hz is a mixed mode that combines transverse deformation and twist and could not be captured by the present 2-DOF model, but indicated the potential of the harvesting system to operate at multiple modes.

Fig. 5-9 schematically illustrates the vibration mode shapes observed experimentally by viewing the beam through a strobe light. It can be observed that the deformation pattern in the first mode (6.5 Hz) is predominantly bending. The ensuing uniaxial strains, which are greatest at the root, leads to a greater electrical output from the extension-mode PZT patch, the lower patch in Fig. 5-6b. The shear-mode PZT patch (upper patch in Fig. 5-6b) is not subjected to significant torsion and hence provides minimal output, as shown in Fig. 5-7. The second mode (37 Hz) was observed to contain primarily twisting motions, superimposed on a bending deformation pattern that is somewhat close to the second bending mode in a homogeneous cantilever beam. In this mode, bending deformations at the root are small, hence output from the lower patch is insignificant, whereas torsional deformations provide a higher output from the upper patch. The third mode (45 Hz) is dominated by twisting, which provides favourable drive conditions for the shear-mode patch and no output from the extension-mode one, which agrees with the output shown in Fig. 5-7.

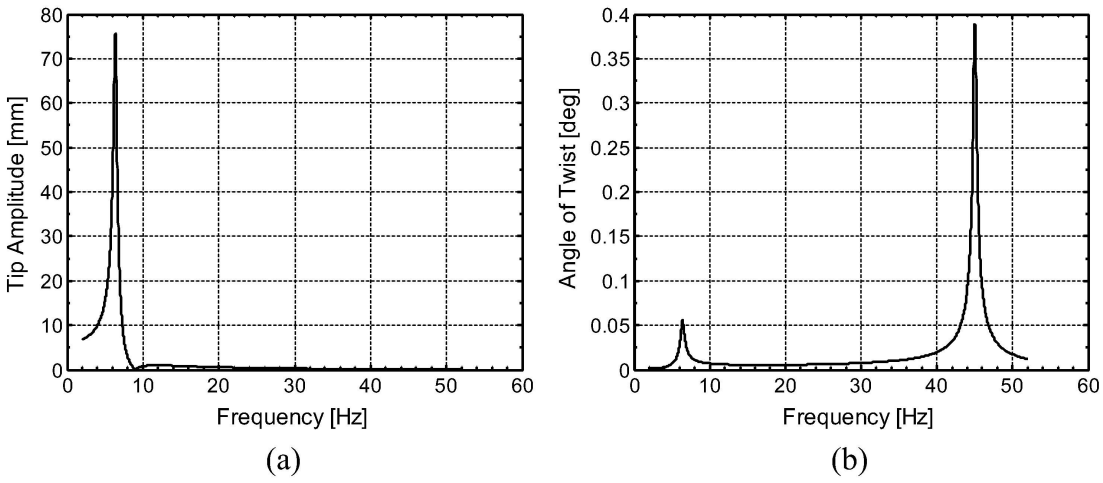

Figure 5-8: *Simulated frequency response of the 2-DOF model at 1 g excitation level. (a) Variation of the tip displacement amplitude with respect to the base motion (x-y); (b) angle of twist ϕ.*

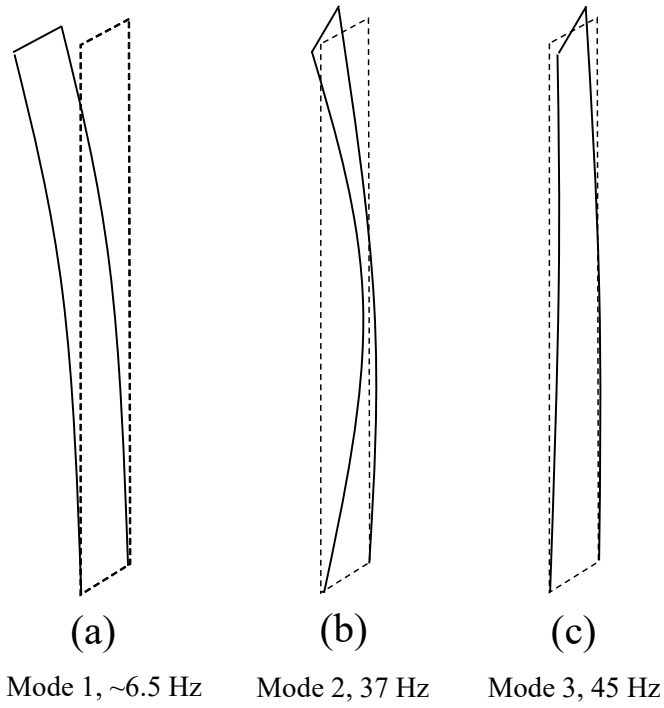

Figure 5-9: *Schematic illustrations of vibration modes observed experimentally.*

While no proof mass was used in this study they are often employed in cantilever-type energy harvesters to maximize the power output without significantly increasing the overall device volume. As the unbalanced CFRP beams presented here have inherent

characteristics that induce bend and twist, adding a proof mass can further enhance bending and twisting effects. It is envisaged that the introduction of point masses in the form of asymmetric masses will induce even more twisting, which will provide favourable output from the shear-mode PZT patch.

Accordingly, the present beam possesses multiple, narrow-band harvestable vibration modes exploiting both bending and torsional deformations. Through design optimization, the spectral spacing between these modes can be minimized to offer a multimodal device that operates across a defined frequency band, which can be effective for applications where the excitation frequency is known to vary within certain limits.

5.1.6 Conclusions

This work has presented the first demonstration of the use of a laminated carbon fibre reinforced polymer to create cantilever beams with coupled bending-twisting oscillations for multi-mode energy harvesting applications. Modelling of this new bend-twist harvesting system is presented, which compares favourably with the experimental results. It is demonstrated that the variety of bend and torsional modes of the harvesters can be utilized to create a harvester that operates in a wider range of frequencies and such device architectures provides a unique approach in which to tune the frequency response of the resonant harvesting system. The advantages of the proposed design is that the structure can be tuned to provide a broader-band energy harvester by adjusting natural frequencies. In addition, torsional modes typically exhibit small displacement amplitudes compared to bending modes; this provides scope for smaller volume device architectures. By exploiting at laminate architecture which inherently exhibits bend-twist coupling the complexity of the system is reduced since there is no need to use an eccentric proof mass or asymmetric tip masses to achieve torsion and the numerous potential lay-ups that exhibit bend-twist coupling provides a large design space to optimise the frequency response of the cantilever. This approach therefore provides new opportunities for the development of broader-band energy harvesting materials and systems.

Acknowledgement

This work was supported by both the European Commission's Marie Skłodowska-Curie Actions (MSCA), through the Marie Skłodowska-Curie Individual Fellowships (IF-EF) (H2020-MSCA-IF-2015-EF-703950-HEAPPs) under Horizon 2020 and the European Research Council under the European Union's Seventh Framework Programme (FP/2007–2013)/ ERC Grant Agreement no. 320963 on Novel Energy Ma-

terials, Engineering Science and Integrated Systems (NEMESIS).

References

[1] M. H. Arafa, "Multi-modal vibration energy harvesting using a trapezoidal plate," *Journal of vibration and acoustics*, vol. 134, no. 4, p. 041010, 2012.

[2] N. Sharpes, A. Abdelkefi, H. Abdelmoula, P. Kumar, J. Adler, and S. Priya, "Mode shape combination in a two-dimensional vibration energy harvester through mass loading structural modification," *Applied Physics Letters*, vol. 109, no. 3, p. 033901, Jul. 2016.

[3] M. R. Chiarelli, V. Binante, S. Botturi, A. Massai, J. Kunzmann, A. Colbertaldo, and D. G. Romano, "On the active deformations of hybrid specimens," *Aircraft Engineering and Aerospace Technology*, vol. 88, no. 5, pp. 676–687, Sep. 2016.

[4] W. Raither, A. Bergamini, F. Gandhi, and P. Ermanni, "Adaptive bending-twist coupling in laminated composite plates by controllable shear stress transfer," *Composites Part A: Applied Science and Manufacturing*, vol. 43, no. 10, pp. 1709–1716, Oct. 2012.

[5] A. Samur and A. Erturk, "Multifunctional double-bimorph piezoelectric composite for bending-twisting actuation, adaptive stiffness change, and energy harvesting," in *54th AIAA/ASME/ASCE/AHS/ASC Structures, Structural Dynamics, and Materials Conference*. American Institute of Aeronautics and Astronautics.

[6] A. Abdelkefi, F. Najar, A. H. Nayfeh, and S. B. Ayed, "An energy harvester using piezoelectric cantilever beams undergoing coupled bending–torsion vibrations," *Smart Materials and Structures*, vol. 20, no. 11, p. 115007, 2011.

[7] S. Gao, G. Zhang, L. Jin, P. Li, and H. Liu, "Study on characteristics of the piezoelectric energy-harvesting from the torsional vibration of thin-walled cantilever beams," *Microsystem Technologies*, vol. 23, no. 12, pp. 5455–5465, Dec. 2017.

[8] X. Shan, J. Deng, R. Song, and T. Xie, "A Piezoelectric Energy Harvester with Bending–Torsion Vibration in Low-Speed Water," *Applied Sciences*, vol. 7, no. 2, p. 116, Jan. 2017.

[9] C. B. York and S. F. M. de Almeida, "On Extension-Shearing Bending-Twisting coupled laminates," *Composite Structures*, vol. 164, pp. 10–22, Mar. 2017.

[10] "MFC," https://www.smart-material.com/MFC-product-main.html.

[11] P. Harris, M. Arafa, G. Litak, C. R. Bowen, and J. Iwaniec, "Output response identification in a multistable system for piezoelectric energy harvesting," *The European Physical Journal B*, vol. 90, no. 1, p. 20, Jan. 2017.

5.2 Summary

An improved mechanical design of an energy harvester, achieved by the incorporation of bend-twist coupling results in an enhanced available strain area available for harvesting, in comparison to conventional bending mode cantilever.

The work presented shows great potential in providing a simple adjustment to most basic vibrating cantilever structures to increase the overall energy harvester performance by means of broader frequency range and larger active area.

Additionally, the high torsional shear strain experienced by the twisting of the beam can result in possible applications of other operating modes, such as the d_{15} – mode, as presented in Chapter 4/ Paper 4 (Section 4.1.5) for further increased performance of a vibration powered piezoelectric energy harvester.

CHAPTER 6

CONCLUSIONS AND FUTURE WORK

The work described in this thesis presents a comprehensive overview on current developments and improvements incorporated into the piezoelectric energy harvesters for increased performance and efficiency.

6.1 Conclusions

A complete description for electrical characterisation of vibration powered energy harvesting devices was presented in Chapter 2. This is a unique measurement system, designed to control complex measurement setups that can be combined with a variety of instrumentation and excitation sources. A detailed analysis of rectification processes, its limitations, and most importantly, the proposed reverse engineering method allowing for calculation of driving current, capacitance and electro-mechanical damping of energy harvester during operation was proposed in Chapter 3.

The key findings describe an effect of incorporating aligned porosity into the piezoelectric ceramics on the energy harvesting performance. This can be described as a porous material with its pores aligned in the poling direction, which results in the highest ratio of active material being poled. Materials manufactured with this method exhibit increased piezoelectric coefficients, such as d_{33}, in comparison to randomly distributed pores. Additionally, the introduction of aligned porosity increases the mechanical robustness of the ferroelectric/piezoelectric ceramic when compared to unstructured (random) porosity. Novel composite materials can further increase energy harvester's efficiency, and this can be achieved with incorporation of a flexible medium within the aligned pore voids, as described in Chapter 4.

Finally, an improved mechanical cantilever beam with a twisted mode of operation can significantly broaden the available and useful frequency range for energy harvesting devices, as presented in Chapter 5.

The novel contributions presented in this thesis can be summarised as:

(i) Development of first existing adjustable measurement system capable of complex characterisation of energy harvesting device.

(ii) Development of novel method for evaluation of piezoelectric energy harvester during operation. A simple method for estimation of core device parameters such as generated current, and system damping without necessity of incorporation of expensive and complicated measuring equipment and techniques.

(iii) Introducing aligned porosity benefiting the overall performance of an energy harvester. This can be further increased with a creation of composite material that also overcomes the main limitations of the applications of piezoelectric ceramics namely its fragility and brittleness.

(iv) Incorporating the twist motion broadening the frequency bandwidth and increasing the power density of harvesters by enlarging the area available for harvesting energy from a cantilever beam.

6.2 Future Work

The work presented in this thesis indicates future directions and improvements in energy harvesting technology. Incorporation of some, or all, of the key findings into one working device is expected to result with an improvement over commonly applied systems to date. One of the possible fields of application of the above mentioned enhancements in piezoelectric energy harvesters and recognise them as a reliable power supply source in vibrating industrial environment would be a technology process called Thick Film Technology (TFT), commonly realised via screen-printing technique.

As reported by Saadon *et al.* [1] different attempts and designs of PZT based MEMS energy harvesting structures resulted in power output in range of 38 nW, to 2.8 μW, while thick-film PZT based cantilevers can deliver power in order to few orders of magnitude higher in a range of 33.2 μW to 375 μW [2, 3].

Such a difference is mainly a result of the size of a cantilever structure, which limits the cantilever resonance frequency at modes of operation. It was reported that screen-printing technology is compatible with isotropic materials, such as stainless steel [4], thus such a base structure could be applied as a main carrier in the final piezoelectric harvester. In addition, by using a cantilever with a custom designed shape, it is possible to incorporate similar bend-twisting coupling effects into isotropic cantilevers and increase the overall performance of the energy harvester. A successful macroscopic structure with introduced twist phenomena was presented in Chapter 5 and further

work for successful validation and miniaturisation with a metallic-based cantilever for its compatibility with Thick Film Technology can be undertaken.

Finally, thick film technology is advantageous since it is dedicated to the manufacture of hybrid circuits which are a combination of screen-printed passive elements with discrete semiconductors, so it is suitable technology to be combined with the high temperature semiconductors, such as the silicon carbide diodes for high temperature industrial applications, as presented in Chapter 2.

It would be also possible to incorporate freeze-cast aligned porosity and polymer composites into such harvesting structures for further increases in the efficiency of a piezoelectric device and enhancement of performance.

Improvements can therefore be achieved by improving the material and/or energy harvester structure. With the dedicated measurement setup and procedure presented in this thesis, especially in Chapters 2 and 3, a complex characterisation of incorporated improvements can be easily introduced at each stage of the development.

References

[1] S. Saadon and O. Sidek, "A review of vibration-based MEMS piezoelectric energy harvesters," *Energy Conversion and Management*, vol. 52, no. 1, pp. 500–504, Jan. 2011.

[2] S. Roundy and P. K. Wright, "A piezoelectric vibration based generator for wireless electronics," *Smart Materials and Structures*, vol. 13, no. 5, p. 1131, 2004.

[3] R. Xu, A. Lei, C. Dahl-Petersen, K. Hansen, M. Guizzetti, K. Birkelund, E. V. Thomsen, and O. Hansen, "Screen printed PZT/PZT thick film bimorph MEMS cantilever device for vibration energy harvesting," *Sensors and Actuators A: Physical*, vol. 188, pp. 383–388, 2012.

[4] N. R. Harris, M. Hill, R. Torah, R. Townsend, S. Beeby, N. M. White, and J. Ding, "A multilayer thick-film PZT actuator for MEMs applications," *Sensors and Actuators A: Physical*, vol. 132, no. 1, pp. 311–316, Nov. 2006.

COMPLETE LIST OF AUTHOR'S COMMUNICATIONS TO DATE

Peer-reviewed international journal articles

[1] **M. J. Kraśny** and C. R. Bowen, 'A System for Characterisation of Piezoelectric Materials and Associated Electronics for Vibration Powered Energy Harvesting Devices', Measurement, p. 108285, Jul. 2020, doi: 10.1016/j.measurement.2020.108285.

[2] **M. J. Kraśny**, C. R. Bowen, C. Michel, and J. T. Taylor, 'Transient Analysis of a Current Driven Full Wave AC/DC Converter for Indirect Characterisation of Piezoelectric Devices During Energy Harvesting', Energy Technology, vol. 8, no. 3, Mar. 2020, doi: 10.1002/ente.201901317.

[3] Y. Zhang, S. Kumar, F. Marken, **M. J. Kraśny**, E. Roake, S. Eslava, S. Dunn, E. Da Como, C. R. Bowen, 'Pyro-electrolytic water splitting for hydrogen generation', Nano Energy, vol. 58, pp. 183–191, Apr. 2019, doi: 10.1016/j.nanoen.2019.01.030.

[4] M. Xie, Y. Zhang, **M. J. Kraśny**, C. Bowen, H. Khanbareh, and N. Gathercole, 'Flexible and active self-powered pressure, shear sensors based on freeze casting ceramic–polymer composites', Energy Environ. Sci., Jul. 2018, doi: 10.1039/C8EE01551A.

[5] M. Xie, Y. Zhang, **M. J. Kraśny**, A. Rhead, C. Bowen, and M. Arafa, 'Energy harvesting from coupled bending-twisting oscillations in carbon-fibre reinforced polymer laminates', Mechanical Systems and Signal Processing, vol. 107, pp. 429–438, Jul. 2018, doi: 10.1016/j.ymssp.2018.01.026.

[6] J. I. Roscow, Y. Zhang, **M. J. Kraśny**, R. W. C. Lewis, J. Taylor, and C. R. Bowen, 'Freeze cast porous barium titanate for enhanced piezoelectric energy harvesting', J. Phys. D: Appl. Phys., vol. 51, no. 22, p. 225301, 2018, doi: 10.1088/1361-6463/aabc81.

[7] J. Blackwell, **M. J. Kraśny**, A. O'Brien, K. Ashkan, J. Galligan, M. Destrade, and N. Colgan, 'Proton Resonance Shift Thermometry: A review of modern clinical practices', Journal of Magnetic Resonance Imaging [Accepted for Publication], Nov. 2020.

[8] J. Blackwell, G. Oluniran, B. Tuohy, M. Destrade, **M. J. Kraśny**, and N. Colgan, 'Experimental assessment of clinical MRI-induced global SAR distributions in head phantoms', Physica Medica, vol. 66, pp. 113–118, Oct. 2019, doi: 10.1016/j.ejmp.2019.09.242.

Posters and Conferences

[1] **M. J. Kraśny** and C. R. Bowen, 'Improved rectification efficiency for low voltage and frequency piezoelectric energy harvesters in high temperature environment', presented at the 4th Workshop in Devices, Materials and Structures for Energy Harvesting and Storage, Oulu, Finland, May 17, 2017, [Online]. Available: http://www.oulu.fi/ehwoulu2017/.

[2] **M. J. Kraśny**, E. Le Boulbar, D. Zabek, H. Khanbareh, and C. R. Bowen, 'High temperature measurement system for characterisation of polymer-based piezoelectric harvesting materials', presented at the Nanotec 2016, Valencia, Spain, Sep. 26, 2016, [Online]. Available: http://www.nanotec2016.com.

[3] J. Blackwell, G. Oluniran, **M. J. Kraśny**, B. Tuohy, and N. Colgan, 'Global head SAR assessment of MRI-induced temperature change', in Physica Medica, Nov. 2019, vol. 67, p. 207, doi: 10.1016/j.ejmp.2019.09.220.

BIBLIOGRAPHY

[1] A. Abdelkefi, F. Najar, A. H. Nayfeh, and S. B. Ayed, "An energy harvester using piezoelectric cantilever beams undergoing coupled bending–torsion vibrations," *Smart Materials and Structures*, vol. 20, no. 11, p. 115007, 2011.

[2] T. Adrega and S. P. Lacour, "Stretchable gold conductors embedded in PDMS and patterned by photolithography: Fabrication and electromechanical characterization," *Journal of Micromechanics and Microengineering*, vol. 20, no. 5, p. 055025, Apr. 2010.

[3] N. R. Alluri, S. Selvarajan, A. Chandrasekhar, B. Saravanakumar, J. H. Jeong, and S.-J. Kim, "Piezoelectric BaTiO3/alginate spherical composite beads for energy harvesting and self-powered wearable flexion sensor," *Composites Science and Technology*, vol. 142, pp. 65–78, Apr. 2017.

[4] A. Alomari, A. Batra, M. Aggarwal, and C. R. Bowen, "A multisource energy harvesting utilizing highly efficient ferroelectric PMN-PT single crystal," *Journal of Materials Science: Materials in Electronics*, vol. 27, no. 10, pp. 10 020–10 030, Oct. 2016.

[5] S. Anton, K. Farinholt, and A. Erturk, "Piezoelectret foam–based vibration energy harvesting," *Journal of Intelligent Material Systems and Structures*, vol. 25, no. 14, pp. 1681–1692, Sep. 2014.

[6] S. R. Anton and H. A. Sodano, "A review of power harvesting using piezoelectric materials (2003–2006)," *Smart Materials and Structures*, vol. 16, no. 3, p. R1, 2007.

[7] M. H. Arafa, "Multi-modal vibration energy harvesting using a trapezoidal plate," *Journal of vibration and acoustics*, vol. 134, no. 4, p. 041010, 2012.

[8] J. J. L. Aranda, S. Bader, and B. Oelmann, "An Apparatus for the Performance Estimation of Pressure Fluctuation Energy Harvesters," *IEEE Transactions on Instrumentation and Measurement*, vol. 67, no. 11, pp. 2705–2713, Nov. 2018.

[9] G. Arlt, D. Hennings, and G. de With, "Dielectric properties of fine-grained barium titanate ceramics," *Journal of Applied Physics*, vol. 58, no. 4, pp. 1619–1625, Aug. 1985.

[10] D. Armani, C. Liu, and N. Aluru, "Re-configurable fluid circuits by PDMS elastomer micromachining," in *Technical Digest. IEEE International MEMS 99 Conference. Twelfth IEEE International Conference on Micro Electro Mechanical Systems (Cat. No.99CH36291)*, Jan. 1999, pp. 222–227.

[11] S. W. Arms, C. P. Townsend, D. L. Churchill, J. H. Galbreath, and S. W. Mundell, "Power management for energy harvesting wireless sensors," vol. 5763, 2005, pp. 267–275.

[12] K. Ashraf, M. H. M. Khir, J. O. Dennis, and Z. Baharudin, "A wideband, frequency up-converting bounded vibration energy harvester for a low-frequency environment," *Smart Materials and Structures*, vol. 22, no. 2, p. 025018, Jan. 2013.

[13] M. Balato, L. Costanzo, A. Lo Schiavo, and M. Vitelli, "Optimization of both Perturb & Observe and Open Circuit Voltage MPPT Techniques for Resonant Piezoelectric Vibration Harvesters feeding bridge rectifiers," *Sensors and Actuators A: Physical*, vol. 278, pp. 85–97, Aug. 2018.

[14] S. Barker, K. V. Vassilevski, N. G. Wright, and A. B. Horsfall, "High temperature vibration energy harvester system," in *2010 IEEE Sensors*, Nov. 2010, pp. 300–303.

[15] S. Barker, D. Brennan, N. G. Wright, and A. B. Horsfall, "Piezoelectric-powered wireless sensor system with regenerative transmit mode," *IET Wireless Sensor Systems*, vol. 1, no. 1, pp. 31–38, Mar. 2011.

[16] A. A. Basari, S. Awaji, S. Wang, S. Hashimoto, S. Kumagai, K. Suto, H. Okada, H. Okuno, B. Homm, W. Jiang, and S. Wang, "Shape Effect of Piezoelectric Energy Harvester on Vibration Power Generation," *Journal of Power and Energy Engineering*, vol. 02, no. 09, pp. 117–124, 2014.

[17] A. K. Batra, J. R. Currie, A. A. Alomari, M. D. Aggarwal, and C. R. Bowen, "A versatile and fully instrumented test station for piezoelectric energy harvesters," *Measurement*, vol. 114, pp. 9–15, Jan. 2018.

[18] S. P. Beeby, M. J. Tudor, and N. M. White, "Energy harvesting vibration sources for microsystems applications," *Measurement Science and Technology*, vol. 17, no. 12, p. R175, 2006.

[19] A. Bell, "Grain size effects in barium titanate-revisited," in *Proceedings of 1994 IEEE International Symposium on Applications of Ferroelectrics*, Aug. 1994, pp. 14–17.

[20] F. C. Y. Benureau and N. P. Rougier, "Re-run, Repeat, Reproduce, Reuse, Replicate: Transforming Code into Scientific Contributions," *Frontiers in Neuroinformatics*, vol. 11, 2018.

[21] Berlincourt D and Jaffe H, "Elastic and piezoelectric coefficients of single crystal barium titanate," *Phys. Rev.*, vol. 111, p. 143, 1958.

[22] D. Berlincourt and C. Near, "Properties of Morgan Electro Ceramic Ceramics," *Morgan Electroceramics*, vol. Technical Publication TP- 226, p. 12, 1999.

[23] P. Biswal, N. Verma, S. K. Kar, and B. Mukherjee, "Development and Performance Analysis of a Low Cost Experimental Set Up for Piezoelectric Based Energy Harvester Using Loudspeaker," in *2018 15th IEEE India Council International Conference (INDICON)*. Coimbatore, India: IEEE, Dec. 2018, pp. 1–5.

[24] C. R. Bowen and M. H. Arafa, "Energy Harvesting Technologies for Tire Pressure Monitoring Systems," *Advanced Energy Materials*, vol. 5, no. 7, pp. n/a–n/a, Apr. 2015.

[25] C. R. Bowen, J. Taylor, E. Le Boulbar, D. Zabek, and V. Y. Topolov, "A modified figure of merit for pyroelectric energy harvesting," *Materials Letters*, vol. 138, pp. 243–246, Jan. 2015.

[26] C. R. Bowen, A. C. Dent, R. Stevens, M. G. Cain, and A. Avent, "A new method to determine the un-poled elastic properties of ferroelectric materials," *Science and Technology of Advanced Materials*, vol. 18, no. 1, pp. 264–272, Dec. 2017.

[27] C. R. Bowen, H. A. Kim, P. M. Weaver, and S. Dunn, "Piezoelectric and ferroelectric materials and structures for energy harvesting applications," *Energy & Environmental Science*, vol. 7, no. 1, pp. 25–44, Dec. 2013.

[28] C. R. Bowen, A. Perry, A. C. F. Lewis, and H. Kara, "Processing and properties of porous piezoelectric materials with high hydrostatic figures of merit," *Journal of the European Ceramic Society*, vol. 24, no. 2, pp. 541–545, Jan. 2004.

[29] C. R. Bowen, J. Taylor, E. LeBoulbar, D. Zabek, A. Chauhan, and R. Vaish, "Pyroelectric materials and devices for energy harvesting applications," *Energy & Environmental Science*, vol. 7, no. 12, pp. 3836–3856, Nov. 2014.

[30] J. Briscoe, N. Jalali, P. Woolliams, M. Stewart, P. M. Weaver, M. Cain, and S. Dunn, "Measurement techniques for piezoelectric nanogenerators," *Energy & Environmental Science*, vol. 6, no. 10, pp. 3035–3045, Sep. 2013.

[31] BS EN 50324, *BS EN 50324-2:2002 - Piezoelectric Properties of Ceramic Materials and Components. Methods of Measurement. Low Power*, Oct. 2002.

[32] ——, *BS EN 50324-1:2002 - Piezoelectric Properties of Ceramic Materials and Components. Terms and Definitions*, Dec. 2001.

[33] BS EN 623-2, *BS EN 623-2:1993 - Advanced Technical Ceramics. Monolithic Ceramics. General and Textural Properties. Determination of Density and Porosity*, 1993.

[34] BS EN 62830-3:2017, *BS EN 62830-3:2017 - Semiconductor Devices. Semiconductor Devices for Energy Harvesting and Generation. Vibration Based Electromagnetic Energy Harvesting.* BSI, Apr. 2017.

[35] BS ISO 21819-2, *BS ISO 21819-2 Fine Ceramics (Advanced Ceramics, Advanced Technical Ceramics) - Characteristic of Piezoelectric Properties under High-Load Conditions. Part 2: Electrical Transient Response Method under High Vibration Levels.*, iso 21819-2:2018 identical ed. BSI, Aug. 2018.

[36] BS ISO 21819:1, *BS ISO 21819-1. Fine Ceramics (Advanced Ceramics, Advanced Technical Ceramics). Characteristic of Piezoelectric Properties under High-Load Conditions. Part 1. Resonant-Antiresonant Method under High Temperature Conditions*, iso 21819-1:2018 identical ed. BSI, Aug. 2018.

[37] L. Burianova, A. Kopal, and J. Nosek, "Characterization of advanced piezoelectric materials in the wide temperature range," *Materials Science and Engineering: B*, vol. 99, no. 1–3, pp. 187–191, May 2003.

[38] M. G. Cain, M. Stewart, and M. G. Gee, "Degradation of piezoelectric materials," National Physical Laboratory Teddington, Tech. Rep. 148, 1999.

[39] R. Caliò, U. B. Rongala, D. Camboni, M. Milazzo, C. Stefanini, G. de Petris, and C. M. Oddo, "Piezoelectric Energy Harvesting Solutions," *Sensors*, vol. 14, no. 3, pp. 4755–4790, Mar. 2014.

[40] W.-C. Chang, A.-B. Wang, C.-K. Lee, H.-L. Chen, W.-C. Ko, and C.-T. Lin, "Photoconductive Piezoelectric Polymer Made From a Composite of P(VDF-TrFE) and TiOPc," *Ferroelectrics*, vol. 446, no. 1, pp. 9–17, Jan. 2013.

[41] X. Chen, X. Li, J. Shao, N. An, H. Tian, C. Wang, T. Han, L. Wang, and B. Lu, "High-Performance Piezoelectric Nanogenerators with Imprinted P(VDF-TrFE)/BaTiO3 Nanocomposite Micropillars for Self-Powered Flexible Sensors," *Small*, vol. 13, no. 23, p. 1604245, 2017.

[42] H.-J. Chen, S. Han, C. Liu, Z. Luo, H.-P. D. Shieh, R.-S. Hsiao, and B.-R. Yang, "Investigation of PVDF-TrFE composite with nanofillers for sensitivity improvement," *Sensors and Actuators A: Physical*, vol. 245, pp. 135–139, Jul. 2016.

[43] C. Chen, B. Zhao, and J. Liang, "Revisit of synchronized electric charge extraction (SECE) in piezoelectric energy harvesting by using impedance modeling," *Smart Materials and Structures*, vol. 28, no. 10, p. 105053, Sep. 2019.

[44] Z. Chen, J. He, J. Liu, and Y. Xiong, "Switching Delay in Self-Powered Nonlinear Piezoelectric Vibration Energy Harvesting Circuit: Mechanisms, Effects, and Solutions," *IEEE Transactions on Power Electronics*, vol. 34, no. 3, pp. 2427–2440, Mar. 2019.

[45] X.-r. Chen, T.-q. Yang, W. Wang, and X. Yao, "Vibration energy harvesting with a clamped piezoelectric circular diaphragm," *Ceramics International*, vol. 38, Supplement 1, pp. S271–S274, Jan. 2012.

[46] M. R. Chiarelli, V. Binante, S. Botturi, A. Massai, J. Kunzmann, A. Colbertaldo, and D. G. Romano, "On the active deformations of hybrid specimens," *Aircraft Engineering and Aerospace Technology*, vol. 88, no. 5, pp. 676–687, Sep. 2016.

[47] L. Costanzo, A. Lo Schiavo, and M. Vitelli, "Power Extracted From Piezoelectric Harvesters Driven by Non-Sinusoidal Vibrations," *IEEE Transactions on Circuits and Systems I: Regular Papers*, vol. 66, no. 3, pp. 1291–1303, Mar. 2019.

[48] F. Dell'Anna, T. Dong, P. Li, Y. Wen, Z. Yang, M. R. Casu, M. Azadmehr, and Y. Berg, "State-of-the-Art Power Management Circuits for Piezoelectric Energy Harvesters," *IEEE Circuits and Systems Magazine*, vol. 18, no. 3, pp. 27–48, thirdquarter 2018.

[49] D. B. Deutz, N. T. Mascarenhas, J. B. J. Schelen, D. M. de Leeuw, S. van der Zwaag, and P. Groen, "Flexible Piezoelectric Touch Sensor by Alignment of Lead-Free Alkaline Niobate Microcubes in PDMS," *Advanced Functional Materials*, vol. 27, no. 24, p. 1700728, 2017.

[50] S. Deville, "Freeze-Casting of Porous Ceramics: A Review of Current Achievements and Issues," *Advanced Engineering Materials*, vol. 10, no. 3, pp. 155–169, 2008.

[51] ——, *Freezing Colloids: Observations, Principles, Control, and Use: Applications in Materials Science, Life Science, Earth Science, Food Science, and Engineering*, ser. Engineering Materials and Processes. Springer International Publishing, 2017.

[52] S. Deville, E. Saiz, R. K. Nalla, and A. P. Tomsia, "Freezing as a Path to Build Complex Composites," *Science*, vol. 311, no. 5760, pp. 515–518, Jan. 2006.

[53] S. Deville, E. Saiz, and A. P. Tomsia, "Ice-templated porous alumina structures," *Acta Materialia*, vol. 55, no. 6, pp. 1965–1974, Apr. 2007.

[54] S. Deville, E. Maire, G. Bernard-Granger, A. Lasalle, A. Bogner, C. Gauthier, J. Leloup, and C. Guizard, "Metastable and unstable cellular solidification of colloidal suspensions," *Nature Materials*, vol. 8, no. 12, pp. 966–972, Dec. 2009.

[55] A. Dziedzic and D. Nowak, "Thick-film and LTCC passive components for high-temperature electronics," *Radioengineering*, vol. 22, no. 1, pp. 218–226, 2013.

[56] ERP UK Ltd, "Why recycle batteries? | ERP Battery Recycling," http://www.erp-batteries.co.uk/why/, 2016.

[57] F. Felten, G. A. Schneider, J. M. Saldaña, and S. V. Kalinin, "Modeling and measurement of surface displacements in BaTiO3 bulk material in piezoresponse force microscopy," *Journal of Applied Physics*, vol. 96, no. 1, pp. 563–568, Jul. 2004.

[58] M. Ferrari, V. Ferrari, M. Guizzetti, D. Marioli, and A. Taroni, "Piezoelectric multifrequency energy converter for power harvesting in autonomous microsystems," *Sensors and Actuators A: Physical*, vol. 142, no. 1, pp. 329–335, Mar. 2008.

[59] D. Fuard, T. Tzvetkova-Chevolleau, S. Decossas, P. Tracqui, and P. Schiavone, "Optimization of poly-di-methyl-siloxane (PDMS) substrates for studying cellular adhesion and motility," *Microelectronic Engineering*, vol. 85, no. 5, pp. 1289–1293, May 2008.

[60] A. M. Gaikwad, G. L. Whiting, D. A. Steingart, and A. C. Arias, "Highly Flexible, Printed Alkaline Batteries Based on Mesh-Embedded Electrodes," *Advanced Materials*, vol. 23, no. 29, pp. 3251–3255, 2011.

[61] Gallantree H R, "Piezoelectric ceramic/polymer composites," *Br. Ceram. Proc.*, vol. 41, p. 161, 1989.

[62] S. Gao, G. Zhang, L. Jin, P. Li, and H. Liu, "Study on characteristics of the piezoelectric energy-harvesting from the torsional vibration of thin-walled cantilever beams," *Microsystem Technologies*, vol. 23, no. 12, pp. 5455–5465, Dec. 2017.

[63] F. Gheorghiu, L. Padurariu, M. Airimioaei, L. Curecheriu, C. Ciomaga, C. Padurariu, C. Galassi, and L. Mitoseriu, "Porosity-dependent properties of Nb-doped Pb(Zr,Ti)O3 ceramics," *Journal of the American Ceramic Society*, vol. 100, no. 2, pp. 647–658, 2017.

[64] P. Gljušćić, S. Zelenika, D. Blažević, and E. Kamenar, "Kinetic Energy Harvesting for Wearable Medical Sensors," *Sensors*, vol. 19, no. 22, p. 4922, Jan. 2019.

[65] P. Glynne-Jones and N. White, "Self-powered systems: A review of energy sources," *Sensor Review*, vol. 21, no. 2, pp. 91–98, Jun. 2001.

[66] M. Goldfarb and L. D. Jones, "On the efficiency of electric power generation with piezoelectric ceramic," *Journal of Dynamic Systems, Measurement, and Control*, vol. 121, no. 3, pp. 566–571, 1999.

[67] H. M. Gomes, F. S. Ferreira, C. A. K. Thomes, and D. S. Gaspareto, "An automatic system for electrodynamic shaker control by acceleration power spectral density," *Mecanica Computacional*, vol. 26, pp. 2959–2970, 2007.

[68] A. V. Goncharenko, V. Z. Lozovski, and E. F. Venger, "Lichtenecker's equation: Applicability and limitations," *Optics Communications*, vol. 174, no. 1, pp. 19–32, Jan. 2000.

[69] A. M. González, Á. García, C. Benavente-Peces, and L. Pardo, "Revisiting the Characterization of the Losses in Piezoelectric Materials from Impedance Spectroscopy at Resonance," *Materials*, vol. 9, no. 2, p. 72, Jan. 2016.

[70] I. S. Grant and W. R. Phillips, *Electromagnetism*. John Wiley & Sons, Oct. 1990.

[71] R. Guo, C.-A. Wang, and A. Yang, "Effects of pore size and orientation on dielectric and piezoelectric properties of 1–3 type porous PZT ceramics," *Journal of the European Ceramic Society*, vol. 31, no. 4, pp. 605–609, Apr. 2011.

[72] D. Guyomar, A. Badel, E. Lefeuvre, and C. Richard, "Toward energy harvesting using active materials and conversion improvement by nonlinear processing," *IEEE transactions on ultrasonics, ferroelectrics, and frequency control*, vol. 52, no. 4, pp. 584–595, 2005.

[73] G. H. Haertling, "Ferroelectric Ceramics: History and Technology," *Journal of the American Ceramic Society*, vol. 82, no. 4, pp. 797–818, 1999.

[74] D. A. Hall and P. J. Stevenson, "High field dielectric behaviour of ferroelectric ceramics," *Ferroelectrics*, vol. 228, no. 1, pp. 139–158, 1999.

[75] D. A. Hall, "Review Nonlinearity in piezoelectric ceramics," *Journal of Materials Science*, vol. 36, no. 19, pp. 4575–4601, Oct. 2001.

[76] T. Hang, J. Glaum, Y. A. Genenko, T. Phung, and M. Hoffman, "Investigation of partial discharge in piezoelectric ceramics," *Acta Materialia*, vol. 102, pp. 284–291, Jan. 2016.

[77] P. B. Harris, C. R. Bowen, D. N. Betts, and A. H. Kim, "Manufacture and characterisation of piezoelectric broadband energy harvesters based on asymmetric bistable laminates," 2014.

[78] N. R. Harris, M. Hill, R. Torah, R. Townsend, S. Beeby, N. M. White, and J. Ding, "A multilayer thick-film PZT actuator for MEMs applications," *Sensors and Actuators A: Physical*, vol. 132, no. 1, pp. 311–316, Nov. 2006.

[79] P. Harris, M. Arafa, G. Litak, C. R. Bowen, and J. Iwaniec, "Output response identification in a multistable system for piezoelectric energy harvesting," *The European Physical Journal B*, vol. 90, no. 1, p. 20, Jan. 2017.

[80] M. W. Hooker, "Properties of PZT-based piezoelectric ceramics between-150 and 250 C," 1998.

[81] Y. Huan, X. Wang, J. Fang, and L. Li, "Grain Size Effects on Piezoelectric Properties and Domain Structure of BaTiO3 Ceramics Prepared by Two-Step Sintering," *Journal of the American Ceramic Society*, vol. 96, no. 11, pp. 3369–3371, 2013.

[82] C. Huang, K. Cai, Y. Wang, Y. Bai, and D. Guo, "Revealing the real high temperature performance and depolarization characteristics of piezoelectric ceramics

by combined in situ techniques," *Journal of Materials Chemistry C*, vol. 6, no. 6, pp. 1433–1444, 2018.

[83] G.-T. Hwang, H. Park, J.-H. Lee, S. Oh, K.-I. Park, M. Byun, H. Park, G. Ahn, C. K. Jeong, K. No, H. Kwon, S.-G. Lee, B. Joung, and K. J. Lee, "Self-Powered Cardiac Pacemaker Enabled by Flexible Single Crystalline PMN-PT Piezoelectric Energy Harvester," *Advanced Materials*, vol. 26, no. 28, pp. 4880–4887, 2014.

[84] G.-T. Hwang, Y. Kim, J.-H. Lee, S. Oh, C. K. Jeong, D. Y. Park, J. Ryu, H. Kwon, S.-G. Lee, B. Joung, D. Kim, and K. J. Lee, "Self-powered deep brain stimulation via a flexible PIMNT energy harvester," *Energy & Environmental Science*, vol. 8, no. 9, pp. 2677–2684, Aug. 2015.

[85] IEEE Std, "IEEE Standard on Piezoelectricity," *ANSI/IEEE Std 176-1987*, pp. 0_1–, 1988.

[86] D. W. Inglis, "A method for reducing pressure-induced deformation in silicone microfluidics," *Biomicrofluidics*, vol. 4, no. 2, p. 026504, Jun. 2010.

[87] R. A. Islam and S. Priya, "Realization of high-energy density polycrystalline piezoelectric ceramics," *Applied Physics Letters*, vol. 88, no. 3, p. 032903, Jan. 2006.

[88] F. J. Jiménez, M. Vázquez-Rodriguez, D. Alonso, and J. de Frutos, "Virtual instrument to obtain an optimal linear model for piezoelectric elements involved in road traffic energy harvesting," *Computer Standards & Interfaces*, vol. 51, pp. 1–13, Mar. 2017.

[89] John D. Ryder, *Electronic Fundamentals and Applications*, 3rd ed. London: Pitman, 1964.

[90] I. Kanno, K. Akama, K. Wasa, and H. Kotera, "Evaluation of Intrinsic Shear Piezoelectric Coefficient d15 of c-Axis Oriented Pb(Zr,Ti)O3 Films," *Applied Physics Express*, vol. 2, no. 9, p. 091402, Sep. 2009.

[91] H. Kara, R. Ramesh, R. Stevens, and C. Bowen, "Porous PZT ceramics for receiving transducers," *IEEE Transactions on Ultrasonics, Ferroelectrics, and Frequency Control*, vol. 50, no. 3, pp. 289–296, Mar. 2003.

[92] L. Karthikeyan and B. Amrutur, "Signal-Powered Low-Drop-Diode Equivalent Circuit for Full-Wave Bridge Rectifier," *IEEE Transactions on Power Electronics*, vol. 27, no. 10, pp. 4192–4201, Oct. 2012.

[93] R. Khachaturyan, S. Zhukov, J. Schultheiß, C. Galassi, C. Reimuth, J. Koruza, H. von Seggern, and Y. A. Genenko, "Polarization-switching dynamics in bulk ferroelectrics with isometric and oriented anisometric pores," *Journal of Physics D: Applied Physics*, vol. 50, no. 4, p. 045303, Dec. 2016.

[94] H. Khanbareh, M. Hegde, J. C. Bijleveld, S. van der Zwaag, and P. Groen, "Functionally graded ferroelectric polyetherimide composites for high temperature sensing," *Journal of Materials Chemistry C*, 2017.

[95] H. Kim, S. Priya, H. Stephanou, and K. Uchino, "Consideration of Impedance Matching Techniques for Efficient Piezoelectric Energy Harvesting," *IEEE Transactions on Ultrasonics, Ferroelectrics, and Frequency Control*, vol. 54, no. 9, pp. 1851–1859, Sep. 2007.

[96] B. Kirking, J. Krevolin, C. Townsend, C. W. Colwell Jr., and D. D. D'Lima, "A multiaxial force-sensing implantable tibial prosthesis," *Journal of Biomechanics*, vol. 39, no. 9, pp. 1744–1751, 2006.

[97] M. Koplow, A. Chen, D. Steingart, P. K. Wright, and J. W. Evans, "Thick film thermoelectric energy harvesting systems for biomedical applications," in *Medical Devices and Biosensors, 2008. ISSS-MDBS 2008. 5th International Summer School and Symposium On.* IEEE, 2008, pp. 322–325.

[98] I. Kosmadakis, V. Konstantakos, T. Laopoulos, and S. Siskos, "An automated measurement bench for vibration-based energy harvesting systems," in *2013 IEEE 7th International Conference on Intelligent Data Acquisition and Advanced Computing Systems (IDAACS)*, vol. 01, Sep. 2013, pp. 15–20.

[99] ——, "Vibration-based Energy Harvesting Systems Characterization Using Automated Electronic Equipment," *Sensors & Transducers*, vol. 187, no. 4, p. 75, 2015.

[100] M. J. Kraśny, C. R. Bowen, C. Michel, and J. T. Taylor, "Transient Analysis of a Current Driven Full Wave AC/DC Converter for Indirect Characterisation of Piezoelectric Devices During Energy Harvesting," *Energy Technology*, vol. 8, no. 3, Mar. 2020.

[101] C. L. Kuo, S. C. Lin, and W. J. Wu, "Fabrication and characteristic of piezoelectric bimorph MEMS generators based on stainless steel substrate for vibration generator," p. 9, 2014.

[102] K. W. Kwok, H. L. W. Chan, and C. L. Choy, "Evaluation of the material parameters of piezoelectric materials by various methods," *IEEE transactions on ultrasonics, ferroelectrics, and frequency control*, vol. 44, no. 4, pp. 733–742, 1997.

[103] Y.-J. Lai, W.-C. Li, C.-M. Lin, V. V. Felmetsger, D. G. Senesky, and A. P. Pisano, "SiC/AlN piezoelectric energy harvesters for pulsed pressure sources in harsh environment applications," in *Dig. Tech. Solid-State Sens. Act. Microsyst. Workshop (Hilton Head'12)*, Hilton Head, SC, Jun. 2012, pp. 505–508.

[104] M. Lallart, C. Richard, Y. Li, Y.-C. Wu, and D. Guyomar, "Load-Tolerant, High-Efficiency Self-Powered Energy Harvesting Scheme Using a Nonlinear Approach," *Energy Harvesting and Systems*, vol. 1, no. 3-4, pp. 197–208, Dec. 2014.

[105] M. Lallart, "Nonlinear technique and self-powered circuit for efficient piezoelectric energy harvesting under unloaded cases," *Energy Conversion and Management*, vol. 133, pp. 444–457, Feb. 2017.

[106] M. Lallart and D. Guyomar, "An optimized self-powered switching circuit for non-linear energy harvesting with low voltage output," *Smart Materials and Structures*, vol. 17, no. 3, p. 035030, 2008.

[107] M. Lallart, D. Guyomar, Y. Jayet, L. Petit, E. Lefeuvre, T. Monnier, P. Guy, and C. Richard, "Synchronized switch harvesting applied to self-powered smart systems: Piezoactive microgenerators for autonomous wireless receivers," *Sensors and Actuators A: Physical*, vol. 147, no. 1, pp. 263–272, Sep. 2008.

[108] E. Le Boulbar and C. Bowen, "Study of Y-cut LiNbO3 (010) crystal under oscillated vibration at high temperature for energy harvesting in hostile environment," in *Applications of Ferroelectric, International Symposium on Integrated Functionalities and Piezoelectric Force Microscopy Workshop (ISAF/ISIF/PFM), 2015 Joint IEEE International Symposium on The*, May 2015, pp. 292–295.

[109] S.-H. Lee, S.-H. Jun, H.-E. Kim, and Y.-H. Koh, "Fabrication of Porous PZT–PZN Piezoelectric Ceramics With High Hydrostatic Figure of Merits Using Camphene-Based Freeze Casting," *Journal of the American Ceramic Society*, vol. 90, no. 9, pp. 2807–2813, 2007.

[110] M. Lee, C.-Y. Chen, S. Wang, S. N. Cha, Y. J. Park, J. M. Kim, L.-J. Chou, and Z. L. Wang, "A Hybrid Piezoelectric Structure for Wearable Nanogenerators," *Advanced Materials*, vol. 24, no. 13, pp. 1759–1764, 2012.

[111] S.-H. Lee, S.-H. Jun, H.-E. Kim, and Y.-H. Koh, "Piezoelectric Properties of PZT-Based Ceramic with Highly Aligned Pores," *Journal of the American Ceramic Society*, vol. 91, no. 6, pp. 1912–1915, 2008.

[112] M. Lee, J. Bae, J. Lee, C.-S. Lee, S. Hong, and Z. L. Wang, "Self-powered environmental sensor system driven by nanogenerators," *Energy & Environmental Science*, vol. 4, no. 9, pp. 3359–3363, Aug. 2011.

[113] T. I. Lee, W. S. Jang, E. Lee, Y. S. Kim, Z. L. Wang, H. K. Baik, and J. M. Myoung, "Ultrathin self-powered artificial skin," *Energy & Environmental Science*, vol. 7, no. 12, pp. 3994–3999, Nov. 2014.

[114] R. W. C. Lewis, A. C. E. Dent, R. Stevens, and C. R. Bowen, "Microstructural modelling of the polarization and properties of porous ferroelectrics," *Smart Materials and Structures*, vol. 20, no. 8, p. 085002, Jun. 2011.

[115] J. Liang and W.-H. Liao, "Improved Design and Analysis of Self-Powered Synchronized Switch Interface Circuit for Piezoelectric Energy Harvesting Systems," *IEEE Transactions on Industrial Electronics*, vol. 59, no. 4, pp. 1950–1960, Apr. 2012.

[116] Y. Liang, C.-Z. Zhao, H. Yuan, Y. Chen, W. Zhang, J.-Q. Huang, D. Yu, Y. Liu, M.-M. Titirici, Y.-L. Chueh, H. Yu, and Q. Zhang, "A review of rechargeable batteries for portable electronic devices," *InfoMat*, vol. 1, no. 1, pp. 6–32, Mar. 2019.

[117] Y. Li, C. Liao, and S. C. Tjong, "Electrospun Polyvinylidene Fluoride-Based Fibrous Scaffolds with Piezoelectric Characteristics for Bone and Neural Tissue Engineering," *Nanomaterials*, 2019.

[118] P. Li, Y. Liu, Y. Wang, C. Luo, G. Li, J. Hu, W. Liu, and W. Zhang, "Low-frequency and wideband vibration energy harvester with flexible frame and interdigital structure," *AIP Advances*, vol. 5, no. 4, p. 047151, 2015.

[119] Linear Technology, "Wireless Sensor Networks with very low power consumption at less than 50 microamper per node," Mar. 2016.

[120] H. Liu, J. Zhong, C. Lee, S.-W. Lee, and L. Lin, "A comprehensive review on piezoelectric energy harvesting technology: Materials, mechanisms, and applications," *Applied Physics Reviews*, vol. 5, no. 4, p. 041306, Dec. 2018.

[121] W. Liu, L. Lv, Y. Li, Y. Wang, J. Wang, C. Xue, Y. Dong, and J. Yang, "Effects of slurry composition on the properties of 3-1 type porous PZT ceramics prepared by ionotropic gelation," *Ceramics International*, vol. 43, no. 8, pp. 6542–6547, Jun. 2017.

[122] W. Liu, N. Li, Y. Wang, H. Xu, J. Wang, and J. Yang, "Preparation and properties of 3–1 type PZT ceramics by a self-organization method," *Journal of the European Ceramic Society*, vol. 35, no. 13, pp. 3467–3474, Nov. 2015.

[123] F. Lu, H. P. Lee, and S. P. Lim, "Modeling and analysis of micro piezoelectric power generators for micro-electromechanical-systems applications," *Smart materials and structures*, vol. 13, no. 1, p. 57, 2003.

[124] K. Makihara and K. Asahina, "Analog self-powered harvester achieving switching pause control to increase harvested energy," *Smart Materials and Structures*, vol. 26, no. 5, p. 055007, May 2017.

[125] K. Makihara, S. Takeuchi, S. Shimose, and J. Onoda, "Innovative Digital Self-Powered Autonomous System for Multimodal Vibration Suppression," *AIAA Journal*, vol. 50, no. 9, pp. 2004–2011, Sep. 2012.

[126] K. Makihara, Y. Yamamoto, K. Yoshimizu, C. Horiguchi, H. Sakaguchi, and K. Fujimoto, "A novel controller to increase harvested energy from negating vibration-suppression effect," *Smart Materials and Structures*, vol. 24, no. 3, p. 037005, Mar. 2015.

[127] Y. Mao, P. Zhao, G. McConohy, H. Yang, Y. Tong, and X. Wang, "Sponge-Like Piezoelectric Polymer Films for Scalable and Integratable Nanogenerators and Self-Powered Electronic Systems," *Advanced Energy Materials*, vol. 4, no. 7, p. 1301624, 2014.

[128] Marcin J. Kraśny, "Enhamer," https://github.com/enhamer/enhamer, Jun. 2020.

[129] S. Marselli, V. Pavia, C. Galassi, E. Roncari, F. Craciun, and G. Guidarelli, "Porous piezoelectric ceramic hydrophone," *The Journal of the Acoustical Society of America*, vol. 106, no. 2, pp. 733–738, Aug. 1999.

[130] E. Mercadelli, A. Sanson, and C. Galassi, "Porous Piezoelectric Ceramics," in *Piezoelectric Ceramics*, E. Suaste-Gomez, Ed. Sciyo, Oct. 2010, vol. Chapter 6.

[131] "MFC," https://www.smart-material.com/MFC-product-main.html.

[132] C. Miclea, C. Tanasoiu, L. Amarande, C. F. Miclea, C. Plavitu, M. Cioangher, L. Trupina, C. T. Miclea, and C. David, "Effect of temperature on the main piezoelectric parameters of a soft PZT ceramic," *Rom. J. Inf. Sci. Technol*, vol. 10, no. 3, pp. 243–250, 2007.

[133] E. Mike, "LTspice," Analog Devices, Apr. 2019.

[134] K. Najafi, T. Galchev, E. E. Aktakka, R. L. Peterson, and J. McCullagh, "Microsystems for energy harvesting," in *Solid-State Sensors, Actuators and Microsystems Conference (TRANSDUCERS), 2011 16th International*. IEEE, 2011, pp. 1845–1850.

[135] A. Navarro, R. W. Whatmore, and J. R. Alcock, "Preparation of Functionally Graded PZT Ceramics Using Tape Casting," *Journal of Electroceramics*, vol. 13, no. 1, pp. 413–415, Jul. 2004.

[136] L. J. Nelson, C. R. Bowen, R. Stevens, M. Cain, and M. Stewart, "High field behaviour of piezoelectric fibre composites," *Proceedings of SPIE - The International Society for Optical Engineering*, vol. 5053, pp. 544–555, 2003.

[137] R. E. Newnham, A. Safari, J. Giniewicz, and B. H. Fox, "Composite piezoelectric sensors," *Ferroelectrics*, vol. 60, no. 1, pp. 15–21, Oct. 1984.

[138] R. E. Newnham, D. P. Skinner, and L. E. Cross, "Connectivity and piezoelectric-pyroelectric composites," *Materials Research Bulletin*, vol. 13, no. 5, pp. 525–536, May 1978.

[139] M. Stewart, M. G. Cain, and D. A. Hall, "Ferroelectric hysteresis measurement and analysis." Teddington, NPL Report, May 1999.

[140] M. Stewart and M. G. Cain, "Measurement of high field dielectric properties of piezoelectric materials." Teddington, Measurement Good Practice Guide, May 1999.

[141] M. G. Cain and M. Stewart, "Piezoelectric resonance." NPL, Teddington, Measurement Good Practice Guide Guide No. 33, Jan. 2001.

[142] M. G. Cain, M. Stewart, and M. G. Gee, "Experimental measurement methods for the evaluation of degradation in piezoelectric ceramics." Teddington, NPL Report, May 1998.

[143] G. K. Ottman, H. F. Hofmann, A. C. Bhatt, and G. A. Lesieutre, "Adaptive piezoelectric energy harvesting circuit for wireless remote power supply," *IEEE Transactions on Power Electronics*, vol. 17, no. 5, pp. 669–676, Sep. 2002.

[144] L. Padurariu, L. P. Curecheriu, and L. Mitoseriu, "Nonlinear dielectric properties of paraelectric-dielectric composites described by a 3D Finite Element Method based on Landau-Devonshire theory," *Acta Materialia*, vol. 103, pp. 724–734, Jan. 2016.

[145] C. Padurariu, L. Padurariu, L. Curecheriu, C. Ciomaga, N. Horchidan, C. Galassi, and L. Mitoseriu, "Role of the pore interconnectivity on the dielectric, switching and tunability properties of PZTN ceramics," *Ceramics International*, vol. 43, no. 7, pp. 5767–5773, May 2017.

[146] G. Pangallo, S. Rao, R. Carotenuto, and F. G. D. Corte, "Piezoelectric energy harvesting system for hostile environments," in *2016 12th Conference on Ph.D. Research in Microelectronics and Electronics (PRIME)*, Jun. 2016, pp. 1–3.

[147] K.-I. Park, M. Lee, Y. Liu, S. Moon, G.-T. Hwang, G. Zhu, J. E. Kim, S. O. Kim, D. K. Kim, Z. L. Wang, and K. J. Lee, "Flexible Nanocomposite Generator Made of BaTiO3 Nanoparticles and Graphitic Carbons," *Advanced Materials*, vol. 24, no. 22, pp. 2999–3004, 2012.

[148] Poonam, K. Sharma, A. Arora, and S. K. Tripathi, "Review of supercapacitors: Materials and devices," *Journal of Energy Storage*, vol. 21, pp. 801–825, Feb. 2019.

[149] S. Priya, "Criterion for material selection in design of bulk piezoelectric energy harvesters," *IEEE Transactions on Ultrasonics, Ferroelectrics, and Frequency Control*, vol. 57, no. 12, pp. 2610–2612, Dec. 2010.

[150] C. Racles, A. Bele, M. Dascalu, V. E. Musteata, C. D. Varganici, D. Ionita, S. Vlad, M. Cazacu, S. J. Dünki, and D. M. Opris, "Polar–nonpolar interconnected elastic networks with increased permittivity and high breakdown fields for dielectric elastomer transducers," *RSC Advances*, vol. 5, no. 72, pp. 58 428–58 438, Jul. 2015.

[151] W. Raither, A. Bergamini, F. Gandhi, and P. Ermanni, "Adaptive bending-twist coupling in laminated composite plates by controllable shear stress transfer," *Composites Part A: Applied Science and Manufacturing*, vol. 43, no. 10, pp. 1709–1716, Oct. 2012.

[152] M. Ramuz, B. C.-K. Tee, J. B.-H. Tok, and Z. Bao, "Transparent, Optical, Pressure-Sensitive Artificial Skin for Large-Area Stretchable Electronics," *Advanced Materials*, vol. 24, no. 24, pp. 3223–3227, 2012.

[153] H. Rao, D. Saxena, S. Kumar, G. V. Sagar, B. Amrutur, P. Mony, P. Thankachan, K. Shankar, S. Rao, and S. Bhat, "Low Power Remote Neonatal Temperature Monitoring Device." in *BIODEVICES*, 2014, pp. 28–38.

[154] A. P. Roberts and E. J. Garboczi, "Elastic Properties of Model Porous Ceramics," *Journal of the American Ceramic Society*, vol. 83, no. 12, pp. 3041–3048, 2000.

[155] J. I. Roscow, Y. Zhang, M. J. Kraśny, R. W. C. Lewis, J. Taylor, and C. R. Bowen, "Freeze cast porous barium titanate for enhanced piezoelectric energy harvesting," *Journal of Physics D: Applied Physics*, vol. 51, no. 22, p. 225301, 2018.

[156] J. I. Roscow, J. Taylor, and C. R. Bowen, "Manufacture and characterization of porous ferroelectrics for piezoelectric energy harvesting applications," *Ferroelectrics*, vol. 498, no. 1, pp. 40–46, Aug. 2016.

[157] J. I. Roscow, R. W. C. Lewis, J. Taylor, and C. R. Bowen, "Modelling and fabrication of porous sandwich layer barium titanate with improved piezoelectric energy harvesting figures of merit," *Acta Materialia*, 2017.

[158] J. Roscow, Y. Zhang, J. Taylor, and C. R. Bowen, "Porous ferroelectrics for energy harvesting applications," *The European Physical Journal Special Topics*, vol. 224, no. 14-15, pp. 2949–2966, Nov. 2015.

[159] S. Roundy and P. K. Wright, "A piezoelectric vibration based generator for wireless electronics," *Smart Materials and Structures*, vol. 13, no. 5, p. 1131, 2004.

[160] J. J. Ruan, R. A. Lockhart, P. Janphuang, A. V. Quintero, D. Briand, and N. de Rooij, "An Automatic Test Bench for Complete Characterization of Vibration-Energy Harvesters," *IEEE Transactions on Instrumentation and Measurement*, vol. 62, no. 11, pp. 2966–2973, Nov. 2013.

[161] X. Rui, Z. Zeng, Y. Zhang, Y. Li, H. Feng, X. Huang, and Z. Sha, "Design and Experimental Investigation of a Self-Tuning Piezoelectric Energy Harvesting System for Intelligent Vehicle Wheels," *IEEE Transactions on Vehicular Technology*, vol. 69, no. 2, pp. 1440–1451, Feb. 2020.

[162] S. Saadon and O. Sidek, "A review of vibration-based MEMS piezoelectric energy harvesters," *Energy Conversion and Management*, vol. 52, no. 1, pp. 500–504, Jan. 2011.

[163] M. Safaei, H. A. Sodano, and S. R. Anton, "A review of energy harvesting using piezoelectric materials: State-of-the-art a decade later (2008–2018)," *Smart Materials and Structures*, vol. 28, no. 11, p. 113001, Oct. 2019.

[164] A. Safari, M. Allahverdi, and E. K. Akdogan, "Solid freeform fabrication of piezoelectric sensors and actuators," *Journal of Materials Science*, vol. 41, no. 1, pp. 177–198, Jan. 2006.

[165] R. Salazar, M. Serrano, and A. Abdelkefi, "Fatigue in piezoelectric ceramic vibrational energy harvesting: A review," *Applied Energy*, vol. 270, p. 115161, Jul. 2020.

[166] A. Samur and A. Erturk, "Multifunctional double-bimorph piezoelectric composite for bending-twisting actuation, adaptive stiffness change, and energy harvesting," in *54th AIAA/ASME/ASCE/AHS/ASC Structures, Structural Dynamics, and Materials Conference*. American Institute of Aeronautics and Astronautics.

[167] E. Sazonov, H. Li, D. Curry, and P. Pillay, "Self-Powered Sensors for Monitoring of Highway Bridges," *IEEE Sensors Journal*, vol. 9, no. 11, pp. 1422–1429, Nov. 2009.

[168] J. Scruggs, "On the Causal Power Generation Limit for a Vibratory Energy Harvester in Broadband Stochastic Response," *Journal of Intelligent Material Systems and Structures*, vol. 21, no. 13, pp. 1249–1262, Sep. 2010.

[169] J. Seuba, S. Deville, C. Guizard, and A. J. Stevenson, "Mechanical properties and failure behavior of unidirectional porous ceramics," *Scientific Reports*, vol. 6, no. 1, p. 24326, Apr. 2016.

[170] F. K. Shaikh and S. Zeadally, "Energy harvesting in wireless sensor networks: A comprehensive review," *Renewable and Sustainable Energy Reviews*, vol. 55, pp. 1041–1054, Mar. 2016.

[171] X. Shan, J. Deng, R. Song, and T. Xie, "A Piezoelectric Energy Harvester with Bending–Torsion Vibration in Low-Speed Water," *Applied Sciences*, vol. 7, no. 2, p. 116, Jan. 2017.

[172] N. O. Shanti, K. Araki, and J. W. Halloran, "Particle Redistribution During Dendritic Solidification of Particle Suspensions," *Journal of the American Ceramic Society*, vol. 89, no. 8, pp. 2444–2447, 2006.

[173] S. Shao, W. C. Lien, A. Maralani, and A. P. Pisano, "Integrated 4H-silicon carbide diode bridge rectifier for high temperature (773 K) environment," in *2014 44th European Solid State Device Research Conference (ESSDERC)*, Sep. 2014, pp. 138–141.

[174] T. Sharma, S.-S. Je, B. Gill, and J. X. J. Zhang, "Patterning piezoelectric thin film PVDF–TrFE based pressure sensor for catheter application," *Sensors and Actuators A: Physical*, vol. 177, pp. 87–92, Apr. 2012.

[175] N. Sharpes, A. Abdelkefi, H. Abdelmoula, P. Kumar, J. Adler, and S. Priya, "Mode shape combination in a two-dimensional vibration energy harvester through mass loading structural modification," *Applied Physics Letters*, vol. 109, no. 3, p. 033901, Jul. 2016.

[176] C. P. Shaw, R. W. Whatmore, and J. R. Alcock, "Porous, Functionally Gradient Pyroelectric Materials," *Journal of the American Ceramic Society*, vol. 90, no. 1, pp. 137–142, 2007.

[177] T. Shiraishi, N. Kaneko, M. Kurosawa, H. Uchida, Y. Suzuki, T. Kobayashi, and H. Funakubo, "Vibration-energy-harvesting properties of hydrothermally synthesized (K,Na)NbO3 films deposited on flexible metal foil substrates," *Japanese Journal of Applied Physics*, vol. 54, no. 10S, p. 10ND06, Sep. 2015.

[178] Y. C. Shu and I. C. Lien, "Analysis of power output for piezoelectric energy harvesting systems," *Smart Materials and Structures*, vol. 15, no. 6, p. 1499, 2006.

[179] Y. Song, Y. Shen, H. Liu, Y. Lin, M. Li, and C.-W. Nan, "Enhanced dielectric and ferroelectric properties induced by dopamine-modified BaTiO3 nanofibers in flexible poly(vinylidene fluoride-trifluoroethylene) nanocomposites," *Journal of Materials Chemistry*, vol. 22, no. 16, pp. 8063–8068, Mar. 2012.

[180] M. Stewart, M. Battrick, and M. G. Cain, "Measuring piezoelectric d33 coefficients using the direct method," NPL, Teddington, Measurement Good Practice Guide Guide No. 44, Jun. 2001.

[181] Y. Su, C. Dagdeviren, and R. Li, "Measured Output Voltages of Piezoelectric Devices Depend on the Resistance of Voltmeter," *Advanced Functional Materials*, vol. 25, no. 33, pp. 5320–5325, Sep. 2015.

[182] Y. Sun, J. Chen, X. Li, Y. Lu, S. Zhang, and Z. Cheng, "Flexible piezoelectric energy harvester/sensor with high voltage output over wide temperature range," *Nano Energy*, vol. 61, pp. 337–345, Jul. 2019.

[183] Y. Su, S. Li, Y. Huan, R. Li, Z. Zhang, P. Joe, and C. Dagdeviren, "The universal and easy-to-use standard of voltage measurement for quantifying the performance of piezoelectric devices," *Extreme Mechanics Letters*, vol. 15, pp. 10–16, 2017.

[184] G. D. Szarka, S. G. Burrow, and B. H. Stark, "Ultralow Power, Fully Autonomous Boost Rectifier for Electromagnetic Energy Harvesters," *IEEE Transactions on Power Electronics*, vol. 28, no. 7, pp. 3353–3362, Jul. 2013.

[185] T. R. Licht, H. Andersen, and H. B. Jensen, "Recent Developments in Accelerometer Design," *Bruel Kjaer Technical Review*, vol. 2, no. 1, pp. 1–22, 1987.

[186] Y. Tan, J. Zhang, Y. Wu, C. Wang, V. Koval, B. Shi, H. Ye, R. McKinnon, G. Viola, and H. Yan, "Unfolding grain size effects in barium titanate ferroelectric ceramics," *Scientific Reports*, vol. 5, no. 1, p. 9953, May 2015.

[187] J. F. Tressler, S. Alkoy, and R. E. Newnham, "Piezoelectric Sensors and Sensor Materials," *Journal of Electroceramics*, vol. 2, no. 4, pp. 257–272, Dec. 1998.

[188] Y. Uchiyama and M. Fujita, "Robust acceleration and displacement control of electrodynamic shaker," in *2006 IEEE Conference on Computer Aided Control System Design, 2006 IEEE International Conference on Control Applications, 2006 IEEE International Symposium on Intelligent Control*, Oct. 2006, pp. 746–751.

[189] M. Vázquez-Rodriguez, F. J. Jiménez, J. de Frutos, and D. Alonso, "Piezoelectric energy harvesting computer controlled test bench," *Review of Scientific Instruments*, vol. 87, no. 9, p. 095004, Sep. 2016.

[190] S. Wada, K. Takeda, T. Muraishi, H. Kakemoto, T. Tsurumi, and T. Kimura, "Preparation of [110] Grain Oriented Barium Titanate Ceramics by Templated Grain Growth Method and Their Piezoelectric Properties," *Japanese Journal of Applied Physics*, vol. 46, no. 10S, p. 7039, Oct. 2007.

[191] M. Walport, "The Internet of Things: Making the most of the Second Digital Revolution," Government Office for Science, Tech. Rep. GS/14/1230, Dec. 2014.

[192] H.-y. Wang, L.-h. Tang, Y. Guo, X.-b. Shan, and T. Xie, "A 2DOF hybrid energy harvester based on combined piezoelectric and electromagnetic conversion mech-

anisms," *Journal of Zhejiang University SCIENCE A*, vol. 15, no. 9, pp. 711–722, Sep. 2014.

[193] X. Wang, J. Song, J. Liu, and Z. L. Wang, "Direct-current nanogenerator driven by ultrasonic waves," *Science*, vol. 316, no. 5821, pp. 102–105, 2007.

[194] Y. Wang, Y. Jia, Q. Chen, and Y. Wang, "A Passive Wireless Temperature Sensor for Harsh Environment Applications," *Sensors*, vol. 8, no. 12, pp. 7982–7995, Dec. 2008.

[195] A. Wang, Z. Liu, M. Hu, C. Wang, X. Zhang, B. Shi, Y. Fan, Y. Cui, Z. Li, and K. Ren, "Piezoelectric nanofibrous scaffolds as in vivo energy harvesters for modifying fibroblast alignment and proliferation in wound healing," *Nano Energy*, vol. 43, pp. 63–71, Jan. 2018.

[196] Z. L. Wang and J. Song, "Piezoelectric Nanogenerators Based on Zinc Oxide Nanowire Arrays," *Science*, vol. 312, no. 5771, pp. 242–246, Apr. 2006.

[197] Z. L. Wang, J. Chen, and L. Lin, "Progress in triboelectric nanogenerators as a new energy technology and self-powered sensors," *Energy & Environmental Science*, vol. 8, no. 8, pp. 2250–2282, Jul. 2015.

[198] A. Wang, M. Hu, L. Zhou, and X. Qiang, "Self-Powered Well-Aligned P(VDF-TrFE) Piezoelectric Nanofiber Nanogenerator for Modulating an Exact Electrical Stimulation and Enhancing the Proliferation of Preosteoblasts," *Nanomaterials*, vol. 9, no. 3, p. 349, Mar. 2019.

[199] W. Wang, T. Yang, X. Chen, and X. Yao, "Vibration energy harvesting using a piezoelectric circular diaphragm array," *IEEE Transactions on Ultrasonics, Ferroelectrics, and Frequency Control*, vol. 59, no. 9, pp. 2022–2026, Sep. 2012.

[200] T. Waschkies, R. Oberacker, and M. J. Hoffmann, "Control of Lamellae Spacing During Freeze Casting of Ceramics Using Double-Side Cooling as a Novel Processing Route," *Journal of the American Ceramic Society*, vol. 92, no. s1, pp. S79–S84, 2009.

[201] J. Watson and G. Castro, "A review of high-temperature electronics technology and applications," *Journal of Materials Science: Materials in Electronics*, vol. 26, no. 12, pp. 9226–9235, Jul. 2015.

[202] P. M. Weaver, T. Stevenson, T. Quast, G. Bartl, T. Schmitz-Kempen, P. Woolliams, A. Blumfield, M. Stewart, and M. G. Cain, "High temperature measurement

and characterisation of piezoelectric properties," *Journal of Materials Science: Materials in Electronics*, vol. 26, no. 12, pp. 9268–9278, Dec. 2015.

[203] M. Wu, Y. Ou, H. Mao, Z. Li, R. Liu, A. Ming, and W. Ou, "Multi-resonant wideband energy harvester based on a folded asymmetric M-shaped cantilever," *AIP Advances*, vol. 5, no. 7, p. 077149, Jul. 2015.

[204] Y. Wu, A. Badel, F. Formosa, W. Liu, and A. Agbossou, "Self-powered optimized synchronous electric charge extraction circuit for piezoelectric energy harvesting:," *Journal of Intelligent Material Systems and Structures*, Jan. 2014.

[205] X. Wu, Y. Ma, G. Zhang, Y. Chu, J. Du, Y. Zhang, Z. Li, Y. Duan, Z. Fan, and J. Huang, "Thermally Stable, Biocompatible, and Flexible Organic Field-Effect Transistors and Their Application in Temperature Sensing Arrays for Artificial Skin," *Advanced Functional Materials*, vol. 25, no. 14, pp. 2138–2146, 2015.

[206] Z. Xiao, T. qing Yang, Y. Dong, and X. cai Wang, "Energy harvester array using piezoelectric circular diaphragm for broadband vibration," *Applied Physics Letters*, vol. 104, no. 22, p. 223904, Jun. 2014.

[207] M. Xie, Y. Zhang, M. J. Kraśny, A. Rhead, C. Bowen, and M. Arafa, "Energy harvesting from coupled bending-twisting oscillations in carbon-fibre reinforced polymer laminates," *Mechanical Systems and Signal Processing*, vol. 107, pp. 429–438, Jul. 2018.

[208] M. Xie, Y. Zhang, M. J. Kraśny, C. Bowen, H. Khanbareh, and N. Gathercole, "Flexible and active self-powered pressure, shear sensors based on freeze casting ceramic–polymer composites," *Energy & Environmental Science*, Jul. 2018.

[209] S. Xu, Y.-w. Yeh, G. Poirier, M. C. McAlpine, R. A. Register, and N. Yao, "Flexible Piezoelectric PMN–PT Nanowire-Based Nanocomposite and Device," *Nano Letters*, vol. 13, no. 6, pp. 2393–2398, Jun. 2013.

[210] R. Xu, A. Lei, C. Dahl-Petersen, K. Hansen, M. Guizzetti, K. Birkelund, E. V. Thomsen, and O. Hansen, "Screen printed PZT/PZT thick film bimorph MEMS cantilever device for vibration energy harvesting," *Sensors and Actuators A: Physical*, vol. 188, pp. 383–388, 2012.

[211] C. Yan, W. Deng, L. Jin, T. Yang, Z. Wang, X. Chu, H. Su, J. Chen, and W. Yang, "Epidermis-Inspired Ultrathin 3D Cellular Sensor Array for Self-Powered Biomedical Monitoring," *ACS Applied Materials & Interfaces*, vol. 10, no. 48, pp. 41 070–41 075, Dec. 2018.

[212] Q. Yang, Y. Liu, C. Pan, J. Chen, X. Wen, and Z. L. Wang, "Largely enhanced efficiency in ZnO nanowire/p-polymer hybridized inorganic/organic ultraviolet light-emitting diode by piezo-phototronic effect," *Nano letters*, vol. 13, no. 2, pp. 607–613, 2013.

[213] A. Yang, C.-A. Wang, R. Guo, Y. Huang, and C.-W. Nan, "Porous PZT Ceramics with High Hydrostatic Figure of Merit and Low Acoustic Impedance by TBA-Based Gel-Casting Process," *Journal of the American Ceramic Society*, vol. 93, no. 5, pp. 1427–1431, 2010.

[214] Y. Yang, Y. Zhou, J. M. Wu, and Z. L. Wang, "Single Micro/Nanowire Pyroelectric Nanogenerators as Self-Powered Temperature Sensors," *ACS Nano*, vol. 6, no. 9, pp. 8456–8461, Sep. 2012.

[215] C. B. York and S. F. M. de Almeida, "On Extension-Shearing Bending-Twisting coupled laminates," *Composite Structures*, vol. 164, pp. 10–22, Mar. 2017.

[216] R. Yu, C. Pan, J. Chen, G. Zhu, and Z. L. Wang, "Enhanced Performance of a ZnO Nanowire-Based Self-Powered Glucose Sensor by Piezotronic Effect," *Advanced Functional Materials*, vol. 23, no. 47, pp. 5868–5874, 2013.

[217] T. Zeng, X. Dong, C. Mao, Z. Zhou, and H. Yang, "Effects of pore shape and porosity on the properties of porous PZT 95/5 ceramics," *Journal of the European Ceramic Society*, vol. 27, no. 4, pp. 2025–2029, Jan. 2007.

[218] T. Zeng, X. Dong, S. Chen, and H. Yang, "Processing and piezoelectric properties of porous PZT ceramics," *Ceramics International*, vol. 33, no. 3, pp. 395–399, Apr. 2007.

[219] L. Zhang, R. Takei, J. Lu, N. Makimoto, T. Itoh, and T. Kobayashi, "Development of energy harvesting MEMS vibration device sensor with wideband response function in low-frequency domain," *Microsystem Technologies*, Mar. 2019.

[220] R. Zhang, B. Jiang, and W. Cao, "Elastic, piezoelectric, and dielectric properties of multidomain 0.67Pb(Mg1/3Nb2/3)O3–0.33PbTiO3 single crystals," *Journal of Applied Physics*, vol. 90, no. 7, pp. 3471–3475, Oct. 2001.

[221] Y. Zhang, X. Liu, G. Wang, Y. Li, S. Zhang, D. Wang, and H. Sun, "Enhanced mechanical energy harvesting capability in sodium bismuth titanate based lead-free piezoelectric," *Journal of Alloys and Compounds*, vol. 825, p. 154020, Jun. 2020.

[222] Y. Zhang, M. Xie, J. Roscow, Y. Bao, K. Zhou, D. Zhang, and C. R. Bowen, "Enhanced pyroelectric and piezoelectric properties of PZT with aligned porosity for energy harvesting applications," *Journal of Materials Chemistry A*, vol. 5, no. 14, pp. 6569–6580, Apr. 2017.

[223] G. Zhang, P. Zhao, X. Zhang, K. Han, T. Zhao, Y. Zhang, C. K. Jeong, S. Jiang, S. Zhang, and Q. Wang, "Flexible three-dimensional interconnected piezoelectric ceramic foam based composites for highly efficient concurrent mechanical and thermal energy harvesting," *Energy & Environmental Science*, vol. 11, no. 8, pp. 2046–2056, Aug. 2018.

[224] H. L. Zhang, J.-F. Li, and B.-P. Zhang, "Microstructure and electrical properties of porous PZT ceramics derived from different pore-forming agents," *Acta Materialia*, vol. 55, no. 1, pp. 171–181, Jan. 2007.

[225] K. Zhang, S. Wang, and Y. Yang, "A One-Structure-Based Piezo-Tribo-Pyro-Photoelectric Effects Coupled Nanogenerator for Simultaneously Scavenging Mechanical, Thermal, and Solar Energies," *Advanced Energy Materials*, vol. 7, no. 6, p. 1601852, 2017.

[226] Y. Zhang, Y. Bao, D. Zhang, and C. R. Bowen, "Porous PZT Ceramics with Aligned Pore Channels for Energy Harvesting Applications," *Journal of the American Ceramic Society*, vol. 98, no. 10, pp. 2980–2983, Oct. 2015.

[227] G. Zhang, Q. Liao, M. Ma, Z. Zhang, H. Si, S. Liu, X. Zheng, Y. Ding, and Y. Zhang, "A rationally designed output current measurement procedure and comprehensive understanding of the output characteristics for piezoelectric nanogenerators," *Nano Energy*, vol. 30, pp. 180–186, Dec. 2016.

[228] Y. Zhao, Q. Liao, G. Zhang, Z. Zhang, Q. Liang, X. Liao, and Y. Zhang, "High output piezoelectric nanocomposite generators composed of oriented BaTiO3 NPs@PVDF," *Nano Energy*, vol. 11, pp. 719–727, Jan. 2015.

[229] L. Zhao, "Synchronization extension using a bistable galloping oscillator for enhanced power generation from concurrent wind and base vibration," *Applied Physics Letters*, vol. 116, no. 5, p. 053904, Feb. 2020.

[230] Q. Zheng, H. Tu, A. Agee, and Y. Xu, "Vibration energy harvesting device based on asymmetric air-spaced cantilevers for tire pressure monitoring system," *Proceedings of power MEMS*, pp. 403–406, 2009.

[231] M. Zhou, M. S. H. Al-Furjan, J. Zou, and W. Liu, "A review on heat and mechanical energy harvesting from human – Principles, prototypes and perspectives," *Renewable and Sustainable Energy Reviews*, vol. 82, pp. 3582–3609, Feb. 2018.

[232] Z. Zhou, H. Tang, and H. A. Sodano, "Vertically Aligned Arrays of BaTiO3 Nanowires," *ACS Applied Materials & Interfaces*, vol. 5, no. 22, pp. 11 894–11 899, Nov. 2013.

[233] D. Zhu, S. P. Beeby, M. J. Tudor, and N. R. Harris, "A credit card sized self powered smart sensor node," *Sensors and Actuators A: Physical*, vol. 169, no. 2, pp. 317–325, Oct. 2011.